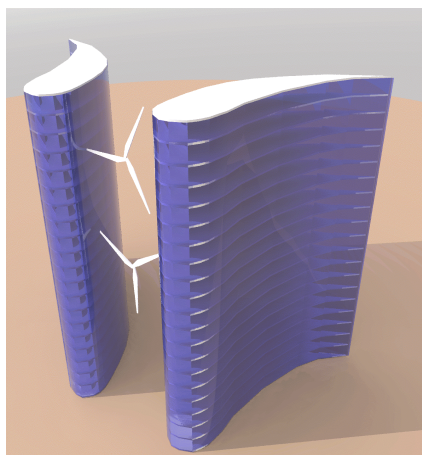# Wind Energy in the Built Environment

Concentrator Effects of Buildings

Sander Mertens

Wind Energy in the Built Environment

Concentrator Effects of Buildings

Proefschrift

ter verkrijging van de graad van doctor
aan de Technische Universiteit Delft,
op gezag van de Rector Magnificus prof. dr. ir. J.T. Fokkema,
voorzitter van het College voor Promoties,
in het openbaar te verdedigen op dinsdag 5 september 2006 om 15.00 uur
door Sander MERTENS
werktuigkundig ingenieur en natuurkundig ingenieur
geboren te Haarlem

Dit proefschrift is goedgekeurd door de promotor:
Prof.dr.ir. G.A.M. van Kuik

Toegevoegd promotor:
Dr. G.J.W. van Bussel

Samenstelling promotiecommissie:

Rector Magnificus, voorzitter
Prof.dr.ir. G.A.M. van Kuik, Technische Universiteit Delft, promotor
Dr. G.J.W. van Bussel, Technische Universiteit Delft, toegevoegd promotor
Prof.dr.ir. M.H. de Wit, Technische Universiteit Eindhoven
Prof.dr.ir. Th. Van Holten, Technische Universiteit Delft
Prof.dr.I. Paraschivoiu, Ecole Polytechnique de Montreal
Prof. J. Twidell, De Montfort University
Prof. dr. M. Graham, Imperial College, London

Cover pictures: artist impressions of the three main principles of power augmentation. From left to right: close to a building (visualization: author), between airfoil-shaped buildings (visualization: dr.ir. L. Aanen, DHV) and in a duct through a building (visualization: author).

Summary

This thesis deals with wind energy conversion in the built environment. It gives a description of the wind resources in the built environment that can be converted into energy by a wind turbine. With a focus on maximum energy yield of the wind turbine, it especially deals with the integration of wind turbine and building in such a way that the building concentrates the wind energy for the wind turbine. Three different basic principles of such "buildings that concentrate the wind" or concentrators are distinguished:

- wind turbines at the roof or sides of buildings,
- wind turbines between two airfoil-shaped buildings,
- wind turbines in ducts through buildings.

The aerodynamics of those three concentrators with their possible wind turbines are investigated with a focus on integration resulting in maximum energy yield of the wind turbine.

The complicated concentrator effects of buildings in the actual flow are simplified to their basic aerodynamic qualities in parallel flow. The properties of these simplified qualities in parallel flow are explored through the three well-known cornerstones of aerodynamic research: mathematical models, verification with measurements and numerical simulations of the flow. The mathematical models are derived with simplified mathematical flow descriptions. The measurements are carried out in the open jet wind tunnel of Delft University of Technology, section Wind Energy and the simulations are performed with a commercial Computational Fluid Dynamics (CFD) code, which solved the basic flow equations numerically. The advantages of both verification tools: measurement and CFD calculation are exploited by pre-selecting the tool with the best prospects for an accurate result in a desired situation.

This thesis gives a broad description of the most important issues concerning the energy yield of a wind turbine in the built environment. It provides descriptions of the average/ global wind speed in the built environment, the local wind speed, the wind speed near buildings and verification of the mathematical models of the three possible concentrator principles mentioned above. Furthermore, it provides information on suitable wind turbines for use in the built environment. The pros and cons of the three concentrator principles are summarized, without mathematics, in the last chapter. This last chapter shows that the "at roofs of buildings" configuration and a variation on the "in ducts through buildings" configuration are promising.

Concerning the "at roofs of buildings" configuration, a sphere-like building concentrates the energy in omnidirectional free stream wind the most: a factor of three to four! Such concentrators are able to overcome the problem of the low average wind speed in the built environment and enable energy yields comparable to rural areas. A variation on the "in ducts through buildings" configuration, two ducted ellipsoids in a cross with the duct at the cross centre, is able to concentrate the energy in omnidirectional free stream wind with a factor of approximately one and a half. The other concentrators provide a smaller energy concentration. The "close to a building" configuration is very efficient in using the acceleration by the building and it is a relatively cheap solution compared to the other possible concentrator principles. Still, this thesis shows that the energy yield for all concentrator configurations is limited because the wind turbines can only profit from the concentrator effects when they are relatively small compared to the building. Yet, they deliver the energy, where it is needed, the built environment, and their energy yield is felt as an energy saving in the building. Consequently, their energy yield is reflected in energy savings on the customer's bill from the utility company, which is a higher reimbursement compared to rural areas. It is thus concluded that wind energy conversion in the built environment making use of the concentrator effects of buildings, is a promising renewable energy source.

Table of contents

List of Symbols

All dimensions of quantities used in this book are consistent with the System International (SI). The dimensions of frequently used quantities and the definition of the quantities are given hereafter. The dimension of a quantity is mentioned at the introduction of the quantity.

a	induction factor, scale parameter in probability distribution	., m/s
A	area	m^2
A_e	area of the stream tube at infinite distance downwind of the rotor	m^2
A_H	percentage of earth surface occupied with obstacles	.
A_r	aspect ratio	.
A_t	rotor swept area	m^2
A_0	area of the stream tube at infinite distance upwind of the rotor	m^2
B	number of blades of the rotor	.
c	chord length airfoil	m
$C_{c,i}$	probability on a certain wind speed from sector i	.
C_d	drag coefficient	.
C_l	lift coefficient of an airfoil	.
C_p	pressure coefficient defined as $C_p = (p - p_0)/(\frac{1}{2}\rho u_0^2)$	.
C_P	power coefficient defined as $C_P = P/(\frac{1}{2}\rho u_0^3 A_t)$	.
$C_{r,i}$	acceleration of free stream reference wind speed	.
C_T	thrust force coefficient	.
d	displacement height	m
D	characteristic size	m
D_t	rotor diameter	m
E	energy yield	kWh
f	vortex shedding frequency, probability distribution of accelerated wind	Hz
f_0	Weibull distribution of reference or free stream free stream wind	.
F_t	thrust force of a wind turbine	N
F_{Bl}	thrust force calculated with blade element theory	N
F_D	drag force	N
F_M	thrust force calculated with momentum theory	N
h	height	m
h_k	kink height or height of the internal boundary layer	m
h_s	height of the single-rotor part	m
h_d	height of the double-rotor part	m
H	building height	m
H_s	stagnation point height	m
H_t	rotor height (Vertical Axis Wind Turbine)	m
I	turbulence intensity	.
k	shape parameter in probability distribution, turbulent kinetic energy	.
K	resistance factor of wire screen	
L	lift force	N
L_c	cavity length	m
L_P	pressure level at location P	N/m^2

L_W	source sound pressure level	dB
n	number of revolutions	Hz
p	static pressure	N/m^2
p_0	free stream or free stream static pressure	N/m^2
P	power	W
Q	torque	Nm
r	radius	m
R	radius	m
R_t	rotor radius	m
Re	Re number	.
s	distance along a free streamline	m
S	Strouhal number	.
T	Time corresponding with the energy yield	s
$u(z)$	horizontal wind speed	m/s
u_p	potential wind speed	m/s
u_r	resultant velocity	m/s
u_*	friction velocity	m/s
u_w	velocity at the ¾-chord point on the airfoil	m/s
v	vertical velocity, lateral velocity	m/s
W	building width	m
x	axial coordinate	m
y	lateral coordinate	m
z	vertical coordinate	m
z_0	roughness height	m

Subscripts

0	free stream, reference or free stream
d	double-rotor part
e	end or infinite downwind of actuator
i	induced
s	separation, single-rotor part
t	at rotor or actuator
max	maximum
min	minimum
opt	optimal i.e. resulting in a maximum
ref	reference
+	upwind
-	downwind

Superscripts

'	fluctuations in turbulent velocity
*	non-dimensional distance or velocity

Greek

α	angle of attack of the flow on the airfoil	rad or deg
β	jet contraction/ expansion	.
γ	vortex strength per metre	m/s
γ	skew angle	rad or deg
Γ	Gamma function, vortex strength	., m^2/s

δ	boundary layer height	m
λ	ratio of tip speed and free stream wind speed	
ρ	density of air	kg/m^3

1 Introduction

The Energy Information Administration [13] stated that the industrialized countries used more than half the world's total energy consumption in 2001. They are the big consumers and have the prosperity and knowledge to switch to renewable energy sources. Moreover, most people in the industrialized countries are aware of the vanishing fossil energy reserves and the environmental impact of the huge consumption of fossil energy nowadays. Changes in energy source and consumption behaviour will probably be initiated here. Consequently, the need for renewable energy in prosperous countries will rise.

It is not certain that the temperature rise in the last decade is caused by the emission of carbon dioxide from burning fossil energy reserves. Experts differ in their opinion whether or not climate change is a result of our pollution (see for instance [87]). Nevertheless, there are serious indications that the consequences of the greenhouse effect may not allow the burning of our fossil energy reserves. The earth's population increases rapidly and energy demand follows. The Energy Information Administration [13] predicts an average annual two percent increase in energy consumption over the coming twenty years largely realized using fossil energy. Why should we take the risk of encountering severe environmental problems? The risk by itself should be enough to switch to renewable energy. But there are more reasons to switch to renewable energy instead of fossil energy. Fossil reserves vanish. Experts [88] predict a peak in production of fossil energy in approximately 5 years. Again, there is much controversy on the timeframe since this largely depends on the definition of our reserves and our energy consumption in the future. Nevertheless, in the future production decreases while consumption increases. This will have a huge impact on energy prices and community. Not "running out" but "peak production" of fossil energy determines the turning point. Furthermore, the unstable situation in the Middle East is responsible for considerable variations in the fossil energy price since we largely depend on their fossil fuel production. A switch to renewable energy can decrease our dependence. However, there is another important reason for switching to renewable energy from fossil energy: the cost of the energy. A fair comparison of the price of energy should be based on the total cost of energy. This includes external costs, such as the costs of people getting ill because of pollution. That is certainly difficult to estimate, but as stated in Chandler [11] "to not incorporate externalities in prices … is demonstrably wrong". Among others, Chandler [11] gives an example of Denmark where the total costs (including external costs) of a kWh fossil energy from coal (7-10 c€/kWh) are higher than that of a kWh wind energy (4-4.5 c€/kWh).

Thus, several strong forces indicate the increased use of renewable energy in the future. Yet, we are used to fossil energy availability and energy density and consume it accordingly but renewable energy sources have a much lower energy density. We need large areas with renewable energy production units. It is just not that easy to fulfil our current energy needs, let alone our future energy needs, with renewable energy. We cannot afford to rely on a few large renewable sources. Every possible renewable energy source has its place and should be utilized. Moreover, it is also wise to diversify the sources (solar, wind, hydro, biomass, geothermal) in order to provide a constant energy source. For instance, wind energy combined with solar energy provides a more constant renewable energy supply since there are stronger winds during the winter when there is less sun. The energy supply system will change to a decentralized one in the future: another very drastic change, which needs a huge effort from the technical community. It does not make sense to deliver a huge effort in producing renewable energy, and then to consume it carelessly. We should combine renewable energy production with decreased energy consumption.

According to the Buildings Energy Data book [7] and the Ministry of Housing, Spatial Planning and the Environment VROM [77], buildings consume up to roughly 40% of total energy consumption, and a lot of work is going on to reduce this. Several pioneers have

introduced Zero Energy Design (ZED) or Lower Energy Design (LED) buildings to avoid the high energy consumption by buildings. However, the enthusiasm for LED buildings is not always voluntary but sometimes enforced by law. In the Netherlands for instance, an energy performance coefficient EPC (see VROM [77]) is used to enforce a reduction of energy consumption by buildings. The ZED or LED buildings use a local -with the building integrated- renewable energy source and have a low energy demand. After all, why not generate the energy where it is needed and at the same time avoid transport costs and horizon pollution in the rural areas? Moreover, small renewable energy sources integrated with buildings result in less energy consumption from the utility. Consequently, they are reimbursed with the customer price of the utility: a roughly three times higher price than the one paid by the utility for large renewable energy sources in rural areas (Mertens [46]). On the other hand, the motives for integrating renewable energy sources with buildings are not only driven by the forementioned environmental issues. Architecture has always reflected society trends and one of those trends nowadays certainly concerns the need to use renewable energy (Mertens [46]).

Wind energy is one of the possible renewable energy sources for the built environment. Comparison of earth's surface of the built environment with the earth's surface in rural areas shows that the latter is much smoother. In other words, the built environment has a high roughness compared to rural areas. This high roughness causes a small wind speed in the built environment compared to the wind speed in rural areas. Some local acceleration of the wind is needed in order to have a viable energy yield in the built environment. The wind speed around taller buildings can be appreciably higher than the average free stream wind speed in the built environment. Maybe it is possible to utilize this effect and design buildings with dedicated wind turbines in order to use the increase of the average free stream wind speed. The building is thus more than a mast for the wind turbine: it is used as a concentrator of the wind energy for the wind turbine. Normally concentrators have doubtful economics. It is not viable to build an expensive concentrator if one could easily make the rotor somewhat bigger to create more power. However, if the concentrator is available without large extra expenses as with buildings that are built anyway, it is clear that one should use this opportunity. The category of wind turbines thus provided with concentrated wind energy will be called the Building-Augmented Wind Turbine (BAWT). This thesis explains the aerodynamics of the BAWT's, concentrator buildings and wind in the built environment. From this aerodynamical background, the promising configurations for wind energy conversion in the built environment are identified.

This thesis deals with "wind energy conversion in the built environment". It thus contains three main topics: wind energy, wind energy conversion and built environment. The built environment is analogous to an environment with a high roughness. Therefore, a large part of this thesis is also instructive for those interested in wind or wind energy conversion in an environment with a high roughness. The thesis is divided into 8 chapters. Apart from the introduction in chapter 1, the chapters 2 and 8 avoid lengthy mathematical calculations. Chapter 2 collects the boundary conditions of wind energy conversion in the built environment and forms the departure of the research. The boundary conditions are analysed in more detail in chapter 3 to 7, which provide mathematical models on wind energy conversion in the built environment. The detailed analysis starts with a description of the wind in chapter 3. Chapter 4 gives the analysis tools used in the research. Chapter 5 to 7 provide mathematical models for the basic concentrators available in the built environment. Chapter 8 summarizes the main results of the thesis and compares the main options for wind energy conversion in the built environment. A quick siting guideline based on this summary can be found in Appendix J.

2 Basic theory

The boundary conditions of the three main topics: wind energy, wind energy conversion and built environment introduce the possibilities and impossibilities for wind energy conversion in the built environment. From these boundary conditions, this chapter formulates the point of departure in search of feasible options for "wind energy conversion in the built environment".

2.1 Drag-driven rotor versus lift-driven rotor

The wind turbines considered in this thesis are intended for the production of electricity. The work is thus directed to the energy yield of the wind turbines in relation to the costs of the wind turbine. Modern wind turbines are sited in open rural areas and look alike: they have a horizontal axis with a three-bladed rotor. Indeed, for open rural areas, this rotor has some advantages compared to other rotor types. Wind turbines for the built environment however are sited differently. Consequently, they do not necessarily need the same rotor. We thus need to study the rotor in somewhat more detail.

There are two ways to convert wind energy into mechanical power in the rotor axis. The conversion can be realized with a drag-driven rotor, a lift-driven rotor or a combination of both concepts: the hybrid rotor. The conversion mechanism of wind power into mechanical power of the lift-driven and drag-driven rotor is different. A lift-driven wind turbine can be a horizontal axis wind turbine (Figure 2, left) or a vertical axis wind turbine (Figure 4, right). The drag-driven wind turbines have a vertical axis (Figure 4, left). They show no clear wake.

It will be shown that the rotor concept is important for the efficiency of the conversion. This efficiency or power coefficient C_P of a rotor is defined as

$$C_P = \frac{P}{\frac{1}{2}\rho u_0^3 A_t} \tag{1}$$

In this equation, P is the mechanical power at the rotor axis, A_t is the swept area of the rotor, $\frac{1}{2}\rho u_0^3$ is the power of the incoming free stream wind per square metre rotor area, ρ is the density of the air and u_0 is the free stream wind speed.

2.1.1   Drag-driven wind turbines

The driving force of the drag-driven rotor originates from the difference in drag of (rotating) bluff bodies. Figure 1 shows an example of a drag-driven rotor. It consists of cups. The cup with the spherical upwind side has the lowest drag of both cups. Hence, this cup dissipates power as it moves in the direction of the wind, while the other cup that moves downwind produces power. It is thus characteristic for the drag-driven rotor that the power is produced with a body that moves downwind.
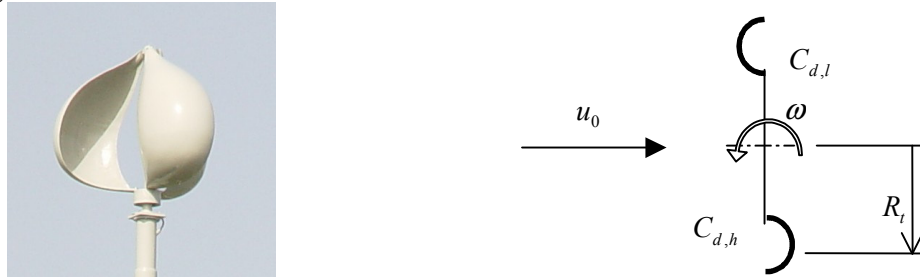
Figure 1 Example of a drag-driven wind turbine (left) and schematic top view of a similar rotor (right).

The torque Q of the rotor axis follows from the difference in drag of the turning bluff bodies. It is clear from the schematic configuration in Figure 1 that the relative velocities on the turning bodies should be used to calculate the drag. At the depicted orientation in Figure 1 (right), the torque of the rotor axis per square metre rotor area is found from

$$Q = C_{d,h} \tfrac{1}{2} \rho (u_0 - \omega R_t)^2 R_t - C_{d,l} \tfrac{1}{2} \rho (u_0 + \omega R_t)^2 R_t \tag{2}$$

where the constants $C_{d,h}$ and $C_{d,l}$ are the drag coefficients of the rotating bluff bodies or cups. A first order approximation for the power of the rotor is found by assuming a pure translation of the cups with assumed constant relative velocities $u_0 - \omega R_t$ and $u_0 + \omega R_t$. The power P of the axis then follows from $P = Q\omega$ and the power coefficient reads

$$C_P = \tfrac{1}{2} \lambda \left[C_{d,h} (1-\lambda)^2 - C_{d,l} (1+\lambda)^2 \right] \tag{3}$$

where $\lambda = \omega R_t / u_0$ is the ratio of the tip speed of the rotor ωR_t and the free stream velocity u_0. Actually, the bodies on the rotor carry out a rotational movement. They deliver a lower average torque than calculated by (2). Equation (3) thus provides an upper value for C_P of a drag-driven rotor.

If the drag of the body that moves upwind is neglected ($C_{d,l} = 0$), the maximum power coefficient $C_{P,\max}$ found by differentiation of (3) with respect to λ, is achieved at $\lambda_{opt} = \tfrac{1}{3}$ and is found to be

$$C_{P,\max} \approx \frac{2}{27} C_{d,h} \tag{4}$$

Hoerner [26] gives $C_{d,h} \approx 1.5$, which gives $C_{P,\max} \approx \tfrac{3}{27} \approx 0.11$. In other words, the drag-driven rotor converts a maximum of 11% of the power available in the free stream wind into mechanical power at the rotor axis.

2.1.2   Lift-driven wind turbines

The $C_{P,\max}$ of a lift-driven rotor can be calculated with use of the actuator concept introduced by Froude [22]. This actuator is defined as an energy-extracting disk or plane of infinite small axial size with a normal force on the surface that decelerates the normal velocity through the disk or plane. This is a model for the rotor of the lift-driven wind turbine at infinite high[1] λ. The actuator is located in a stream tube in parallel flow with the entrance and exit of the stream tube at infinite distance from the actuator (Figure 2, right).

---

[1] In this thesis the words large and small are used when related to dimension while high and low are used in al other cases.
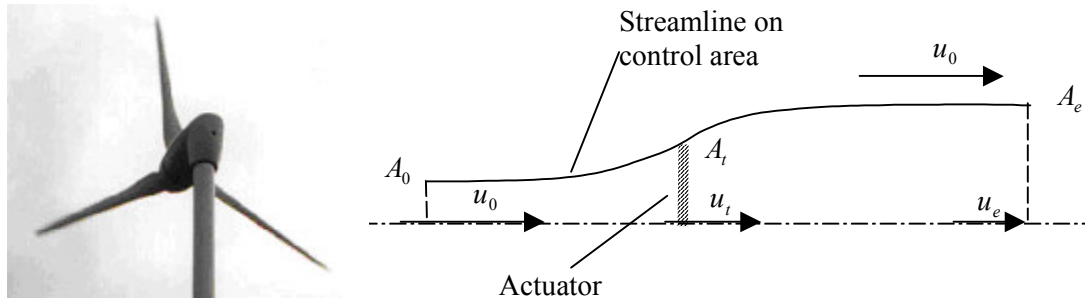
Figure 2 Example of a lift-driven wind turbine and a schematic top view of an actuator in parallel flow.

We define a control area bounded by the stream tube that forms the boundary of the flow through the actuator. Thoma [70] and Glauert [22] showed that the pressure forces on the control area give no contribution to the momentum balance. Hence, conservation of axial momentum within the control area in the assumed irrotational and divergence-free flow shows that the thrust force of the actuator is found with

$$F_M = \rho\, u_0^2 A_0 - \rho\, u_e^2 A_e \tag{5}$$

Substitution of the result from conservation of mass within the stream tube: $\rho u_0 A_0 = \rho u_t A_t = \rho u_e A_e$ then gives

$$F_M = \rho A_t u_t \left(u_0 - u_e \right) \tag{6}$$

The thrust force of a bare actuator is equal to the mass flow rate through the actuator times the rate of change of velocity in the stream tube. This important result will be used throughout the thesis.

The thrust force of the actuator can also be found with Bernoulli's theorem on a streamline upwind of the actuator and downwind of the actuator (not across the actuator because energy is extracted at the actuator). This gives

$$F_t = \tfrac{1}{2}\rho A_t \left(u_0^2 - u_e^2 \right) \tag{7}$$

Equating (6) and (7) gives the velocity through the actuator

$$u_t = \tfrac{1}{2}\left(u_0 + u_e \right) \tag{8}$$

It should be noted that momentum theory brakes down as $u_e \leq 0$. In that case, the assumed stream tube definition is no longer valid.

In most textbooks, an induction factor a is used to denote the deceleration of the air by the rotor. In that case, the velocity through the rotor u_t is defined as $u_t = u_0(1-a)$. With (8), this results in $u_e = u_0(1-2a)$. Hence, the induced velocity infinitely far downwind of the actuator: $2au_0$, is twice the induced velocity at the location of the actuator: au_0. This important result, which can also be obtained with simplified vortex theory (section 4.1.2), will be called "bare actuator wake expansion".

The power absorbed by the actuator can be found by subtracting the outlet power from the inlet power in the stream tube.

$$P = \tfrac{1}{2}\rho u_0^3 A_0 - \tfrac{1}{2}\rho u_e^3 A_e \tag{9}$$

With mass conservation in the stream tube ($\rho u_0 A_0 = \rho u_t A_t = \rho u_e A_e$) this results in a power coefficient of

$$C_P = \frac{u_t \tfrac{1}{2}\rho A_t \left(u_0^2 - u_e^2\right)}{\tfrac{1}{2}\rho u_0^3 A_t} \tag{10}$$

With substitution of (7), this results in

$$C_P = \frac{F_t \, u_t}{\tfrac{1}{2}\rho u_0^3 A_t} \tag{11}$$

By equating with (1), this shows that the power absorbed by an actuator can be found by multiplying the thrust force of the actuator with the velocity through the actuator. This is another important result that we will use throughout the thesis.

With use of (8) the power coefficient found in (10) can be written as

$$C_P = \tfrac{1}{2}\left(1 - \frac{u_e}{u_0}\right)\left(1 + \frac{u_e}{u_0}\right)^2 \tag{12}$$

$C_{P,\max}$ or the Lancester-Betz limit, after Lancester [37] and Betz [4], is found by setting the derivative of (12) with respect to u_e equal to zero. This provides $u_{e,opt} = \tfrac{1}{3}u_0$, which gives

$$C_{P,\max} = \tfrac{16}{27} \approx 0.59 \tag{13}$$

The actuator absorbs a maximum of approximately 59% of the power available in the free stream wind. The derivation of this $C_{P,\max}$ follows from the use of the actuator concept, which is a model for the idealized lift-driven rotor. We thus found $C_{P,\max} \approx 0.59$ for a lift-driven rotor.

2.1.3   Hybrid-driven wind turbines

The Savonius wind turbine with a gap between the turning bluff bodies is shown at the right of Figure 3.
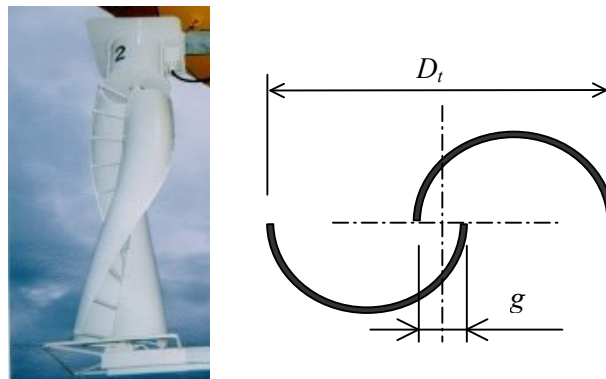
Figure 3 Example of a Twisted Savonius (left) and top view of a Savonius rotor with gap between the turning bodies (right).

This device is mainly drag-driven. However, due to the gap in this particular Savonius configuration, the bluff bodies are driven by drag and suction, which makes this particular configuration "hybrid-driven". The additional driving force caused by suction is responsible for a higher $C_{P,\max}$ than found with a pure drag-driven rotor. The highest $C_{P,\max}$ is found for a two bladed Savonius with a gap of $g/D_t = 0.10 - 0.15$. Measurements at Sandia laboratories showed that this particular configuration has $C_{P,\max} \approx 0.24$ at $\lambda_{opt} \approx 0.9$ (see Blackwell et al. [5] or Paraschivoiu [53]).

2.1.4 Comparison of the wind turbines

The projected blade area of the drag-driven rotor is approximately equal to the rotor area. The projected blade area of the lift-driven rotor is a fraction of that area. The difference in material use is clear from the following figure.

Figure 4 Example of two Vertical Axis Wind Turbines. Left, a drag-driven and right a lift-driven wind turbine.

From the previous sections we know that the lift-driven rotor has a much higher $C_{P,\max}$ than the drag-driven rotor. The drag-driven rotor thus combines a low $C_{P,\max}$ with a high material use while the lift-driven wind turbine combines a high $C_{P,\max}$ with a low material use. Perhaps, the material of a drag-driven rotor can be cheaper but in order to produce energy at the same costs, the drag-driven wind turbine needs to be a factor $\frac{16}{27}/\frac{3}{27} \approx 5$ cheaper. This is only possible for rare situations since the main difference between the drag-driven and lift-driven wind turbine is the rotor, which costs approximately 20% of the total wind turbine (Hau [24]). Hence, the lift-driven wind turbine has the best prospect to deliver energy at low cost. The drag-driven wind turbine is therefore abandoned for the generation of electricity in this thesis.

$C_{P,\max}$ of the Savonius rotor with gap is appreciably higher than that of the drag-driven rotor. Compared to the lift-driven rotor, the Savonius with gap still couples a high material use with a moderate $C_{P,\max}$. Consequently, the Savonius with gap should be the first to be examined as an alternative for the lift-driven rotor. This thesis focuses on lift-driven wind turbines.

2.2 Constraints

This section deals with a first analysis of the boundary conditions of wind energy conversion in the built environment that are introduced by built environment, wind turbine and building.

Table 1 Main boundary conditions for wind energy conversion in the built environment.

Built environment	Wind turbine	Building
Wind	Rotor size	Acceleration
Noise emission	Yawed flow	Resonance
Vibrations	Re number effects	

Shadow flicker	Safety	

They provide the contours of wind energy conversion in the built environment and are analysed in more detail later on in this thesis.

2.2.1   Built environment

Wind

One of the most dominant effects of the high roughness in the built environment is that it causes a low average velocity. Wind energy conversion becomes feasible for higher wind speeds. The combination: "wind energy conversion" and "built environment" is thus not so obvious from an energy yield point of view. Sites well above the average building height are most promising. At those sites, the wind speed is high enough to harvest the wind energy.

Noise emission

Burton et al. [8] states that the aerodynamic noise emission of a lift-driven HAWT is approximately proportional to the fifth power of the tip speed. A low tip speed is thus desired for a wind turbine in the built environment.

Furthermore, all sources of vortex shedding from the rotor should be avoided since the velocity differences and consequently the pressure differences in the flow are responsible for the noise emission. Stall of the rotor blades should thus be avoided.

The total noise level at homes has to stay below some maximum allowable noise level enforced by law. The allowable noise level at homes during the night is the lowest noise level. It is approximately 40 dB(A) in the Netherlands. Burton et al. [8] shows that this is equal to the noise level in a rural area with a wind speed of approximately 9 m/s. According to Verkerk [73] the 40 dB(A) is also equal to the noise level of a refrigerator at 1m distance.

Burton et al. [8] gives some equations that can be used for the calculation of the noise level. If the wind turbine is modelled as a point source with spherical spreading, the noise at a certain distance r from the source L_P at location P shows a reduction in noise level found with

$$L_P = L_W - 10\log_{10}\left(4\pi r^2\right) \tag{14}$$

where L_W is the source sound pressure level in dB. This shows a 6 dB decrease per doubling of distance to the source. At an allowed sound pressure level of 40 dB, (14) gives the following allowed L_W as a function of r.

Table 2 Allowable L_W of a wind turbine in the built environment as a function of the distance r to a sound pressure level of 40 dB.

r [m]	Allowed L_W [dB]
10	71
20	77
30	81
40	83

The total sound pressure level $L_{P,n}$ from n sources at a certain point can be calculated with

$$L_{P,n} = 10\log_{10}\sum_{j=1}^{j=n}10^{0.1L_{P(j)}} \tag{15}$$

Suppose we have a background sound pressure level of 40 dB and 10 wind turbines with a resulting sound pressure level at location P of 40 dB each. Then the total sound pressure level due to background noise level and 10 wind turbines is 50 dB.

Normally the sound pressure level is A-weighted -denoted by dB(A)- to account for the selective sensitiveness of the human ear. This A-weighting reduces sound pressures with frequencies other than 1000 Hz because 1000 Hz is the most sensitive region of the human ear. The rotor generates a broadband aerodynamic noise with dominating frequencies of several kHz perceived as a swishing noise. Consequently, for the dominating frequencies of a wind turbine, the A-weighted filter does not have much influence on the noise levels. The sound pressure levels in dB around 1000 Hz found with (14) and (15) are roughly equal to the sound pressure levels in dB(A).

There are two further important issues for noise emission. First, in contrast to low frequencies, the higher frequencies of several kilohertz have a strong direction dependency. They can only be heard within the straight path of the source or as reflections from that straight path. Secondly, alternating noise levels are a nuisance. This kind of noise emission should thus be avoided.

Vibrations
A HAWT induces vibrations in the building with frequencies equal to the rotational frequency of the rotor n_H and frequencies iBn_H where i is an integer and B is the number of blades of the rotor. The lowest induced vibration n_H is a consequence of mass unbalance and difference in aerodynamic loads of the blades. The tower shadow and turbulent structures cause the higher frequencies. More specifically, the tower shadow causes an induced frequency Bn_H because -at each revolution-, B blades move through the low velocity region upwind or downwind of the tower. Furthermore, the blades that move through a turbulent structure with a velocity that differs from the average velocity induce a frequency Bn_H. This phenomenon is called rotational sampling. If the blades move through two regions with a velocity different from the average velocity, they induce a frequency $2Bn_H$ and so on. We thus find an induced frequency caused by rotational sampling equal to iBn_H.

A VAWT will induce frequencies in the building at the rotational frequency n_V because of mass unbalance and difference in aerodynamic loads of the blades and frequencies $2iBn_V$ caused by rotational sampling.

Hence, compared to the HAWT, the rotational sampling frequency of a VAWT is twice as high, because the blades of the VAWT pass the turbulent structures twice: once at the upwind side of the VAWT and once at the downwind side of the VAWT. Care should be taken to avoid frequencies of the HAWT or VAWT close to the eigenfrequencies of the support structure (building roof, building walls, mast, etc.) on which they are mounted (see section 2.2.3 below resonance).

Shadow flicker
Situations where the wind turbines blades are within the direct path of the sunrays to the eyes or reflections of the sun's rays on the wind turbine blades should be avoided. The latter is simple to solve with dull paint. Situations where the blades are within the direct path of the sun's rays are a nuisance if the observer is close to the wind turbine and at visible frequencies

below some 20 Hz (see Burton et al. [8] for more details). Compared to the Darrieus, HAWT's have more problems in avoiding those low frequencies because of the single-blade passage where the Darrieus has a double-blade passage between the sunrays and the observer instead. The HAWT is thus more likely to cause hindrance because of shadow flickering below 20 Hz.

2.2.2   Wind turbine

Rotor size

The built environment aerodynamically differs from rural areas by the high average height of the (roughness) obstacles i.e. the average building height $\overline{H}$. The largest turbulent structures in the wind, scale with this average characteristic size of the built environment. These big turbulent structures will change the local wind direction in the built environment with a time scale τ_{turb} equal to the characteristic size of the turbulent structures $\overline{H}$ divided by the average velocity u_0.

$$\tau_{turb} = \frac{\overline{H}}{u_0} \tag{16}$$

For $\overline{H} = 25\,\text{m}$ and $u_0 = 5$ m/s (a lower u_0 is not so interesting from an energy yield point of view) we find $\tau_{turb} = 5\,\text{s}$ for the largest time scale of mechanical turbulence in the built environment.

In the momentum theory that leads to the Lancester-Betz limit, the stream tube where the energy is extracted is of infinite length. In simulated viscous flow, a similar stream tube[2] expands up to a certain diameter and then decreases in diameter again. This is a consequence of the reenergizing/ speeding up of the flow in the wake by the flow around the wake. The area where the streamlines of the stream tube are roughly parallel is taken as the virtual "beginning" or "end" of the stream tube where the energy is extracted. With this definition for viscous flow the stream tube length where the energy is extracted is finite.

A CFD calculation with an actuator (Appendix A) shows that this definition gives a virtual stream tube length of approximately six times the diameter of the rotor ($6D_t$) in viscous flow. A time scale τ_t found by

$$\tau_t = \frac{6D_t}{u_0} \tag{17}$$

thus characterizes the time needed to create a quasi-stationary stream tube for an actuator in which the Lancester-Betz limit is applicable. For $\tau_{turb} < 6D_t/u_0$, unsteady effects become important and the Lancester-Betz limit based on steady flow is no longer applicable. In order to avoid the fast changes in load that are coupled with the unsteady effects we need to insure that $\tau_{turb} > 6D_t/u_0$. With (16) and (17) this results in

$$\tau_{turb} > \tau_t \Rightarrow D_t < \tfrac{1}{6}\overline{H} \tag{18}$$

For $\overline{H} = 25\,\text{m}$ we find $D_t < 4$ m.

---

[2] The stream tube is assumed to be defined by the average path of particles in the flow with a very small mass.

Of course, this calculation can only give a very crude estimate of the suitable diameter of a wind turbine for the built environment but the point is clear: the wind turbine for the built environment is limited in rotor size.

Yawed flow
Until now, the question whether the lift-driven wind turbine is a Vertical Axis Wind Turbine (VAWT) or a Horizontal Axis Wind Turbine (HAWT) has not been mentioned. This is indeed irrelevant for the restriction in size as a single actuator can model both rotor types. The necessary yawing of the HAWT gives additional demands. Suppose that we have a rotor that fulfils (18). Then, if both rotor types are modelled as a single actuator in a single stream tube, the lift-driven VAWT as well as the lift-driven HAWT can achieve the Lancester-Betz limit. However, due to the changes in wind direction, the HAWT needs to yaw at least every τ_{turb} seconds. For an average building height $\overline{H} = 25\,\text{m}$ and $u_0 = 5$ m/s, (16) shows that this is approximately every 5 seconds. This is very demanding because of the inertia of the HAWT around the yaw axis that prevents a fast yaw.

Often, small HAWT's have a vane based yaw system. The combination of inertia around the yaw axis and vane force results in an eigen-frequency of the yaw system. Resonance at this eigen-frequency is possible if the frequency coupled with the large turbulent structures $f_{turb} = 1/\tau_{turb}$ equals the eigen-frequency of the yaw system. Observations of small vane-guided HAWT's operated in the built environment confirm this by showing large sinusoidal yaw movements that often result in spinning around of the rotor (Vries [75], Plomp [58]).

The rotor of a HAWT in the built environment is thus frequently misaligned with the flow. In other words, the rotor performs in an average yaw that results in an average power drop compared to straight flow (section 5.2). Furthermore, the frequent yawing results in an accompanying frequent load change, which results in an increased fatigue load. The lift-driven VAWT or Darrieus rotor that does not need to yaw is thus preferred for the general wind conditions[3] in the built environment.

Safety
Wind turbines for the built environment are meant to operate in a dense populated area. As a consequence the probability of injuries in case of malfunctioning of the wind turbine is higher than that for a wind turbine in rural areas. In order to arrive at the same safety level for trespassers as with rural wind turbines, a wind turbine for the built environment is restricted to a smaller malfunctioning probability.

But the turbulence level and as a result, the fatigue loads on the blades are higher in the built environment that in rural areas. As a consequence of the restriction to a smaller malfunctioning probability and the higher fatigue loads of the blades, the blade design is a very important issue. In order to decrease the risk of blade rip-off, some manufactures mount steel cables within the rotor blades (Turby [89]) while others shroud the rotor with a steel cage (Windwall [90]).

Reynolds number effects
Reynolds effects play a major role for wind turbines in the built environment. As we have seen in this section, the rotors of wind turbines for the built environment need to be small. The consequence of the combined low number of revolutions (noise) and the small wind turbine size is that the Re number of the flow around the rotor blades is small. Compared to high Re numbers, a low Re number causes the drag of blades to increase and the lift to decrease. This combination of lift reduction and drag increase causes a large decrease in power output. Measurements in the wind tunnel on the prototype of the Darrieus Turby in

---

[3] Particular wind conditions that occur in concentrators may require different rotor concepts.

Mertens [44] show that a design $\lambda = 3$ with $D_t = 1.5$ m gives an acceptable $C_{P,\max} \approx 0.3$ at $u_0 = 10$ m/s. Figure 5 depicts the measurements results, which show a strong dependence of $C_{P,\max}$ on the average Re number[4]. Not surprising because the Re number is order 10^5 and at this particular Re number the lift and drag of the used Naca 0018 airfoil changes drastically with Re number. A design Re number above $\text{Re} \approx 2 \times 10^5$ is therefore desirable. However, the noise emission restricts the design λ to low values. A good guideline is found by limiting the design to $\lambda \approx 2 \sim 4$. This gives an acceptable material usage, power coefficient and noise emission.
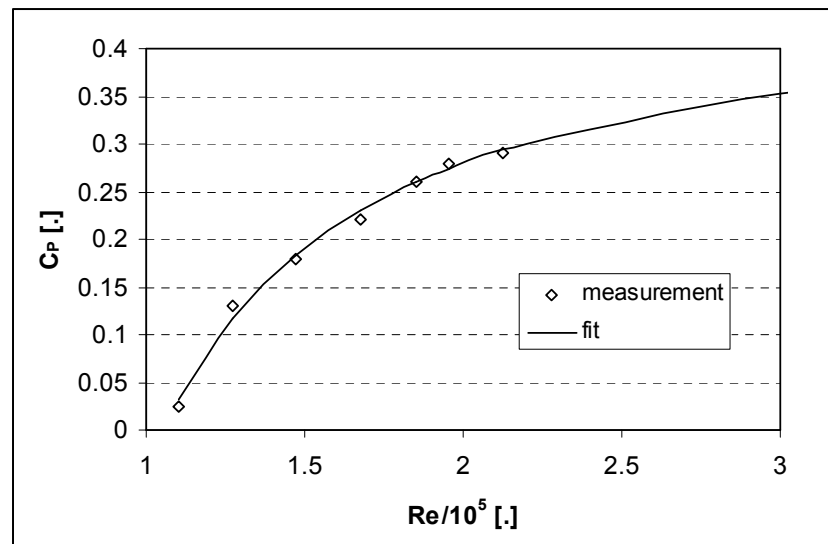
Figure 5 $C_{P,\max}$ **from measurements as a function of the Re number on the blades of the Turby prototype[5] see Mertens [44].**

2.2.3   Building

Acceleration
All bodies cause an acceleration of the free stream wind speed at certain locations close to the body. At higher distance to the body the velocity approaches the free stream wind speed. In order to profit from the acceleration, the wind turbine should thus be close to the body and its size should be limited compared to the building size. Larger BAWT's that are able to achieve appreciable $C_{P,\max}$ are consequently coupled with taller buildings.

As the velocity around a body approaches the undisturbed velocity at larger distances from the body, a rotor close to a body operates in a spatial non-uniform flow. This causes changing blade loads and consequently fatigue of the blades.

Resonance
Ellis [12] gives measurements of the eigenfrequency f_e of buildings as a function of the building height H. The large amount of data is fit with $f_e = 46/H$. Small wind turbines have rotational frequencies of several Hz. Resonance of the total building is thus only likely for low building heights. Fortunately, this seems no big problem since low buildings are not so

---

[4] The average Re number for the airfoils is based on the velocity λu_0.

[5] The prototype has the following rotor characteristics: height=1.12[m], diameter=1.5[m], chord length=0.057[m], airfoil=Naca 0018.

interesting for integration of wind turbine and building as the average wind speed is small close to the earth's surface. The eigenfrequencies of parts of the building are more likely to give problems. The eigenfrequencies of floors, walls, windows, etc., are considerable higher and small wind turbines induce frequencies that are able to cause resonance in parts of the building. Such resonance should be avoided by choosing very stiff support structures for the small wind turbines so that the eigenfrequency of the support structure is well above the induced frequencies by the small wind turbine.

2.3 The Building-Augmented Wind Turbine

In rural areas, the average wind speed is considerably higher than the wind speed in the built environment. Yet everyone knows that the wind speed in the built environment close to high buildings is sometimes astonishingly high. Such locations with concentrated wind energy are perhaps interesting for wind turbines. This idea results in the main research topics of the thesis: the building that concentrates the wind energy for the wind turbine and the wind turbine that operates in the concentrated wind. The research topic thus concerns:

"the performance of a wind turbine at a location near a building where the building concentrates the wind energy".

The name "Building-Augmented Wind Turbine" or BAWT furthermore refers to the wind turbine that operates in the wind energy concentrated by the building. According to 2.2, the size of the BAWT is limited by the size of the buildings in its direct environment. Among others, it is qualitatively shown that the characteristic dimension D of the building that concentrates the wind energy for the BAWT restricts the BAWT size. Later on, it is shown that the restriction of the BAWT size to $O(0.1D)$ assures an efficient use of the concentrated wind energy.

There are three basic BAWT configurations that can be distinguished by their aerodynamic operating principle:
- close to (on top or beside) a building,
- between airfoil-shaped buildings or
- in a duct through a building.
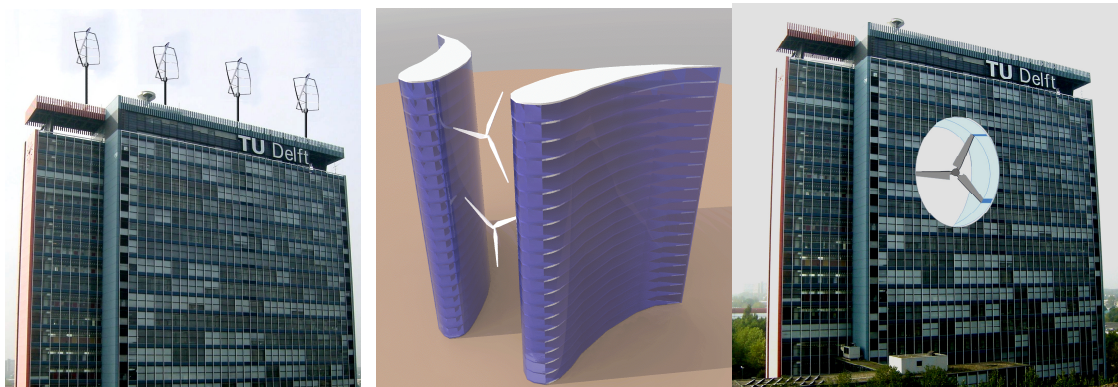
Figure 6 Artist impressions of BAWT's. From left to right: close to a building, between airfoil-shaped buildings (visualisation Lourens Aanen, DHV) and in a duct through a building.

All other possible BAWT configurations have operating principles based on these three main aerodynamic principles (Mertens [42]). Combinations of the aerodynamic operating principles are also possible. The aerodynamic operating principles of these BAWT's are discussed in the sections 5, 6 and 7.

2.4 The twisted H-Darrieus wind turbine

In the sections 2.1, 2.2 and 2.3, it is shown that a promising wind turbine for the general wind conditions in the built environment is:

- a small (< 4m),
- lift-driven,
- vertical axis wind turbine,
- with a low λ (approximately 2~4).

Such a wind turbine is known as the Darrieus wind turbine after the French inventor G.J.M. Darrieus (U.S. patent office, 1931). We will refer to this wind turbine as "Darrieus". Particular wind conditions that occur in concentrators as shown in Figure 6 may require other rotor concepts.

The Darrieus rotor has an eggbeater shape (Figure 7), which results in pure tension forces in the blades.

Figure 7 A Darrieus.

The Darrieus rotor is not self-starting because, at low λ, the average absolute angle of attack on the blades is high. Hence, at low λ the blades are stalled and the lift force of the blades is small compared to the high drag force of the stalled blades. At higher λ, the blades are below stall so that the lift force increases while the drag force of the blades decreases.

A simple design guideline for the Darrieus can be found in Wilson & Lissaman [84]. They modelled a Darrieus with a single actuator and multiple stream tubes. The multiple stream tube approach enables a local performance to be calculated. This is necessary for an accurate model since the part of the Darrieus where the blades move parallel with the wind differs in operation from the part where the blades move perpendicular to the wind. They determined that, in order to achieve $C_{P,\max}$, any slice of the rotor has to fulfil

$$\frac{Bc\lambda}{D_t} = 0.401 \tag{19}$$

In this equation, B is the number of blades of the rotor with chord length c and local rotor diameter D_t. This simple geometry condition is found with an assumed lift coefficient of the blades equal to $C_l = 2\pi \sin\alpha$ where α denotes the angle of attack on the blade. In other words, it is assumed that the flow is attached to the blades. This is a valid assumption for high λ.

According to (19), for $C_{P,\max}$ and certain λ and B, c should be proportional to D_t. In other words, c needs to be smaller at the top and bottom of the rotor since D_t goes to zero there.

This is of course not allowed since the highest tension force occurs at the blade roots. Moreover, the blades are commonly manufactured with the extrusion process, which results in a constant c. A Darrieus with a constant D_t seems to be favourable: the H-Darrieus[6] is introduced.
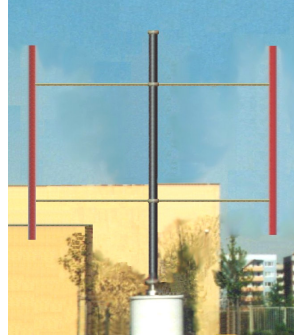
Figure 8 An H-Darrieus.

Although this design seems to work well at the entire blade span, it suffers from finite aspect ratio effects of the blades. The blade creates a pressure difference across its surface and this induces a flow from the high-pressure to the low-pressure side of the blade. The resulting vortices at the tips of the blades reduce the lift of the total blade and with this decrease the $C_{P,\max}$ of the H-Darrieus. Furthermore, rods are needed to keep the blades fixed at a certain D_t. These rods do also reduce $C_{P,\max}$ as they increase the drag of the rotor. Fortunately, the losses caused by the joints of the rods and blades can be reduced by changing the configuration shown in Figure 8 to the configuration shown in Figure 9 (Mertens [44]). In this configuration, the blades bend to the rods with a certain rounding radius and are no longer extending outside the rods as shown in Figure 8.
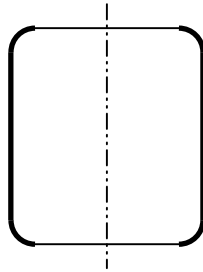
Figure 9 Reducing the losses caused by the joints of rods and blades.

This configuration is chosen as most promising rotor for general use in the built environment.

The H-Darrieus blades move from a position with zero angle of attack at the sides of the H-Darrieus to a position of maximum angle of attack at the upwind and downwind side of the H-Darrieus. Accordingly, the lift force on the blades varies periodically. This causes a periodic load on the H-Darrieus but moreover this can result in periodic noise emission. An odd number of blades has the consequence that the load of the blades is not in phase. This causes a smaller torque ripple in the rotor axis, which induces smaller forces on the building compared to the configuration where the blades are in phase with their torque. The H-Darrieus is thus best fitted with an odd number of blades. Furthermore, as few blades as possible are desired because each blade increases the rotor costs. Only one blade results in unrealistic large

---

[6] The name of the H-Darrieus with constant rotor diameter is based on the H-shape that is introduced by the configuration of two opposite airfoils with a rod to fix the airfoils at constant D_t.

twisting of the blade in order to achieve a constant torque. We thus choose three blades for the built environment H-Darrieus.

Periodic loading of the blades as well as periodic noise emission should be avoided. Periodic loading of the blades results in high fatigue loads and vibrations and periodic noise emission is a nuisance. Within the assumptions and limitations of the model that is presented hereafter, it can be shown that a twist of the H-Darrieus rotor with angle $\Delta\theta$ is able to change the periodic load at the rotor axis and periodic noise emission to a constant load and noise emission (Mertens [44]). The configuration of the H-Darrieus with twisted rotor is depicted in Figure 10.
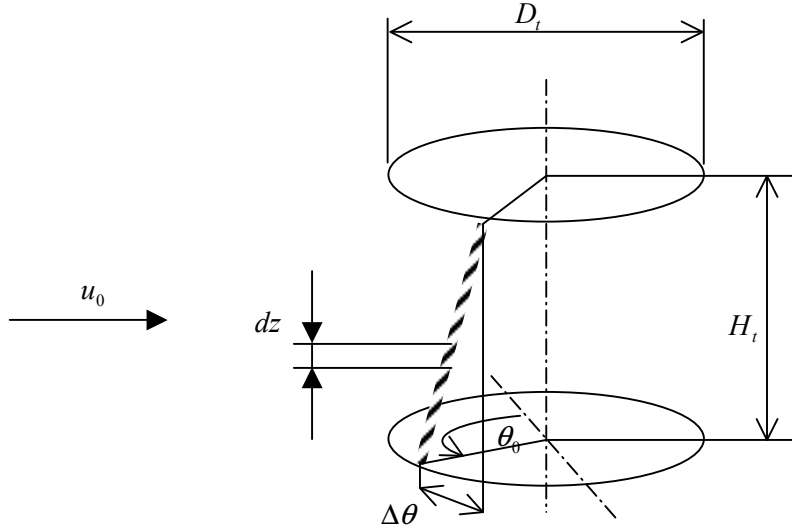
Figure 10 Configuration with a twisted H-Darrieus. The blade is shaded.

Again, we use the simple model of Wilson & Lissaman [84] for a Darrieus with high λ and lift coefficient of the blades $C_l = 2\pi \sin\alpha$. Based on these assumptions and with use of a "multiple stream tube single actuator" approach, they determined that the torque Q of a slice of a Darrieus per blade per metre Darrieus height can be found with

$$Q = \tfrac{1}{2}\rho\pi c D_t u_0^2 (1-a)^2 \sin^2(\theta) \tag{20}$$

with local induction factor of the Darrieus given by

$$a = \frac{Bc\lambda}{D_t}|\sin\theta| \tag{21}$$

According to the configuration, the angle θ of a certain blade at a certain height z can be defined by

$$\theta = \theta_0 + (j-1)\frac{2\pi}{B} + \frac{z\Delta\theta}{H_t} \tag{22}$$

where j denotes a certain blade ($j = 1\cdots B$). The total torque of the rotor with B twisted blades can be found with

$$Q_{tot} = \tfrac{1}{2} \rho \pi c D_t u_0^2 \frac{1}{H_t} \sum_{j=1}^{B} \int_{z=0}^{z=H_t} (1-a)^2 \sin(\theta) dz \qquad (23)$$

This equation together with the equations (21) and (22) may be used to calculated the torque ripple. It reveals that the total torque of an H-Darrieus with twisted blades is constant (Q_{tot} is not a function of θ_0) if

$$\Delta\theta = \frac{\pi}{B} \qquad (24)$$

The calculations that lead to (24) are carried out numerically. Within the model assumptions, (24) defines a kind of helix shape of the H-Darrieus that causes a constant load and constant noise emission.

The following figure shows the result of the design of a suitable wind turbine for the built environment: a three-bladed helix shaped H-Darrieus called Turby.
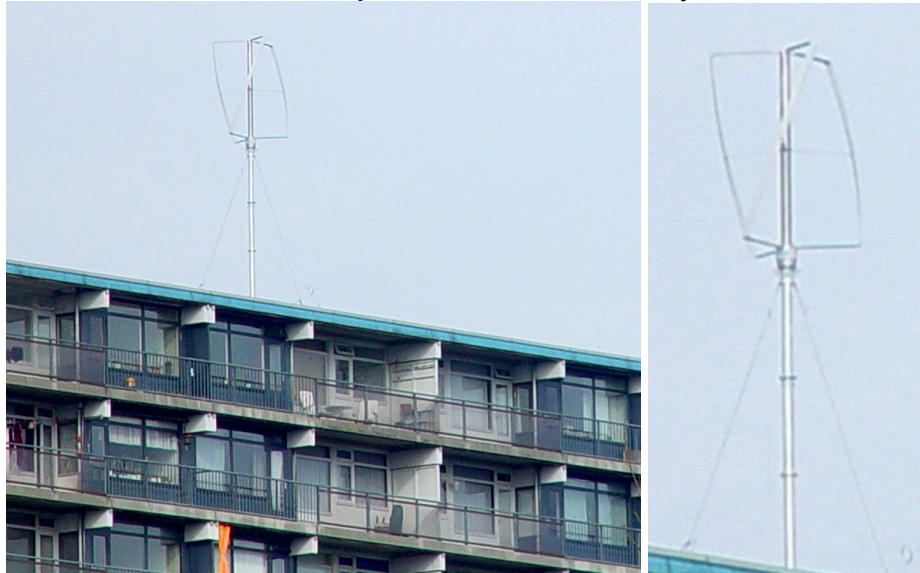
Figure 11 Turby on a roof in Tilburg, The Netherlands (right: overview, left: zoom in).

The aerodynamic design of the prototype of Turby together with several wind tunnel tests for verification of the design are given in Mertens [44].

The flow on the roof of sharp-edged buildings is not parallel to the roof. The flow approaches the H-Darrieus on the roof of most common square buildings from below. One of the tests in Mertens [44] showed a power increase for flow from below. This makes the H-Darrieus very suitable for operation on a roof of sharp-edged buildings. Section 5.2 goes into detail on the behaviour of an H-Darrieus in such flow.

The design guidelines in this section can be used for a first dimensioning of the H-Darrieus. However, they are too simple for design of a prototype. It thus seems wise to accompany a rough design of the H-Darrieus for the built environment with wind tunnel tests in order to verify the demanded performance.

3   Wind characteristics

In this chapter, the properties of the wind that concern wind energy conversion in the built environment will be analysed. The chapter is divided into three sections. Section 3.1 deals with the global properties of the wind in the built environment. Section 3.2 zooms in at the local properties of the wind around buildings. Finally, section 3.3 deals with the flow at the building.

3.1 Global wind in the built environment

This section analyses the wind in the built environment that is influenced by the average roughness of the built environment. Because of the average character, the analyses are not applicable close to the individual roughness elements such as buildings.

Numerous properties of the built environment and atmosphere influence the wind speed. The wind speed in the built environment thus shows a very complex behaviour that is difficult to model. Only few particular situations allow modelling of the atmosphere and wind speed in the built environment. This is often forgotten and results of calculations are used without the restrictions of the models.

3.1.1   Log-law

In order to fulfil the no-slip condition at the earth's surface, the wind speed decreases to zero at the ground. This results in the so-called atmospheric boundary layer (Figure 12).
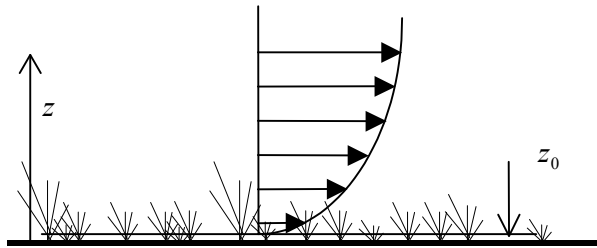
Figure 12 Sketch of an average horizontal velocity profile as a function of the height z in the atmospheric boundary layer developed over grassland with roughness height z_0.

Log-law at low roughness
Mechanical turbulence is the main driving force for the structure of the atmospheric boundary layer above an average wind speed of 6 m/s at 10m height (Wieringa & Rijkoort [79]). Above this wind speed, the fully developed turbulent atmospheric boundary layer is mostly neutral and temperature effects can be neglected. Further observations show that the flow in the neutral boundary layer can be divided into two regions with equal shear stress but different scaling: an inner and an outer layer (Prandtl [59]). Matching of the velocity gradient in the outer and inner region results in a logarithmic boundary layer profile or log-law (see for instance Nieuwstadt [51]).

$$u(z) = \frac{u_*}{\kappa} \ln\left(\frac{z}{z_0}\right)$$
(25)

In (25) $u(z)$ denotes the wind speed at height z, u_* is the friction velocity, κ is the Von Kármán constant taken as $\kappa = 0.4$, z is the height above the earth's surface and z_0 is called the earth's surface roughness height. The derivation of the log-law shows that z_0 is a measure

for the small structures in the boundary layer. The log-law is valid up to at least 150~200 m (Panofsky & Dutton [52], Simiu & Scanlan [67]) in a neutral atmosphere with strong winds.

Wind maps, such as for instance those presented in the wind atlas [80], give the average reference wind speed at $z_{ref} = 10$ m and $z_{0,ref} = 0.03$ m. This reference wind speed is called the potential wind speed u_p. The velocity for a different z_0 and z can be found by matching of the velocity from reference situation and new situation at 60 m (Wieringa & Rijkoort [79]). The velocity at z_0 and z found from the reference situation thus reads

$$u(z) = 1.31 \frac{\ln\left(\dfrac{z}{z_0}\right)}{\ln\left(\dfrac{60}{z_0}\right)} u_p \tag{26}$$

Log-law at high roughness
For the built environment, the log-law needs a modification to account for the high roughness. Fitting of the log-law with measurements of $u(z)$ well above the average height of the roughness elements shows a new virtual surface level at $d + z_0$ above the earth's surface (see Figure 13), where d is called the displacement height.
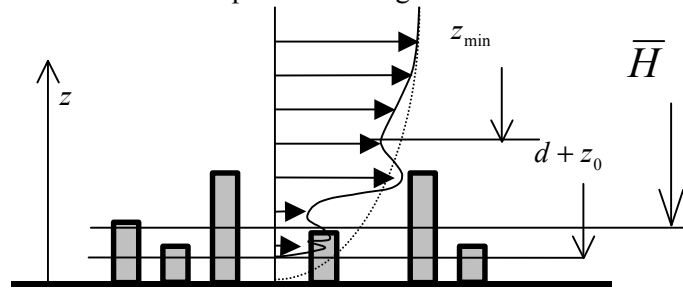
Figure 13 Sketch of an average local horizontal velocity profile in the atmospheric boundary layer developed over the built environment (solid line). The average local horizontal velocity profile for grassland roughness shown in Figure 12 is also shown in order to visualize the profile differences (dotted line).

The log-law for the built environment thus reads

$$u(z) = \frac{u_*}{\kappa} \ln\left(\frac{z-d}{z_0}\right) \tag{27}$$

Close to the roughness elements, the wind speed is influenced by the local roughness and the log-law ceases to be valid. The high roughness in the built environment influences the wind speeds well above the average building height. It is therefore inaccurate to assume a height of 60 m above the city surface where the average velocity is approximately constant as was done for the derivation of (26). The calculation of the velocity in the built environment requires a different procedure that is showed in section 3.1.2.

References on input for the log-law
Several references (Table 3) provide recommended values for z_{min}, d and z_0. Their information refers to the average height of the roughness elements $\overline{H}$ and the percentage of the total area occupied by the roughness elements A_H. Only the equation for z_0 given by

Wieringa & Rijkoort [79] refers to the height H defined as the height of the most important regularly occurring roughness elements.

Table 3 Recommended values for d, z_0, $z_{\min}$ and $\overline{H}$ found in literature.

Reference	d [m]	z_0 [m]	$z_{\min}$ [m]	$\overline{H}$ [m]
Pannofsky & Dutton [52]	$0.7\overline{H} \sim 0.8\overline{H}$		$10z_0$	
Wieringa & Rijkoort [79]	$0.5\overline{H} \sim 0.75\overline{H}$	$0.5A_H H$	$20z_0 + d$	
Simiu & Scanlan [67]	$\overline{H} - \dfrac{z_0}{\kappa}$			
ESDU 82026 [14]	$\overline{H} - 4.3z_0(1 - A_H)$ if $0.2 \le A_H \le 0.8$		$1.5d$	
ESDU 82026 [14], Typical for city	$\overline{H} - 2.5z_0$	0.8		25

Displacement height
ESDU 82026 [14] provides the most solid basis for a calculation of d because their result is based on numerous wind tunnel measurements.

$$d = \overline{H} - 4.3z_0(1 - A_H) \quad \text{if} \quad 0.2 \le A_H \le 0.8 \tag{28}$$

Equating of (28) and the typical $d = \overline{H} - 2.5z_0$ according to ESDU 82026 [14] gives $A_H = 0.42$. Typically, 42% of the total area of a city is occupied with buildings.

Roughness height
If good measurements of $u(z)$ at different heights are available, z_0 should be calculated from a fit of the log-law with the measurements. Yet, calculations of z_0 for different cities show a large variation and are subject of discussion (Wieringa [78], de Wit [85]). Apparently z_0 values above cities are difficult to estimate. Without measurements, z_0 can be estimated by comparison of appearance of the roughness with reference pictures. Such references are unfortunately not available for the built environment. The equation for z_0 given by Wieringa & Rijkoort [79] seems to be useful. Yet, the use of $z_0 = 0.5A_H H$ is somewhat difficult because of the subjective definition of H (see definition just before Table 3). Some small changes make it more useful. Suppose the distribution of the roughness elements shows a standard deviation in building height σ_H. Then, if $A_H \to 1$ while $\sigma_H = 0$ (densely packed buildings with the same height) the changed model should give $z_0 \to 0$. It will thus be assumed that

$$z_0 = c_{z0}(\sigma_H)A_H\overline{H} \tag{29}$$

where $c_{z0}(\sigma_H)$ has to be estimated. The boundaries of the area A_H should be approximately two kilometres upwind from the point where z_0 is estimated in order to provide an average value of the roughness across which the boundary layer is developed. With $z_0 = 0.8$, $A_H = 0.42$ and $\overline{H} = 25$, (29) gives

$$c_{z0}(\sigma_H) = 0.08 \tag{30}$$

which is typical for a city according to the input. Cities with other σ_H give a different $c_{z0}(\sigma_H)$. In case of lack of data, $c_{z0}(\sigma_H)$ can be taken equal to the typical 0.08.

Substitution of (29) in (28) shows a parabolic character of d as a function of A_H with a minimum d at $A_H = 0.5$. The origin of the parabolic character is perhaps found in the growth of a recirculation zone upwind and downwind of the roughness elements at $A_H = 0.5$. Such recirculation zones enable a smoother flow or skimming flow (Hussain [28]) across the roughness elements with less turbulent mixing and consequently a lower d.

Minimum height for log-law
Substitution of the typical values of ESDU 82026 [14] (Table 3) in the equations for z_{min} gives the following recommended values for z_{min} in a city.

Table 4 Reference values for z_{min} in a city.

Reference	z_{min} [m]
Pannofsky & Dutton [52]	8
Wieringa & Rijkoort [79]	39
ESDU 82026 [14]	34.5

The $z_{min} = 8$ [m] of Pannofsky & Dutton [52] is far below the typical value for d in a city according to ESDU 82026 [14]. Hence, their equation is rejected. The z_{min} values according to both other references are comparable but the equation of ESDU 82026 [14] will be used as it is based on the numerous measurements that lead to (28). z_{min} should accordingly be calculated by

$$z_{min} = 1.5d \tag{31}$$

Wind energy conversion below z_{min} needs a (time-consuming) study on the suitability of each specific site while wind energy conversion above z_{min} can straightforwardly be based on (27).

Summary input for the log-law
The following equations and reference values will thus be used for calculations with the log-law.

Table 5 Recommended values for the log-law in a city.

Quantity	Equation	Equation No.	Typical for a city
A_H			0.42
$\overline{H}$			25
$c_{z0}(\sigma_H)$			0.08
d	$d = \overline{H} - 4.3 z_0 (1 - A_H)$	(28)	23
z_0	$z_0 = c_{z0}(\sigma_H) A_H \overline{H}$ with $c_{z0}(\sigma_{H,typical}) = 0.08$	(29)	0.8
z_{min}	$z_{min} = 1.5d$	(31)	35

The equation of the log-law, the input for the log-law and the reference values should be used with great care. These equations are all semi-empirical and too simple to model the complex

flow phenomena in the built environment. They are therefore restricted in application. Yet, they are often found to be used without their restrictions, simply because of lack of other data or in ignorance. Their results are of course questionable in that case.

3.1.2   Step in roughness height

Let us assume that the quantities that determine the log-law outside a city, where $z_0 = z_{01}$ is small, are determined via -for instance- the wind atlas [80]. We would like to find the wind speed in a city where $z_0 = z_{02}$ is high.

The flow that enters a city experiences a step in roughness from z_{01} to z_{02}. A new boundary layer, called internal boundary layer, will develop at the new z_{02}. The effects of the step in roughness are not instantaneously present in the whole atmosphere but are limited to the height h_k of the internal boundary layer. Outside the internal boundary layer, the atmosphere behaves according to the upwind roughness z_{01} (Simiu & Scanlan [67]). Due to turbulent mixing, h_k will grow downwind of the roughness change. The situation is depicted in Figure 14.
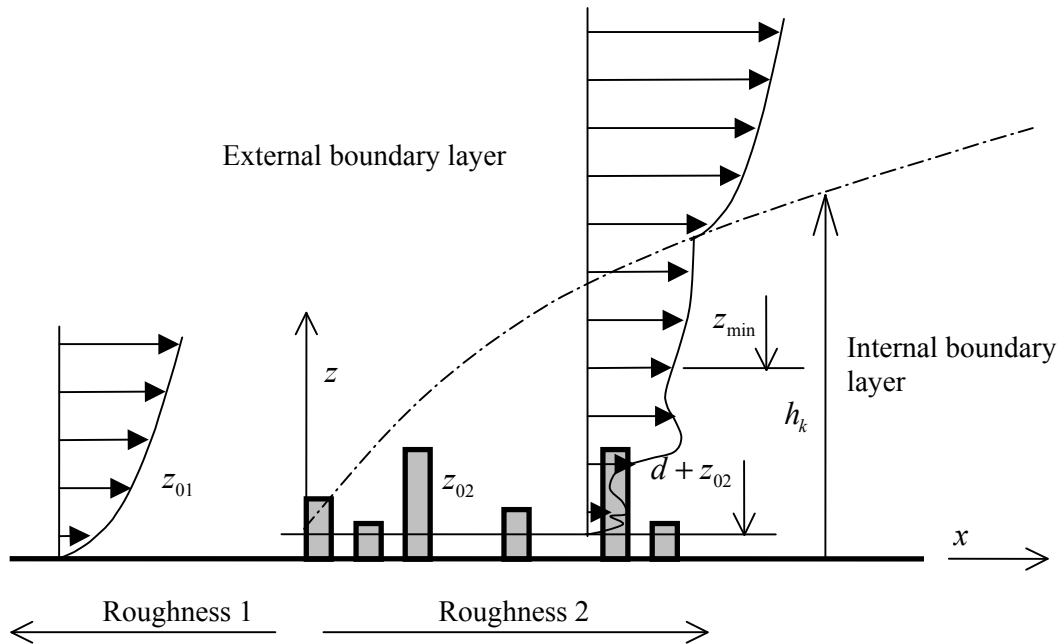
Figure 14 Sketch of a boundary layer profile change due to a step in roughness height.

Wood [86] gives an empirical model for the growth of the internal boundary layer based on a dimensional analysis and a considerable amount of data

$$h_k(x) = 0.28 z_{0,\max} \left(\frac{x}{z_{0,\max}} \right)^{0.8} \tag{32}$$

where $z_{0,\max}$ is the higher of z_{01} and z_{02}. Equation (32) is valid for smooth-to-rough and rough-to-smooth changes in the wall region $h_k(x) < 0.2\delta$, where δ denotes the boundary layer height, which is approximately 1000 m for neutral flow and strong winds across a city.

After some transient effects closely downwind of the step in roughness, the internal boundary layer will be logarithmic in a neutral atmosphere. According to Simiu & Scanlan the log-law

for the internal boundary layer can be applied if $500 \text{ m} \leq x \leq 5 \text{ km}$. Within the approximation of the model of the internal and external boundary layer as depicted in Figure 14, matching of the velocity above and below $h_k(x)$ thus gives the velocity in the internal boundary layer.

$$u(z) = 1.31 \frac{\ln\left(\dfrac{h_k}{z_{01}}\right)}{\ln\left(\dfrac{60}{z_{01}}\right)} \frac{\ln\left(\dfrac{z-d}{z_{02}}\right)}{\ln\left(\dfrac{h_k-d}{z_{02}}\right)} u_p \tag{33}$$

For frequently changing roughness height, Wieringa & Rijkoort [79] argued that $h_k = 60 \text{ m}$ should be taken since roughness changes occur from high to low roughness and visa versa so that their effects cancel. Substitution of $h_k = 60 \text{ m}$ in (33) results in (26) derived in section 3.1.1.

3.1.3   Turbulence

The turbulence intensity I is defined as

$$I = \frac{\sqrt{\overline{u'^2}}}{\bar{u}} = \frac{\sigma_u}{\bar{u}} \tag{34}$$

with $u = \bar{u} + u'$ and where σ_u denotes the standard deviation of the wind speed u. The standard deviation is mostly written in terms of u_*. For a neutral atmosphere, Pannofsky & Dutton [52] give

$$\sigma_u = 2.4 \, u_* \tag{35}$$

Substitution of (27) and (34) in (35) gives

$$I \approx \frac{1}{\ln\left|\dfrac{z-d}{z_0}\right|} \quad \text{if} \quad z > z_{\min} \tag{36}$$

This shows an increasing turbulence level with increasing roughness and decreasing height to the earth's surface. Substitution of the typical values for the built environment from Table 3 and use of (29) and (31) with $z = z_{\min}$ gives $I_{\max} \to 0.77$.

3.2 Local wind in the built environment

This section describes the flow properties that are observed around buildings. Firstly, the building shapes allow a characterization in aerodynamic, bluff and blunt buildings. Secondly, the flow around the buildings is characterized by the use of the Reynolds and Strouhal number. Finally, the probability distribution of the velocity at a certain location around a building is derived.

3.2.1   Building characterization

A first characterization of building shapes distinguishes aerodynamic buildings from bluff buildings. Aerodynamic buildings have a thin boundary layer attached to the surface of virtually the whole building. They are characterized by a small wake. Bluff buildings are characterized by early separation of the boundary layer from their surface and a large wake (see Figure 15). Blunt buildings show a combination of the flow phenomena of bluff and aerodynamic buildings.
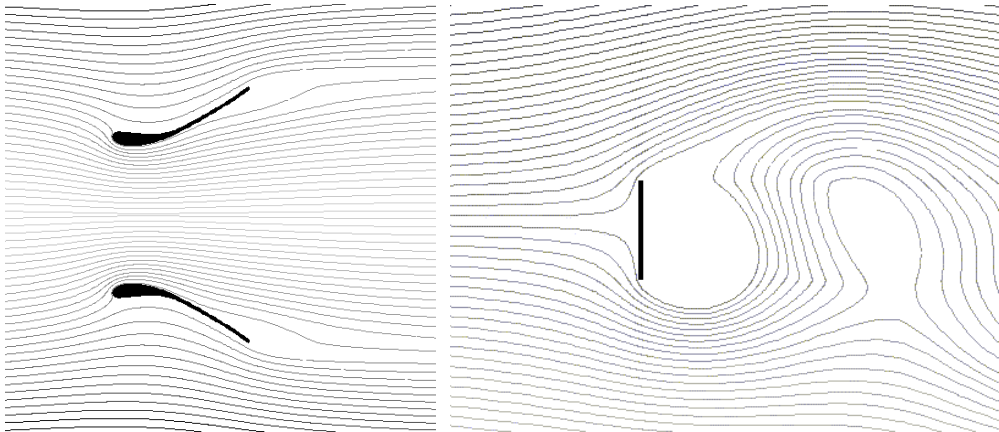
Figure 15 CFD calculation of the streamlines around an aerodynamic body (left) and a bluff body (right) in parallel flow. Flow direction from left to right.

It should be noted that the characterization of buildings as aerodynamic or bluff depends on the flow direction. An aerodynamic building for flow from direction ϕ (Figure 15, left) will change to a bluff building for flow from a direction perpendicular to ϕ (Figure 15, right).

At a building with sharp upwind edges, the boundary layer separates at the upwind edges (Schlichting [63]) and separation bubbles are formed on the sides and on top of the building. The main stream is deflected around the building and a large wake downwind of the building is formed (see Figure 16). Such a building is thus called a bluff building.
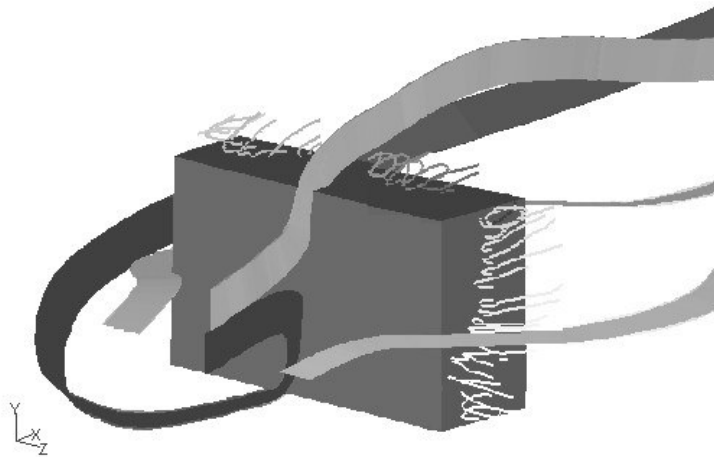
Figure 16 CFD calculation of the streamlines around a sharp-edged building.

The drag force of a building is made up of two contributions. The difference in local velocity around a building results in pressure differences at the surface of the building. This gives a contribution in the total drag called "pressure drag". The "no slip condition" at the surface of the building causes the contribution in total drag called "viscous drag". The pressure drag of an aerodynamic building is found to be zero by assuming potential flow around the building (Paradox of D'Alembert, see for instance Batchelor [2]). Consequently, the viscous drag dominates the pressure drag at an aerodynamic building. At a bluff building, the viscous drag is of the same order as the viscous drag at the aerodynamic building but the pressure drag is high as a result of the separated boundary layer. Consequently, at a bluff building, the pressure drag dominates the viscous drag.

3.2.2   Flow characterization

This section gives basic flow properties that are found from the dimension of the flow, the Re number and the Strouhal number.

3D versus 2D flow
Bodies with their height, width and length approximately equal are characterized as 3D bodies. Bodies with one size very large compared to the other sizes can be characterized as 2D bodies. The flow properties around 2D or 3D bodies are different as will be shown later in this section. According to measurements summarized in Hoerner [26], a 2D flow is approximated around bodies that have one size more than ten times higher than the other sizes. The flow around all bodies with one size smaller than ten times the other sizes can consequently be characterized as 3D flow.

The differences between the flow around 3D and 2D bodies have important consequences for BAWT's. These differences can be illustrated by comparison of flow around a sphere and a cylinder. The (2D) cylinder is found from the (3D) sphere by infinite elongation of the sphere in one direction. Consequently, both bodies have the same basic shape and only their dimensions vary. The differences in flow around the sphere and cylinder thus provide an illustration of the differences in flow between 3D and 2D bodies. The velocity at the surface of a sphere and cylinder can be found with potential theory. If attached flow is assumed, the velocity on the surface of both blunt bodies u_θ reads (see for instance Batchelor [2])

$$\left[\frac{u_\theta}{u_0}\right]_{sphere} = \sin(\theta)\left(1+\tfrac{1}{2}\left(\frac{R}{r}\right)^3\right) \tag{37}$$

at a sphere whereas at the cylinder u_θ reads

$$\left[\frac{u_\theta}{u_0}\right]_{cylinder} = \sin(\theta)\left(1+\left(\frac{R}{r}\right)^2\right) \tag{38}$$

The configuration for $\theta = 90^o$ is shown in Figure 17.
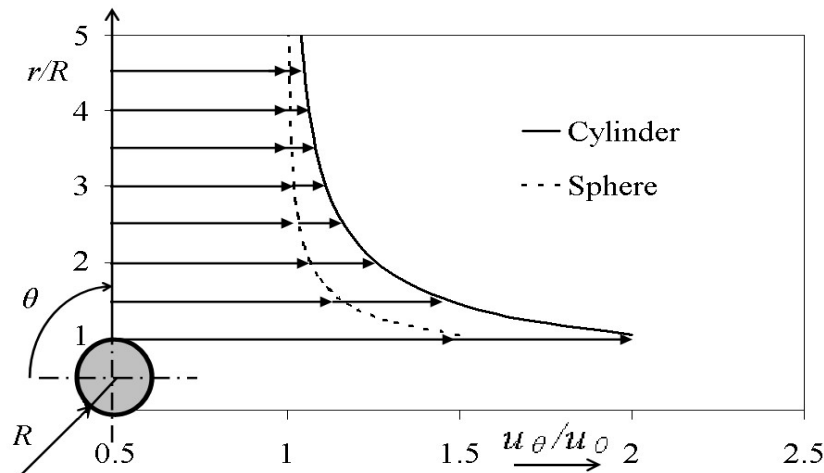
Figure 17 Potential flow velocities at the side of a sphere (3D) and a cylinder (2D).

The difference in u_θ between 3D and 2D bodies can be understood with the following argumentation. In 2D flow, the flow has just one plane to move around the body: the plane with normal vector parallel with the largest size of the body. At a 3D bluff body, the flow can

also move perpendicular to that plane. Therefore, the velocities at the sides of 2D bodies are higher.

At $\text{Re} \gg 1$, the boundary layer will separate at the along-wind sides of the blunt bodies and a wake will be formed. This results in a difference between the potential flow results for attached flow (37) and (38), and the actual velocity at $\text{Re} \gg 1$. The velocity at $\text{Re} \gg 1$ can be calculated from measurements of the pressure coefficient C_p in Hoerner [26]. The pressure coefficient is defined as

$$C_p = \frac{p - p_0}{\frac{1}{2}\rho u_0^2} \tag{39}$$

where p denotes the pressure at the location where C_p is defined and where the index 0 refers to the free stream quantities. Now, if we calculate p with Bernoulli's theorem, the tangential velocity u_θ at a certain point with pressure coefficient C_p is found from

$$\frac{u_\theta}{u_0} = \sqrt{1 - C_p} \tag{40}$$

Comparing (37), (38) and (40) with C_p at $2.10^5 < \text{Re} < 4.10^5$ found from measurements shown in Hoerner [26] gives the following result.
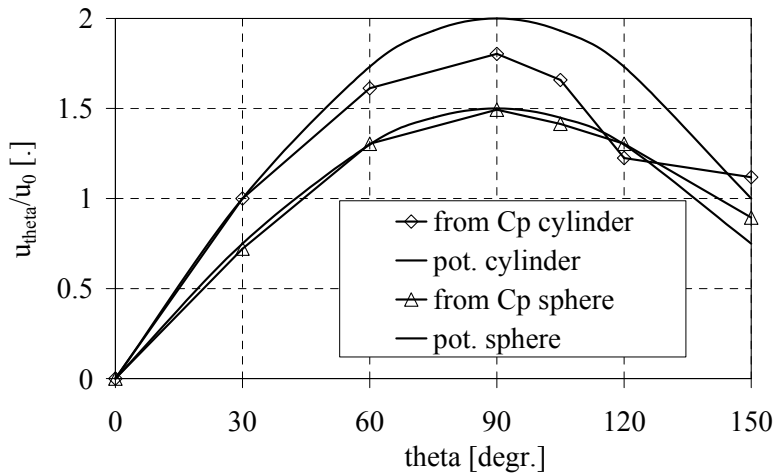
Figure 18 u_θ **at the surface of a cylinder and sphere, found from potential theory with attached flow, compared with** u_θ **found from measured** C_p **and (39) at separated flow with** $2.10^5 < \text{Re} < 4.10^5$.

Figure 18 shows that the sphere and cylinder with separated flow can be sufficiently accurate (error <10%) modelled with (37) respectively (38) up to a circumferential angle $\theta \approx 90^o$.

With $r/R \approx 1.1$ and $\theta = 90^o$, (37) and (38) show that $u_\theta(r) \approx 0.9 u_\theta(R)$. In other words, the velocity at $0.1R$ from the surface is reduced to 90% of the surface velocity.

Four important conclusions are extrapolated from the previous results and (37) and (38):
- $u_\theta(\theta = 90, R)$ at a 2D blunt body is higher than $u_\theta(\theta = 90, R)$ at a 3D blunt body,

- at $\theta = 90^{\text{o}}$, for the sphere as well as the cylinder, the velocity at $0.1R$ from the surface is reduced to 90% of the surface velocity,
- for $r/R = $ constant, the acceleration is independent from the absolute size of the body,
- for BAWT's, buildings that cause 2D flow are preferred above buildings that cause 3D flow because the wind speed close to a 2D building is considerable higher.

Reynolds and Strouhal number

The Reynolds number Re of a fluid is defined as

$$\text{Re} = \frac{\rho \, uD}{\eta} \tag{41}$$

where ρ is the density of the fluid, u is a characteristic velocity of the fluid, D is a characteristic size of a body within the fluid and η is the dynamic viscosity of the fluid. The Re number is a measure for the ratio of inertial and viscous forces in the flow (see for instance Batchelor [2]). A high Re number shows that inertial forces dominate the viscous forces while a low Re number shows that the viscous forces dominate the inertial forces. With the Re number we are thus able to judge whether viscous effects in the flow can be neglected.

At certain Re numbers, a regular flow pattern can be observed in the wake of a bluff body. Vortices of opposite sign are shed from the upwind edges of the bluff body in an alternately and regular way as depicted in Figure 19.
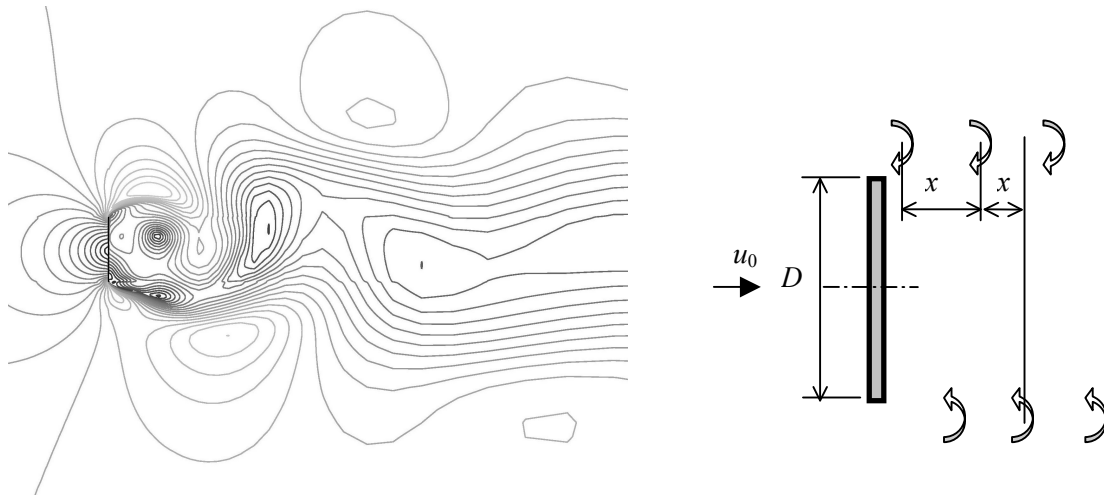
Figure 19 Vortex street downwind of a bluff body. Left: velocity contours found with a CFD calculation (section 4.3.5). Right: definitions

This flow pattern is mostly referred to as "vortex street" and often called after Von Kármán. Shedding of vortices is important for building and BAWT. By means of their high local velocity, these shed vortices induce a regular suction at the sides of the bluff body. This can cause resonance at the eigenfrequency of the body. It has to be certain that the frequency of the vortex shedding f is not in the neighbourhood of the eigenfrequency of the body ($f_e = 46/H$ for a building see section 2.2.3). Concerning the operation of the BAWT, the regular high velocities at the sides of bluff bodies cause an alternating power production of the BAWT.

In non-dimensional form, the Strouhal number S represents the frequency of the vortices leaving one side of the body. Hoerner [26] shows that a good fit of S with measurements at 2D blunt as well as bluff body shapes is achieved with

$$S = 0.21 C_d^{-3/4} \qquad (42)$$

For most bluff bodies, the drag coefficient C_d is (approximately) known. This allows us to calculate an (approximated) S. By definition, S is found from

$$S = \frac{fD}{u_0} \qquad (43)$$

where D is the characteristic size of the body and u_0 is the free stream velocity. The shedding frequency of the vortices can thus be found from

$$f = 0.21 \frac{u_0}{D} C_d^{-3/4} \qquad (44)$$

Suppose that the time coupled with (44) is enough for allowing a quasi-steady approach of the BAWT in the shedding region. With (17) we then find that a steady approach of the operation of the BAWT with diameter D_t is allowed if $1/f > 6 D_t/u_0$ or

$$\frac{D_t}{D} < 0.8 \, C_d^{3/4} \qquad (45)$$

For blunt to bluff bodies, $C_d \approx 0.5...2$ (Hoerner [26]) so that a restriction of the BAWT size to $D_t/D < 0.5$ avoids unsteady operation of the BAWT. This is no extra restriction since the BAWT diameter is limited to $D_t/D < 0.1$ in section 2.3 in order to profit efficiently from the acceleration effects close to buildings.

The vortex street originates from the interaction of the flow on the two sides of the body and is thus more frequently observed behind 2D bodies compared to 3D bodies. Adjustments on the body that reduce the interaction between the vortices can prevent the vortex street. Such adjustments are for instance serrated upwind edges of the body. An example of this is found at the TU Delft building in the Netherlands depicted in Figure 30. A so called splitter plate, a plate at the symmetry axis in the wake of the body, can also prevent the vortex street.

3.2.3   Wind speed probability distribution

This section first shows the derivation of the probability distribution of the wind for a BAWT i.e. the probability distribution at the location where the wind speed is changed by a concentrator building. Secondly, this section shows the derivation of the energy yield of a BAWT from this probability distribution.

Probability distribution
The probability distribution of wind in the atmospheric boundary layer can be given by a Weibull distribution. Wieringa [79] shows that the description with a Weibull distribution works well for wind speeds 4~16 m/s, the range where a wind turbine operates most of the time.

At locations:
- close to a sharp-edged building,

- in a duct through a sharp-edged building and
- between airfoil-shaped buildings,

the change of the free stream wind speed in the local wind speed near the building is Reynolds-independent. Hence, the change in free stream wind speed caused by the majority of buildings used as a concentrator is Reynolds-independent and it will be assumed that the change of the free stream wind speed by the concentrator building is Reynolds-independent. Then, the wind speed u_i at the concentrator, for free stream wind from windrose sector *i*, can be found from the free stream wind speed $u_{0,i}$ at a certain reference height (for instance roof height) with

$$u_i = C_{r,i}\ u_{0,i} \tag{46}$$

where $C_{r,i}$ gives the Re-independent change of $u_{0,i}$ to u_i.

The Weibull distribution $f_{0,i}$ of the free stream wind speed $u_{0,i}$ from wind rose sector *i* reads

$$f_{0,i} = \frac{k}{a_i}\left(\frac{u_{0,i}}{a_i}\right)^{k-1}\exp\left(-\left(\frac{u_{0,i}}{a_i}\right)^k\right) \tag{47}$$

where the scale parameter a_i of the free stream wind speed $u_{0,i}$ can be found from

$$a_i = \frac{\overline{u}_{0,i}}{\Gamma\left(1+\dfrac{1}{k}\right)} \tag{48}$$

where Γ is the gamma function

$$\Gamma\left(1+\frac{1}{k}\right) = \int\limits_0^\infty \exp(-x)\ x^{\frac{1}{k}}dx \tag{49}$$

and *k* is the shape parameter. Wieringa and Rijkoort [79] shows that *k* varies with height and roughness. Their result for the dependence of *k* on height at Cabauw, The Netherlands, is given in Figure 20.
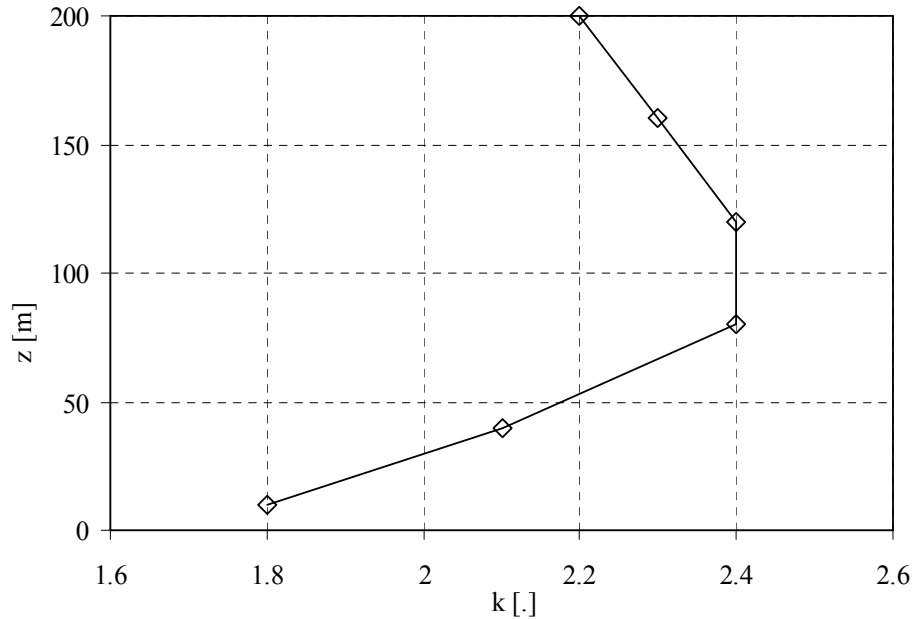
Figure 20 Shape parameter k as a function of the height above the earth's surface z at Cabauw, The Netherlands (Wieringa and Rijkoort [79]).

For a height of approximately 20 m Figure 20 shows that $k = 2$ is a good approximation. Wieringa and Rijkoort [79] give a variation of k with roughness of 5% for a roughness change from $z_0 = 0.5$ to $z_0 = 0.03$. We shall assume that $k = 2$. For $k = 2$ the Weibull distribution is called the Rayleigh distribution and the value of the gamma function is found to be

$$\Gamma\left(1 + \frac{1}{2}\right) = \sqrt{\frac{\pi}{4}} \, . \tag{50}$$

The probability of a wind speed interval du_i at the concentrator $f_i du_i$ where f_i is the probability distribution of the wind at the concentrator, is equal to the probability of a free stream wind speed from sector i: $C_{c,i} f_{0,i} du_{0,i}$, where $C_{c,i}$ is the probability of wind from wind rose sector i. We thus have

$$f_i du_i = C_{c,i} f_{0,i} du_{0,i} \tag{51}$$

with

$$\sum_{i=1}^{N} C_{c,i} = 1 \tag{52}$$

where N is the number of sectors of the wind rose. Substitution of (46) and (47) in (51) gives

$$f_i du_i = C_{c,i} \frac{k}{a_i C_{r,i}} \left(\frac{u_i}{a_i C_{r,i}}\right)^{k-1} \exp\left(-\left(\frac{u_i}{a_i C_{r,i}}\right)^k\right) du_i \tag{53}$$

The probability distribution of the wind speed at the concentrator f_i for free stream wind from wind rose sector i thus reads

$$f_i = C_{c,i} \frac{k}{a_i C_{r,i}} \left(\frac{u_i}{a_i C_{r,i}} \right)^{k-1} \exp\left(-\left(\frac{u_i}{a_i C_{r,i}} \right)^k \right) \tag{54}$$

Hence, the probability distribution of the wind at the concentrator for all wind directions f is given by

$$f = \sum_{i=1}^{N} C_{c,i} \frac{k}{a_i C_{r,i}} \left(\frac{u_i}{a_i C_{r,i}} \right)^{k-1} \exp\left(-\left(\frac{u_i}{a_i C_{r,i}} \right)^k \right) \tag{55}$$

Comparing (47) and (55) shows that the probability distribution of the wind speed at the concentrator is the sum of a weighted (factor $C_{c,i}$) Weibull distribution with different scale parameter $a_i C_{r,i}$ compared to the free stream scale parameter a_i. Consequently, in general f is no Weibull distribution. The bandwidth of f can be much higher (see section 5.1.2).

With (54) the average wind speed at the concentrator $\bar{u}$ is found by

$$\bar{u} = \sum_{i=1}^{N} \int_{0}^{\infty} u_i f_i du_i \tag{56}$$

A measure for the energy density at the concentrator is

$$\overline{u^3} = \sum_{i=1}^{N} \int_{0}^{\infty} u_i^3 f_i du_i \ . \tag{57}$$

Energy yield
Generally, the power output of the wind turbine will be a function of the wind direction. For instance in yawed flow, the power output decreases if the wind turbine does not have a yaw mechanism. In such cases, the energy yield dE_{u_i} for a certain wind speed du_i and wind direction i reads

$$dE_{u_i} = T P_i f_i du_i , \tag{58}$$

where $P_i = C_P \frac{1}{2} \rho u_i^3 A$ denotes the power of the wind turbine at wind direction i and T is the time the wind turbine runs (a year to find the yearly energy production). The total energy yield for a certain wind direction is thus found with

$$dE_i = T \int_{u=u_{ci}}^{u=u_{co}} P_i f_i du_i \tag{59}$$

where u_{ci} is the cut-in wind speed of the wind turbine, u_{co} is the cut-out wind speed of the wind turbine and P_i is a function of u_i. The total energy yield for all wind directions and wind speeds is then found from

$$E = T \sum_{i=1}^{i=N} \int_{u=u_{ci}}^{u=u_{co}} P_i f_i du_i \; . \tag{60}$$

All concentrator models in this thesis have $C_P = \frac{16}{27}$ for the bare actuator as they are based on the actuator concept. With definition $P_i = C_P \frac{1}{2} \rho u_i^3 A$ in (60), $C_P = \frac{16}{27}$ and $u_i = C_{r,i} u_{o,i}$, the power of such actuator in a concentrator reads

$$P_i = \tfrac{16}{27} \tfrac{1}{2} \rho u_i^3 A = \tfrac{16}{27} \tfrac{1}{2} \rho \left(C_{r,i} u_{0,i} \right)^3 A \; . \tag{61}$$

It is not always $C_{r,i}$ that is known for a particular concentrator. Sometimes, the performance coefficient of the concentrator $C_{P,conc}$ is known instead of $C_{r,i}$. The power of the actuator in such concentrator is defined as $P_i = C_{P,conc} \frac{1}{2} \rho u_{0,i}^3 A$ where $C_{P,conc}$ is known via experiments, CFD calculations or mathematical models. Equating with (61) leads to

$$C_{r,i} = \left(\frac{C_{P,conc,i}}{\frac{16}{27}} \right)^{\frac{1}{3}} \; . \tag{62}$$

3.3 Wind at buildings

This section deals with the flow phenomena down to the surface of the building such as:
- the stagnation point at the upwind surface of the building,
- the velocity in the separated boundary layer for sharp-edged buildings and
- the shape of the separation bubble at the sides of sharp-edged buildings.

3.3.1 Stagnation point

The height of the stagnation point H_s is an important aerodynamic quantity. It characterizes the flow around the building and gives the point on the upwind building façade with the highest pressure. In a city, the situation looks as depicted in Figure 21.
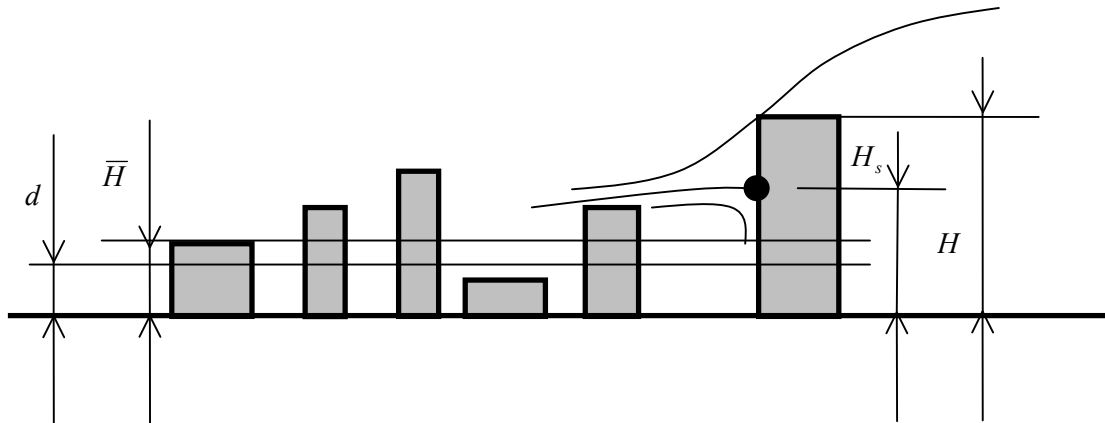
Figure 21 Location of the stagnation point.

The height of the stagnation point on a sharp-edged building in a boundary layer with negligible d will be denoted by $H_{s,0}$. At approximately squared buildings, the

measurements of Sharan [65] show a 10% change in $H_{s,0}$ for a change in z_0 with a factor 7. Jensen [32] gives $H_{s,0} \approx 0.8$ for relative roughness $H/z_0 = 13 \sim 4400$. The influence of z_0 on $H_{s,0}$ seems small and will furthermore be neglected. $H_{s,0}$ according to several references is given in Table 6.

Table 6 Ratio of stagnation point height and building height at negligible displacement height according to various references.

Reference	Building size depth : width : height	$\dfrac{H_{s,0}}{H}$
Sharan [65]	1:1:2	0.85
	1:1:3	0.85
Baines [3]	1:1:1	0.8
	1:1:8	0.9
	$1:\infty:1$	0.85
Jensen [32]	1:2:1.1	0.8

From Table 6 it is clear that the influence of the building size on $H_{s,0}/H$ is also small and can be neglected. It will accordingly be assumed that

$$\frac{H_{s,0}}{H} \approx 0.85 \tag{63}$$

independent of building size and z_0.

The stagnation point height as a function of d, is denoted by H_s. For $d \to H$, the building experiences flow at the upper part of the building and accordingly $H_s \to H$. We already know that for $d \to 0$, $H_s \to H_{s,0}$. As a first approximation, let us assume a linear dependence of H_s on d for $0 \le d \le H$. This gives

$$\frac{H_s}{H} = \frac{H_{s,0}}{H} + \left(1 - \frac{H_{s,0}}{H}\right)\frac{d}{H} \tag{64}$$

With (28), (29), (30) and (63) this reads

$$\frac{H_s}{H} = 0.85 + 0.15\frac{\overline{H}}{H}\left(1 - 1.25 A_H(1 - A_H)\right) \tag{65}$$

This relation will be used as a rule of thumb for estimation of H_s as a function of the roughness properties.

3.3.2   Separation

At a sharp upwind edge of the roof, the boundary layer separates from the building. The separation results in a region with low velocities, a high turbulence level and recirculation of the flow at the roof and sides of a building. This recirculation region should be avoided for siting of a wind turbine. It is thus important to know the size of the recirculation region.
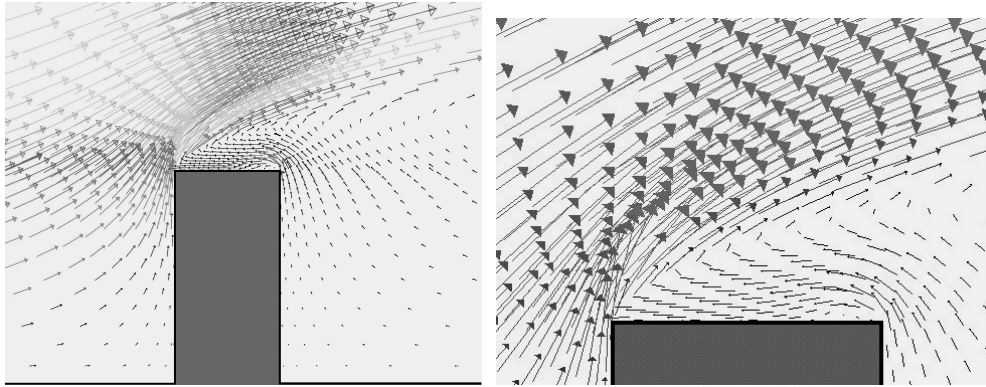
Figure 22 CFD calculation of the velocity vectors around a 2D building (left) and zoomed in at the roof (right). The flow comes from the left.

Because of the separation at the upwind roof edge, the velocity vector outside the recirculation region is not parallel to the roof. The angle between roof and velocity vector outside the recirculation region is called the skew angle to distinguish it from the yaw angle in the horizontal plane. The skew angle varies with:
- position on the roof,
- roughness of the upwind area,
- sizes of the building,
- upwind edge rounding and
- yaw of the free stream wind to the building.

The dependence on the position on the roof is easy to understand. The velocities close to the building are high and decrease with increasing distance to the building. The pressures close to the building are consequently low and increase with increasing distance to the building. This pressure gradient forces the flow in a curved path. On the curved path, the radius of the curvature is defined by equilibrium between the force caused by the pressure gradient and the centrifugal force caused by the curvature (Simiu & Scanlan [67]). The effect of roughness and size of the building on the skew angle can be understood from the amount of lateral momentum caused by blockage of the building. Compared to a low roughness, a high roughness results in a smaller mass flow towards the building (reduced velocities in the boundary layer for high roughness). A high roughness thus results in less lateral momentum because a smaller mass-flow has to move around the building. The same argumentation is valid for small building sizes. Therefore, the flow stays closer to the building for high roughness or small building sizes compared to low roughness and large building sizes.

3.3.3 Wake and recirculation zone models

Literature does provide theory, models and measurements that can be used to find the size of a wake or recirculation zone on a roof of isolated buildings. The models on the size of a wake or recirculation zone are compared and discussed in the following paragraphs.

Turbulent growth of a 3D and 2D wake
A model for the size of a wake uses the boundary layer equations derived from the Navier-Stokes equation by assuming small lateral length scales compared to the axial length scales. From these boundary layer equations and self-preservation of the structures in the turbulent wake (see for instance Tennekes & Lumley [69]), the growth of a wake of a bluff body reads

$$y \propto x^n \quad \text{for} \quad x \gg y \tag{66}$$

where y is the lateral size and x is the axial size of the wake. The origin of the coordinate system is located at the upwind edge of the body that causes the wake. Depending on the dimension of the wake, the exponent n in (66) reads

$$n = \tfrac{1}{2} \quad \text{for a 2D wake}$$
$$n = \tfrac{1}{3} \quad \text{for a 3D wake}$$

(67)

Empirical model for the growth of a 3D recirculation zone
A model for the size of a 3D recirculation zone downwind of the leading edge of a sharp-edged model building is given in Wilson [83]. The model is a fit of a dimensional analysis on numerous measurements for wide as well as tall model buildings. The model is based on a characteristic size of the upwind building façade D found by

$$D = D_{small}^{\frac{2}{3}} D_{large}^{\frac{1}{3}}$$

(68)

D_{small} denotes the smallest crosswind size of the building and D_{large} denotes the largest crosswind size. We add one simple change in this equation to account for a large displacement height d. At $d = H$, we have skimming flow (section 3.1.1) and the flow experiences no additional blockage of the building. The building height in D_{small} or D_{large} is therefore defined as $H - d$. For $d = H$ this definition results in $D = 0$, which means that the flow experiences no building so that it smoothly flows across the roof instead of bumping into the building. For a 3D wake Wilson [83] found a good correlation with measurements at various building shapes if

$$y = 0.28 D^{\frac{2}{3}} x^{\frac{1}{3}} \quad \text{for} \quad 0.1 < \frac{x}{D} < 0.4$$

(69)

where D is found by (68). The x-exponent is in agreement with (66) and (67), i.e. it can be concluded that the growth rate of the recirculation zone is equal to the growth rate of a turbulent wake. It is furthermore interesting to see the same constant 0.28 in both (69) and (32) for the growth of the internal boundary layer height: $h_k(x) = 0.28 \left(z_{0,\max} \right)^{0.2} x^{0.8}$. According to (67), $n = \tfrac{1}{2}$ is expected in case of a 2D wake, yet (32) gives 0.8. This illustrates that the internal boundary layer is indeed no wake. Furthermore, (69) and (32) differ in dimension of the flow. Equation (69) is found for 3D recirculation zones while (32) is found for the growth of a 2D internal boundary layer. Consequently, there seems to be no physical origin for the similarity of (69) and (32) and it is surprising that a constant 0.28 shows up in both models.

Free Streamline Theory for the growth of a 2D wake
A second model for a 2D wake of a bluff body is found in Batchelor [2] and is based on Free Streamline Theory (FST). In FST, the upstream conditions of a high Re number flow are assumed irrotational everywhere except near the boundaries of the flow. The model is based on the following additional conditions:
- a backpressure equal to the free stream pressure
- uniform upwind speed

Because of the necessary condition of a backpressure equal to the free stream pressure, FST ceases to be valid close to the separation point where the pressures are considerable lower than free stream pressure. Therefore, FST inhabits the same far field assumption $x \gg y$ as in (66). Within the frame of the assumptions, Batchelor [2] gives the resulting equations for the shape of the free streamlines of a 2D wake in parametric form

$$x = \left(s^2 + sk \right)^{\frac{1}{2}} - k \ln \left| \left(\frac{s}{k} + 1 \right)^{\frac{1}{2}} + \left(\frac{s}{k} \right)^{\frac{1}{2}} \right|$$

(70)

$$y = 2\left(sk + k^2\right)^{\frac{1}{2}} + \tfrac{1}{2}\pi k \tag{71}$$

where s is the distance along the free streamline and k may be determined from

$$k = \frac{2b}{\pi + 4} \tag{72}$$

with b as the distance from stagnation point to the point of separation. The origin of the coordinate system is located at the stagnation point i.e. substitution of $s = 0$ results in $(x, y) = (0, b)$. In case of separation at the roof of a building, we use the flow similarity with the FST to derive the shape of the separation streamlines at the roof. Both flow configurations are shown in Figure 23. From the analogy of both flows, it is clear that

$$b = H - H_s \tag{73}$$

can be taken, where H is the building height and H_s is the height of the stagnation point found with (65).
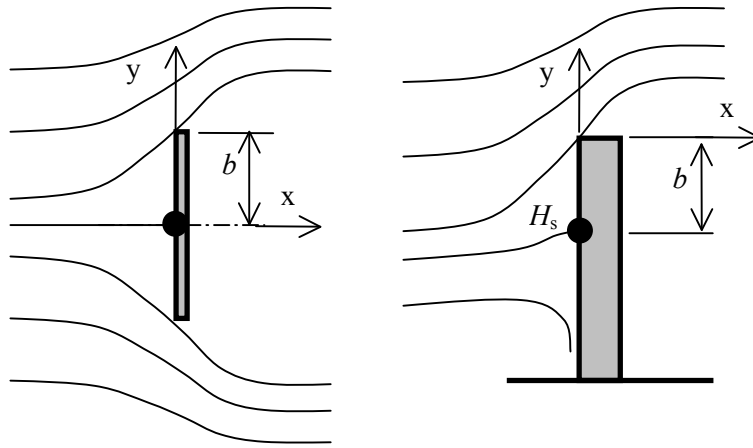
Figure 23 Configuration of the 2D flow in the derivation of free streamline theory (left), and analogue configuration for the purpose of separation on the roof of a building (right).

For large distance downwind of the separation point, we find the following asymptotic expansion of FST.

$$\lim_{s \to \infty} x = \left[\left(s^2 + sk\right)^{\frac{1}{2}} - k \ln\left| \left(\frac{s}{k} + 1\right)^{\frac{1}{2}} + \left(\frac{s}{k}\right)^{\frac{1}{2}} \right| \right]_{\lim s \to \infty} = s \tag{74}$$

$$\lim_{s \to \infty} y = \left[2\left(sk + k^2\right)^{\frac{1}{2}} + \tfrac{1}{2}\pi k \right]_{\lim s \to \infty} = 2\sqrt{sk} \tag{75}$$

so that substitution of (72) with $b = H - H_s$ results in

$$y = 2\sqrt{k}\,x^{0.5} = 0.8\left(H - H_s\right)^{0.5} x^{0.5} \quad \text{for} \quad x \gg y \tag{76}$$

where H_s can be found from (65). The x-exponent in (76) is in agreement with the 2D result (67) of Tennekes & Lumley [69]. This agreement is somewhat surprising because FST lacks the turbulent mixing on which (67) is based. The agreement can therefore be characterized as a lucky coincidence.

For further calculations on the separation streamline, we shall use the model of Wilson (66) for an isolated 3D building and the asymptotic expansion of FST (76) for an isolated 2D building.

Verification of the models
The models for the size of the recirculation region of isolated buildings are compared with CFD calculations. For this verification, a 2D and 3D building with a height of 20 m in an atmospheric boundary layer with $z_0 = 0.03$ m are chosen.

Table 7 Building sizes for the verification.

Dimension	depth:width:height
3D	1:3:2
2D	1:∞:2

The CFD calculation (Appendix C) showed that the recirculation region is smaller at the corners of the roof. The separation streamlines around the building are depicted in Figure 24. The largest expansions that were found at the roof centre and 2m above the earth's surface were compared with the recirculation region models.
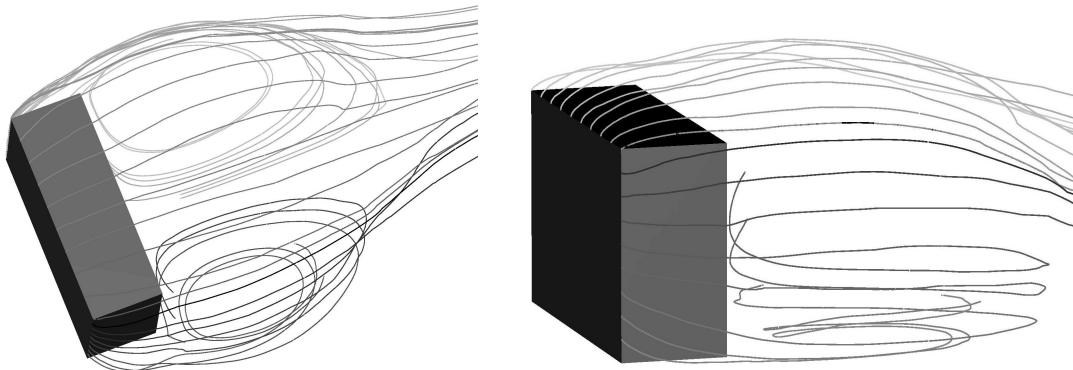
Figure 24 CFD calculation of the separation streamlines on the side (left) and roof (right) of a 3D building.

3D building
The results for the separation streamline at both sides of the 3D building 2 m above the earth's surface are shown in Figure 25.
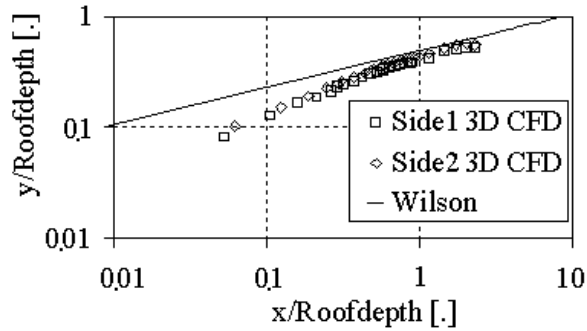
Figure 25 CFD calculation of the separation streamlines at the sides of a 3D building (depth:width:height=1:3:2) at 2 m height above the earth's surface with $z_0 = 0.03\,\text{m}$ compared with the model of Wilson [83]**.**

The results for the separation streamline above the centre line of the roof are shown in Figure 26.

Figure 26 CFD calculation of the separation streamline above the centreline on the roof of a 3D building (depth:width:height=1:3:2) with surrounding surface roughness $z_0 = 0.03\,\text{m}$ compared with the model of Wilson [83]**.**

At the downwind roof edge, the CFD calculation shows a change in orientation of the separation streamline (Figure 26). This is caused by the up-wash at the downwind face of the building (see Figure 22). The up-wash pushes the separation streamline upwards in the wake.

Wilson [83] gives a variation of the measurement results around the model location of the separation streamline of approximately 25%. Some of the tested buildings have a 10 times higher width compared to the height. In this section, it is shown that the growth of a 2D wake is different from a 3D wake. Consequently, part of the differences between the measurement results and the model is caused by the fact that some of the tested buildings cannot be classified as real 3D buildings. Furthermore, Wilson's model is fitted on measurements at one z_0. Other z_0 can give a different fit. The verification in Figure 25 and Figure 26 also shows a difference between model and CFD result. Accurate prediction of the (time-averaged) location of the separation streamline for a 3D building is consequently unlikely. Yet, the fit on numerous measurements at wide and tall buildings in Wilson [83] shows that the model is useful. The overall conclusion is that the model of Wilson is useful but not able to give accurate predictions of the separation streamline.

2D building
The results for the separation streamline above the roof of a 2D building are shown in Figure 27.

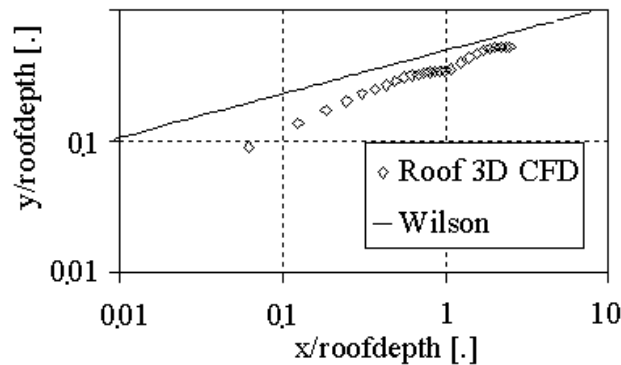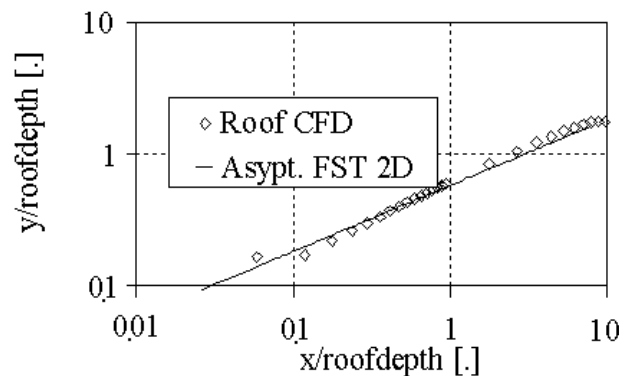**Figure 27 CFD calculation of the separation streamline above the roof of a 2D building (depth:width:height=1: ∞ :2) with surrounding surface roughness $z_0 = 0.03$ m compared with FST.**

According to the nice fit of the asymptotic expansion of FST with the CFD results, it is likely that the separation trajectory can be accurately predicted for 2D buildings. This is not surprising because the characteristic building size of a 2D building is unambiguous H, which makes the flow configuration for 2D buildings well defined.

3.3.4   Reattachment distance

Downwind of the separation point, reattachment of the boundary layer can occur for large enough downwind distances. Based on numerous measurements at wide and tall buildings, Wilson [83] gives the length of the recirculation region L_c in terms of the characteristic building size D found with (68):

$$L_c = 0.9D \quad \text{for} \quad 0 < \frac{W}{H} < 10 \qquad\qquad (77)$$

where W is the width of the building. The measurements were carried out at Re numbers up to a factor 1000 smaller compared to the actual Re numbers with full-scale buildings. Furthermore, the measurements are carried out for a single z_0. It is therefore expected that the actual L_c is different at a different z_0 and other Re number.

For the common plate-like buildings, reattachment can only occur for flow parallel to the long side of the roof. For this flow direction, D is small and a large length downwind of the separation point is available for reattachment.

3.3.5   The cavity model

This section discusses the origin of the backpressure of blunt and bluff bodies.

The cavity model
We will now study the relation between backpressure, drag and velocity at the separation point. Batchelor [2] shows a simple approach that couples C_d of a body immerged in water with the velocity at the separation point. Let the velocity at the wetted surface of the bluff body be denoted by u and the velocity at the point of separation by u_s (see Figure 28).
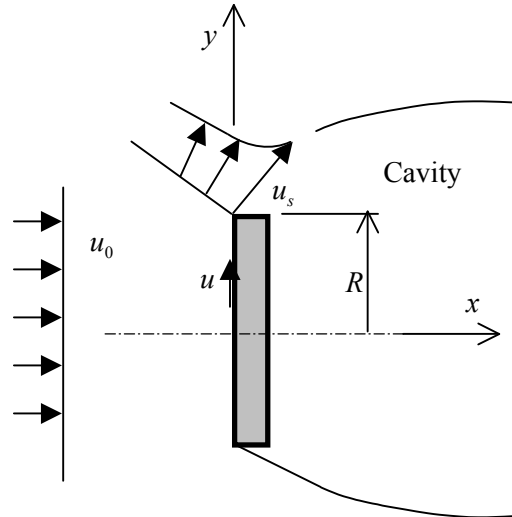
Figure 28 Flow around a bluff body.

According to potential theory, the velocities at the surface of a sphere or cylinder are found by (37) and (38). At the surface of these bodies potential theory gives $u_\theta(\theta, R) = \sin(\theta) u_\theta(\theta = 90, R)$. With $u = u_\theta(\theta, R)$, $u_s = u_\theta(\theta = 90, R)$ and $\sin(\theta) = y/R$ this results in

$$u = \frac{y}{R} u_s \quad \text{with} \quad 0 \leq y \leq R \tag{78}$$

It is assumed that the linear dependence $u \propto y$ in (78) is valid for all blunt and bluff bodies. With upstream flow conditions such that the flow is irrotational everywhere except at the boundaries, Bernoulli's theorem gives the static pressure on the free streamlines around the bluff body. With the additional assumption of a cavity or wake with constant pressure, the static pressure on the free streamlines is equal to the static pressure in the cavity. Then, the pressure difference Δp across the body at location y reads

$$\Delta p = \tfrac{1}{2} \rho u_s^2 \left(1 - \left(\frac{y}{R} \right)^2 \right) \tag{79}$$

The drag coefficient C_d of the body then follows from

$$C_d = \frac{1}{A} \int \left(1 - \left(\frac{y}{R} \right)^2 \right) dA \left(\frac{u_s}{u_0} \right)^2 \tag{80}$$

If we define a constant, $C_{d,0} = \frac{1}{A} \int \left(1 - \left(\frac{y}{R} \right)^2 \right) dA$ we have

$$C_d = C_{d,0} \left(\frac{u_s}{u_0} \right)^2 \tag{81}$$

where -according to the definition- $C_{d,0}$ describes the influence of the shape of the windward face on C_d of the bluff body. Batchelor [2] shows that (81) is in good agreement with measurements for several 3D blunt and bluff bodies immersed in water. In other words, the linear dependence in (78) and the assumed cavity are good approximations for the actual flow around these bodies in water.

In water, the interaction of the air in the wake with the velocity at the free streamlines can be neglected because there is a big difference in density between both fluids. Consequently, in water, u_s is well defined with "the velocity on the free streamlines". For bodies in air, this density difference is absent and the interaction of the air in the wake with the air around the wake cannot be neglected. Care should be taken with the definition of u_s. We define u_s for bluff and blunt bodies in air as the velocity that reproduces the measured average backpressure $\overline{C_{p,b}}$ at the body. With (40) and the assumption of a cavity with average cavity pressure $\overline{C_{p,b}}$, this definition results in

$$\frac{u_s}{u_0} = \sqrt{1 - \overline{C_{p,b}}} \tag{82}$$

This identifies one fixed u_s, which is easy to work with. The actual flow does not provide such straight definition because it is unclear where u_s should be measured. Substitution of (82) in (81) gives

$$C_d = C_{d,0}\left(1 - \overline{C_{p,b}}\right) \tag{83}$$

We will furthermore refer to (81), (82) or (83) and the underlying assumptions with "the cavity model".

Verification of the cavity model
The C_d and $\overline{C_{p,b}}$ values in Table 8 are measured and shown in Hoerner [26]. The $C_{d,0}$ values given in Table 8 fit measurements shown in Batchelor [2]. The values of u_s/u_0 are calculated from
- (81) and the measured $C_{d,0}$ and C_d found in Batchelor [2] and
- (82) and the measured $\overline{C_{p,b}}$ found in Hoerner [26].

The results of the forementioned two ways to calculate u_s/u_0 are shown in Table 8.

Table 8 Calculated values of u_s/u_0 found with the cavity model and measured $C_{d,0}$, C_d and $\overline{C_{p,b}}$ values.

Body	$C_{d,0}$	C_d	u_s/u_0 from $C_{d,0}$, C_d and (81)	$\overline{C_{p,b}}$	u_s/u_0 from $\overline{C_{p,b}}$ and (82)
Disk	0.79	1.17	1.22	-0.42	1.19
Filled half sphere	0.21	0.42	1.41	-1.14	1.46

These results show that:
- $u_s = 1.41\cdots1.46$ for the filled half-sphere is approximately equal to $u_s/u_0 = 1.5$, which is expected from (37) according to potential theory and that

- the u_s/u_0 values found with (81) and (82) and independent measurements are approximately equal.

Furthermore the value $u_s/u_0 = 1.2$ for a disk is also confirmed by independent measurements in section 7.2.3 carried out for this thesis.

Hence, it is concluded that:

- the direct coupling between u_s, C_d and $\overline{C_{p,b}}$ as suggested by the cavity model works well and
- the cavity model is very useful to reveal and compare the basic properties of the concentrator buildings.

We will therefore make ample use of the cavity model. It should however be kept in mind that the flow fields of bluff and blunt bodies that are calculated by assuming potential flow and wake absence are different from the actual flow fields because of the sometimes large wakes of blunt and bluff bodies. These wakes smooth the contours of the bodies and virtually elongate them. By doing so they decrease the velocities upwind of the wake. The potential flow assumption together with the assumed wake absence therefore overestimates the velocities compared to the actual velocities.

Section 3.2.2 showed that buildings that cause a 2D flow are preferred for BAWT's because of their high u_s/u_0. From this paragraph, it is furthermore clear that the most promising buildings for BAWT's are characterized as blunt.

3.3.6 Influencing the separation velocity and backpressure

Equation (82) shows that the acceleration u_s/u_0 significantly influences the backpressure $\overline{C_{p,b}}$. For the wind turbine in a plate concentrator (chapter 7), a large negative $\overline{C_{p,b}}$ is preferred but for normal buildings, a less negative $\overline{C_{p,b}}$ and accordingly lower drag of the building is preferable. Equipment to change u_s/u_0 can consist of plates or airfoils close to the upwind edge of the building as depicted in Figure 29. The airfoils change u_s/u_0 by means of the inclination angle of the airfoil φ. For large φ, u_s/u_0 is increased, while a small φ decreases u_s/u_0.
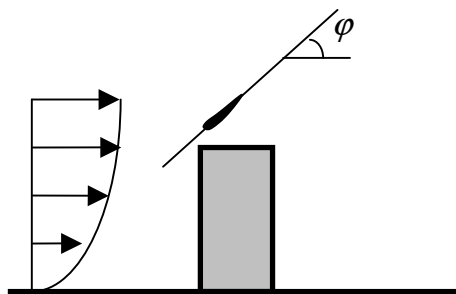
Figure 29 Top view of a building with airfoils close to the upwind edge to influence the separation velocity.

Strangely enough, this method to reduce the drag of a building is not often seen. The GSW building in Berlin, Germany shows such airfoil-like structure on the roof although the author does not know if this is meant to reduce the drag of the building. Furthermore, a Delft University building in the Netherlands reduces the separation velocity by a screen-like structure on the roof.

Figure 30 Influencing of the drag of a building by changing the separation velocity. Left: building of Delft University of Technology, The Netherlands. Right: building of GSW, Berlin, Germany.

4   Analysis tools

Aerodynamic research can be based on three main pillars:
- mathematical models,
- measurements and
- simulations or Computational Fluid Dynamic (CFD) calculations.

They form the foundation of the aerodynamical knowledge we have today and are used as analysis tools for aerodynamic phenomenon in this thesis. The separate analysis tools have specific advantages and drawbacks that define the suitability of a tool for a certain analysis. The measurements and CFD calculations provide numbers. For the coherence between those numbers and a physical explanation of the observations, for design purposes, we need a mathematical model. The mathematical model does also need the measurements and CFD calculations. They should verify the model assumptions. Accurate measurements of a certain quantity are sometimes difficult to obtain. In that case, the measurements can be supported by CFD calculations.

4.1 Mathematical

The Navier-Stokes equation (see for instance Batchelor [2]) describes the flow behaviour but is difficult to use because of its complex nature. Fortunately, there are a number of flows that can be approximated with a special case of the Navier-Stokes equation. If we assume that the flow can be characterized as homogeneous and inviscid, the Navier-Stokes equation simplifies to the so called Euler Equations. A divergence-free flow without vorticity gives a non-trivial solution of the Euler equations. This solution is the class of potential flows. In spite of these restrictions of the Navier-Stokes equation, potential flows describe a considerable range of actual flows. This range of flows will be characterized in the next sections.

4.1.1   Potential flow

Suppose we have a flow with high Re number but with a velocity smaller than 30% of the speed of sound (in air: $u_{sound} \approx 341\,[\text{m/s}]$). Then, the flow can be treated as incompressible (Batchelor [2]) and approximated with the Euler equations except in a small boundary layer close to the body (Prandtl [59]). According to Kelvin [34], a solution of the Euler equations is curl-free if it starts curl-free and the volume forces in the Euler equations are conservative[7]. An important class of curl-free flows is formed by all flows that start at zero velocity with a conservative velocity field.

Consequently, all flows with velocity u
- outside the boundary layer,
- at high Re,
- with $u < 0.3u_{sound}$,
- that started at $u = 0$ and have
- conservative volume forces,

can be approximated with potential theory. A large number of flows can thus be approximated with the relatively simple mathematical description of potential theory.

---

[7] i.e. the volume forces can be found from the gradient of a one-valued force potential like for instance the gravity field. In such conservative fields, the work done by taking a body from one place to another is independent of the path taken between those points.

4.1.2   Vortex sheets

Within the assumptions of potential theory, it can be shown that the effect of forces on the flow field is connected to vortices (see for instance Saffman [61]). An example of this is the bound vortex of an airfoil on which a lift force acts. Küchemann & Weber [36] provide another example: the wake of a loaded actuator. The latter is studied in more detail in this section.

Simplified vortex theory
Suppose, we have two straight infinite long vortex sheets (2D) or an infinite long vortex tube (3D) as shown in Figure 31. It can be shown with Biot-Savart that the velocity between the vortex sheets or inside the vortex tube is uniform (Batchelor [2]). Let this uniform induced velocity u_i at location $(x,y)=(a,b)$ between the vortex sheets or inside the vortex tube be $u_i = u_{i,\infty}$.
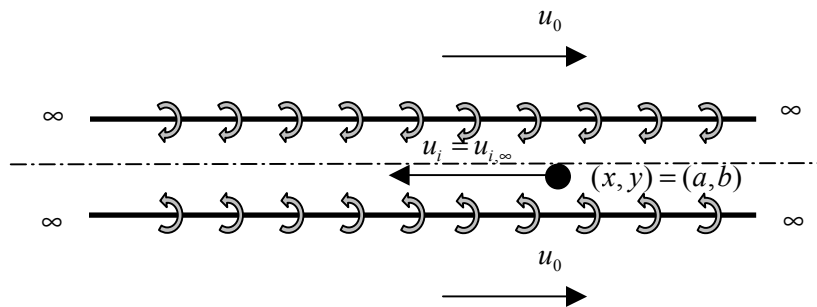
Figure 31 Two straight infinite vortex sheets (2D) or an infinite vortex tube (3D).

Removing the upwind part of the vortex sheets or vortex tube gives the following half-infinite configuration. A result of removing the upwind half is that the vortex sheets or the vortex tube have a pressure drop across their surface.
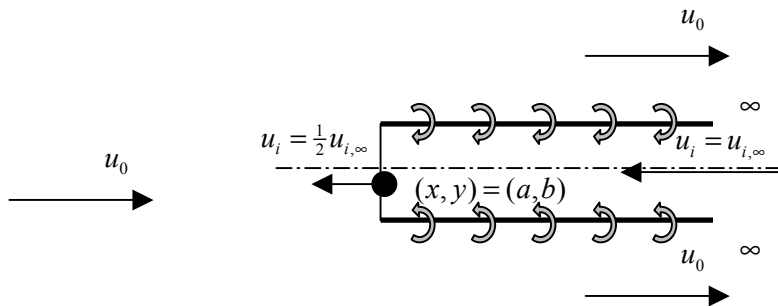
Figure 32 Two straight half-infinite vortex sheets (2D) or a half-infinite vortex tube (3D).

Only half the uniform induced velocity $\frac{1}{2}u_{i,\infty}$ can be generated at $(x,y)=(a,b)$ now because only half the portion of vortex sheets or half the vortex tube induces a velocity at (a,b). The half-infinite configuration shown in Figure 32 can be used as a model for the wake of a 2D or 3D actuator. In that case, the free streamlines at the actual widening wake boundary of the actuator are exchanged by the shown straight boundary. This approximated model for the induced velocities of a straight wake will be referred to as "simplified vortex theory".

Let us compare the results of simplified vortex theory with momentum theory for an actuator (section 2.1). According to simplified vortex theory, the induction factor at the actuator is equal to 0.5 if $u_{i,\infty}=u_0$, which gives a resultant velocity equal to zero at infinite distance downwind of the actuator. This situation cannot be modelled with straight vortex sheets or a vortex tube. Hence, we find the breakdown of simplified vortex theory if the induction factor

at the actuator exceeds 0.5, which is analogous to momentum theory for an actuator (section 2.1).

2D Vortex theory

Suppose we have a 2D loaded actuator and we model the velocity discontinuity at the wake boundary with straight half-infinite vortex sheets (Figure 33). The originally free vortex sheets at the expanding wake are thus -like in simplified vortex theory- exchanged by straight vortex sheets with a pressure drop across the vortex sheets.
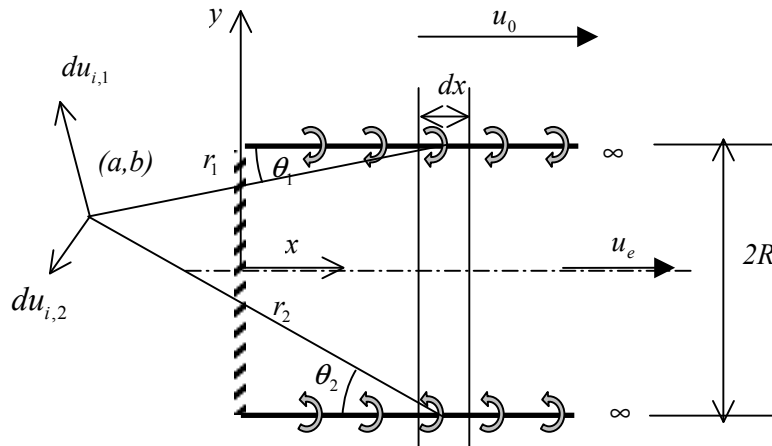
Figure 33 Wake of a loaded 2D actuator (shaded line) modelled by straight vortex sheets.

Biot-Savart (see for instance Batchelor [2]) gives the induced velocities at coordinate (a,b). The calculation is carried out in Appendix E where it is found that the resultant induced velocities in x and y-direction respectively u_i and v_i at coordinate $(x,y)=(a,b)$ are

$$u_i = \frac{\gamma}{2\pi}\left[\pi - \arctan\left(\frac{-a}{R-b}\right) - \arctan\left(\frac{-a}{R+b}\right)\right] \tag{84}$$

and

$$v_i = -\frac{\gamma}{4\pi}\ln\left|\frac{a^2+(R+b)^2}{a^2+(R-b)^2}\right| \tag{85}$$

where γ denotes the vortex strength per metre vortex sheet. Some manipulation with (84) and (85) shows the results given in Table 9.

Table 9 Induced velocities at $(x,y)=(a,b)$ by half infinite straight vortex sheets.

$a \gg 1$, $0<b<R$	$a=0$, $b=0$	$a=0$, $0<b<R$
$u_i = \gamma$	$u_i = \frac{1}{2}\gamma$	$u_i = \frac{1}{2}\gamma$
$v_i = 0$	$v_i = 0$	$v_i \neq 0$

At $a \gg 1$, the velocity u_e is found from $u_e = u_0 - u_i = u_0 - \gamma$ so that the vortex strength per metre vortex sheet reads

$$\gamma = u_0 - u_e \tag{86}$$

Comparison of Table 9 and the results of simplified vortex theory (Figure 32) shows that simplified vortex theory is exact for u_i at the symmetry plane or actuator ($a = 0$).

4.1.3   Momentum theorem

The equation of conservation of momentum in integral form has some interesting applications where it directly reveals required flow properties without the need to know details of the flow inside the area of integration (Batchelor [2]). This makes the momentum theorem a powerful tool.

Conservation of axial momentum in integral form for a stationary, incompressible fluid within a control area A reads (Prandtl & Tietjens [60])

$$\sum_i F_{i,ax} = I_{i,out,ax} - I_{i,in,ax} \tag{87}$$

where $\sum_i F_{i,ax}$ is a sum of the external axial forces acting on the fluid within A and $I_{i,out,ax} - I_{i,in,ax}$ is the difference in axial momentum between the outlet and inlet of A. The difficulty and challenge with this simple equation is to find a suitable control area that reveals the required flow properties. Often a control area bounded by streamlines is a good choice that allows particularly simple algebraic handling.

4.2 Experimental

This section deals with wind tunnel measurements. In order to avoid errors in the measurements, the size of tested bodies in the wind tunnel is limited because of blockage of the flow of the wind tunnel. Unfortunately, there are numerous other effects that influence the measured result, which should be carefully considered. This chapter shows some major effects that influenced the wind tunnel measurements carried out for this thesis.

4.2.1   The open jet wind tunnel

The measurements for this thesis were carried out in the open jet wind tunnel of Delft University of Technology. The open jet wind tunnel is made of a large circular tube (Figure 34) that encloses a fan at the suction side of the tube. There is no collector for the flow and the hall is used as return channel for the flow.

Figure 34 Overview of the open jet wind tunnel of Delft University of Technology during the experiments with a small H-Darrieus in skewed flow (Sardo [62]).

The fan speeds up the air to the measurement section close behind the exit of the tube. At the tunnel exit, four pitot tubes measure the "tunnel velocity". The velocity found by the four pitot tubes is averaged. This average velocity is considered to be "the tunnel velocity". Screens and straighteners in the tube take care of the delivered flow quality. They minimise the effect of the flow rotation caused by the rotating fan, increase the uniformity of the velocity field and decrease the turbulence level[8].

Some characteristics of the open jet wind tunnel of Delft University of Technology are found in Toet & Vermeer [72] and summarized in Table 10.

Table 10 Characteristics of the open jet wind tunnel of Delft University of Technology

Quantity	value
Tunnel diameter	2.24 m
Tunnel length	10.85 m
Maximum tunnel speed	14 m/s
Non-uniformity of velocity[9]	7%
Turbulence level[9]	0.8 %

The non-uniformity introduces an important measurement error that is described in section 4.2.2.

4.2.2 Tunnel correction

A body downwind of the tunnel exit blocks part of the flow of the wind tunnel. This blockage influences the flow and corrections to account for this are needed. The boundaries of the test section of open jet wind tunnels are not fixed so that the flow can easily move around a tested body. Open jet wind tunnels are therefore less sensitive to blockage than wind tunnels with closed test sections. In order to reduce the effects of blockage, the tests for this thesis are carried out with a small blockage of approximately 5% of the tunnel exit area. Measurements in Ewald [15] show nevertheless that a flat plate with 5% blockage has a considerable 6% lower C_d compared to the C_d at zero blockage[10].

Two major error sources for an open jet wind tunnel without collector can be identified:
1. the jet over expansion caused by blockage of the jet and
2. the higher velocity at the boundaries of the jet as the tested body approaches the tunnel exit.

There are mathematical models to calculate corrections that account for these error sources, but the blockage corrections for wind tunnels with open test sections are not precise known (Ewald [15]). We therefore avoid the use of these mathematical corrections and instead use an overall correction based on measurements carried out for this thesis.

The free stream velocity experienced by a disk at the test section of the wind tunnel $u_{0,d}$ is calculated from the measured drag of the disk F_D. Hoerner [26] shows that $C_d = 1.17$ if $\mathrm{Re} > 5 \times 10^{-3}$ at the turbulence level of our wind tunnel (0.8%, see Table 10). With a measured F_D, $u_{0,d}$ can be calculated from

---

[8] Details of the effect of configuration changes in the open jet wind tunnel are found in Toet & Vermeer [72].

[9] At a test section of 0.9×1.2 m², 1.2 m downwind of the tunnel exit with a tunnel speed of 6 m/s.

[10] C_d at zero blockage is found by extrapolation of C_d measurements at various nonzero blockage ratios.

$$u_{0,d} = \sqrt{\frac{F_D}{C_d \frac{1}{2} \rho A}} \tag{88}$$

Statistical error

The $u_{0,d}$ found with (88) is compared with the measured velocity at the tunnel exit by pitot tubes $u_{0,p}$. By doing such, with:

- a disk area of $A = 0.196\,\mathrm{m}^2$, which is equal to a tunnel blockage of 5% and
- the disk placed 1.5 m behind the tunnel exit,

Fokkema [18] obtained the following results.
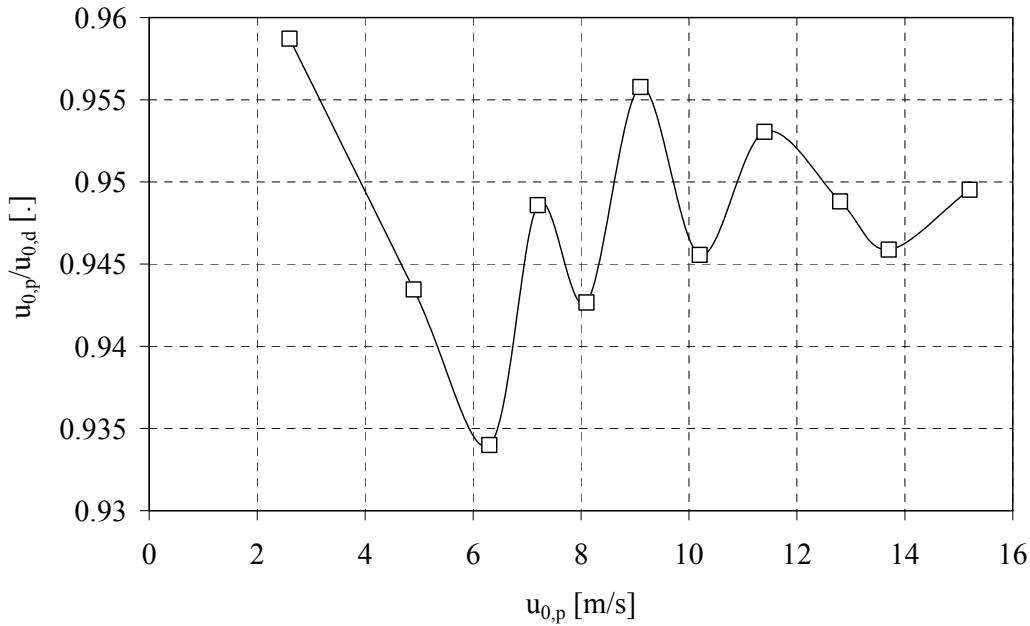
Figure 35 Ratio of the tunnel velocity measured with pitot tubes $u_{0,p}$ and the experienced free stream velocity at the test section based on the drag of a disk $u_{0,d}$ as a function of $u_{0,p}$ with a tunnel blockage of 5%.

A statistical analysis of $u_{0,d}/u_{0,p}$ with the measured standard deviation and the student t distribution (see for instance Taylor [68]) shows that $\overline{u_{0,d}/u_{0,p}}$ has a probability of 95% to be within the interval

$$\overline{u_{0,d}/u_{0,p}} = (94{,}8 \pm 0.5)\ 10^{-2} \tag{89}$$

Calculated error

The error in (89) will be verified with a calculation based on the physical quantities in the measurement of $\overline{u_{0,d}/u_{0,p}}$. The minimum error in $\overline{u_{0,d}}$ is found from (88) with $C_d = 1.17$, $\delta C_d = 0.01$ and all other errors in the quantities in (88) absent. The error in $\overline{u_{0,d}}$ then reads (Taylor [68])

$$\frac{\delta \overline{u_{0,d}}}{\overline{u_{0,d}}} > \tfrac{1}{2}\frac{\delta C_d}{C_d} = 0.43 \times 10^{-2} \tag{90}$$

The velocities $\overline{u_{0,p}}$ and $\overline{u_{0,d}}$ are calculated from stochastically independent measurements. The error in $\overline{u_{0,d}/u_{0,p}}$ can thus be found by a summation of the quadratic errors is $\overline{u_{0,p}}$ and $\overline{u_{0,d}}$ (Taylor [68]). With an infinite number of measurements, the statistical error in $\overline{u_{0,p}}$ vanishes. With (90), it is then found that

$$\frac{\delta \left(\overline{u_{0,d}/u_{0,p}} \right)}{\overline{u_{0,d}/u_{0,p}}} > 0.43 \times 10^{-2} \tag{91}$$

With a large number of measurements, the statistical analysis (89) would give an error below that given by (91), which is impossible because of the limited accuracy of $C_d = 1.17$. The error in (89) is slightly higher than the error given by (91). Consequently, the overall tunnel correction $\overline{u_{0,d}/u_{0,p}}$ for a tunnel blockage of 5% is sufficiently accurately known by (89). We will use (89) whenever a body at the test section has a tunnel blockage of approximately 5%.

As stated in the beginning of this section, Ewald [15] showed that a flat plate with 5% blockage has a C_d, which is 6% too small because of the blockage. Because of the quadratic dependence of C_d on the velocity, the velocity at the test section is a factor $\sqrt{1-0.06} \approx 0.97$ too small.

According to (89), we found a 0.95 times too small velocity. Our 2% ($0.97 - 0.95 = 0.02$) lower velocity compared to Ewald [15] is probably a result of the velocity non-uniformity or more specific the reduction in velocity caused by the hub of the fan.

4.2.3 Error in power coefficient from measurements

The power coefficient is found with (1)

$$C_P = P \Big/ \left(\tfrac{1}{2}\rho u_0^3 A_t \right) \tag{1}$$

The quantities in (1) are independently measured. Taylor [68] shows that the error in C_P can then be found from the summation of the squared relative errors

$$\frac{\delta C_P}{C_P} = \sqrt{ \left(\frac{\delta P}{P} \right)^2 + \left(\frac{\delta \rho}{\rho} \right)^2 + 3^2 \left(\frac{\delta u_0}{u_0} \right)^2 + \left(\frac{\delta A_t}{A_t} \right)^2 } \tag{92}$$

Now suppose that all errors in (92) are small except the error in u_0. This gives a minimum error of $\delta C_P / C_P = 3\,\delta u_0 / u_0$. Including of the other errors in (92) therefore gives

$$\frac{\delta C_P}{C_P} > 3\frac{\delta u_0}{u_0} \tag{93}$$

The free stream velocity u_0 in (93) is the free stream velocity experienced at the test section. For a disk with 5% blockage of the tunnel area, (89) gives the free stream velocity. For the

different operating states of a wind turbine or for a wind turbine in yaw, (89) can only give an approximation of u_0. The flow around and through a wind turbine at different loads is in general not comparable with the flow around a disk. The estimation of the error $\delta u_0 / u_0$ in (93) is therefore difficult. At the end of section 4.2.2, it was found that the non-uniformity introduces a 2% reduction in free stream velocity for a disk at the test section. In general, for other tested bodies, the effect of the non-uniformity is unknown. It is therefore assumed that $\delta u_0 / u_0 = 0.02$ at 5% blockage of the tunnel area. Based on this error, (93) gives

$$\frac{\delta C_P}{C_P} > 0.06 \qquad\qquad (94)$$

This error cannot be avoided in general. Therefore, C_P suffers from a significant error. Calculations of C_P from measurements are therefore avoided as far as possible and instead CFD calculations that are verified on quantities that could be measured more accurately are used to calculate C_P.

4.2.4 Scaling rules

Some major errors in the measurements are introduced in the previous sections. Unfortunately, more effects influence the quality of the measurement. The flow properties are mostly measured on scaled versions of the full-scale model. The effect of this scaling deserves our attention. The measured flow properties at the scaled model should represent the flow properties at the full-scale model. This requires some similarity rules between scaled and full-scale model to be fulfilled.

With the same fluid at full-scale and scaled model, the Re number (41) changes proportional to the characteristic velocity times the characteristic size. For a scaled version of a building, the characteristic size can be a factor 200 smaller. In order to maintain the same Re number, the velocity should then be an impossible factor 200 higher. The Re number at the scaled model will therefore differ from the full-scale model. This Re change can only be ignored if the measured properties are Re-independent. Such a Re-independent property is for instance C_d of some bluff bodies. It is concluded that the effects of scaling should be considered carefully because they can prevent a (direct) translation to the full-scale properties. CFD calculations do not have this scaling problem because the flow can be simulated at full-scale models. They form the alternative in case of inevitable scaling problems in measurements.

4.2.5 Wind turbine power

Measurements of the performance of the rotor of a wind turbine can be carried out on:
- a (scaled) version of the rotor if the geometry of the rotor is to be studied and the tested rotor is not too small or with
- a direct translation of the actuator concept: wire screens with different porosity, if the rotor is small or if the operation of a wind turbine in a certain environment is studied.

Both measurements are carried out for this thesis.

Power of a (scaled) wind turbine
The power of a rotor can be calculated from the measured torque of the rotor axis at a certain measured number of revolutions. The power P is then found by multiplication of the torque Q and the rotational velocity ω: $P = Q\omega$. A Prony brake can be used to measure Q. The Prony brake consists of a wheel on the axis of the rotor with a pulley around the wheel that brakes the wheel. On one side of the pulley, a weight causes a tension F_w in the pulley while

on the other side of the pulley, the tension F_s is measured with a sensor. The measurement configuration[11] with the Prony brake is depicted in Figure 36.
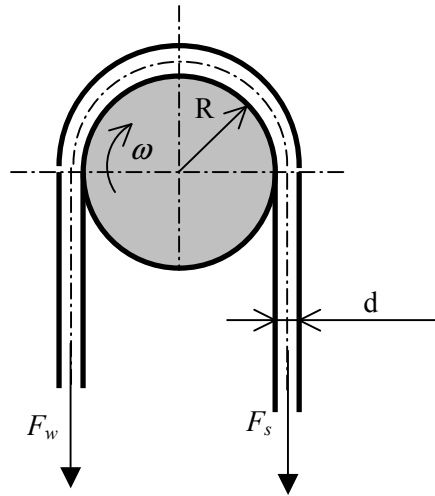
Figure 36 Prony brake.

In the steady situation the forces are in equilibrium and the total torque around the axis is zero

$$-F_w\left(R+\tfrac{1}{2}d\right)+F_f R+F_s\left(R+\tfrac{1}{2}d\right)=0 \tag{95}$$

where F_f is the friction force at the circumference of the wheel caused by the pulley. The absorbed power $P(\omega)$ by the Prony brake is found from $P=Q\omega=F_f R\omega$, which gives with (95)

$$P=\left(F_w-F_s\right)\left(R+\tfrac{1}{2}d\right)\omega \tag{96}$$

With (96) and measurement of F_s and ω at a known load F_w the power $P(\omega)$ of the rotor can be calculated.

Power dissipated by a wire screen
The large influence of Re effects (section 2.2.2) makes measurements with small rotor diameters not convenient. For small rotor diameters, measurements with a wire screen that simulates the rotor provide results that are easier to interpret.

The thrust force of an actuator F_t can be written as $F_t=\Delta p A_t$, where Δp denotes the pressure drop across the actuator and A_t denotes the area of the actuator. With (11) this shows that $C_P=\Delta p\,u_t\big/\tfrac{1}{2}\rho u_0^3$. Now suppose a wire screen is put in a parallel flow. If the wire diameters of the wire screen are small compared to the screen diameter, the wire screen shows an abrupt drop in pressure across the screen Δp, combined with a velocity u_t through the screen (Ward-Smith [78]). A wire screen can therefore be used to simulate an actuator or a

---

[11] In Appendix F it is shown that a rotational direction opposite to the direction shown in Figure 36 is not suitable for measurements.

rotor of a wind turbine at a certain load. C_P of the actuator or simulated rotor at a certain load is consequently found from

$$C_P = \frac{\Delta p \ u_t}{\frac{1}{2} \rho u_0^3} \tag{97}$$

where Δp together with u_t are measured at a free stream wind speed u_0.

The pressure drop across a wire screen is mostly defined as

$$\Delta p = K \tfrac{1}{2} \rho u_t^2 \tag{98}$$

where K is the resistance factor of a certain wire screen. The power coefficient of the simulated rotor is then found as

$$C_P = K \left(\frac{u_t}{u_0} \right)^3 \tag{99}$$

Wire screens with different porosity and accordingly different K simulate the different loads of the actuator. $C_{P,\max}$ is found on the curve of C_P values for different K. This shows that measurements with a set of screens are necessary to obtain $C_{P,\max}$ (De Vries [76]).

The pressure drop Δp across the screen can be measured with static pressure tubes some 10 wire diameters downwind of the screen. At that downwind distance to the wire screen, the local effects of the individual wires are absent (Ytsma [91]).

The screen in a turbulent flow shows small axial movements that make it impossible to measure the velocity directly downwind of the screen (collision of the measurement equipment with the screen). The velocity through the screen u_t can therefore only be approximated with the velocity measured downwind of the wire screen $\tilde{u}_t$. For small screen diameters, this introduces an important uncertainty in u_t because of the widening of the wake downwind of the screen. CFD calculations can be used to find u_t from $\tilde{u}_t$. In that case, the measurements provide $\tilde{u}_t$, which is also calculated with a CFD calculation. If both $\tilde{u}_t$ values agree, the CFD calculation is used to find u_t. This approach is used in the verification of a model in section 7.2.

4.3 Computational Fluid Dynamics

Computational Fluid Dynamics (CFD) calculations are used to verify the results of the mathematical models and wind tunnel tests. These CFD calculations evaluate the governing flow equations in finite volumes or cells defined by a grid. Different approximations of the flow equations or turbulence models decrease the computational effort to solve the flow equations. The constraints lie in the choice of the turbulence model and the grid configuration.

4.3.1   The turbulence model

Turbulent flows show very small as well as large structures. The large structures have the size of the characteristic length in the domain. The small structures size with the Kolmogorov length (see for instance Tennekes & Lumley [69] or Nieuwstadt [51]). In atmospheric flows, the large structures scale with the boundary layer height δ and the small structures scale with the roughness height z_0. In a neutral atmosphere for grassland roughness we have $\delta \approx 1000 \, \mathrm{m}$

and $z_0 \approx 0.03$ m. In order to simulate both the large and the small structures, it is thus necessary to have large domain $O(\delta)$ with a resolution that allows the smallest structures to be represented $O(z_0)$. In other words, we need to simulate the flow in a very wide domain with a very high accuracy. Even for the fast computers today this is too time-consuming. Approximations of the governing flow equations are needed in order to reduce the computational effort.

The approximated flow equations are found with the following procedure. The governing flow equations (the Navier Stokes equations and equation of state) are rewritten with use of a decomposition in an average component and a fluctuating component. For instance, the instantaneous velocity component u_i is decomposed by

$$u_i = \overline{u}_i + u_i' \tag{100}$$

where $\overline{u}_i$ is the ensemble average of u_i and u_i' is the fluctuating component of u_i. This decomposition is used for the velocity, the pressure and the temperature and is called the Reynolds decomposition. The decomposed flow equations are Reynolds or ensemble averaged. For the Navier Stokes equations, this results in the Reynolds Averaged Navier Stokes equations (RANS). The RANS equations show some new unknown terms like $\overline{u_i'u_j'}$ i.e. they are not closed. These $\overline{u_i'u_j'}$ terms are called the Reynolds stresses and they must be modelled with so-called turbulence models in order to close the RANS equations. Several turbulence models are available in literature and discussed hereafter in order to show the pros and cons of the models.

The standard $k - \varepsilon$ model
The $k - \varepsilon$ turbulence model is the most widely used and verified model. It needs a small computational effort, but the model has limited physical background.

In the $k - \varepsilon$ model, $\overline{u_i'u_j'}$ is modelled with use of the Boussinesq closure hypothesis[12]. Analogues to the constitutive relation[13], this closure hypothesis calculates $\overline{u_i'u_j'}$ from the local gradients of the average velocity (see for instance Tennekes & Lumley [69] or Nieuwstadt [51])

$$-\rho\overline{u_i'u_j'} = \mu_t \left(\frac{\partial \overline{u}_i}{\partial x_j} + \frac{\partial \overline{u}_j}{\partial x_i} \right) - \tfrac{2}{3} \left(\rho k + \mu_t \frac{\partial \overline{u}_i}{\partial x_i} \right) \delta_{ij} \tag{101}$$

where the Einstein Summation convention is used and μ_t is the eddy viscosity or turbulent viscosity, k is the turbulent kinetic energy and δ_{ij} is the Kronecker-delta[14]. The eddy viscosity μ_t is assumed to be isotropic and is calculated with

$$\mu_t = \rho \, C_\mu \frac{k^2}{\varepsilon} \tag{102}$$

---

[12] The Bousinesq closure hypothesis is also known as K-theory.
[13] The relation that couples stresses in the fluid with velocity gradients.
[14] $\delta_{ij} = 1$ if $i = j$, while $\delta_{ij} = 0$ if $i \neq j$

where $C_\mu = 0.09$ is assumed constant and ε is the turbulent dissipation rate. The $k - \varepsilon$ model thus formed is the simplest two-equation model. It uses one model transport equation for k and one model transport equation for ε.

Nieuwstadt [51] shows that the Bousinesq closure hypothesis (101) can only give satisfactory results if the characteristic turbulent length scale ℓ is much smaller than the characteristic length scale of the geometry of the flow D. In general, this is not the case because $\ell = O(D)$. The assumptions in the Bousinesq hypothesis give rise to the following properties of the standard $k - \varepsilon$ model:

- a limited applicability restricted to fully turbulent wall bounded and free shear flows (because $\ell \ll O(D)$),

- not sensitive to free stream turbulence (because $\overline{u_i' u_j'}$ is calculated from local flow properties)

- cannot be trusted in flows that involve strong streamline curvature (because μ_t is not isotropic in such flows).

- a spuriously large generation of k and a resulting overprediction of μ_t around a stagnation point (Kim & Boysan [35]). This large k is transported downwind where it causes:
  - separation of the boundary layer to be suppressed,
  - the velocities outside recirculation region s to be too small and accordingly
  - the pressure coefficient in the recirculation region to be too high,
- a non-physical behaviour at large strain rate.

The last property needs some more explanation. The Bousinesq hypothesis (101) for incompressible flow ($\partial \overline{u}_i / \partial x_i = 0$) gives

$$\overline{(u')^2} = -2 \frac{\mu_t}{\rho} \frac{\partial \overline{u}}{\partial x} + \tfrac{2}{3}\mathrm{k} \tag{103}$$

With (102) this shows that $\overline{(u')^2} < 0$ if

$$\frac{k}{\varepsilon} \frac{\partial \overline{u}}{\partial x} > \frac{1}{3C_\mu} \approx 3.7 \tag{104}$$

i.e. at large strain rate $\partial \overline{u} / \partial x$ the standard $k - \varepsilon$ model gives $\overline{(u')^2} < 0$, which is physically impossible or unrealizable because the normal stress or turbulent pressure stress is positive by definition. Similarly, it can be shown that the Schwarz inequality for shear stresses ($\left(\overline{u_\alpha' u_\beta'}\right)^2 \le \overline{(u_\alpha')^2} \overline{(u_\beta')^2}$ without summation over α and β) can be violated at large strain rate (Fluent [16]).

The standard $k - \varepsilon$ model is not used because the model assumptions and weaknesses make it unsuitable for the flows of interest in this thesis.

The realizable $k - \varepsilon$ model
In order to reduce some shortcomings of the standard $k - \varepsilon$ model, the CFD package Fluent[15] that is used for the calculations in this thesis, provides a more elaborate $k - \varepsilon$ model: the

---

[15] Fluent 6.1.18

realizable $k-\varepsilon$ model[16]. This model has additional terms and functions in the transport equation for k and ε, which make the model applicable to a wider range of flows. As in the standard $k-\varepsilon$ model, μ_t is calculated with (102) but with the improvement that C_μ is no longer constant but sensitised to gradients in the main flow. The variable C_μ is well substantiated by experimental evidence and suggested by many modellers including Reynolds (Fluent [16]). It reduces the spuriously large generation of k around the stagnation point found with the standard $k-\varepsilon$ model. Furthermore, the realizable $k-\varepsilon$ model gives physical or realizable results at large strain rate while the other $k-\varepsilon$ models give non-physical or unrealizable results (104). This explains its prefix, "realizable". The additional information in the realizable $k-\varepsilon$ model results in some important advantages compared to the standard $k-\varepsilon$ models. According to the improvements, the realizable $k-\varepsilon$ model should give better results for (Fluent [16]):
- the spreading rate of planar and round jets and
- boundary layers under strong pressure gradients,
- separation and
- recirculation.

This makes the realizable $k-\varepsilon$ model a promising candidate for our CFD calculations.

The Reynolds Stress model

The Reynolds Stress (RS) model is the most advanced turbulence model in Fluent. It uses the exact transport equations for $\overline{u_i' u_j'}$ in the RANS equations and closes the exact transport equations with empirical models. The model thus involves most physics of all turbulence models. Consequently, it offers a greater potential of all turbulence models to give accurate predictions for complex flows. Yet, the closure is still based on empirical models, which are considered responsible for sometimes compromising results of the RS model (Fluent [16]).

The RS model is less stable than the $k-\varepsilon$ models. It therefore needs sophisticated grids[17] and converged results of other less advanced turbulence models. A good calculation procedure for the RS model:
1. starts with a converged solution of a $k-\varepsilon$ model then
2. changes the turbulence model to the default[18] RS model and
3. slowly adds complexity to the simplest RS model with a close watch on the convergence.

The RS model uses about 50-60% more CPU time per iteration compared to the $k-\varepsilon$ models (Fluent [16]) and needs more iterations to converge. The facts that the model:
- is unstable,
- uses more CPU time for a converged solution and
- not always produces better results,

make the RS model not very beloved. Most CFD users stick to the $k-\varepsilon$ models. However, the RS model is a must when anisotropy has a dominant effect on the mean flow or where features of interest are the result of anisotropy. With a focus on the topic of the thesis, such flows are characterized by (Fluent [16]):
- stress driven secondary flows or

---

[16] The other more elaborated $k-\varepsilon$ model in Fluent: the RNG $k-\varepsilon$ model, is not discussed because initial studies show that the realizable model gives the best performance of all $k-\varepsilon$ models (Fluent [16]).

[17] Grids with a small growth rate and small skewness of the cells. The model is observed to diverge in the outer flow region only if the grid in the outer region has medium growth rate although the flow gradients in the outer region were small.

[18] There are several optional complex models in Fluent.

- flows involving separation,
- flows involving strong adverse pressure gradients.

The RS model is likely to give better results compared to the $k - \varepsilon$ models in flows that involve (Fluent [16]):

- rapid changes of strain rate,
- complex flows.

An optional quadratic pressure strain model can be used because of its improved accuracy for complex flows. Particularly basic shear flows are demonstrated to be more accurately predicted with this option (Fluent [16]). Unfortunately, this option often results in divergence of the solution.

Concluding remarks
The RS model has the greatest potential to accurately predict and is even necessary for several flows of interest for this thesis (see discussion of the RS model). Yet, its results are still compromised by model assumptions and the use of the RS model does not justify the extra computational effort for simple flows. For the CFD calculations in this thesis the use of a certain turbulence model is founded on verifications of the CFD calculation with measurements. The pros and cons of the turbulence models are used for an initial guess of the most suitable turbulence model for a certain flow.

4.3.2   Near-wall region

There are two ways to deal with the near-wall region:

- the wall function approach and
- the near-wall model approach.

The wall function approach bridges the viscosity affected region (buffer and viscous sub layer, see for instance Nieuwstadt [51]) with a wall function. This wall function is the log-law that we already know from section 3.1.1. The near-wall model approach calculates the flow all the way down to the wall. Consequently, the wall function approach needs few cells close to the wall while the near-wall model needs many cells (because of the large flow gradients close to the wall) all the way down to the wall.

Wall function
The wall function or log-law is measured to be valid for $y^* > 30 \sim 60$ (see for instance Nieuwstadt [51]), where y^* is a non-dimensional distance defined by

$$y^* = \frac{\rho \, C_\mu^{\frac{1}{4}} k_p^{\frac{1}{2}} y_p}{\mu} \tag{105}$$

In (105), the quantity ρ denotes the density, k_p is the turbulent kinetic energy at point p, y_p is the distance from the wall to a point p and μ is the dynamic viscosity of the fluid. In Fluent, the default option applies (105) if $y^* > 11.225$.

Near-wall model
The wall function or log-law ceases to be valid if the flow conditions depart too much from the assumed (see section 3.1.1):

- constant shear stress and
- fully turbulent near-wall flow.

According to the assumptions of the log-law, the wall function is unreliable for flows with:

- a low Re number (no fully turbulent flow near the wall),
- severe pressure gradients leading to separation (shear stress not constant).

In those cases, the near-wall model is needed, i.e. the flow needs to be solved all the way down to the wall in spite of the extra computational effort.

For a fine mesh, where $y^* < 11.225$, the default option in Fluent applies the laminar stress-strain relationship

$$u^* = y^* \tag{106}$$

with y^* found by (105) and $u^* = \dfrac{u_p C_\mu^{\frac{1}{4}} k_p^{\frac{1}{2}}}{\tau_w / \rho}$, where u_p is the velocity at point p and τ_w is the

shear stress at the wall.

4.3.3   The grid

The use of an advanced turbulence model can be totally cancelled out by a bad grid. The grid configuration thus needs a lot of attention. A good grid also enhances the convergence. The major grid design guidelines are that:

- regions with large flow gradients need many (small) cells,
- the flow through all cells should -as much as possible- be normal to the inlet as well as normal to the outlet side of the cell,
- non-uniform grids should have a small growth rate (<1.2).

In order to reduce the computational effort, the number of cells in the domain has to be kept within limits. Non-uniform grids are introduced to fulfil the grid design guideline of many small cells at regions with large flow gradients and as few as possible cells within the total domain. The grid design is simplified by the introduction of block-structured grids. This involves a domain divided into several smaller domains or blocks, which are easier to fill with cells. The blocks should already take care of the grid guideline that the main flow through all cells should be normal to the inlet as well as the outlet side of the cells.

Fluent offers the possibility to use a structured or an unstructured grid. The structured grid has to be defined by the designer while the unstructured grid is largely automatically generated. Because manufacturing of a structured grid is time-consuming, the automatic generation of an unstructured grid is an interesting option. However, the unstructured grid can cause considerable angles between the flow direction and the normal on the inlet and outlet of the cells. This generates an error. In every cell, the components of the velocity through the cell surfaces are calculated and represented with a finite precision. The effect of this finite precision is sometimes referred to as numerical viscosity because it has the same effect as viscosity. Compared to a first order calculation scheme, a second order calculation scheme can reduce the numerical viscosity. Unfortunately, the second order scheme makes the calculation unstable and needs more computational effort.

A solution of a CFD calculation needs to be grid-independent. The grid size should be small enough to achieve this. The independency of the grid can be checked by comparing two converged solutions for two different grids: a fine and a course grid. Grid-independency is reached as the solutions are approximately the same. This is of course time-consuming. Guidelines, for instance for the near-wall region, can provide some of the necessary information for the grid size. However, grid-independence is only assured if it is checked with the above described method of refinement of the grid. Time-consuming but necessary! For all grids used for the CFD calculations in this thesis, grid-independency is assured by the forementioned method.

4.3.4   The atmospheric boundary layer

This section describes the simulation of a neutral atmospheric boundary layer in Fluent[15] .

Log-law inlet parameters
The turbulence parameters, of a neutral atmospheric boundary layer (see section 3.1.1) can be defined by (Wilcox [82]) the turbulent kinetic energy k

$$k = \frac{u_*^2}{\sqrt{C_\mu}} \approx 3.3 u_*^2 \tag{107}$$

with $k - \varepsilon$ model parameter $C_\mu = 0.09$, and the turbulent dissipation rate $\varepsilon(z)$

$$\varepsilon(z) = \frac{u_*^3}{\kappa(z + z_0)} \tag{108}$$

Log-law in Fluent
For the simulation of an atmospheric boundary layer, the wall function approach (section 4.3.3) can be used to avoid a large computational effort. By doing such, it has to be kept in mind that we implicitly assume a constant shear stress and fully turbulent flow near the earth surface (section 4.3.2).

It is not physically meaningful to have a first cell at the surface with a centroid height below the average height of the roughness elements. The example in section 4.3.5 furthermore shows that it also produces valueless results. For the built environment the average height of the roughness elements is the average building height $\overline{H}$. We thus demand $h_{cell} \geq 2\overline{H}$ for the first cell height h_{cell} adjacent to the surface. Consequently, h_{cell} is too large to be able to calculate details of the flow around buildings with a height slightly higher than $\overline{H}$. This observation is analogue to the observations that lead to (31): $z_{min} = 1.5d$, or in words "the velocity close to the roughness elements is determined by the local roughness and can not be found from the average roughness". The velocity close to the roughness elements can only be obtained if the individual roughness elements in the domain are modelled instead of the average roughness that they cause. This time-consuming job is not carried out for the simulations in this thesis.

At high z_0, the flow at the earth's surface is dominated by separation on the individual roughness elements and viscous effects are negligible. Consequently, the height of the roughness elements H is much higher than the height of the viscous sublayer $\rho u_*/\mu$. The regime of the boundary layer is then characterized as fully rough (see for instance Nieuwstadt [51]). In a fully rough regime, Fluent uses the law of the wall modified for roughness (Fluent [16])

$$u(z) = \frac{u_*}{\kappa} \ln\left(\frac{E\rho u_* z}{\mu}\right) - \frac{u_*}{\kappa} \ln\left(1 + C_{hb}H^+\right) = \frac{u_*}{\kappa} \ln\left(\frac{z}{\frac{\mu\left(1 + C_{hb}H^+\right)}{E\rho u_*}}\right) \tag{109}$$

where $E = 9.8$ for the default wall functions, C_{hb} is a constant that models the type of roughness and

$$H^+ \equiv \frac{\rho \overline{H} u_*}{\mu} \tag{110}$$

where $\overline{H}$ is the average physical roughness height[19] and μ is the dynamic viscosity (Fluent [16]). In a fully rough regime, $\overline{H}u_* >> \mu/\rho$ so that $H^+ \gg 1$. For uniform roughness, the roughness constant can be taken as $C_{hb} = 0.5$, while for non-uniform roughness a higher value $C_{hb} = 0.5 \sim 1$ is more appropriate (Fluent [16]). We will assume $C_{hb} = 0.75$ for non-uniform roughness.

Without the roughness elements being individually modelled, it must be assumed that $d = 0$ in the log-law for the neutral atmospheric boundary layer (27). Equating of (109) and (27) then gives the condition where both log-law models have equal velocity profiles

$$z_0 = \frac{\mu(1 + C_{hb}H^+)}{E\rho u_*} \tag{111}$$

Because $H^+ \gg 1$ with $C_{hb} = 0.75$ (Fluent [16]) we have $C_{hb}H^+ \gg 1$ and thus with substitution of (110)

$$z_0 \approx \frac{C_{hb}}{E}\overline{H} \tag{112}$$

With $E = 9.8$ and $C_{hb} = 0.75$ we thus have

$$\overline{H} \approx \frac{E}{C_{hb}}z_0 \approx 13z_0 \qquad \text{for non-uniform roughness}$$

$$\overline{H} \approx \frac{E}{C_{Ks}}z_0 \approx 20z_0 \qquad \text{for uniform roughness} \tag{113}$$

$\overline{H}$ given by (113) is the input for the roughness of the simulated atmospheric boundary layer in Fluent. Equation (113) can be compared with the rule of thumb (30): $z_0 \approx 0.29 A_H \overline{H}$ or $\overline{H} = 4z_0/A_H$ (section 3.1.1). Apparently, the law of the wall modified for roughness assumes a certain density of the roughness at the surface. If $A_H \approx 0.24$, the rule of thumb gives $\overline{H} \approx 17z_0$.

The atmospheric boundary layer profile and turbulence parameters at the boundaries of the domain in Fluent can be specified with a User Defined Function (UDF). This UDF is a small c-program, which is read by Fluent. The UDF for the boundary layer simulations for this thesis specified $u(z)$ with (27), $k(z)$ with (107) and $\varepsilon(z)$ with (108). They were specified at three boundaries of the domain:
- the inlet,
- the top of the boundary layer and
- the outlet.

At the top of the simulated boundary layer, the velocity is specified because this gives the best similarity with the actual neutral atmospheric boundary layer where most energy is supplied by the upper layer and dissipated in the lower part of the boundary layer. It is emphasized that (113) is restricted to small z_0 say $z_0 < 0.5$ because it had to be assumed that $d = 0$.

4.3.5   Some initial verifications

The flow in the built environment can be characterized as flow around buildings in an atmospheric boundary layer. Those buildings can have a bluff, blunt or aerodynamic shape (section 3.2.1). The flow in the built environment therefore involves separation and large strain rates and can be qualified as complex flow. Murakami [50] shows that the $\kappa - \varepsilon$ models

---

[19] For the built environment, we have an average physical roughness height equal to the average building height $\overline{H}$. We therefore substituted $\overline{H}$ instead of the symbol used in Fluent [16].

as well as the RS model have difficulties to predict such complex flows, although they do not qualify the predictions as poor except for the standard $\kappa - \varepsilon$ model in stratified flow. Kim & Boysan [35] shows that the realizable $\kappa - \varepsilon$ model and the RS model can achieve accurate results for flows that involve separation.

Some initial quantitatively verified CFD calculations of flow characteristics of interest for this thesis should prove the ability to support the measurements in this thesis. For this purpose, the following aspects of the flow in the built environment are simulated.

Table 11 Initial verifications

Aspect	Verification with
Flow around a bluff body	Flat plate
Flow around an aerodynamic body	NACA 0018
Flow in the atmospheric boundary layer	$z_0 = 0.03 \, \text{m}$

Flat plate

As an example of the flow around a bluff body, the flow around a 2D and 3D flat plate is simulated. The drag coefficient C_d, the backpressure $C_{p,b}$ and Strouhal number S of the flat plate were calculated from the simulation and compared to measurements. The 3D calculation is carried out with an axi-symmetric grid and a steady formulation of the turbulence model because measurements do not show regular vortex shedding for a disk. The 2D calculation is carried out with a full 2D grid and an unsteady formulation of the solver to allow the observed vortex shedding in measurements. The results of measurements together with the results of the simulations are given in Table 12.

Table 12 C_d, S and $C_{p,b}$ of a flat plate, calculated with the realizable $k - \varepsilon$ model and RS model (see Appendix C) compared to the measurements (Hoerner [26]).

Source	3D axi-symmetric steady		2D unsteady		
	C_d	$C_{p,b}$	C_d	$C_{p,b}$	S
Hoerner [26]	1.17 $\text{Re} > 2 \times 10^3$	-0.42	1.98 $10^4 < \text{Re} < 10^6$	-1.13	0.13
Realizable $k - \varepsilon$ model	1.15 $\text{Re} = 8 \times 10^5$	-0.37	1.95 $\text{Re} = 10^5$	-1.08	0.19
RS model	1.18 $\text{Re} = 8 \times 10^5$	-0.39	2.05 $\text{Re} = 10^5$	-1.18	0.25

Table 12 clearly shows that the RS model does not always give the best results in spite of the more advanced modelling compared to $k - \varepsilon$ models. Several other researchers compare measurements and simulations with various turbulence models. Kim & Boysan [35] found that the advanced (non-standard) $k - \varepsilon$ models give to high (less negative) backpressures at bodies with separated boundary layers. This is in agreement with the results in Table 12 where it is furthermore shown that the RS model produces a more accurate backpressure. This more accurate backpressure is the reason for adoption of the RS model in chapter 7 in spite of the other less accurate results with the RS model (Table 12).

Atmospheric boundary layer

A 2D atmospheric boundary layer is simulated with the inlet conditions given in section 4.3.4 (turbulence models see Appendix C). The domain for the simulation has a height of 500 m and a length of 4km and the simulated roughness is $z_0 = 0.03 \, \text{m}$. The inlet profiles of velocity

$u(z)$, turbulent kinetic energy $k(z)$ and turbulent dissipation $\varepsilon(z)$ give the following agreement with the profiles at the outlet of the domain.
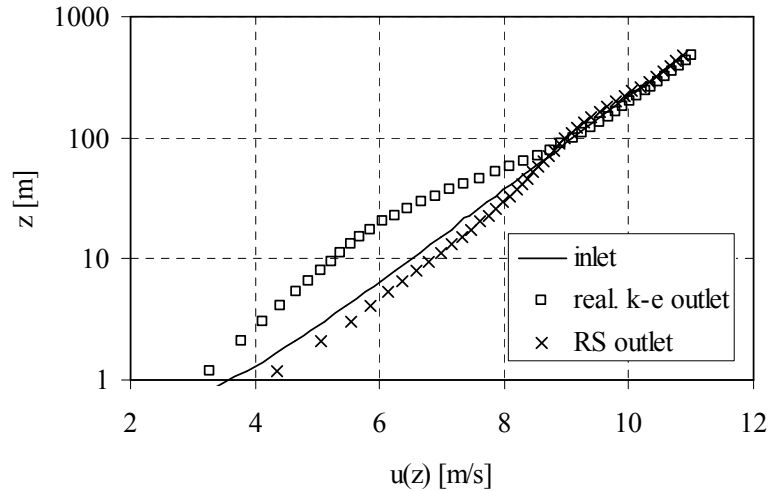

Figure 37 $u(z)$ **at inlet and outlet of the simulated flow domain calculated with the realizable** $k-\varepsilon$ **model and the RS model for** $z_0 = 0.03$ **m.**
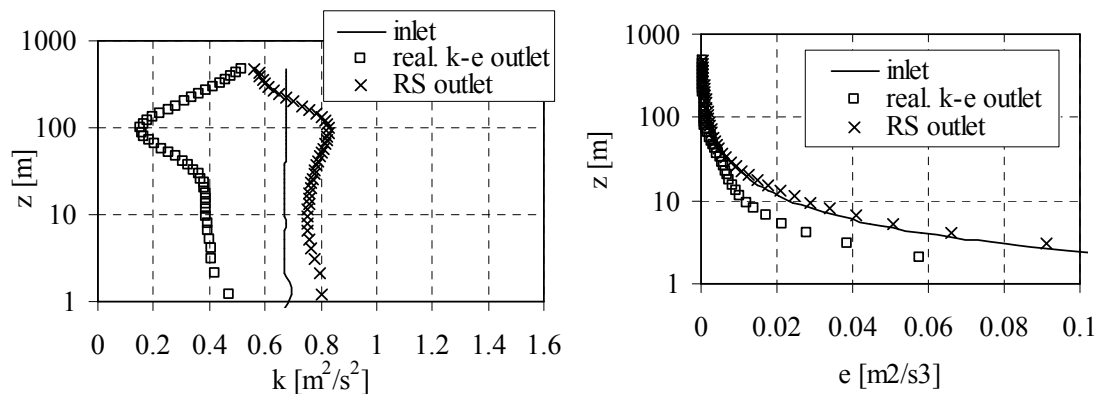
Figure 38 $k(z)$ **profiles (left) and** $\varepsilon(z)$ **profiles (right) at inlet and outlet of the simulated flow domain calculated with the realizable** $k-\varepsilon$ **model and the RS model for a roughness** $z_0 = 0.03$ **.**

From the figures, it is clear that the RS model gives a better performance than the realizable $k-\varepsilon$ model for all profiles. Consequently, in this thesis the RS model is used if the flow in atmospheric boundary layers needs to be simulated. Furthermore, the good agreement of the inlet and outlet profiles for the RS model (except for $k(z)$) proves that the simulation setup in section 4.3.4 is adequate if the RS model is used.

Two important guidelines for the simulation of an atmospheric boundary layer are: $h_{cell} \geq 2\overline{H}$ and $d \approx 0$ (section 4.3.4). The effect of disobeying the guidelines is shown by simulating a boundary layer with $z_0 = 1\,\text{m}$ with h_{cell} fitting a simulation for $z_0 = 0.03$ m i.e too small cells at the surface. The result is depicted in Figure 39.

Figure 39 $u(z)$ **at inlet and outlet of the simulated flow domain calculated with the realizable** $k - \varepsilon$ **model and the RS model for** $z_0 = 1$ **with too small** h_{cell} **at the earth's surface.**
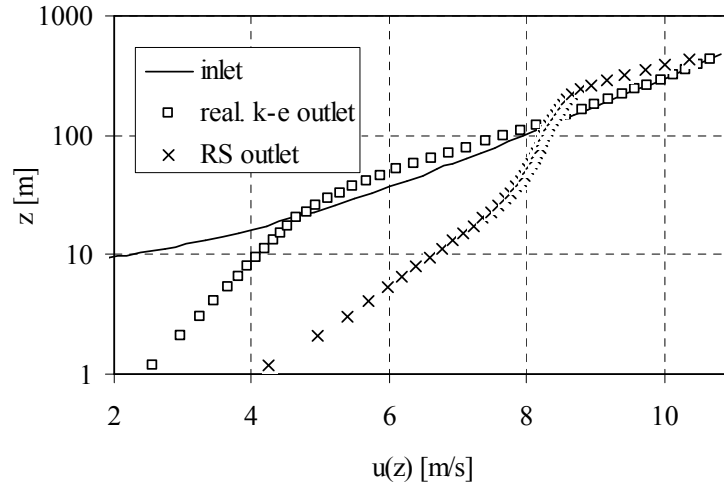
It is clear from Figure 39 that this gives very poor results.

NACA 0018 Airfoil

Airfoil-shaped buildings exist. Such airfoil-shaped buildings form part of the topic of chapter 6. Consequently, an initial exploration of CFD for aerodynamic bodies is necessary and carried out hereafter.

Several turbulence models are used to calculate the lift of a NACA 0018 (Jacobs [30]) airfoil at 8° angle of attack. The simulation results are compared with results of calculations given in Paraschivoiu [87]. The near-wall model approach is adopted for the grid of the CFD simulation. The simulations show that the realizable $k - \varepsilon$ model with a 2nd order upwind scheme gives the best results for this configuration combined with a fast convergence (Appendix H). The RS model diverged at the boundaries of the domain because of the non-uniform grid (although the growth factor of the grid was only 1.2). The realizable $k - \varepsilon$ model with a 2nd order upwind scheme (Appendix C) is used in a further verification of C_l and C_d for different α up to angles above stall. These CFD simulation results are again compared with results of calculations given in Paraschivoiu [87] and calculations with a commercial panel code (RFOIL) and shown in Figure 40.
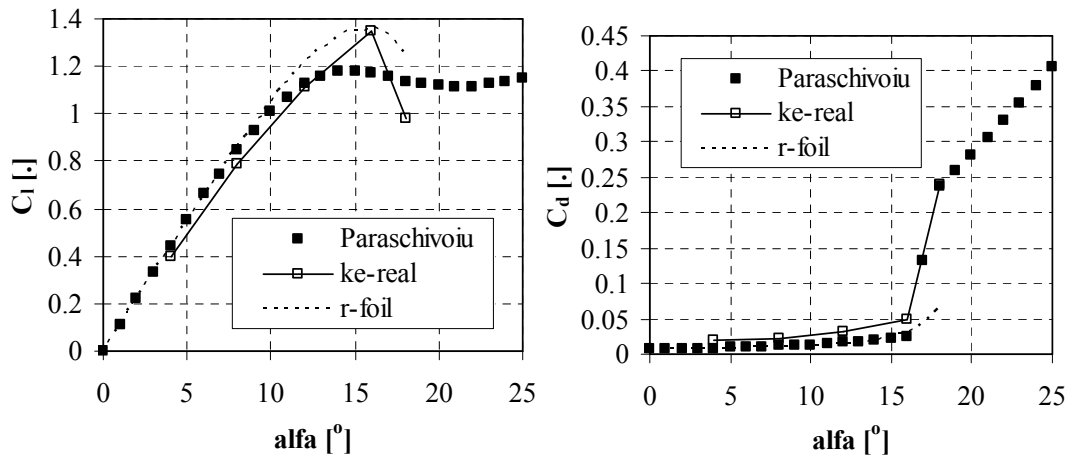
Figure 40 C_l **and** C_d **of a NACA 0018 airfoil at** $\mathrm{Re} = 2.10^{6}$ **as a function of** α.

From Figure 40, we conclude that the realizable $k - \varepsilon$ model gives:
- a good performance concerning trend prediction,

- • a sufficient quantitative agreement for C_l below stall and
- • a poor quantitative agreement for C_d.

Overall conclusion concerning initial verifications
From the shown initial verifications, it is clear that CFD simulations according to the guidelines in section 4.3 give:
- • good qualitative results and
- • acceptable-to-good quantitative results.

The measurements for this thesis are therefore supported by CFD calculations with:
- • the RS model for simulation of boundary layers and flow around bluff bodies and
- • the realizable $k - \varepsilon$ model with a 2nd order upwind scheme for the simulation of flow around aerodynamic bodies.

In order to be able to rely on the quantitative results of the simulations, backing by measurements is shown to be necessary. The CFD calculations for this thesis are therefore verified with measurements or other quantitative information.

5 Wind turbines close to buildings

Wind turbines close to (beside or on top of) a building operate in the flow region influenced by the building. If the whole stream tube, with an approximate length of six rotor diameters (section 2.2.2), lies within the region with accelerated wind, the power can be calculated from the cube of the accelerated wind speed. For a cylindrical or spherical building shape, the acceleration found in section 3.2.2 then gives the following power augmentation compared to the power in the free stream wind speed.

Table 13 Maximum power augmentation for small wind turbines close to buildings.

Building shape	Acceleration (section 3.2.2)	Power augmentation
Cylinder (2D)	2	8
Sphere (3D)	1.5	3.4

This chapter deals with the performance of the wind turbines close to buildings and provides the energy yield of a wind turbine above the roof of a sharp-edged building. Wind turbines high enough above the roof do not suffer from the low velocities in the recirculation region (section 3.3.2) and operate in accelerated wind for all wind directions while wind turbines beside buildings are sited in the wake of the building for certain wind directions. This is an important advantage for the energy yield of wind turbines at the roof but the acceleration beside 2D buildings (for instance buildings with cylindrical shape) can be higher and reduce this advantage. Chapter 8 gives example energy yields for a cylindrical and spherical building shape.

5.1 The wind turbine's performance close to a building

It is clear that a high acceleration of the free stream wind speed is wanted for the wind turbine close to the building. But more detailed flow information is necessary for additional understanding of the performance. This section therefore analyses the flow close to a building.

5.1.1 Performance in partly accelerated flow

Wind turbines with a large rotor compared to the characteristic building size do not solely perform in the accelerated wind close to the building. The power augmentation for those wind turbines can therefore not be found with the cube of the acceleration.

Definition large rotor

Let us examine the flow configuration for a wind turbine with a large rotor diameter D_t compared to the characteristic building size. The virtual inlet of the stream tube of the rotor is located approximately $2.5D_t$ upwind of the rotor (section 2.2.2, Appendix A) in partly accelerated or decelerated flow upwind of the building façade. The downwind part of the stream tube with approximate length $3.5D_t$ (section 2.2.2, Appendix A) is located in the accelerated wind speed $C_r u_0$ with $C_r > 1$ at the sides of the building. The flow configuration is shown in Figure 41 for a wind turbine above the roof and a wind turbine besides a building. Locations on the virtual inlet and outlet of the stream tube are marked with a dot.
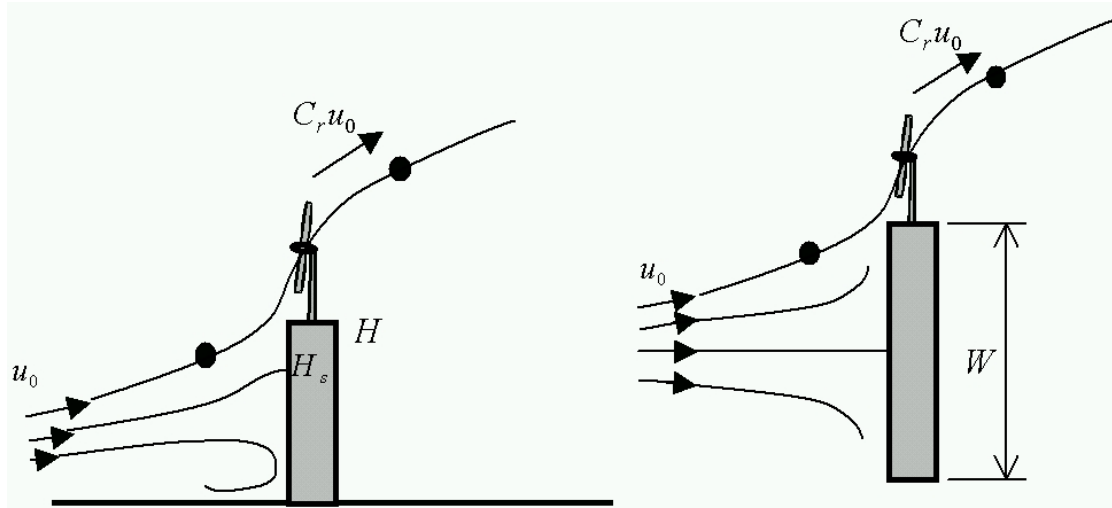
Figure 41 Streamline through the rotor of a wind turbine on the roof of a building (left) and besides a building (right).

Very approximately, the wind speed around the inlet of the stream tube is u_0 while the velocity around the rotor and outlet of the stream tube is $C_r u_0$. Therefore, the velocity around the upwind part of the stream tube with length $2.5 D_t$ accelerates from u_0 to $C_r u_0$ in a distance of $O(H - H_s)$ for the "at the roof configuration" and $O(0.5W)$ for the "beside the building configuration" (see Figure 41). Accordingly, the power augmentation will be smaller than the cube of the acceleration if $2.5 D_t > O(H - H_s)$, where H_s is found by (63). This gives

$$\frac{D_t}{H} > O(0.1) \tag{114}$$

for the wind turbine at the roof. A similar reasoning gives

$$\frac{D_t}{W} > O(0.2) \tag{115}$$

for the wind turbine beside the building. Equation (114) and (115) once more illustrate that the BAWT has a small size compared to the characteristic size of the building.

Performance large rotor
Suppose $D_t/H > O(0.1)$ or $D_t/W > O(0.2)$ so that the large rotor performs in partly accelerated flow. The complex configuration of the wind turbine in the curved stream tube in the accelerating flow (Figure 41) is simplified to an actuator in accelerating parallel flow as shown in Figure 42. Locations on the virtual inlet and outlet of the stream tube are again shown with dots.
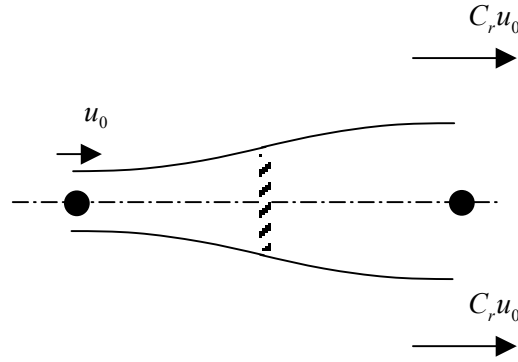
Figure 42 Performance of an actuator (shaded line) in accelerating parallel flow from u_0 around the virtual stream tube inlet to $C_r u_0$ around the virtual stream tube outlet.

The accompanying large loads of relatively large rotors will affect the speed up of the flow C_r so that C_r depends on the load. It is however assumed that the load and the rotor size are such that this interaction can be neglected i.e. it is assumed that $C_r = const$.

Simplified vortex theory (see section 4.1.2) can be used to calculate the power coefficient of a wind turbine in such configuration. The model for the flow in Figure 42 is shown in Figure 43.
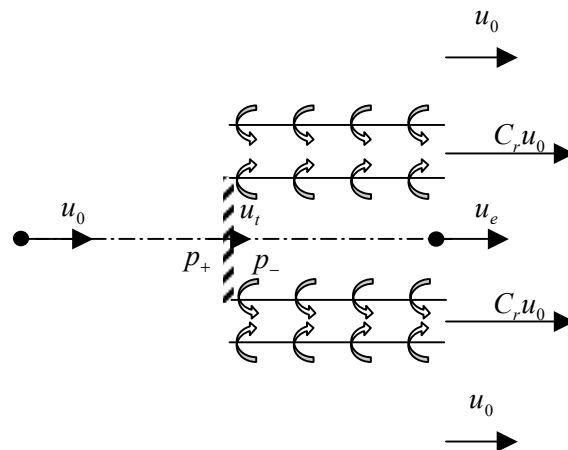
Figure 43 Vortex sheet model of an actuator (shadowed line) in partly accelerated flow.

The outer vortex sheets are used to model the increase of the velocity from u_0 to $C_r u_0$. The inner vortex sheets are the boundary of the wake caused by the actuator, as in Figure 33. The configuration shown in Figure 43 will be referred to as the "half-stream-tube configuration" because approximately half the stream tube of the actuator lies within accelerated flow. If the half-infinite outer sheets in Figure 43 are continued to an infinite distance upwind of the actuator, the whole stream tube lies within the accelerated flow. The power augmentation is then found from the cube of C_r so that $C_{P,\max} = \frac{16}{27} C_r^3$ where $C_{P,\max}$ is defined on u_0. This configuration will be referred to as "whole-stream-tube configuration".

From simplified vortex theory (section 4.1.2), the velocity through the actuator in the half-stream-tube configuration reads

$$u_t = u_0 + \tfrac{1}{2}\left(C_r u_0 - u_0\right) - \tfrac{1}{2}\left(C_r u_0 - u_e\right) \tag{116}$$

which produces exactly the same equation as found for an actuator in uniform flow (section 2.1.2, (8)):

$$u_t = \tfrac{1}{2}\left(u_0 + u_e\right) \tag{117}$$

With Bernoulli's theorem and assumption of equal static pressure in the wake and the location with velocity $C_r u_0$, the pressure difference across the actuator reads

$$p_+ - p_- = \tfrac{1}{2}\rho\left(\left(C_r u_0\right)^2 - u_e^2\right) \tag{118}$$

this gives for the power coefficient of the actuator in partly accelerated flow

$$C_P = \tfrac{1}{2}\left(C_r^2 - \left(\frac{u_e}{u_0}\right)^2\right)\left(1 + \frac{u_e}{u_0}\right) \tag{119}$$

The maximum power coefficient $C_{P,\max}$ is found by differentiation of (119) with respect to u_e. The optimal end velocity in the stream tube reads

$$\frac{u_{e,opt}}{u_0} = -\tfrac{1}{3} + \tfrac{1}{3}\sqrt{1 + 3C_r^2} \tag{120}$$

which gives

$$C_{P,\max} = \tfrac{1}{27}\left(3C_r^2 - 1 + \sqrt{1 + 3C_r^2}\right)\left(2 + \sqrt{1 + 3C_r^2}\right) \tag{121}$$

This result is applicable for:
- 2D and 3D actuators (the used simplified vortex sheet theory is valid for 2D and 3D configurations)
- in the half-stream-tube configuration.

Figure 44 shows that the $C_{P,\max}$ in the half-stream-tube configuration (121) is less than the $C_{P,\max}$ for the whole-stream-tube configuration ($C_{P,\max} = \frac{16}{27} C_r^3$).
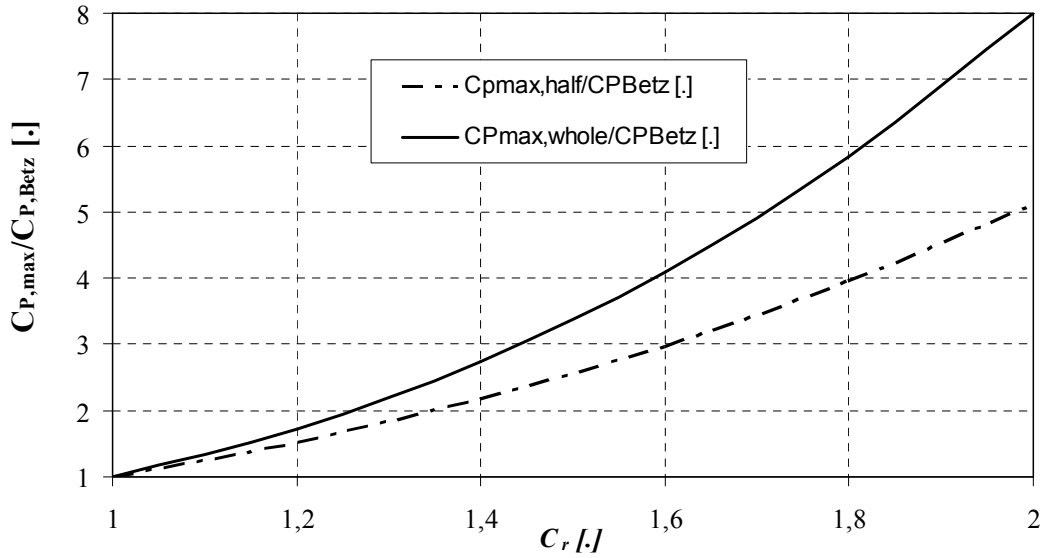
Figure 44 $C_{P,\max}$ **found for the half- and whole-stream-tube configuration as a function of** C_r **.**

An example of the performance in the half-stream-tube configuration gives additional information. At $C_r = 1.2$, (121) gives 34% less power for the half-stream-tube configuration compared to the whole-stream-tube configuration. It is clear, although a bit remarkable, that the actuator in the half-stream-tube configuration produces only slightly less power than the whole-stream-tube configuration with just half the stream tube within accelerated flow. With Bernoulli's theorem, the pressure coefficient at large distance downwind of the actuator reads

$$C_{p,e} = \sqrt{1 - C_r^2} \qquad (122)$$

The Betz limit (section 2.1.2), (120) and (122) provide the following information on the operation at $C_r = 1.2$.

Table 14 Differences between the performance in the whole- and half-stream-tube configuration with $C_r = 1.2$ **.**

Quantity	Whole-stream-tube configuration	Half-stream-tube configuration
$u_{e,opt}/u_0$	0.4	0.44
$C_{p,e}$	0	-0.44

Table 14 shows that the difference in $u_{e,opt}/u_0$ for the half- and whole-stream-tube configuration is small while the difference in $C_{p,e}$ is large. Dumping of the decelerated air at the low pressure in the region with accelerated flow is clearly the origin of the small power drop in the half-stream-tube configuration compared to the whole-stream-tube configuration.

5.1.2   The acceleration at the roof

In section 3.2.3, the wind speed close to the building u_i is defined in terms of the free stream wind speed $u_{0,i}$ at a certain reference height (for instance roof height) and wind direction i.

$$u_i = C_{r,i}\, u_{0,i}$$

The factor $C_{r,i}$ is assumed Re-independent. Furthermore, $C_{r,i}$ is a function of:

- the (local) surface roughness around the building,
- the building shape,
- the wind direction,
- the height above the roof.

A CFD calculation (Appendix C) provided the $C_{r,i}$ values for the following configuration.

Table 15 Configuration for the CFD calculation of $C_{r,i}$ where $u_{0,i}$ is defined on the roof height (Mertens [49]).

depth:width:height	1:3:2
Building height [m]	20
Surrounding roughness [m]	$z_0 = 0.03$

The wind speed u_i was calculated with a CFD calculation on three locations above the roof that are marked with a dot (Figure 45).
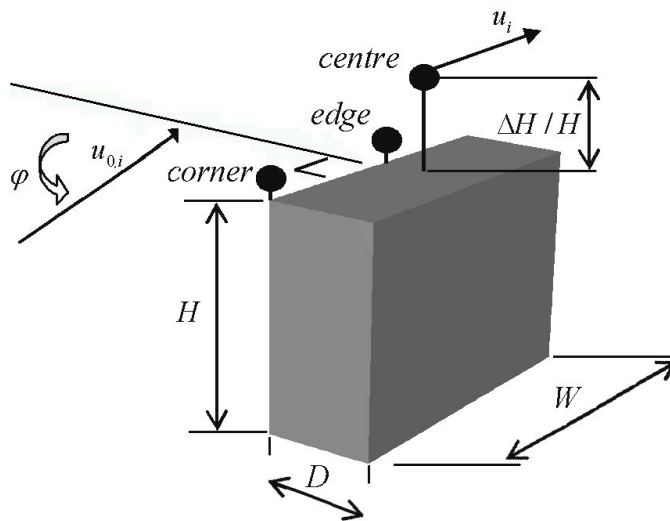

Figure 45 Locations where the wind speed is calculated with a CFD calculation.

For those locations above the roof the calculated $C_{r,i}$ values for different wind directions φ are given in Table 16. The heights above the roof $\Delta H/H$ were chosen because they showed the highest acceleration for a wind direction perpendicular to the largest facade of the building.

Table 16 $C_{r,i}$ **defined on** u_0 **at roof height for a height** $\Delta H/H$ **above the roof and a surrounding roughness of** $z_0 = 0.03$ **m (Mertens [49]).**

	$C_{r,i}$		
	Centre	Edge	Corner
φ	$\Delta H/H = 0.25$	$\Delta H/H = 0.05$	$\Delta H/H = 0.05$
0	1.09	1.06	1.14
45	1.26	1.25	1.25
90	1.05	0.89	1.19
135	1.26	1.11	1.20
180	1.09	0.38	0.13
225	1.26	1.11	0.22
270	1.05	0.89	0.98
315	1.26	1.25	1.06

At the edge and corner location the $C_{r,i}$ values at $\varphi = 180^o$ are very low, which points to presence in or downwind of the recirculation region . This is also clear from the streamlines in Figure 46 found with the CFD calculation.
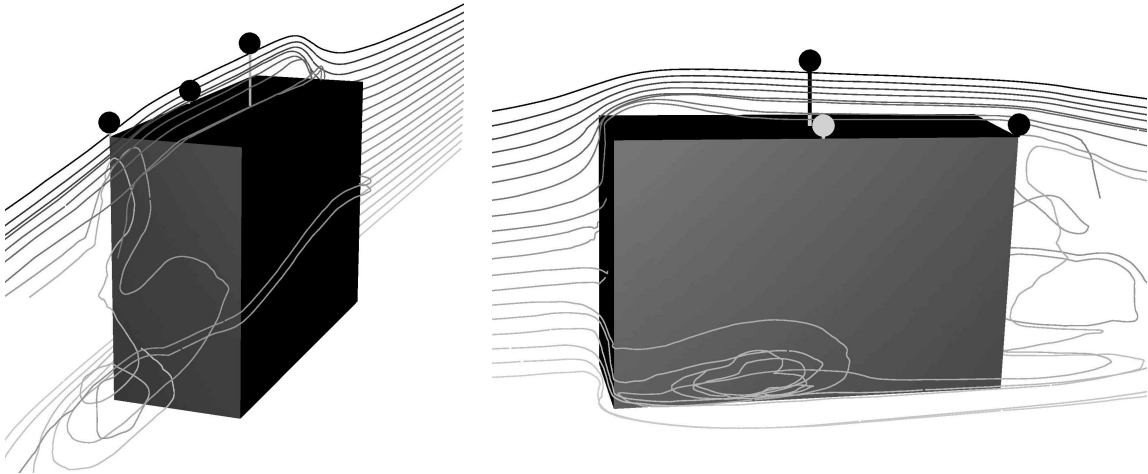
Figure 46 Flow configuration at $\varphi = 180^o$.

The $C_{r,i}$ values for the centre location show the smallest influence from the recirculation region . For the centre location, the height above the roof is taken as $\Delta H/H = 0.25$ (Table 16). The height of the separation streamline above the roof of this 3D building at $\varphi = 0^o$ is found with (69) to be $\Delta H/H = 0.195$. Other φ will gives smaller recirculation region s. Hence the centre location is above the recirculation region for all φ.

Comparison of centre- with the edge- and corner location shows that:
- the measure for the energy density at the centre location found with (57) is 40% higher than the edge- and corner location,
- the angle of the flow with the roof at the centre location shows less variation than the edge- and corner location,
- the angle of the flow with the roof at the edge- and corner location can be large at $\varphi = 0^o$ and
- Table 16 shows that the velocity variations for different wind directions at the centre location are smaller than at the edge- and corner location.

The smaller velocity variations for different wind directions at the centre location are also clear from the probability distributions (55) that give the result shown in Figure 47.
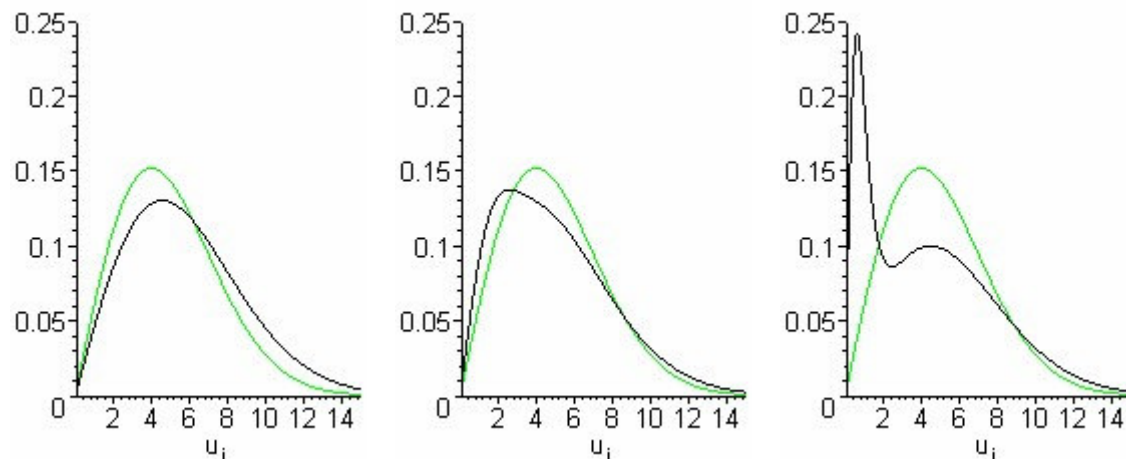
Figure 47 Wind speed probability distributions on the roof (black curve) compared with the free stream wind speed probability distribution (grey curve); for the centre (left), edge (middle) and corner location (right).

The centre location is consequently strongly favourable.

5.2 The lift-driven HAWT in skewed flow

Many buildings have a cubic shape: the roof is flat and sharp-edged. In section 3.3.2 it was shown that the flow separates at such sharp edges. Consequently, the flow makes an angle with the roof that varies with the position on the roof. This angle will be called the skew angle to distinguish it from the yaw angle in the horizontal plane. Similar skewed flow is found beside a building. Wind turbines above the roof or beside a building have to operate in the "skewed flow" (Figure 48). A tilt mechanism at the mast that creates normal flow for the rotor is too expensive and increases the probability of failure. Therefore, the rotor is operated in skewed flow.
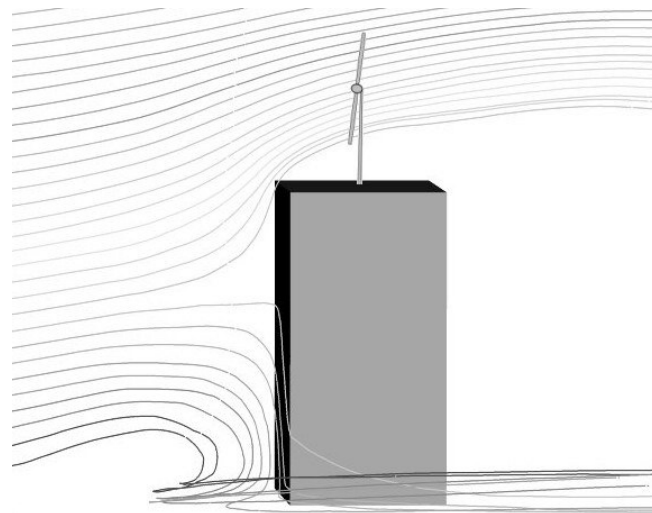
Figure 48 A HAWT in the flow above the recirculation region on the roof (streamlines found by a CFD calculation).

The behaviour of a HAWT in skewed flow can be investigated with Glauert momentum theory, which shows good agreement with measurements (Madsen et al. [39]). Glauert momentum theory is a mix of momentum theory and engineering assumptions. It is based on

two different derivations for the induced velocity. One derivation is valid for large skew angle and one derivation is valid for zero skew angle. Because both derivations give the same result for the induced velocity, Glauert assumed that the result should also be applicable to intermediate skew angles. The thrust- and power coefficient found with Glauert momentum theory for a lift-driven HAWT in skewed flow read (Burton et al. [8])

$$C_t = 4a\sqrt{1-a\left(2\cos\gamma - a\right)} \tag{123}$$

and

$$C_P = 4a\sqrt{1-a(2\cos\gamma - a)}\left(\cos\gamma - a\right) \tag{124}$$

where a is defined on the total free stream velocity. $C_{P,\max}$ found from differentiation of (124) with respect to a decreases with γ as shown in Figure 49.

Figure 49 $C_{P,\max}$ **of a HAWT as a function of the skew angle** γ **(** $C_{P,\max,0} = \frac{16}{27}$ **).**
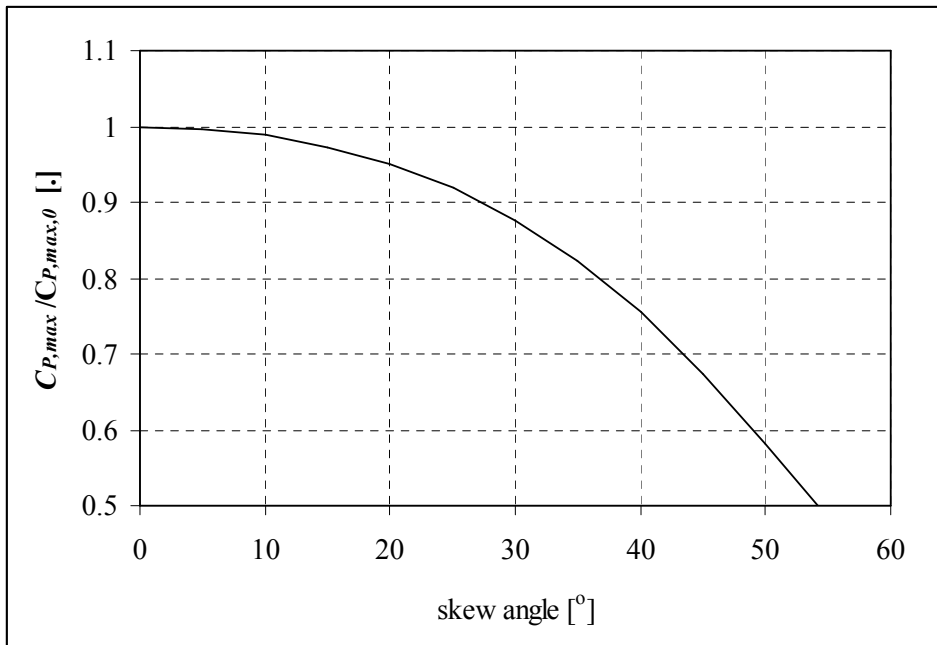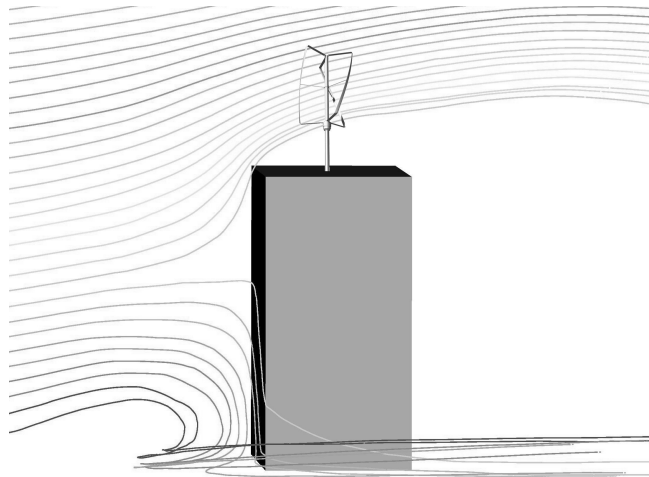
5.3 The H-Darrieus in skewed flow

Figure 50 An H-Darrieus (Turby) in the flow above the recirculation region on the roof (streamlines found by a CFD calculation).

In section 2.4 it was shown that an H-Darrieus is very suitable for operation in the built environment. However, the performance of an H-Darrieus in skewed flow is unknown. The prototype of our aerodynamic H-Darrieus design, Turby, was therefore tested in skewed flow in the open jet wind tunnel (Mertens [44], Sardo [62]). Surprisingly, operation in skewed flow showed an appreciable increased power output compared to normal flow.

Modelling the operation of an H-Darrieus and even more an H-Darrieus in skewed flow with low λ (design guidelines built environment, section 2.4) is very difficult, and numerous complicated issues need to be addressed:
1. finite aspect ratio effects of the H-Darrieus blades in skewed flow i.e. for swept blades,
2. behaviour of local thrust in skewed flow at large induction factor,
3. interaction of the different flow regimes through the H-Darrieus,
4. behaviour of the blades at low Re number,
5. behaviour of the blades in dynamic stall.

There is a variety of models available to calculate the performance of an H-Darrieus (Paraschivoiu [53]). Three of those models are based upon blade element and momentum theory. The simplest is a model that assumes a single stream tube through the whole rotor, modelled by a single actuator. A more advanced model is the single actuator multiple stream tube model. This model is based on multiple non-interacting stream tubes through the rotor. The most advanced model in this row is the double actuator multiple stream tube model, which separately models the upwind and downwind rotor part of the H-Darrieus by two actuators instead of the single actuator in the forementioned models. Furthermore, an advanced model based on vortex theory is available. For our goal, we choose the single actuator multiple stream tube model as a compromise between the simple and advanced models.

5.3.1   Induction factor at small load

The single actuator multiple stream tube model first developed by Wilson & Lissaman [84] will be used. The basic assumptions, important for the model of an H-Darrieus in skewed flow, are that:
- the deceleration of the air by the upwind and downwind part of the rotor can be modelled with one actuator between the upwind and downwind rotor part,

- the flow through the rotor can be modelled as flow through multiple stream tubes that do not interact with each other,
- the chord length of the blades c is much smaller than the radius R of the H-Darrieus.

The first model of an H-Darrieus in skewed flow was published by Mertens et al.. [48]. A second -more elaborated- model that forms the basis of the model presented in this section was also published by Mertens et al.. [47].

In skewed flow with skew angle γ to the horizontal, the rotor can be divided into two parts as shown in Figure 51. One part of the rotor decelerates the flow with only one rotor part: the upwind or downwind rotor part (subscript s) and the other part of the rotor decelerates the flow with two rotor parts: the upwind and downwind rotor part (subscript d).
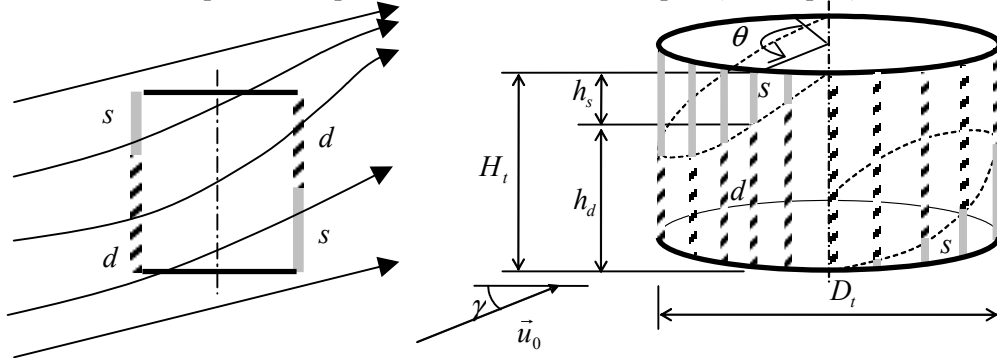
Figure 51 Deceleration of the flow by a single- or double-rotor part of an H-Darrieus. A cross-section of the rotor at the left side is shown at the right side.

The vertical length of the blade h_s or h_d that operates in respectively the single- or double-rotor part configuration depends on:
- the skew angle of the flow,
- the induction factor,
- the angle θ and
- the ratio H_t/D_t .

The last influence immediately reveals an important operation quality of the H-Darrieus in skewed flow. For a large skew angle and a wide rotor of the H-Darrieus, almost the whole rotor operates in the single-rotor part configuration while a slender rotor almost entirely operates in the double-rotor part configuration.

An elegant train of thought described in Hoerner [27] can be used to find the lift of an airfoil in skewed flow. Consider the set-up of a non-swept airfoil in potential parallel flow. The lift force of that airfoil is determined by the angle of attack α of the flow and the free stream velocity. Now translate that airfoil perpendicular to the flow direction. The potential flow experiences the same airfoil boundaries. Hence, the lift of the translated non-swept airfoil will be unchanged and determined by the same α and velocity of the parallel flow. It is concluded that, as long as skin friction is of no importance, the normal velocity component $u_{0,\perp,d}$ determines the lift and the velocity component parallel to the airfoil $\vec{u}_{0,\parallel,d}$ is not important.

According to this so-called "cross-flow principle", the lift force of a swept airfoil or an airfoil in skewed flow is determined by the component perpendicular to the airfoil.

Leishman [38] shows some measurements, which make clear that above stall, C_l as well as α at $C_{l,max}$ largely increase with increasing sweep angle. Above stall, the use of the cross-flow principle is thus not allowed.

First, the double-rotor part operation is analysed. According to the adopted single actuator model of the H-Darrieus, the double-rotor part is modelled with a single actuator. By definition in the actuator concept, the pressure force and consequently the induction factor point perpendicular to the actuator. We thus find the velocity perpendicular to the double-rotor part of the actuator as

$$u_{0,\perp,d} = u_0(\cos\gamma - a_d) \tag{125}$$

where u_0 is the skewed velocity, γ is the skew angle and a_d is the local induction factor of the double-rotor part. The situation is shown in Figure 52.
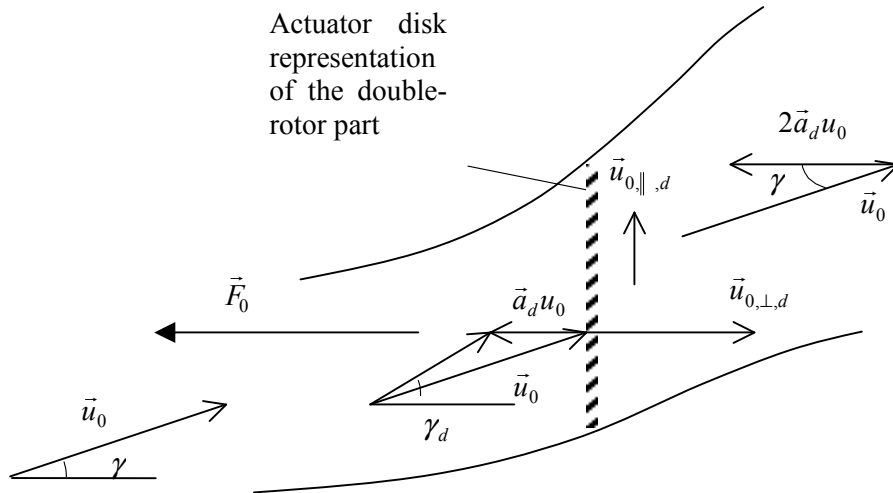
Figure 52 The flow through the actuator that models the double-rotor part in skewed flow.

There is no need to model the local flow angle γ_d for HAWT's because C_t and C_P can be found as a function of γ (section 5.2, (123) and (124)). For an H-Darrieus however, the local flow angle γ_d needs to be modelled because:

- γ_d determines the blade lengths h_s or h_d (Figure 51) and with this the performance of the H-Darrieus and
- γ_d can be very different from γ because of the sometimes very large a_d compared to the local induction factor of a HAWT[20].

According to Figure 52, γ_d can be found from

$$\gamma_d = \arctan\left(\frac{\sin\gamma}{\cos\gamma - a_d}\right) \tag{126}$$

The horizontal component of the velocity infinitely downwind of the actuator (see Figure 52): $u_0(\cos\gamma - 2a_d)$, equals zero or becomes negative for too large induction factors. This causes

---

[20] In section 2.4, it is shown by (21) that a_d varies across the rotor as $a_d \propto |\sin\theta|$, where θ denotes the rotational angle θ of the rotor blades. A moderate a_d at small θ is consequently coupled with a very high a_d at $\theta = 90^\circ$.

the flow assumptions in momentum theory to be violated. We therefore require that $\cos\gamma - 2a_d > 0$, which gives the restriction

$$a_d < \tfrac{1}{2}\cos\gamma \tag{127}$$

Blade element theory

By definition, the magnitude of the lift force $\left|\vec{L}_d\right|$ per unit blade length can be found from

$$\left|\vec{L}_d\right| = C_{l,d}\,\tfrac{1}{2}\rho\,u_{r,d}^2 c \tag{128}$$

This gives for the strength of the bound vortex at the blade (see for instance Katz & Plotkin [33])

$$\left|\vec{\Gamma}_d\right| = C_{l,d}\,\tfrac{1}{2}u_{r,d}c \tag{129}$$

where ρ is the air density, $u_{r,d}$ is the magnitude of the resultant velocity on the blade (see Figure 53), $\left|\vec{\Gamma}_d\right|$ is the strength of the bound vortex of the blade, c is the chord length of the blade, and $C_{l,d}$ is the lift coefficient of the blade of the double-rotor part.
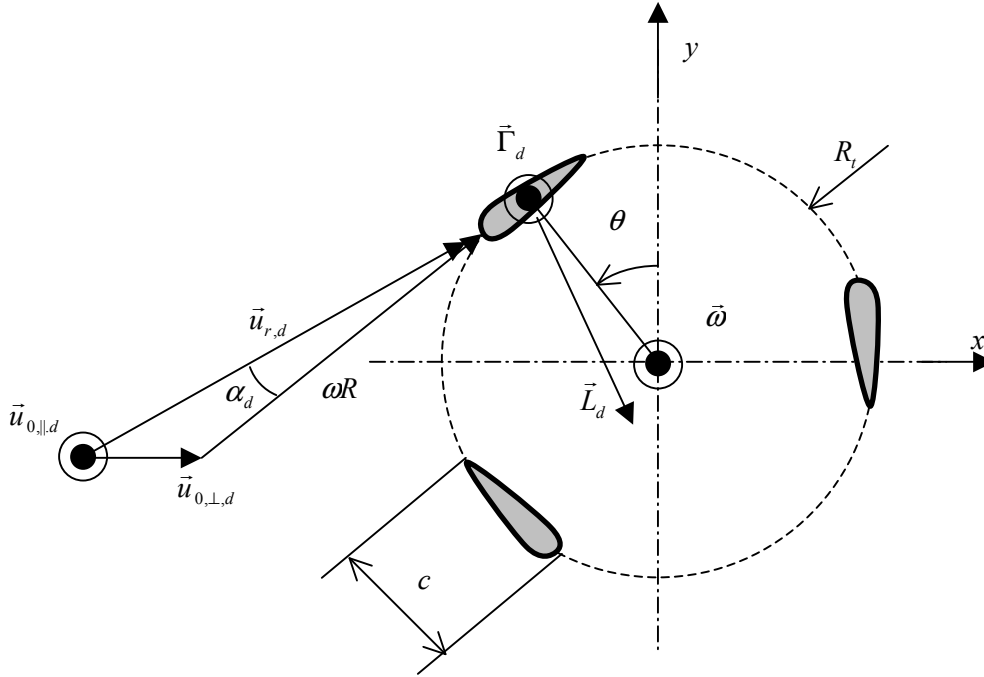
Figure 53 Top view of the H-Darrieus in skewed flow.

The C_l and C_d of the airfoil should be found from measurements or simulations/ calculations. The airfoil can be tripped at 20% chord length because this evokes a fixed location of the recirculation region at the airfoil. Without tripping, the recirculation region can move downwind of the trailing edge, which increases the noise emission of the airfoil. In Appendix I, calculated C_l-C_d data for a tripped NACA 0018 airfoil at different Re numbers are shown. Paraschivoiu [53] gives calculated C_l-C_d data from Sheldahl & Klimas [85],

which are -based on x-foil calculations- for an untripped NACA 0018 airfoil. They show a lower lift at low Re number and faster stall compared to the tripped NACA 0018 airfoil. Consequently, the tripping seems to have a positive influence on the C_l and with this on the performance of the rotor as well. Calculated results deduced from measurements on a NACA 0018 airfoil for low Re numbers are found in Eastman et al. [30].

The lift force of the blade per unit blade length can be found from

$$\vec{L}_d = \rho \vec{u}_{r,d} \times \vec{\Gamma}_d \tag{130}$$

with

$$\vec{u}_{r,d} = \begin{pmatrix} u_{r,d,x} \\ u_{r,d,y} \\ 0 \end{pmatrix} \quad \text{and} \quad \vec{\Gamma}_d = \begin{pmatrix} 0 \\ 0 \\ \Gamma_d \end{pmatrix} \tag{131}$$

This results in a lift force of

$$\vec{L}_d = \left(u_{r,d,y} \Gamma_d \right) \hat{i}_x - \left(u_{r,d,x} \Gamma_d \right) \hat{i}_y \tag{132}$$

Substitution of $u_{r,d,y}$ (see Figure 53) gives

$$L_{d,x} = \omega R_t \sin \theta \, \Gamma_d \tag{133}$$

With (129) this gives the lift force in the x-direction at the double-rotor part as

$$L_{d,x} = \tfrac{1}{2} C_{l,d} \rho \omega R_t \sin \theta \, c u_{r,d} \tag{134}$$

with radius of the H-Darrieus R_t, rotational speed ω, and rotational angle θ, where $\theta = 0$ corresponds to the location where the blade moves parallel to the wind direction $\vec{u}_{0,\perp,d}$ (see Figure 53).

The stream tube width is equal to

$$dy = R_t d\theta |\sin \theta| \tag{135}$$

Because of periodicity, the analysis on $L_{d,x}$ is limited to one revolution. In double-rotor part operation, the blade passes the flow in the stream tube twice in one revolution. The blade thus stays in the stream tube for a fraction of $2d\theta/(2\pi)$ of the total time of one revolution. So, (134) should be multiplied with $d\theta/\pi$ to find the average $L_{d,x}$ in the stream tube. For the single-rotor part, this averaging factor is half this value because the blade passes the flow in the stream tube just one time. From (134) and the foregoing averaging discussion, the average force $dF_{Bl,d}$ for B blades in the direction of the stream tube at operation in the double-rotor part now follows from $L_{d,x}$ as

$$dF_{Bl,d} = \tfrac{1}{2} B C_{l,d} \rho \omega R_t \sin \theta \, c u_{r,d} \frac{d\theta}{\pi} \tag{136}$$

where the index Bl at $dF_{Bl,d}$ refers to the so-called blade element theory.

Momentum theory

The thrust force found with (136) can also be found with momentum theory, which is then denoted as $dF_{M,d}$. Glauert momentum theory shows good agreement with measurements (Madsen, et al. [39]) and will therefore be used for the calculation of $dF_{M,d}$. It gives (see for instance Burton et al.. [8])

$$dF_{M,d} = \rho R_t d\theta |\sin\theta| w_d 2a_d u_0 \tag{137}$$

where w_d is the magnitude of the resultant velocity towards the actuator (see Figure 52)

$$w_d = u_0 \sqrt{\sin^2\gamma + (\cos\gamma - a_d)^2} \tag{138}$$

Equating of $dF_{Bl,d}$ (136) and $dF_{M,d}$ (137), gives an implicit relation for a_d for an H-Darrieus with B blades for operation in the double-rotor part configuration in skewed flow

$$a_d = \frac{1}{4\pi} \frac{Bc}{R_t} C_{l,d} \lambda \frac{u_{r,d}}{w_d} \tag{139}$$

where λ is found from $\lambda = \omega R_t / u_0$.

The same derivation for (139) is carried out for the single-rotor part operation. However, the blades moves only one time through the flow in the stream tube so that the averaging factor within blade element theory is found by $\frac{1}{2} d\theta/\pi$. The result is

$$a_s = \frac{1}{8\pi} \frac{Bc}{R_t} C_{l,s} \lambda \frac{u_{r,s}}{w_s} \tag{140}$$

The local flow angle is then found as

$$\gamma_s = \arctan\left(\frac{\sin\gamma}{\cos\gamma - a_s}\right) \tag{141}$$

Note the different induction factor in the double- and single-rotor part operation and consequently the different flow angles in the double- and single-rotor part operation (see also Figure 51, left). To illustrate the difference, we substitute $C_{l,d} = 2\pi\sin\alpha_d$, $C_{l,s} = 2\pi\sin\alpha_s$ and $\gamma = 0$ and find after some manipulation that $a_s = \frac{1}{2} a_d$. This should indeed be the outcome because only half the number of blades decelerates the air in the single-rotor part operation compared to double-rotor part operation.

5.3.2   Induction factor at high load

For an induction factor that does not fulfil (127) i.e. if $a_d \geq \frac{1}{2}\cos\gamma$, momentum theory for an actuator in skewed flow brakes down. The velocity far downwind of the actuator approaches zero or becomes negative and the assumed flow pattern is violated. The (local) a_d value can be well above the value given by (127) so that the use of momentum theory is not allowed and

a_d has to be determined by other means. Hereafter a_d for $a_d \geq \frac{1}{2}\cos\gamma$ will be determined from measurements and rather crude deductions.

Let us first look at the double-rotor part operation at high induction factor. At $a_d = \cos\gamma$, the rotor blocks all the flow through the rotor and the flow experiences a solid plate. The thrust force of a solid plate $F_{t,p}$, which points normal to the plate reads

$$F_{t,p} = C_{t,p} \tfrac{1}{2}\rho u_0^2 A \quad \text{solid plate} \tag{142}$$

where A denotes the plate area. The thrust coefficient of a solid plate $C_{t,p}$ as a function of γ can be found from measurements (see Figure 54).
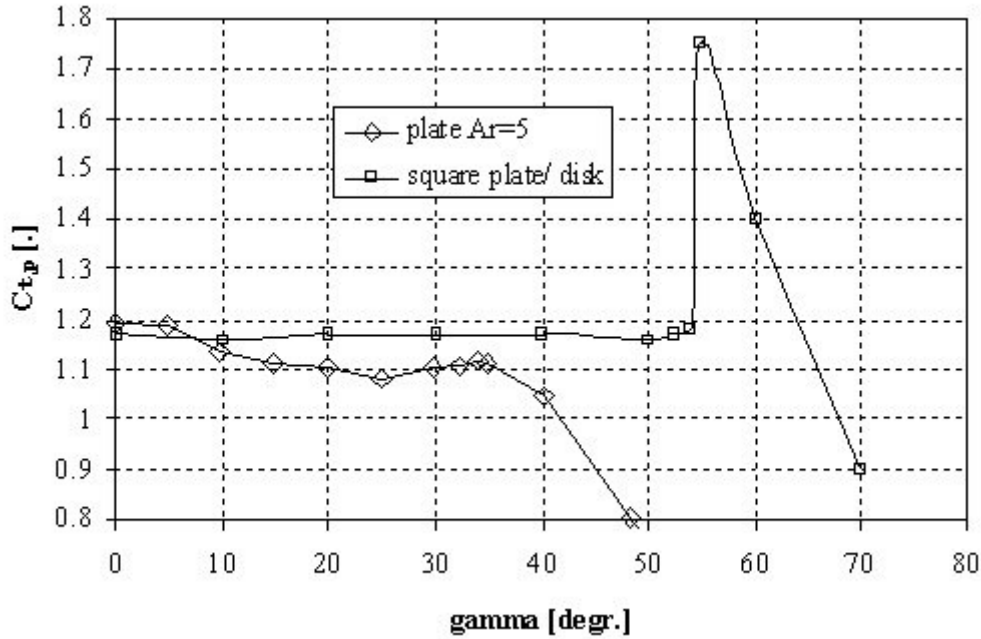
Figure 54 $C_{t,p}$ **as a function of** γ **(from** C_d **of a plate with aspect ratio 5 given in Simiu & Scanlan [67] and** $C_{t,p}$ **of a squared plate or disk given in Hoerner [26]).**

Measurements of the thrust force of a HAWT in normal flow provide an extrapolated thrust coefficient of $C_{t,b} = 1.6 \sim 2$ or $\overline{C_{t,b}} = 1.8$ at $a = 1$ (Burton et al.[8]). Hoerner [26] and Simiu & Scanlan [67] give $C_{t,p} \approx 1.2$ (see also Figure 54) for a rotating or non-rotating disk in normal flow. Apparently, $C_{t,b}$ is a factor $1.8/1.2 = 1.5$ times $C_{t,p}$. Hence,

$$C_{t,b} = 1.5\, C_{t,p} \quad \text{at } a = \cos\gamma. \tag{143}$$

where $C_{t,p}$ is found from Figure 54 for the appropriate shape of the H-Darrieus rotor. We will assume that (143) can be used for all wind turbines at $a = \cos\gamma$.

The thrust coefficient found with Glauert momentum theory in the double-rotor part operation (index d) is

$$C_{t,M,d} = \frac{dF_{M,d}}{\frac{1}{2}\rho\, u_0{}^2 R_t d\theta \sin\theta} \tag{144}$$

or with (137)

$$C_{t,M,d} = \frac{4 a_d w_d}{u_0 \cos\gamma} \tag{145}$$

The first order approximation of a straight line from $C_{t,b}$ to a point tangent to $C_{t,M,d}$, shows a good fit with measurements on a HAWT in normal flow (see for instance Burton et al.[8]). We will use a straight-line, tangent to $C_{t,M,d}$ at $\gamma = 0$ and equal to $C_{t,b}$ at $a_d = \cos\gamma$.

$$C_{t,lin,d} = \frac{C_{t,M,d} - C_{t,b}}{a_T - 1}\left(a_d - 1\right) + C_{t,b} \quad \text{for } a_d > a_T \tag{146}$$

where the so called transition induction factor a_T marks the change from momentum theory to the empirical straight line. In normal flow, a tangent straight line is achieved with $a_T = 1 - \frac{1}{2}\sqrt{C_{t,b}(\gamma = 0)}$ (Burton et al. [8]). Based on an approximate ratio of $C_{t,b}/C_{t,d}(a_d = a_T) \approx 0.5$ for all γ, we find a_T in skewed flow as

$$a_T = \left(1 - \tfrac{1}{2}\sqrt{C_{t,b}(\gamma = 0)}\right)\cos^3\gamma \tag{147}$$

It should be noted (see Figure 55 at $\gamma = 50$ or $\gamma = 60$) that a_T marks a change in the derivative $\dfrac{dC_{t,d}}{da_d}$ at $\gamma > 0$. This seems unphysical but is neglected as it is a direct result of the first order approximation of a linear relation (146) for $a_d > a_T$.
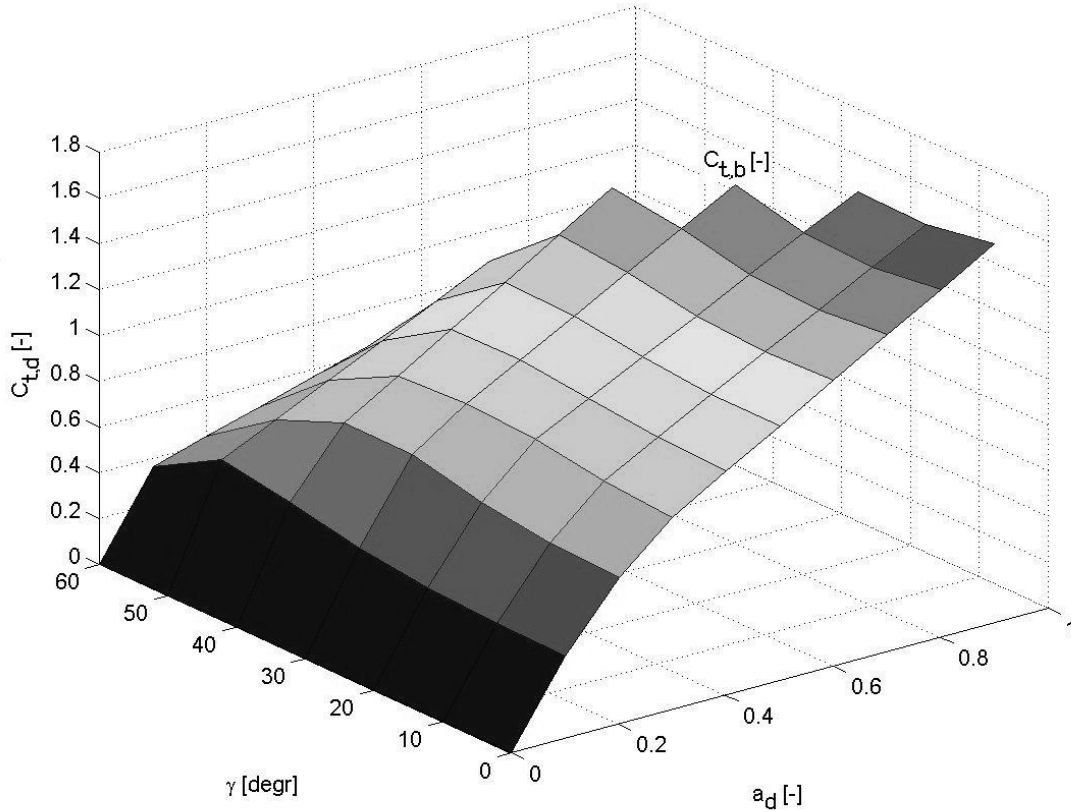
Figure 55 Example of $C_{t,d}$ **in skewed flow with** $C_{t,b}$ **calculated with (143) from a plate with aspect ratio 5 (Figure 54).**

In agreement with the usual assumption in normal flow, we will assume the set of equations for $a_d > a_T$ to be applicable to local conditions of the rotor of the H-Darrieus in skewed flow.

The same derivation is carried out for the single-rotor part, which results in

$$C_{t,M,s} = \frac{4a_s w_s}{u_0 \cos \gamma} \tag{148}$$

and

$$C_{t,lin,s} = \frac{C_{t,M,s} - C_{t,b}}{a_T - 1}(a_s - 1) + C_{t,b} \quad \text{for } a_s > a_T \tag{149}$$

5.3.3   Power coefficient

In section 5.3.1, it was shown that the power of the H-Darrieus in skewed flow is coupled with the flow angles through the rotor and the blade lengths in the single- and double-rotor part operation. Firstly, this section shows the model for the influence of the flow angle. Secondly, the power coefficient of the H-Darrieus in skewed flow is calculated.

The flow angle
In section 5.3.1, the flow angle in the double-rotor part operation is found to be different from the flow angle in the single-rotor part operation. In other words, the flow through one rotor

part pushes aside the flow through the other rotor part (see also Figure 51). It is assumed that the flows do not mix but instead have an average flow angle $\tilde{\gamma}$.

According to Figure 51, if

$$\tilde{\gamma} \leq \arctan\left(\frac{H_t}{2R_t}\right) \tag{150}$$

the blade length h_s for the single-rotor part operation, reads

$$h_s = 2R_t \tan\tilde{\gamma}\sin\theta \tag{151}$$

For the double-rotor part operation we have consequently

$$h_d = H_t - h_s = H_t - 2R_t \tan\tilde{\gamma}\sin\theta \tag{152}$$

If

$$\tilde{\gamma} > \arctan\left(\frac{H_t}{2R_t}\right) \tag{153}$$

and

$$\arcsin\left(\frac{H_t}{2R_t \tan\tilde{\gamma}}\right) \leq \theta \leq \pi - \arcsin\left(\frac{H_t}{2R_t \tan\tilde{\gamma}}\right) \tag{154}$$

h_s is limited to

$$h_s = H_t \tag{155}$$

and

$$h_d = 0 \tag{156}$$

For $\tilde{\gamma} > \arctan\left(\frac{H_t}{2R_t}\right)$ and θ outside the boundaries defined by (154), h_s and h_d can again be found with (151) and (152).

It is now possible to find $\tilde{\gamma}$ from the implicit weighted average of h_s and h_d defined by

$$\tilde{\gamma} = \frac{2h_s}{H_t + h_s}\gamma_s + \frac{H_t - h_s}{H_t + h_s}\gamma_d \tag{157}$$

which gives $\tilde{\gamma}(h_s = H_t) = \gamma_s$ and $\tilde{\gamma}(h_d = H_t) = \gamma_d$.

Local power coefficient
With assumption of the cross-flow principle (section 5.3.1), the extracted power dP, per unit blade length, in a stream tube with width dy, can be found from blade element theory. Based on the result of blade element theory in De Vries [76], we have

$$dC_{P,d} = \frac{B\,c\lambda}{2\pi R_t} \frac{h_d}{H_t} \left(\frac{u_{r,d}}{u_0}\right)^2 C_{l,d} \sin\alpha_d \left(1 - \frac{C_{d,d}}{C_{l,d}} \cot\alpha_d\right) d\theta \qquad (158)$$

for the double-rotor part operation and

$$dC_{P,s} = \frac{B\,c\lambda}{4\pi R_t} \frac{h_s}{H_t} \left(\frac{u_{r,s}}{u_0}\right)^2 C_{l,s} \sin\alpha_s \left(1 - \frac{C_{d,s}}{C_{l,s}} \cot\alpha_s\right) d\theta \qquad (159)$$

for the single-rotor part operation. The lift- and drag coefficients of the blades can be found from calculations or measurements (see for instance Appendix I).

Finite aspect ratio effects
At HAWTS, finite A_r effects are usually modelled with a tip loss factor that corrects the local induction factor at the blade for the downwash of the tip vortex of the blade. This approach results in a span-wise variation of the induction factor. For an H-Darrieus, the incorporation of finite A_r effects can be modelled with the integral effect of the tip vortex on blade drag and lift by assuming elliptic span wise loading. Such approach is not suitable for a HAWT because the required unrealistic assumption of elliptic span wise loading does not make sense for a HAWT.

For elliptic span-wise loaded blades, the effect of a finite A_r is given by (see for instance Abbott & von Doenhoff [1]).

$$\hat{C}_d = C_d + \frac{C_l^2}{\pi A_r} \qquad (160)$$

and

$$\hat{C}_l = C_l \left(1 + \frac{2}{A_r}\right)^{-1} \qquad (161)$$

where $^\wedge$ refers to finite A_r and absence of $^\wedge$ refers to infinite A_r.

Decrease in power coefficient caused by drag of bearings and rods
The total decrease in power caused by friction in the bearings and drag of the rods is calculated with a so-called equivalent drag coefficient of the blade $C_{d,eq}$. We find the power loss from this equivalent drag coefficient as $P_{loss} = F_{d,eq} R\omega$, where the equivalent drag force $dF_{d,eq}$ of a blade area dA is calculated with (see Figure 53)

$$dF_{d,eq} = C_{d,eq}\,\tfrac{1}{2}\rho u_{r,d}^2\,dA \qquad (162)$$

From the geometry in Figure 53 we see that the velocity $u_{r,d}$ can be found from

$$u_{r,d}^2 = u_0^2 \left[\left(\lambda + (1-a_d)\sin\theta\right)^2 + \left((1-a_d)\cos\theta\right)^2 \right] \qquad (163)$$

For high λ, this can be approximated with

$$u_{r,d}^2 \approx \left(\lambda u_0\right)^2 \tag{164}$$

With $R\omega = \lambda u_0$ and (164) dP_{loss} is found as

$$dP_{loss} \approx C_{d,eq} \tfrac{1}{2} \rho \left(\lambda u_0\right)^3 dA \tag{165}$$

For B blades this gives

$$dC_{P,loss} = \tfrac{1}{2} B C_{d,eq} \lambda^3 \frac{c}{R_t} \frac{d\theta}{\pi} \tag{166}$$

For an H-Darrieus in normal flow, with $\lambda_{opt} \approx 3$, it can be shown that (164) results in a difference in total C_P of 4% compared to the result found with (163). Within the model, the approximation (164) is therefore not restricted to high λ.

Integrated power coefficient
The total power coefficient dC_P of a rotor part within a stream tube with width $Rd\theta \sin\theta$, can be found by adding production and loss in power

$$dC_P = dC_{P,d} + 2dC_{P,s} - dC_{P,loss} \tag{167}$$

We counted the power production of the single-rotor part twice because there is one single-rotor part at the windward side of the rotor and one single-rotor part at the leeward side of the rotor.

The total power coefficient of the H-Darrieus in skewed flow C_P, can be found from integration of dC_P found from (168)

$$C_P = \int\limits_{\theta=0}^{\theta=\pi} dC_P \, d\theta \tag{168}$$

We now have a closed set of equations to calculate the performance of an H-Darrieus in skewed flow. Maple provides an environment for exploring and applying mathematics, which allows the set of equations for the H-Darrieus in skewed flow to be iteratively solved. The output of the Maple program is given in the next section.

5.3.4   Performance

The difference in a_s and a_d found in section 5.3.1 is important for the performance of the H-Darrieus in skewed flow. In order to achieve $C_{P,\max}$ of both the single- and the double-rotor part, $a_{opt,s}$ and $a_{opt,d}$ should be equal, which is of course impossible. Therefore, $C_{P,\max}$ of the whole rotor is achieved at non-optimal $\lambda_{opt,s}$ and $\lambda_{opt,d}$. In order to achieve $C_{P,\max,s}$, the single-rotor part enforces the double-rotor part to operate with $\lambda_{opt,s}$. On the other hand, the double-rotor part enforces the single-rotor part to operate with $\lambda_{opt,d}$ fitting $C_{P,\max,d}$. The compromise value λ_{opt} that results in $C_{P,\max}$ of the whole rotor depends on the relative portions of rotor area that operate in single- or double-rotor part operation. Because $a_{opt,d} > a_{opt,s}$, we know that $\lambda_{opt,s} > \lambda_{opt,d}$ so that $\lambda_{opt,d} < \lambda_{opt} < \lambda_{opt,s}$, which shows that λ_{opt}

increases with increasing rotor area in single-rotor part operation. Hence, λ_{opt} increases with increasing γ. Above a certain γ where the whole rotor operates in single-rotor part operation, $\lambda_{opt} = \lambda_{opt,s}$ and λ_{opt} decreases again with increasing γ because less mass flow through the rotor has to be decelerated by the rotor.

As γ increases, an increased rotor area experiences the free stream velocity. To be more precise, the rotor area that experiences the free stream velocity increases with the rotor part operating in single-rotor part operation at the downwind side of the rotor. This gives a possible power increase in skewed flow. Possible and not certain because the effect of the non-optimal $\lambda_{opt,s}$ and $\lambda_{opt,d}$ can cancel the effect of the increased rotor area that experiences the free stream velocity.

5.3.5   Verification of the model

The model for the H-Darrieus in skewed flow, presented in section 5.3.1 to 5.3.3, is first verified with measurements in normal flow. Secondly, the model is verified with measurements in skewed flow. The results are then interpreted and discussed.

Model input
A small H-Darrieus is tested in the open jet wind tunnel to verify the model. The characteristics of the small test H-Darrieus are given in Table 17.

Table 17 Characteristics of the small test H-Darrieus

B	2
Airfoil	NACA 0018 tripped at $0.2c$
c [m]	0.08
H_t [m]	0.5
D_t [m]	0.755
$\dfrac{Bc}{R_t}$ [.]	0.457

The C_l and C_d values of the tripped NACA 0018 airfoils are given in Appendix I.

Verification of the model in normal flow
Sardo [62] carried out two measurements of the power of the H-Darrieus as a function of λ, in normal flow (Figure 56). The measurements showed that $C_{P,\max} = 0.15$, at $\lambda_{opt,low} = 2.9$, where the index low is added to λ_{opt} to indicate the relatively low value of λ_{opt} as most Darrieus operate at much higher λ_{opt}.

At high λ, (dynamic) stall at the H-Darrieus blades is avoided. Since this fits the model assumptions best, the model is fitted by tuning $C_{d,eq}$ on the measurements at high λ. Such fit of the model with $A_r \gg 1$ and C_l, C_d from Appendix I resulted in $C_{d,eq} = 0.024$. The measurement and model results are shown in Figure 56. By assuming $A_r \gg 1$, the finite A_r effects were implicitly assumed to be represented by $C_{d,eq}$. This can indeed not model the finite A_r effects. The bad agreement with the results derived from measurements at low λ is therefore not surprising.

A fit of the model at high λ with the actual $A_r = 6.25$ of the tested H-Darrieus (Table 17), with C_l and C_d from Appendix I and correction for finite A_r resulted in $C_{d,eq} = 0.015$. The $C_{d,eq}$ value indeed shows an appreciable decrease compared to $C_{d,eq} = 0.024$ at $A_r \gg 1$ because part of the losses are now modelled with finite A_r instead of assuming all losses to be represented by $C_{d,eq}$. Figure 56 shows that the result with finite A_r effects incorporated is slightly closer to the measurement although the improvement is small.
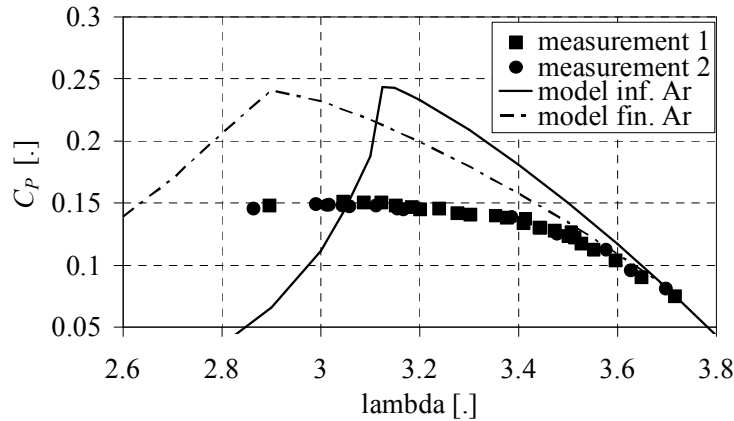
Figure 56 C_P **as a function of** λ **(lambda) in normal flow, as found from measurements and the model with:** $C_{d,eq} = 0.024$ **and infinite** A_r **(solid line) and with** $C_{d,eq} = 0.015$ **and finite** A_r **(dotted line).**

The improvement by modelling finite A_r effects in normal flow is small and the difficulties encountered in modelling finite A_r effects in skewed flow are numerous. Finite A_r effects in skewed flow were therefore not taken into account.

Verification of the model in skewed flow
According to the verification in normal flow, $C_{d,eq} = 0.024$ should be used if $A_r \gg 1$ is assumed. The model with $C_{d,eq} = 0.024$ is compared with the results derived from measurements in skewed flow (Sardo [62]). The results are shown in Figure 57, where $C_{P,\max}$ of the total rotor with the accompanying λ_{opt} at different skew angles are given. Within the Maple code, α_d and α_s are calculated and reported. This shows stalled blades of the H-Darrieus at all γ except for $20^o < \gamma < 25^o$. For an H-Darrieus with stalled blades, the results of the model cannot be trusted because dynamic stall, which is present (see section 5.3.6), gives a different lift of the blades and accordingly a different performance.

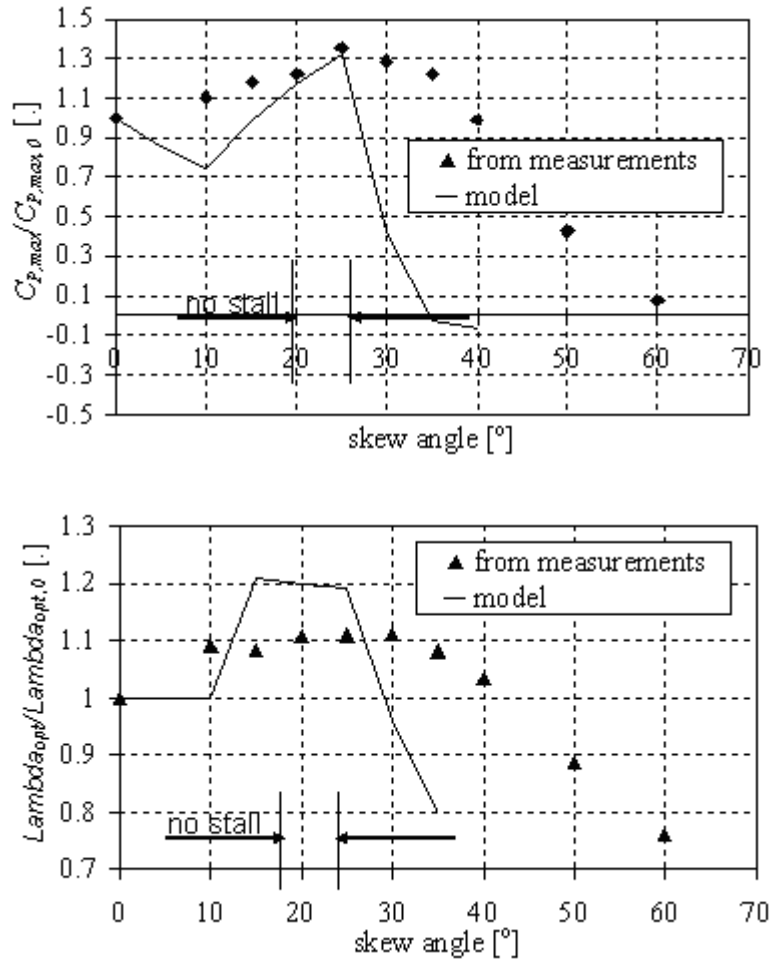**Figure 57** $C_{P,\max}$ **and** λ_{opt} **derived from measurements in skewed flow compared with the model results for** $C_{d,0} = 0.024$ **. The model applicability is restricted to** $20^o < \gamma < 25^o$ **. The index 0 refers to** $\gamma = 0^o$ **.**

The model seems able to predict the $C_{P,\max}$ in skewed flow for $20^o < \gamma < 25^o$ with a discrepancy of only 2% compared to the test results. The model result of λ_{opt} for $20^o < \gamma < 25^o$ gives a less satisfying discrepancy of 9% compared to the test results.

As discussed in section 5.3.1, it is expected that λ_{opt} increases with increasing γ up to a certain γ where the whole rotor operates in the single-rotor part operation and then decreases. The model shows a qualitative agreement with the measurements concerning this λ_{opt} behaviour.

5.3.6   Discussion on the validity of the model

It is interesting to compare two H-Darrieus with the same height and diameter but different λ_{opt}, respectively $\lambda_{opt,low}$ and $\lambda_{opt,high}$ where $\lambda_{opt,high} > \lambda_{opt,low}$. The viscous power losses (165) are found to be proportional to λ^3. A small increase in λ_{opt}, which is expected in skewed flow, will therefore cause a much higher increase in viscous losses for the H-Darrieus operating around $\lambda_{opt,high}$ compared to the H-Darrieus that operates around $\lambda_{opt,low}$. Yet, for both H-Darrieus, the possible power increase in skewed flow is a function of the extra rotor

area in skewed flow, which is equal for both H-Darrieus as they have the same height and diameter. Hence, the power increase will be much smaller for an H-Darrieus at $\lambda_{opt,high}$ compared to the H-Darrieus at $\lambda_{opt,low}$. This is illustrated with use of the model hereafter.

Performance in skewed flow at high λ_{opt}

Suppose we have an H-Darrieus in skewed flow with ¼ of the solidity of the H-Darrieus in Table 17.

Table 18 Characteristics of a small H-Darrieus for a model calculation

B	2
Airfoil	NACA 0018 tripped at $0.2c$
c [m]	0.02
H_t [m]	0.5
D_t [m]	0.755
$\dfrac{Bc}{R_t}$ [.]	0.114

The model shows that $\lambda_{opt,high} > 4.9$ for the H-Darrieus of Table 18 compared to $\lambda_{opt,low} = 2.9$ of the H-Darrieus of Table 17. The low solidity and accordingly high $\lambda_{opt,high}$ make sure that stall of the blades is avoided in both the single- and the double-rotor part operation. Therefore, the total skew angle bandwidth $0^o \leq \gamma \leq 60^o$ is covered with the presented model for the H-Darrieus in skewed flow. The model results are shown in Figure 58.
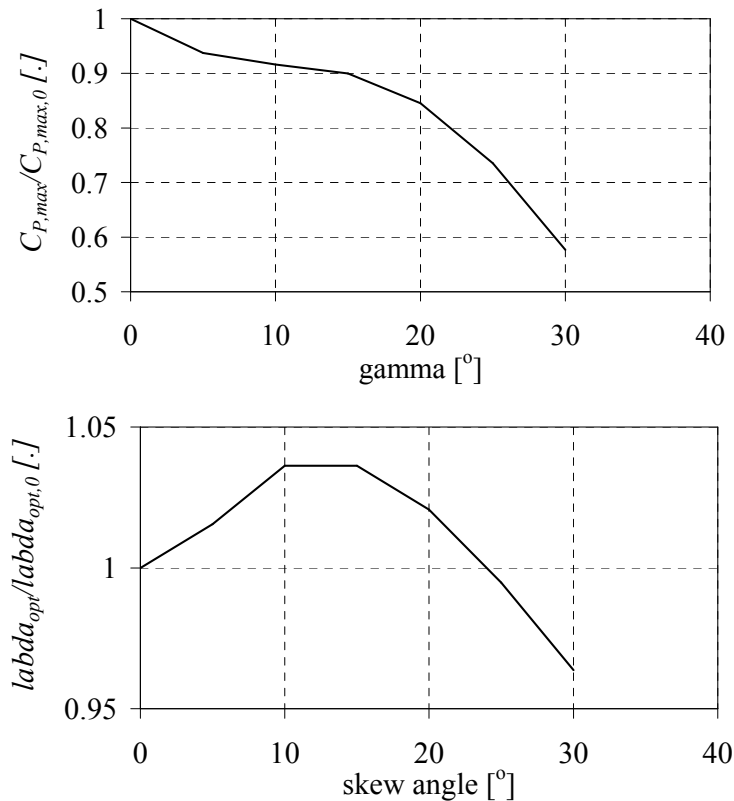

Figure 58 Optimal power coefficient versus optimal λ in skewed flow and $C_{d,0} = 0.024$ at low solidity.

The model thus shows that $C_{P,\max}$ decreases with increasing γ while λ_{opt} only slightly increases with γ. In contrast to the H-Darrieus with low λ_{opt} (Table 17), the increase of $C_{P,\max}$ in skewed flow is absent at the H-Darrieus (Table 18) with high λ_{opt}. This is in agreement with the discussion at the beginning of the section. We thus know that the increase in power of an H-Darrieus in skewed flow is restricted to low λ_{opt} H-Darrieus.

Re effects
Figure 59 shows the calculated values of static $C_{l,\max}$ and C_d at the same angle of attack for a NACA 0018 airfoil tripped at 20% derived from Appendix I.
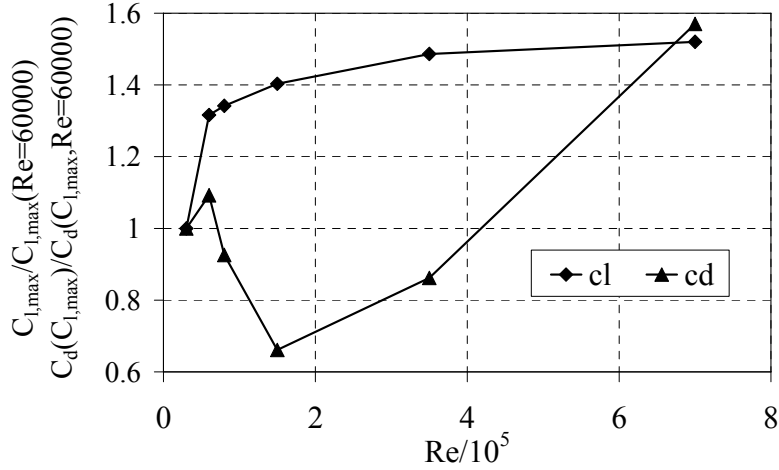

Figure 59 Calculated normalized lift and drag coefficient versus Re number of a NACA 0018 airfoil tripped at 20%.

Figure 59 shows a bandwidth $\mathrm{Re} = 60\,000 \sim 150\,000$ where $C_{l,\max}$ increases and C_d decreases with increasing Re number or λ_{opt}. We know that λ_{opt} increases in skewed flow. Consequently, an H-Darrieus with blades that operate at for example $\mathrm{Re} = 60000$ at $\gamma = 0^o$ experience an increasing $C_{l,\max}$ and decreasing C_d as γ increases. This is very profitable for the power increase in skewed flow. In this context, it is important to note that the blades of the high solidity H-Darrieus operate at Re=71000 at $\gamma = 0^o$, while the blades of the low solidity H-Darrieus operate around Re=270000 at $\gamma = 0^o$. Hence, the high solidity H-Darrieus profits from the decreased drag while the low solidity H-Darrieus suffers from increased drag.

Dynamic stall
Dynamic stall can occur if the lift changes rapidly as is the case with the lift of the H-Darrieus blades. An important parameter for dynamic stall is the reduced frequency of the motion defined as $k = \dfrac{\omega c}{u_0}$ where ω is the rotational speed of the H-Darrieus, c is the chord length of the blades and u_0 is the free stream velocity. Seto and Galbraith [64] measured[21] that dynamic stall occurs if $k > 0.004$. For the H-Darrieus defined by Table 17 and Table 18, k is much higher so that dynamic stall occurs for both H-Darrieus in case of stalled blades. In order to fit the model assumptions, stall of the blades should thus be avoided. Stall is absent at a high design λ_{opt} of the H-Darrieus. However, it is demonstrated that the power increase in

---

[21] The measurements were carried out at Re=1.5×10^6 and the blade was subjected to pitch rate motions around the ¼-chord point.

skewed flow is absent for an H-Darrieus with high λ_{opt}. The verification of the presented model for the H-Darrieus in skewed flow is therefore unavoidable with low design λ_{opt} and therefore restricted to a small bandwidth of γ.

The model of an H-Darrieus in skewed flow depends on input of several -very-difficult-to-measure- or related -not-accurately-known- quantities. For instance the input of
- a local C_t at high a_d in skewed flow (section 5.3.2) and
- C_l and C_d at low Re number

are impossible to measure accurately. However, in order to profit from a maximum increase in $C_{P,\max}$ in skewed flow, a model to design the H-Darrieus for skewed flow is indispensable. We thus look forward to a large research effort coupled with the generation of accurate input data for the model of the H-Darrieus in skewed flow.

5.4 The energy yield at the roof

This section discusses the power output of a wind turbine on a roof of a building. Based on the knowledge shown in the previous sections, it is possible to give estimates of the power output at all flow angles. This allows a first order calculation of the energy yield of a wind turbine on a roof of a building in omnidirectional wind.

At a sharp-edged building surrounded by low roughness
Suppose we have a 2.5 kW H-Darrieus, which will be installed above the centre of a sharp-edged roof of a 20 m high building with width 30 m and depth 10 m. The Darrieus has the following characteristics.

Table 19 Model H-Darrieus data.

Rated power	2.5 kW
Cut in wind speed	4 m/s
Rated wind speed	13 m/s
Cut out wind speed	20 m/s
Rotor area	6 m^2
Variable λ	
C_P	0.3

A characteristic size of the rotor is found from the rotor area: $D_t = \sqrt{6} \approx 2.5\,\text{m}$. The building has $H = 20$ m so that $D_t/H = 0.1$ and the H-Darrieus can be characterized as small (section 5.1.1). The power of the H-Darrieus can thus be found from the cube of the local wind speed.

The height of the separation trajectory at the roof can be calculated with (68) and (69) and is found at 4 m above the roof centre. We site it at 5 m above the roof centre. Then, the acceleration of the free stream wind speed by the sharp-edged roof is given in section 5.1.2, Table 16. The skew angle above the centre of the roof can be found from the derivative of the separation trajectory (69) and is found to be 14$^\text{o}$. Figure 57 gives a 20% increase of the power output of the H-Darrieus[22] at 14$^\text{o}$ skew angle. For flow parallel to the long side of the building or $\varphi = 90^\text{o}$, (77) in section 3.3.4, gives reattachment at 21 m. Hence, the skew angle at the centre of the roof for $\varphi = 90^\text{o}$ is small and the power increase of the H-Darrieus is

---

[22] The power increase in skewed flow is restricted to the particular H-Darrieus used in the measurements so that it is assumed that the H-Darrieus in this calculation has the same properties.

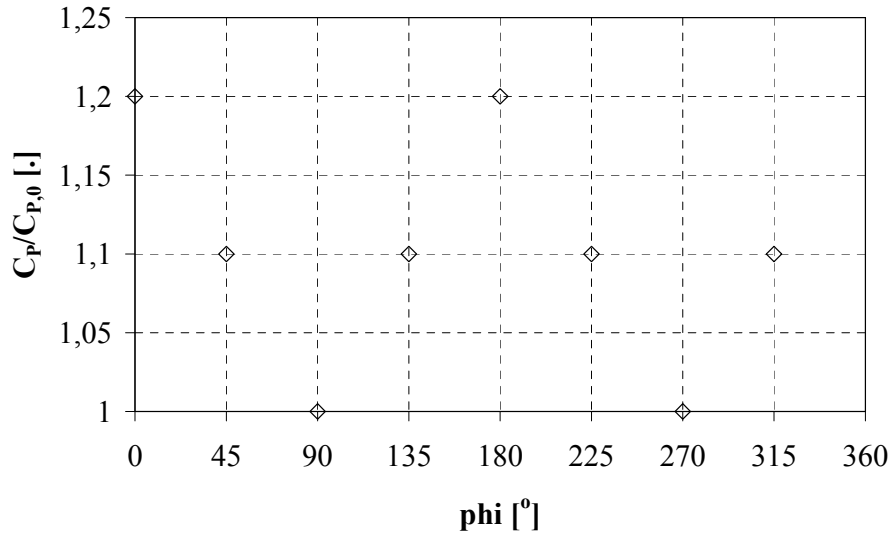approximated by zero. The following behaviour of the power increase of the H-Darrieus in skewed flow at other φ is assumed.

Figure 60 Increase in power for different wind directions φ.

Suppose that the particular building is located in a region with a potential wind speed of 4.5 m/s with a surrounding roughness of grassland or $z_0 = 0.03$ m. The free stream wind speed at roof height for $z_0 = 0.03$ m is found with (26) to be 5.0 m/s. The change from free stream wind speed to the local wind speed at the roof $C_{r,i}$ is given in section 5.1.2, Table 16 and the velocity for the shrouded wind turbine u_i is found by $u_i = C_{r,i} u_0$. The energy yield of the H-Darrieus above the roof centre can be calculated with (60), derived in section 3.2.3. This gives an energy yield of the H-Darrieus of 3717 $kWh/year$ or 620 $kWh/(m^2 year)$.

At a sharp-edged building surrounded by high roughness
Now suppose that the same configuration of H-Darrieus and building as used in the previous energy yield calculation is located at the following site.

Table 20 Location of the building in a city.

z_0	1 m
d	7.5 m
Upwind city border at	3 km

With (32), the step in roughness 3 km upwind of the building results in $h_k = 169$ m. The building height of 20 m lies above $z_{min} = 1.5d \approx 11$ m so that the log-law can be used (see section 3.1.1) to calculate the average free stream wind speed at roof height. Substitution of $h_k = 169$ m and the data in Table 20 in (33) is thus meaningful and a free stream wind speed at roof height of 3.3 m/s is found. Suppose that $C_{r,i}$ does not depend on z_0 but only on building shape. $C_{r,i}$ is then equal to the simulated values given in section 5.1.2, Table 16. The skew angle will be smaller than the skew angle with the same building at grassland roughness as the effective height of the building is decreased with d. The derivative of the separation trajectory (69) gives a skew angle of 12°. This is only 2° less than the skew angle with $z_0 = 0.03$ m in the previous example. It is therefore assumed that Figure 60 can be used to

approximate the power increase of the H-Darrieus in skewed flow. According to (114) in section 5.1.1 and the data in Table 20, the relative size of the H-Darrieus should obey $D_t/H < O(0.1)$ in order to be treated as small, while the actual size of the Darrieus gives $D_t/H = 0.1$. The Darrieus size is accordingly at the edge of the criterion. If the Darrieus is assumed to be small, the energy yield of the H-Darrieus above the roof centre can be calculated with (60), derived in section 3.2.3. This gives an energy yield of the H-Darrieus of 1046 $kWh/year$ or 174 $kWh/(m^2 year)$. Because of the relatively large H-Darrieus size, this is an upper limit for the energy yield at this site.

At a spherical building
Spherical buildings cause a much higher acceleration than sharp-edged buildings. On top of a sphere in potential parallel flow it is found that $C_{r,i} = 1.5 \; \forall i$ (section 3.2.2).

Figure 61 Artist impression of a spherical building with BAWT's.

With this, the energy yield can then be calculated with (60). This gives an upper limit for the energy yield of a small BAWT at a spherical building in an atmospheric boundary layer because the blockage of a sphere in an atmospheric boundary layer is smaller compared to a sphere in parallel flow.

It is assumed that $u_0 = 5.0$ m/s at $z_0 = 0.03$ and $u_0 = 3.3$ m/s at $z_0 = 1$ (section 3.1.1). This gives the following energy yields.

Table 21 Upper limit of the energy yield of a 2.5 kW BAWT at the roof of a spherical building.

site	Energy yield $kWh/(m^2 year)$
$u_0 = 5.0$ m/s at $z_0 = 0.03$ m	1032
$u_0 = 3.3$ m/s at $z_0 = 1$ m	353

5.5 The energy yield at the sides of a building

Cylinder-like 2D buildings cause a high acceleration of the free stream wind speed.
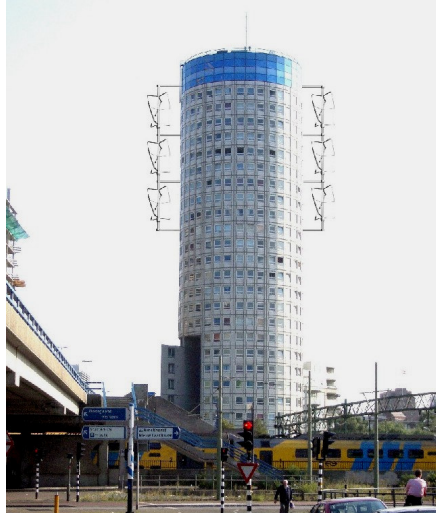
Figure 62 Artist impression of cylindrical building with BAWT's.

Suppose we have the following configuration of a small actuator close to the surface of a cylinder.
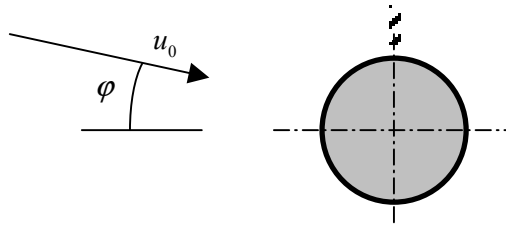
Figure 63 Top view of a small BAWT at the side of a cylinder.

Potential theory provides an approximation of the change in wind speed $C_{r,i}$ around a cylinder in parallel flow (section 3.2.2). At the surface of the cylinder, potential theory gives the following $C_{r,i}$ values at the site of the small actuator close to the cylinder surface.

Table 22 $C_{r,i}$ **at the side of a cylinder.**

φ	$C_{r,i}$
$0^\text{o}, 180^\text{o}$	2
90°	0
$45^\text{o}, 135^\text{o}$	1.4

The use of $C_{r,i}$ from potential theory as an approximation of $C_{r,i}$ at a cylindrical building is allowed except at $\varphi \approx 225^\text{o} \cdots 315^\text{o}$ (section 3.2.2). At $\varphi \approx 225^\text{o} \cdots 315^\text{o}$, the actuator is located in the wake of the cylinder so that $C_{r,i} = 0$ can be assumed. $C_{r,i}$ for a BAWT at the side of a cylindrical building can thus be approximated with the following values.
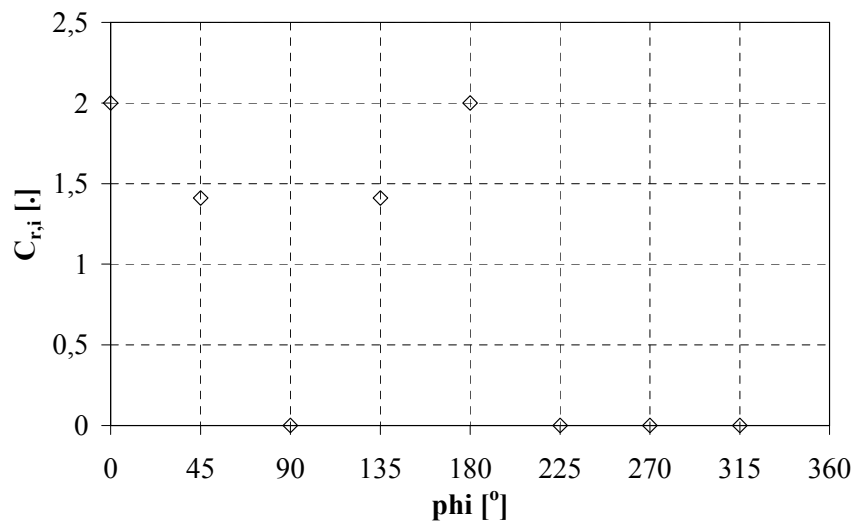
Figure 64 Assumed $C_{r,i}$ **for a BAWT at the side of a cylindrical building as a function of** φ **(phi).**

With the same wind conditions as used for Table 21, (60) and Figure 64, give the following energy yields.

Table 23 Energy yield of a 2.5 kW BAWT at the side of a cylindrical building.

site	Energy yield $kWh/(m^2\,year)$
$u_0 = 5.0$ m/s at $z_0 = 0.03$ m	617
$u_0 = 3.3$ m/s at $z_0 = 1$ m	268

6 Wind turbines between airfoil-shaped buildings

This chapter deals with the performance of a wind turbine "between airfoil-shaped buildings". This BAWT option is introduced in section 2.3, where it is described as one of the three basic aerodynamic configurations for concentrators in the built environment. Compared to the "close to a building" concentrator (chapter 5), the design of this configuration requires more effort. Not only the BAWT needs to be designed but also the building and moreover the interaction of both. This design is therefore not one of the first concentrators for BAWT's that will be utilized.

Solitary tall buildings with an airfoil shape or aerodynamic shape exist (Figure 65). This ingredient of the concentrator that is discussed in this chapter is therefore not too far from everyday practice.
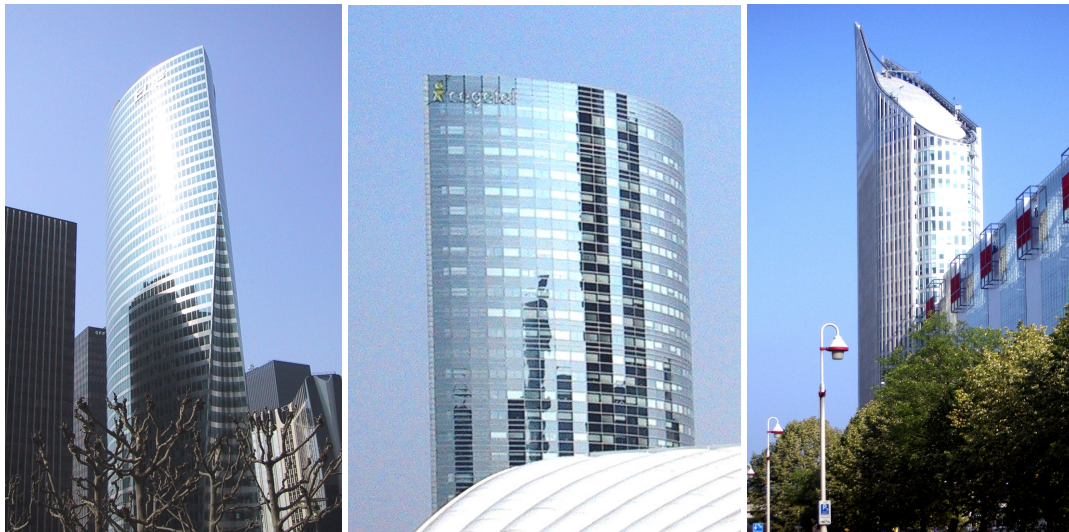

Figure 65 Examples of single buildings with aerodynamic shapes. From left to right: EDF and Cegetel building La Defense, France, Hoftoren the Hague, the Netherlands.

The configuration of BAWT's between tall aerodynamic buildings is schematically shown in Figure 66.
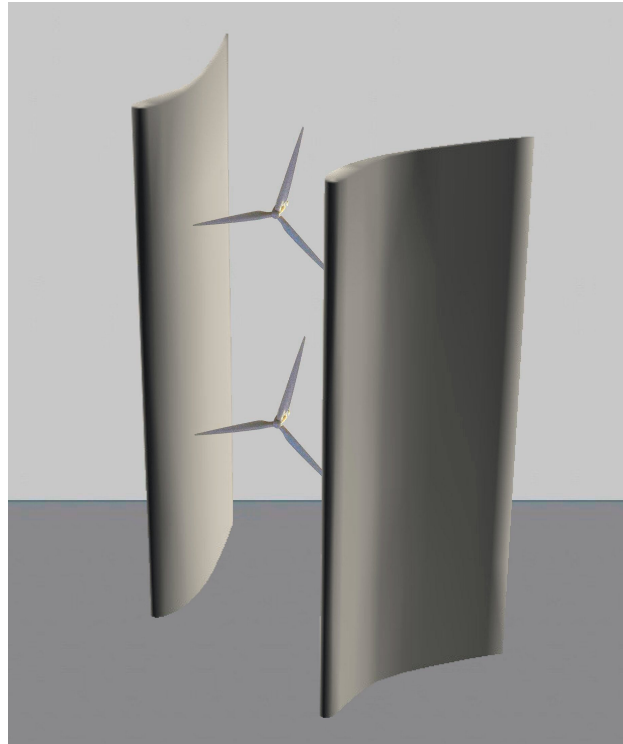
Figure 66 Schematic configuration of BAWT's between aerodynamic buildings.

In this configuration, two single aerodynamic buildings are symmetrically positioned around the axis of the BAWT's. In this way, the aerodynamic buildings are able to accelerate the undisturbed wind speed for certain wind directions.

The height of the buildings in Figure 66 is much higher than the other sizes of the buildings. The configuration therefore shows dominant 2D effects (section 3.2.1). In wind energy literature, the concept of a wind turbine between ring airfoils (3D/ axi-symmetric) is well known. Within the context of the BAWT, such configuration requires a building designed as a ring airfoil. This seems not convenient for the utilisation of the building itself and complex to build. A large part of the ring-shaped building is furthermore located close to the earth's surface so that it has to perform at low wind speeds. This leads to a low energy yield of the BAWT. The research in this chapter is therefore focussed on the 2D configuration of a wind turbine between airfoil-shaped bodies as showed in Figure 66.

Literature uses several names for the configuration with aerodynamic bodies around a wind turbine. This configuration is often called:
- a ducted wind turbine,
- a shrouded wind turbine or
- a diffuser-augmented wind turbine.

In this thesis, the generic term "ducted wind turbine" is used to denote the main principle of power augmentation with aerodynamic bodies around a wind turbine. We will distinguish "shrouded wind turbine" from "diffuser-augmented wind turbine" by the shape of the duct as shown in Figure 67. The shrouded configuration on the left of Figure 67 is based on an airfoil shape of the duct while the duct of the diffuser-augmented configuration on the right of Figure 67 is basically a widening tube or diffuser.
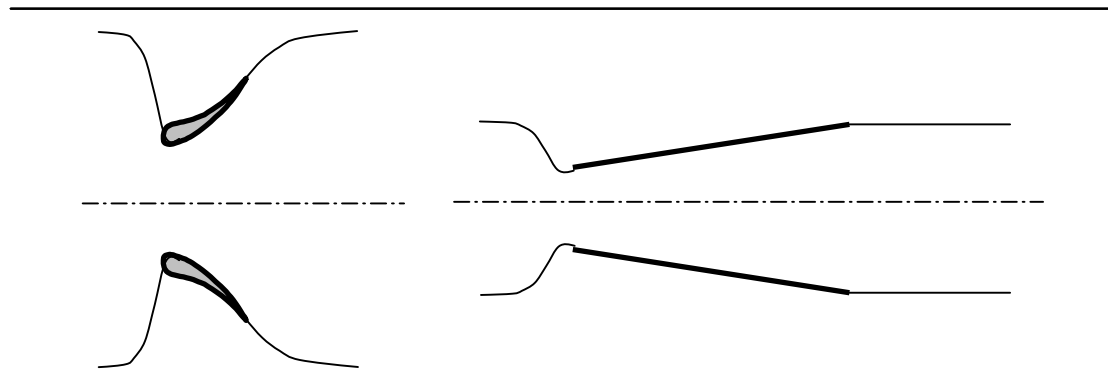
Figure 67 Duct configurations called shrouded (left) and diffuser-augmented (right). The flow comes from the left side and the streamlines are shown as thin lines.

The two duct shapes have an historical origin. One could say that the shrouded wind turbine is inspired by aerospace engineering while the diffuser-augmented wind turbine is inspired by mechanical engineering. The first experiments with ducted wind turbines were carried out with diffusers (Igra [29], Foreman et al. [85]). Follow up experiments of Igra [29] showed that ring airfoils at the diffuser exit cause a higher concentrator effect of the diffuser. This marked the development towards the much shorter shrouded wind turbine configuration. Other experiments and simulations concerning the performance of the ducted wind turbine are found in De Vries [76], Phillips et al. [57] and Hansen [23]. The historical origin of the two duct shapes is reflected in the development of two different mathematical models: those that model the performance based on diffuser properties (Wilson & Lissaman [84], De Vries [76] and Van Bussel [9]) and those that model the performance with airfoil characteristics (De Vries [76] and Van Holten [25]). The models will be discussed together with improvements in section 6.1 and section 6.2.

Most mathematical models for the ducted wind turbine in literature are not closed in the sense that the set of equations is not enough to calculate the performance of the ducted wind turbine. Additional input is required to close the model. Such additional information is often obtained by experiments or by heuristic arguments taken from similar flow modelling efforts. The model of Van Holten [25] uses the lift coefficient of the airfoils of the duct as closure. This is appealing as there is ample theory and measurements on lift of airfoils. The model is derived for lightly loaded ducted wind turbines as it neglects wake expansion. This chapter shows that such restriction is unnecessary by derivation of an analogue model, but with wake expansion, which shows that wake expansion is appreciable. The closure is also achieved with the lift coefficient of the airfoils that form the duct. Hence, the model is classified as a model for a shrouded wind turbine.

6.1 Momentum theory

This section describes mathematical models for the ducted wind turbine that are derived with the equation of conservation of momentum in integral form (section 4.1.3). The starting point of all models in this section is 1D flow through the ducted wind turbine i.e. a uniform flow is assumed at all areas perpendicular to the axis of the ducted wind turbine and variation of the flow qualities is only possible parallel to the axis of the ducted wind turbine.

6.1.1   Shrouded wind turbine

Suppose we have a shrouded actuator as shown in Figure 68.
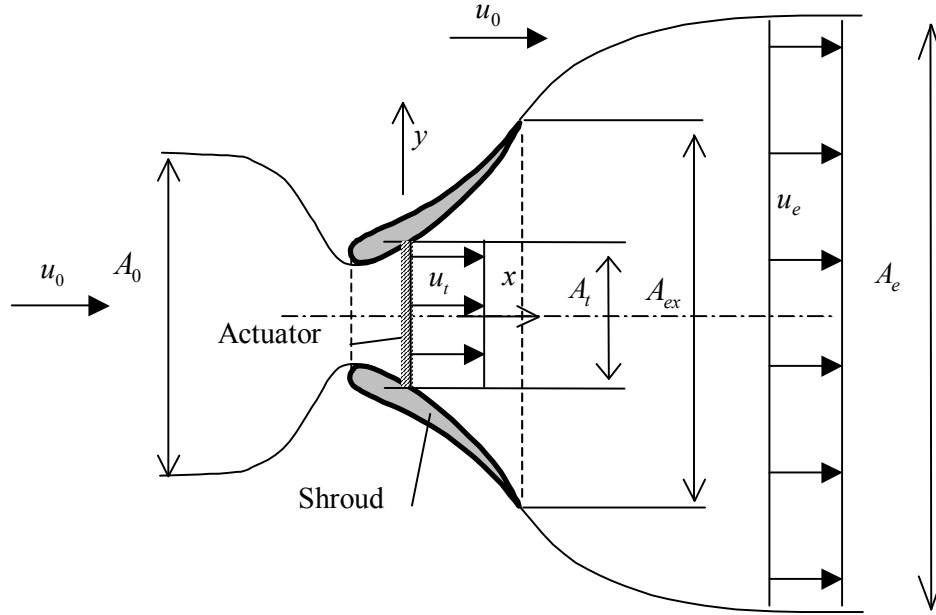
Figure 68 Top view of a shrouded actuator.

Within the usual assumptions of momentum theory, conservation of axial momentum yields

$$F_t + F_S = \rho\, u_t A_t \left(u_0 - u_e\right) \tag{169}$$

where F_t is the thrust force of the actuator and F_S is the axial force of the airfoils on the flow.

The thrust force of the actuator found with Bernoulli's theorem reads

$$F_t = \tfrac{1}{2}\rho\left(u_0^2 - u_e^2\right)A_t \tag{170}$$

Combination of (169) and (170) using $C_{t,S} = F_S \big/ \tfrac{1}{2}\rho u_0^2 A_t$ gives an expression for u_t, the wind speed through the actuator.

$$u_t = \tfrac{1}{2}\left(u_0 + u_e\right) + \tfrac{1}{2}\frac{C_{t,S}u_0^2}{\left(u_0 - u_e\right)} \tag{171}$$

According to (11), multiplying u_t with F_t gives the absorbed power of an actuator. C_P of the ducted actuator is consequently found as

$$C_P = \tfrac{1}{2}\left(1 - \frac{u_e}{u_0}\right)\left(1 + \frac{u_e}{u_0}\right)^2 + \tfrac{1}{2}C_{t,S}\left(1 + \frac{u_e}{u_0}\right) \tag{172}$$

Comparing C_P of the shrouded rotor (172), with C_P of a bare wind turbine (12), shows that a power increase is only possible if $C_{t,S} > 0$. All measurements and simulations of references mentioned in the introduction of chapter 6 show a power increase of the ducted wind turbine.

Equation (11) shows that this is only possible with $C_{t,S} > 0$. In potential flow, the drag force of an airfoil is zero (Paradox of D'Alembert). Hence, $C_{t,S} > 0$ shows that the lift force of the airfoils has an axial component. This makes furthermore clear that airfoils with high-lift -such as cambered airfoils- are wanted for the shrouded wind turbine as they cause a high power output.

By assumption of $C_{t,S} = \text{constant}$, $C_{P,\text{max}}$ can be found from (172) by differentiation of C_P with respect to u_e (De Vries [76]). Yet, $C_{t,S}$ is possibly a function of u_e so that $C_{P,\text{max}}$ stays unknown without assuming $C_{t,S} = \text{constant}$. Momentum theory for the bare wind turbine (section 2.1.2) provides help. It shows that $C_{P,\text{max}}$ is achieved at $u_e = \frac{1}{3} u_0$ independent of the energy extraction process upwind of an area with axial velocity $\frac{1}{2}(u_0 + u_e)$ bounded by undisturbed flow. It is therefore assumed that a shrouded wind turbine also achieves $C_{P,\text{max}}$ at $u_e = \frac{1}{3} u_0$ as long as an area with velocity $\frac{1}{2}(u_0 + u_e)$ bounded by undisturbed flow can be found at or downwind of the duct.

If it is assumed[23] that there is an area with axial velocity $\frac{1}{2}(u_0 + u_e)$ bounded by undisturbed flow at or downwind of the duct exit, substitution of $u_e = \frac{1}{3} u_0$ in (172) gives $C_{P,\text{max}}$ of the shrouded wind turbine as

$$C_{P,\text{max}} = \tfrac{16}{27} + \tfrac{2}{3} C_{t,S} \tag{173}$$

Within the contours of momentum theory, $C_{t,S}$ stays unknown (the closure problem) and it is difficult to estimate $C_{t,S}$ by calculations as this involves integration of the (complex) pressure distribution on the airfoils of the loaded shrouded actuator (De Vries [76]). Measurements can be used to estimate $C_{t,S}$ but in that case the measurements are also able to reveal $C_{P,\text{max}}$.

Comparing (7) and (170) at $u_e = \frac{1}{3} u_0$ shows that F_t is equal for the shrouded wind turbine and bare wind turbine. As the extracted power of both the bare and ducted actuator is found by multiplying F_t with u_t, the ratio of $C_{P,\text{max}}$ of the shrouded wind turbine and bare wind turbine is found as

$$\frac{C_{P,\text{max},shroud}}{C_{P,\text{max},bare}} = \frac{u_{t,shroud}}{u_{t,bare}} \tag{174}$$

In other words, the power increase of the ducted wind turbine is proportional to the increase of the velocity through the actuator. For a bare wind turbine, the power can be found by $P = C_P \frac{1}{2} \rho u_0^3 A_t$, where u_0 is the free stream velocity. A velocity increase $u_0 \to u_0'$ thus results in $P'/P = (u_0'/u_0)^3$. In other words, the power increase of a bare wind turbine caused by a velocity increase is proportional to the cube of the velocity increase. The difference between this result and (174) shows that the velocity in the duct $u_{t,shroud}$ cannot be treated as free stream velocity for the ducted wind turbine.

---

[23] This assumption is treated in more detail in the extended diffuser model in section 6.1.2, where CFD calculations are used to show the validity of the assumption.

6.1.2   Diffuser-augmented wind turbine

Wilson & Lissaman [84] introduced a model for a ducted wind turbine that is based on the assumption that the duct operates as a diffuser or tube widening downwind of the wind turbine. Van Bussel [9] introduced wake expansion in this model. This section presents the models of Van Bussel with a split up in a "simplified diffuser model" and an "extended diffuser model".

Simplified diffuser model
According to Van Bussel [9] it is assumed that bare actuator wake expansion (see section 2.1) takes place from the diffuser exit to a distance infinitely downwind of the exit. With this assumption, the set of equations on the performance of the diffuser-augmented wind turbine is closed i.e. no further input is required to solve the set of equations and unknowns. We will refer to this diffuser-augmented wind turbine model, which is shown in Figure 69, by "the simplified diffuser model".
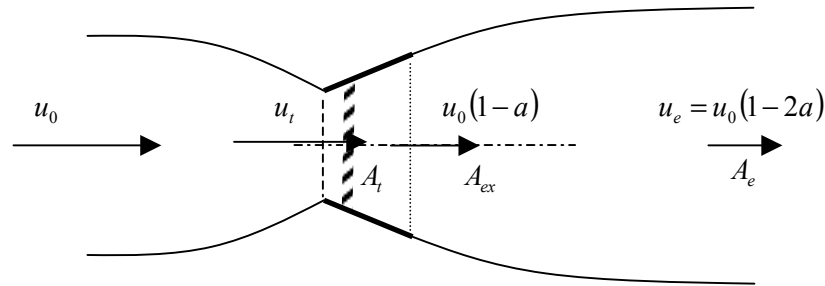
Figure 69 Operation of a shrouded rotor according to the simplified diffuser model.

Bernoulli's theorem gives the pressure drop across the actuator as

$$\Delta p = \tfrac{1}{2} \rho \left(u_0^2 - u_e^2 \right) \tag{175}$$

According to the hypothesis above (173), the maximum power extracted by the actuator is found at $a = \tfrac{1}{3}$. Mass conservation between A_{ex} and A_e then gives

$$u_{t,opt} = \tfrac{2}{3} \frac{A_{ex}}{A_t} u_0 \tag{176}$$

The power dissipated by the actuator is found by multiplication of the thrust force of the actuator ($ = \Delta p A_t$) with u_t. This gives

$$C_P = \left(1 - \left(\frac{u_e}{u_0} \right)^2 \right) \frac{u_t}{u_0} \tag{177}$$

With substitution of $u_e = \tfrac{1}{3} u_0$ and (176) in (177), $C_{P,\max}$ is found as

$$C_{P,\max} = \tfrac{16}{27} \frac{A_{ex}}{A_t} \tag{178}$$

By substitution of the result of mass conservation in the diffuser and $C_{P,\max,bare} = \tfrac{16}{27}$ in (174), it is clear that (178) is equal to (174). This is not surprising as the use of bare actuator wake expansion is in fact equal to using momentum theory. Both models for the ducted actuator

thus show that the power augmentation caused by the diffuser is proportional to the area ratio of the diffuser A_{ex}/A_t .

Extended diffuser model
Let us return to the assumption of bare actuator expansion. Measurements (Igra [29], Foreman et al. [85], De Vries [76]) show that the pressure at the diffuser exit is below ambient pressure. This results in an extra expansion compared to bare actuator expansion. Van Bussel [9] introduced this extra expansion by moving the area with velocity $u_0(1-a)$ downwind of the diffuser exit area A_{ex} where the area is then denoted by $\widetilde{A}_{ex}$. The extra expansion of the wake can then be realized between the areas A_{ex} and $\widetilde{A}_{ex}$ where $\widetilde{A}_{ex}$ has the assumed velocity $u_0(1-a)$. The model is shown in Figure 70 and will be referred to as the "extended diffuser model". The actuator is situated $\frac{1}{4}c$ downwind of the diffuser entrance[24] to allow easy comparison with the vortex model in section 6.2. It is however not relevant for the model described here.
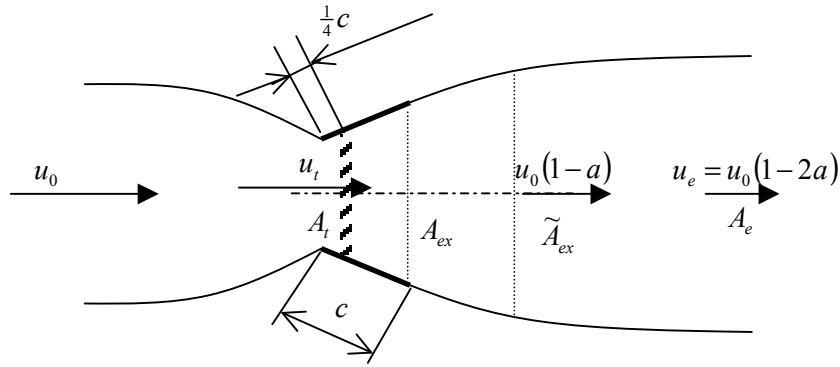
Figure 70 Operation of a diffuser-augmented rotor according to extended diffuser theory.

The Lancester-Betz limit again provides $a=\frac{1}{3}$ (see explanation above (173)) so that mass conservation downwind of the diffuser exit results in

$$u_{t,opt} = \tfrac{2}{3}\frac{\widetilde{A}_{ex}}{A_t}u_0 \tag{179}$$

Instead of (178), $C_{P,\max}$ is now found as

$$C_{P,\max} = \tfrac{16}{27}\frac{\tilde{A}_{ex}}{A_t} \tag{180}$$

Closure of extended diffuser model with the vortex model for a shrouded rotor
The vortex model for the shrouded rotor (section 6.2) is able to close the extended diffuser model. It gives $\overline{u_t}$ in (199) as $\overline{u_t}=\frac{1}{2}(u_0+u_e)(1+\xi)$, where ξ given by (198) describes the

---

[24] The choice for $\frac{1}{4}c$ is based on airfoil theory as briefly discussed in section 6.2 and cannot be found within the diffuser-augmented wind turbine models.

concentrator effect of the duct found with the vortex model. Substitution of $u_e = \frac{1}{3}u_0$ from the Lancester-Betz limit in $\overline{u_t} = \frac{1}{2}(u_0 + u_e)(1+\xi)$ results in

$$u_t = \tfrac{2}{3}u_0(1+\xi) \tag{181}$$

where the average sign on $\overline{u_t}$ is skipped as $\overline{u_t} = u_t$ within the extended diffuser model. This gives with (179) that

$$\frac{\widetilde{A}_{ex}}{A_{ex}} = (1+\xi)\frac{A_t}{A_{ex}} \tag{182}$$

If $A_t = D_t h$, where D_t is the actuator diameter and h is the height of the airfoil, A_{ex} is found from the geometry of the diffuser.

$$A_{ex} = D_t h + \tfrac{3}{2}ch\sin\alpha \tag{183}$$

where α is half the cone angle of the diffuser. Substitution of (183) in (182) gives $\widetilde{A}_{ex}/A_{ex}$ at $C_{P,\max}$ as

$$\frac{\tilde{A}_{ex}}{A_{ex}} = \frac{1+\xi}{1+\tfrac{3}{2}\dfrac{c}{D_t}\sin\alpha} \tag{184}$$

In order to calculate some values for the ratio $\widetilde{A}_{ex}/A_{ex}$ we use the results from section 6.2.5, Table 26. This gives the following ratios $\widetilde{A}_{ex}/A_{ex}$.

Table 24 Ratios $\widetilde{A}_{ex}/A_{ex}$ derived from a closure of the extended diffuser model with the vortex model (Table 26).

D_t/c	ξ	$\widetilde{A}_{ex}/A_{ex}$
2.1	0.50	1.31
1.6	0.61	1.35
1.1	0.80	1.40
0.6	1.23	1.47

Apparently, the assumption $\widetilde{A}_{ex}/A_{ex} = 1$ in the simplified diffuser model can be a crude approximation.

6.2 2D Vortex model for a shrouded rotor

A first description of a shrouded wind turbine modelled with vortices is found in Van Holten [25]. Such a model will be referred to as "vortex model". The vortex model derived in this section differs from Van Holten's model by wake expansion and consequently by an induced velocity of the airfoils that depends on the velocity in the wake of the shrouded wind turbine. Compared to other models, the vortex model provides additional information on the operation of a shrouded wind turbine. The vortex model includes a non-uniform axial velocity distribution through the actuator and is able to handle finite aspect ratio effects of the airfoils.

6.2.1 Set-up of the model

A representation of the forces of a loaded shrouded actuator by vortices in potential flow is shown in Figure 71. The actuator is located between the ¼ chord points on the airfoils as that particular location gives the highest induced velocities according to a single-bound vortex representation of airfoils.
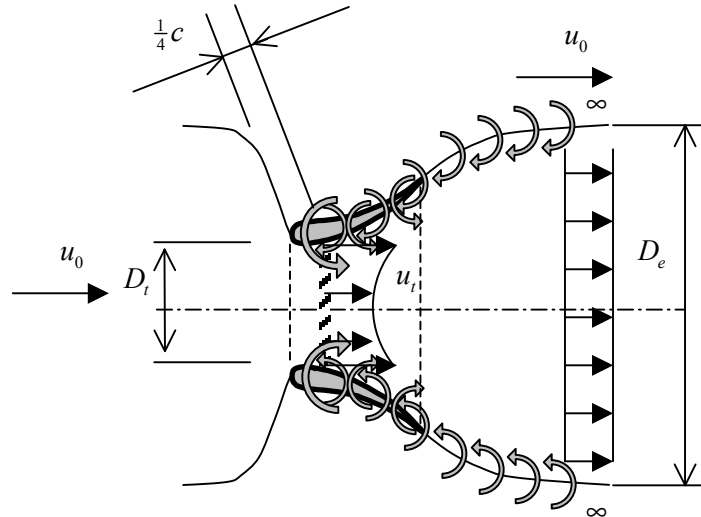
Figure 71 Vortex representation of a loaded shrouded wind turbine in potential flow.

The airfoils are represented by a vortex distribution that accelerates u_0 between the airfoils. The deceleration of u_0 caused by the actuator is represented by curved vortex sheets around the wake of the actuator. u_e is defined as the velocity at infinite distance downwind of the shrouded actuator. Hence, the vortex distributions at the entrance of the vortex sheets that represent the wake, have a negligible effect on u_e. In other words, u_e must be uniform. The unknown diameter D_e and shape of the streamlines around the wake are a function of the performance of the shrouded actuator, which is a function of the wake shape as the wake induces a velocity at the airfoils. A very complex iterative procedure is necessary to calculate the performance of the shrouded wind turbine from this intensive feedback system. An approximated vortex representation shown in Figure 72 results in a model of the shrouded rotor that is much easier to handle but that is still capable of modelling the main features of the shrouded rotor.

Figure 72 Vortex model of 2D loaded shrouded actuator in potential flow.

The shrouded wind turbine will be modelled with the following assumptions (see Figure 72):

1. the thrust force of the actuator F_t is represented by half infinite straight vortex sheets and a sudden wake expansion, with $D_e/D_t \gg 1$,

   $\rightarrow$ velocities in y-direction can be neglected,
   $\rightarrow$ the angle of attack on the airfoils α is constant,
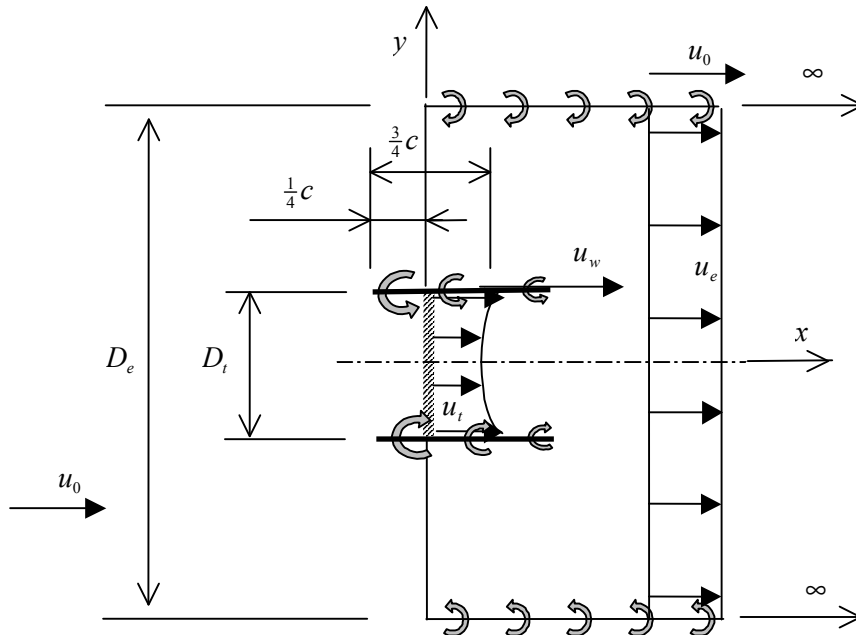2. the airfoils with assumed $\alpha \ll 1$ are modelled by a triangular vortex distribution,
3. the velocity experienced by the airfoils is modelled by a single axial velocity u_w, which acts on the ¾-chord point of the airfoils,
4. the HAWT is modelled by an actuator,
5. the flow field is described by potential theory.

This model, see Figure 72, will be referred to as the "vortex model of the shrouded wind turbine". The assumptions are discussed and substantiated hereafter. A thorough substantiation of assumption 1 is postponed to section 6.2.6 as this requires the results of the vortex model.

On assumption 1

The assumptions of straight vortex sheets and $D_e/D_t \gg 1$ allow determination of the induced velocities of the wake on the shrouded actuator by simplified vortex theory (section 4.1.2), so that the velocities in y-direction can be neglected and the approximation $\alpha = \text{constant} \rightarrow C_l = \text{constant}$ is justified. C_l should be found from external sources like measurements, simulations or mathematical models. This is the closure of the vortex model.

On assumption 2

A bound triangular chord-wise vortex distribution is a first order approximation of the bound vortex distribution at an airfoil found in potential flow calculations (see for instance Katz & Plotkin [33]). The assumption $\alpha \ll 1$, ensures attached flow on the airfoils and largely simplifies the calculations of the induced velocities.

On assumption 3

Within the single-bound vortex model of a thin symmetrical airfoil, Katz & Plotkin [33] shows that the boundary condition of zero normal velocity at the surface of an airfoil should be specified at one point. This point is called: the ¾-chord point or collocation point. Within

the thin airfoil single-bound vortex approximation, the ¾–chord is apparently the location where the airfoil "experiences the flow". The ¾-chord point is thus the appropriate location for the velocity u_w to "act on the airfoil".

On assumption 4
This HAWT model is introduced by Froude [22] and is discussed in section 2.1.2.

On assumption 5
Because of the large characteristic size of the buildings that form the airfoils, it is obvious that $\text{Re} \gg 1$. Consequently, the flow around the shrouded rotor can be approximated with potential flow (section 4.1.1).

6.2.2 Induced velocities

This section gives the derivations of the induced velocities of wake and airfoils.

Induced velocities of the wake and airfoils
As explained in "on assumption 1", the induced axial velocity of the wake $u_{i,wake}$ on both the actuator and the airfoil profiles can be approximated with simplified vortex theory (section 4.1.2)

$$u_{i,wake} = \tfrac{1}{2}\left(u_0 - u_e\right) \tag{185}$$

The induced velocity of the triangular vortex distribution of one airfoil on the ¾-chord point of the other airfoil $u_{i,w,shroud}$ is calculated as if a single-bound vortex at the ¼-chord point of one airfoil induces an axial velocity at the ¾-chord point of the other airfoil. The situation is shown in Figure 73.

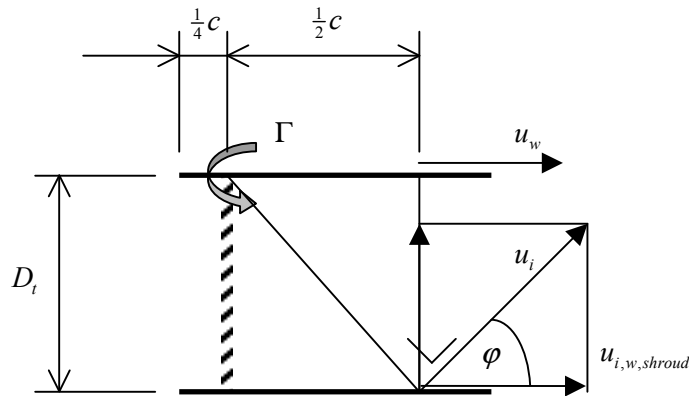**Figure 73 Induced velocity at the ¾-chord point caused by a single-bound vortex at the ¼-chord point.**

$u_{i,w,shroud}$ then reads

$$u_{i,w,shroud} = \chi_s \frac{\Gamma}{2\pi D_t\left(1+\left(\dfrac{c}{2D_t}\right)^2\right)} \tag{186}$$

where

$$\Gamma = \tfrac{1}{2} C_l u_w c \tag{187}$$

is the strength of a single-bound vortex at the airfoils (see for instance Batchelor [2] or Katz & Plotkin [33]), C_l is the constant lift coefficient of the airfoils (assumption 1) in parallel flow with velocity u_w and χ_s is a correction factor. This correction is needed as the triangular vortex distribution is written as a single-bound vortex at the ¼-chord point of the airfoils. In Appendix G, the complex equation for χ_s is found to be well fitted by the much simpler equation

$$\chi_s = \frac{1}{1 - 0.0511 \left(\dfrac{D_t}{2c}\right)^{-1.6211}} \qquad \text{if } \frac{D_t}{2c} \geq 0.3 \tag{188}$$

As u_e is independent of y (introduction of section 6.2), the local thrust force F_t found by (170) is also independent of y. The local power of the shrouded actuator $P(y)$ is found by multiplying F_t with the local velocity through the actuator $u_t(y)$ (section 2.1.2). The total power P extracted by the actuator thus reads

$$P = \int_{y=0}^{y=\frac{1}{2}D_t} F_t u_t(y) dy = F_t \frac{1}{\frac{1}{2}D_t} \int_{y=0}^{y=\frac{1}{2}D_t} u_t(y) dy = F_t \overline{u_t} \tag{189}$$

where $\overline{u_t}$ can be found from the average induced velocity through the actuator by the airfoils $\overline{u_{i,t,shroud}}$. This average induced velocity $\overline{u_{i,t,shroud}}$ is calculated as if a single-bound vortex on the ¼-chord point of the airfoils induces a velocity at the symmetry axis.

$$\overline{u_{i,t,shroud}} = 2\chi_a \frac{\Gamma}{2\pi\left(\frac{1}{2}D_t\right)} \tag{190}$$

The factor χ_a accounts for the non-uniform velocity through the actuator and the fact that the triangular vortex distribution is calculated as a single-bound vortex on the ¼-chord point of the airfoil that induces a velocity at the axis. The complex equation for χ_a is well fitted by the much simpler equation (Appendix G)

$$\chi_a = 0.5051 \ln\left(\frac{R_t}{c}\right) + 1.4447 \quad \text{for} \quad 0.2 \leq \frac{R_t}{c} \leq 5 \tag{191}$$

6.2.3 Resulting velocities

The resulting velocities u_w en $\overline{u_t}$ can be found from

$$u_w = u_0 + u_{i,w,shroud} - u_{i,w,wake} \tag{192}$$

and

$$\overline{u_t} = u_0 + \overline{u_{i,t,shroud}} - u_{i,t,wake} \tag{193}$$

Substitution of (185), (186) and (187) in (192) gives the velocity at the ¾-chord point of the airfoils

$$u_w = u_0 + \chi_s \frac{\frac{1}{2}C_l u_w c}{2\pi D_t \left(1 + \left(\frac{c}{2D_t}\right)^2\right)} - \frac{1}{2}(u_0 - u_e) \tag{194}$$

Rewriting gives u_w as an explicit function of the properties of the shrouded actuator

$$u_w = \frac{\frac{1}{2}(u_0 + u_e)}{1 - \dfrac{\chi_s C_l c}{4\pi D_t \left(1 + \left(\frac{c}{2D_t}\right)^2\right)}} \tag{195}$$

$\overline{u_t}$ is found from substitution of (185) and (191) in (193), which gives

$$\overline{u_t} = u_0 + \chi_a \frac{C_l u_w c}{\pi D_t} - \frac{1}{2}(u_0 - u_e) \tag{196}$$

With substitution of (195) in (196) this gives

$$\overline{u_t} = \frac{1}{2}(u_0 + u_e)\left(1 + \frac{\chi_a C_l c}{\pi D_t} \frac{1}{1 - \dfrac{\chi_s C_l c}{4\pi D_t \left(1 + \left(\frac{c}{2D_t}\right)^2\right)}}\right) \tag{197}$$

We define an augmentation factor ξ

$$\xi = \frac{\chi_a C_l c}{\pi D_t} \frac{1}{1 - \dfrac{\chi_s C_l c}{4\pi D_t \left(1 + \left(\frac{c}{2D_t}\right)^2\right)}} \tag{198}$$

Then (197) reads

$$\overline{u_t} = \frac{1}{2}(u_0 + u_e)(1 + \xi) \tag{199}$$

Comparing (199) with $u_t = \frac{1}{2}(u_0 + u_e)$ for the bare actuator (section 2.1.2) shows that ξ denotes the velocity increase at the actuator caused by the airfoils.

6.2.4 Power coefficient

With (189), (170) and (199), C_P of the shrouded rotor reads

$$C_P = \tfrac{1}{2}\left(1 - \frac{u_e}{u_0}\right)\left(1 + \frac{u_e}{u_0}\right)^2 (1 + \xi) \tag{200}$$

$C_{P,\max}$ can be found by differentiating C_P with respect to u_e. As (198) shows that ξ is independent of u_e, $C_{P,\max}$ is achieved at

$$u_{e,opt} = \tfrac{1}{3}u_0 \tag{201}$$

This is in agreement with the Lancester-Betz limit (see explanation above (173)). Substitution of (201) in (200) gives the final equation for $C_{P,\max}$ of the shrouded actuator

$$C_{P,\max} = \tfrac{16}{27}(1 + \xi) \tag{202}$$

where ξ is found from (198).

It is clear that a high ξ is wanted in order to achieve a high $C_{P,\max}$. By consulting (198) it is clear that a high ξ is achieved at a high lift coefficient. The practical limitation of the augmentation of the power by the shrouded actuator is therefore formed by stall of the airfoils.

6.2.5 Verification of the model

In experiments with a shrouded wind turbine in our open jet wind tunnel either scale effects or blockage effects would give large errors in the measurements (section 4.2). CFD calculations have neither of the problems. They were therefore used instead of the measurements. In order to pick the right turbulence model, some initial CFD calculations on C_l and C_d of an airfoil were carried out. They showed that the $k - \varepsilon$-realizable turbulence model provides (section 4.3.5):

- a good performance concerning trend prediction of C_l and C_d,
- a sufficient quantitative agreement with other references on C_l below stall and
- a poor quantitative agreement with other references on C_d.

Except for C_d, this is a good basis to rely on the $k - \varepsilon$-realizable turbulence model in a performance calculation of the shrouded wind turbine. The combination of momentum theory and the vortex model for the shrouded rotor helps to judge the importance of an inaccurate C_d. With (211), $C_{t,S}$ at $u_{e,opt} = \tfrac{1}{3}u_0$ is found as $C_{t,S} = \tfrac{8}{9}\xi$. For airfoils below stall, $C_d \ll 1$ so that $C_{t,S} \gg C_d$ as $\xi > 1$. Hence, C_d has a negligible effect on $C_{t,S}$ and $C_{t,S}$ is mainly determined by the axial component of C_l. We can therefore rely on the $k - \varepsilon$-realizable turbulence model to verify the vortex model for the shrouded wind turbine.

The verification will be carried out with two airfoil shapes: cambered airfoils and symmetrical airfoils. As C_l of the used cambered airfoils is much higher than C_l of the symmetrical airfoils, it is expected that $D_e / D_t \gg 1$ in assumption 1 is better approximated for the cambered airfoils. The vortex model is therefore expected to produce more accurate results with cambered airfoils. This is verified by a performance calculation of the shrouded rotor with both airfoil shapes.

Verification shrouded actuator with cambered airfoils

A cambered high-lift airfoil developed at Delft University, section wind energy, is used for the airfoils (Appendix D). The performance of a 2D shrouded actuator is determined with an axi-symmetric CFD calculation. The result for the velocity field at $C_{P,\max}$ is shown in Figure 74.

Figure 74 CFD calculation of the shrouded actuator with cambered airfoils at zero load with $D_t/c = 1.1$ (low velocities: dark grey, high velocities light grey).

The configuration details of the shrouded actuator are given in Table 25.

Table 25 Configuration details shrouded actuator with cambered airfoils.

Cambered airfoil	Da2-1999
α	12°
C_l at $\alpha = 12°$ (Appendix D)	2.28
Actuator location	between $\frac{1}{4}c$ points airfoils
D_t/c	Different ratios
Re	2.10^6

The results of the CFD calculations are compared with the vortex model for the shrouded rotor (section 6.2, (199) and (202)) and momentum theory for the shrouded rotor (section 6.1.1, (170), (171)). The vortex model was closed with $C_l = 2.28$ at $\alpha = 12°$ for the airfoils and needed no more input. The model obtained with momentum theory was closed by the

CFD results for $C_{t,S}$ at the different F_t values. With (172), a given F_t of the actuator in the CFD calculation provided the input for u_e in (170) and (171). Table 26 summarizes the results for $C_{P,\max}$ and $u_{t,opt}$ of the vortex model and momentum theory.

Table 26 Comparison of the model and CFD results for the shrouded actuator with cambered airfoils.

D_t/c	ξ	Vortex model		Momentum theory	
		$\dfrac{u_{t,opt,vort}}{u_{t,opt,cfd}}$	$\dfrac{C_{P,\max,vort}}{C_{P,\max,cfd}}$	$\dfrac{u_{t,opt,mom}}{u_{t,opt,cfd}}$	$\dfrac{C_{P,\max,mom}}{C_{P,\max,cfd}}$
2.1	0.51	1.03	1.03	0.92	0.92
1.6	0.61	1.02	1.03	0.93	0.93
1.1	0.76	1.07	0.99	1.02	0.94
0.6	1.02	1.05	0.92	1.22	1.07

It can be concluded from Table 26 that the vortex model shows a remarkable good agreement with the CFD calculations except for $u_{t,opt}$ at small D_t/c. The momentum theory model, closed with CFD results for $C_{t,S}$, shows a higher discrepancy with the CFD results in both $u_{t,opt}$ and $C_{P,\max}$. The results of $C_{P,\max}$ from the CFD calculation are shown in Figure 75.
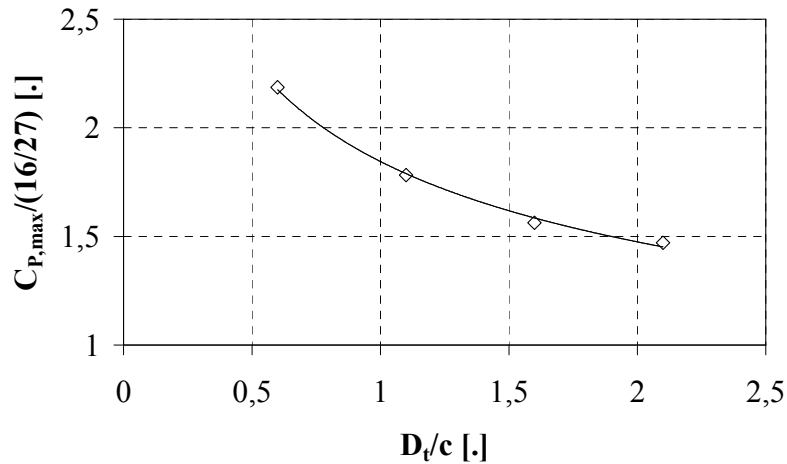
Figure 75 $C_{P,\max}$ **of the shrouded actuator as a function of** D_t/c **as found by the CFD calculations.**

Verification of shrouded actuator with symmetrical airfoils
A Naca 0018 airfoil (Jacobs [30]) is used for the duct. The performance of a 2D shrouded actuator is determined with an axi-symmetric CFD calculation. The results for the velocity field at $C_{P,\max}$ of the actuator are shown in Figure 76.
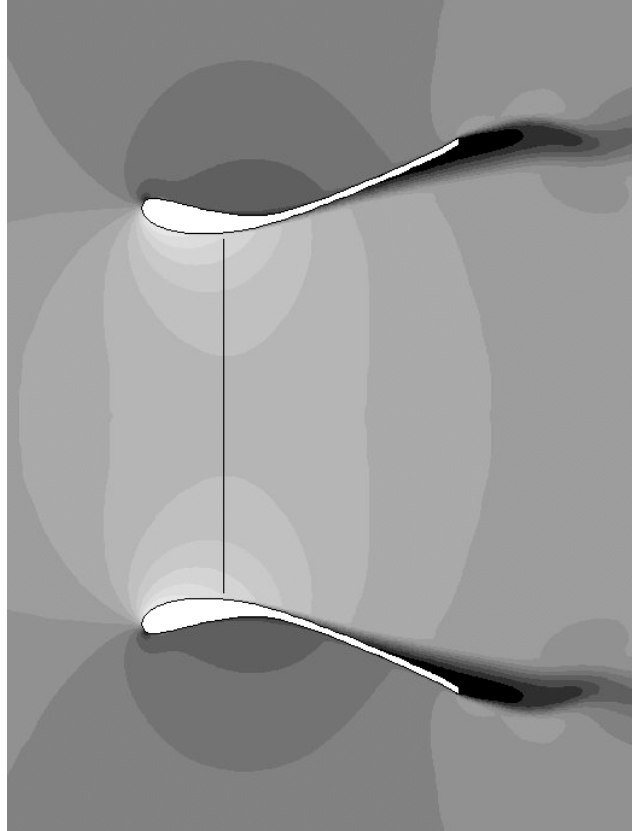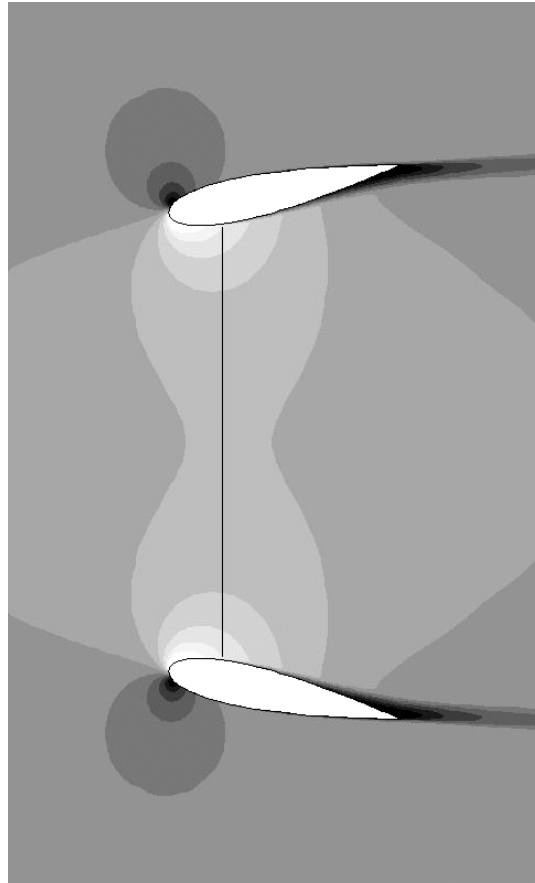
Figure 76 CFD calculation of the shrouded actuator with symmetrical airfoils at zero load with $D_t/c = 1.84$ **(low velocities: dark grey, high velocities light grey).**

The configuration details of the shrouded actuator are given in Table 27.

Table 27 Configuration details shrouded actuator with symmetric airfoils.

symmetrical airfoil	Naca 0018
α	12$^\mathrm{o}$
C_l at $\alpha = 12^\mathrm{o}$ (Paraschivoiu [53])	1.13
Actuator location	Between $\frac{1}{4}c$ points airfoils
D_t/c	1.84
Re	2.10^6

Table 28 summarizes the results for $C_{P,\max}$ and $u_{t,opt}$ of the vortex model and momentum theory.

Table 28 Comparison of the model and CFD results for the shrouded actuator with cambered airfoils.

		Vortex model		Momentum theory	
D_t/c	ξ	$\dfrac{u_{t,opt,vort}}{u_{t,opt,cfd}}$	$\dfrac{C_{P,\max,vort}}{C_{P,\max,cfd}}$	$\dfrac{u_{t,opt,mom}}{u_{t,opt,cfd}}$	$\dfrac{C_{P,\max,mom}}{C_{P,\max,cfd}}$
1.84	0.28	1.03	1.13	1.05	0.96

Table 28 shows that the result of the vortex model for the symmetrical airfoils is less accurate than the results for the cambered airfoils (Table 26). Nevertheless, the result of the vortex model is still good as comparing it with the CFD results shows 13% difference in $C_{P,\max}$ and only 3% difference in $u_{t,opt}$!

6.2.6 Discussion on the validity of the model

Let us look in more detail at the assumption $D_e/D_t \gg 1$ in the vortex model. From mass conservation in the stream tube downwind of the actuator, D_e/D_t reads $D_e/D_t = u_t/u_e$. With substitution of (199) for u_t found by the vortex model this gives

$$\frac{D_e}{D_t} = \tfrac{1}{2}\left(1+\frac{u_0}{u_e}\right)(1+\xi) \tag{203}$$

With $u_{e,opt} = \tfrac{1}{3}u_0$ at $C_{P,\max}$ of the actuator it is then found that

$$\left.\frac{D_e}{D_t}\right|_{opt} = 2 + 2\xi \tag{204}$$

Thus the approximation $[D_e/D_t]_{opt} \gg 1$ is justified for $\xi \gg 1$, which is achieved with high-lift airfoils. Substitution of ξ given in Table 26 and Table 28 in (204) gives $[D_e/D_t]_{opt} = 2.6 \sim 4.0$. The good agreement of the vortex model with the CFD calculations even at small ξ leads to the conclusion that $[D_e/D_t]_{opt} > 2.6$ seems already enough to justify the approximation $[D_e/D_t]_{opt} \gg 1$.

An important result of the assumption $[D_e/D_t]_{opt} \gg 1$ is $C_l = \text{constant}$. Because $C_l = \text{constant}$, it is implicitly assumed that $\alpha = \text{constant}$. As long as the lateral velocity at the ¾-chord point of the airfoils v_i is small compared to the axial velocity u_w, the assumption $\alpha = \text{constant}$ is justified. Within the vortex model assumptions of a straight wake and a sudden wake expansion (Figure 72), vortex theory (85) provides v_i and the vortex model (195) provides u_w . Table 29 summarizes the input needed for a calculation of v_i and u_w at $u_{e,opt} = \tfrac{1}{3}u_0$.

Table 29 Input for a calculation of v_i and u_w at $u_{e,opt} = \tfrac{1}{3}u_0$.

$u_{e,opt}$	a	b	$R = \tfrac{1}{2}D_e$
$\tfrac{1}{3}u_0$	$\tfrac{1}{2}c$	$\tfrac{1}{2}D_t$	$(1+\xi)D_t$

With (85) and Table 29 v_i reads

$$v_i = \frac{\tfrac{2}{3}u_0}{4\pi}\ln\left|\frac{\tfrac{1}{4}c^2+\left(\xi+\tfrac{3}{2}\right)^2 D_t^2}{\tfrac{1}{4}c^2+\left(\xi+\tfrac{1}{2}\right)^2 D_t^2}\right| \tag{205}$$

With (195) and Table 29, u_w reads

$$u_w = \frac{\frac{2}{3}u_0}{1 - \dfrac{\chi_s C_l c}{4\pi D_t \left(1 + \left(\dfrac{c}{2D_t}\right)^2\right)}}$$

(206)

The ratio v_i/u_w gives the change in angle of attack $\Delta\alpha$ caused by the lateral velocity.

$$\Delta\alpha = \arctan\left(\frac{v_i}{u_w}\right)$$

(207)

For the shrouded actuator configuration with cambered and symmetrical airfoils given in Table 25 and Table 27, $\Delta\alpha/\alpha$ and $\Delta C_l/C_l = [C_l(\alpha - \Delta\alpha) - C_l(\alpha)]/C_l(\alpha)$ are calculated and shown in Figure 77.
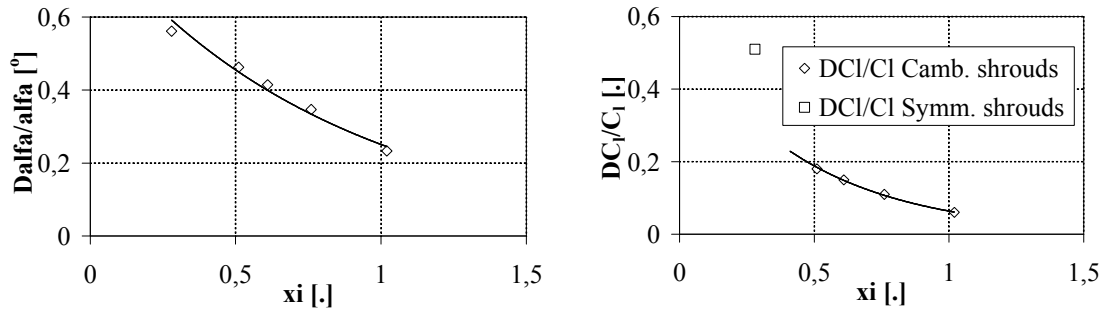
Figure 77 $\Delta\alpha/\alpha$ **and** $\Delta C_l/C_l$ **at** $u_{e,opt} = \frac{1}{3}u_0$ **as a function of** ξ **.**

Figure 77 confirms that the approximation $C_l = \text{constant}$ is allowed for $\xi \gg 1$ or $[D_e/D_t]_{opt} \gg 1$. It additionally shows that $\Delta C_l/C_l < 0.1$ or $C_l \approx \text{constant}$ for cambered airfoils with $\xi > 0.8$. $\Delta C_l/C_l$ for the symmetrical airfoils does not seem to fit the curve through the $\Delta C_l/C_l$ values for the cambered airfoils. The reason is found in C_l of the airfoils, which can be obtained from potential theory (see for instance Batchelor [2])

$$C_{l,camb} = 2\pi \frac{\sin(\beta + \alpha)}{\cos(\beta)}$$

(208)

for the cambered airfoils and

$$C_{l,symm} = 2\pi \sin(\alpha)$$

(209)

for the symmetrical airfoils. Taking the derivative of $C_{l,camb}$ and $C_{l,symm}$ with respect to α with substitution of $\beta = 11°$ for the camber angle of the airfoils (Appendix D) and $\alpha = 12°$ gives

$$\frac{dC_{l,camb}}{C_{l,camb}} = \cot(\beta + \alpha)d\alpha = 2.4 d\alpha$$

(210)

$$\frac{dC_{l,symm}}{C_{l,symm}} = \cot(\alpha)d\alpha = 4.7d\alpha$$

Hence, cambered airfoils show a much smaller influence of changes in α. Furthermore, the influence of changes in α are small for airfoils operated around stall as $dC_{l,camb}/d\alpha = dC_{l,symm}/d\alpha = 0$ at stalled airfoils. Within the attached flow description on the airfoils in the vortex model, the most accurate results are thus expected for cambered airfoils operated just before stall occurs.

6.3 Application of vortex model results to momentum theory

Comparison of u_t from the vortex model for the shrouded rotor (199) with the result of momentum theory for the shrouded rotor (171) gives

$$C_{t,s} = \xi\left(1 - \left(\frac{u_e}{u_0}\right)^2\right) \tag{211}$$

Hence, $C_{t,s}$ is a function of u_e and one may not assume $C_{t,s}$ to be independent of u_e in momentum theory (see discussion below (172)).

6.4 Finite aspect ratio effects

In a configuration where buildings are used as airfoils (Figure 66), the finite height of the buildings introduces finite A_r effects in the performance of the shrouded wind turbine. This paragraph gives an approximation of the deviation on the 2D vortex model for the shrouded wind turbine calculated by including the 3D effects of finite A_r of the airfoils.

Suppose that the airfoils are located in a uniform parallel flow (such flow is approximated in an atmospheric boundary layer developed over low roughness) and have elliptical span-wise loading. For such loading, the effect of finite A_r is given by (161)

$$\hat{C}_l = C_l\left(1 + \frac{2}{A_r}\right)^{-1}$$

where the $\wedge$ refers to finite A_r and absence of $\wedge$ refers to infinite A_r. The airfoils are sited on the earth's surface, i.e. the earth's surface is a symmetry plane for the flow around the airfoils. The characteristic length of the airfoils for the calculation of A_r should thus be double the height of the airfoils h.

$$A_r = 2\frac{h}{c} \tag{212}$$

Because of the finite A_r, ξ found by (198) decreases to

$$\hat{\xi} = \frac{\chi_a \hat{C}_l c}{\pi D_t} \frac{1}{1 - \dfrac{\chi_s \hat{C}_l c}{4\pi D_t \left(1 + \left(\dfrac{c}{2D_t}\right)^2\right)}} \tag{213}$$

where $\hat{C}_l$ is found by (161).

An example shows the importance of the effect of finite A_r. Suppose we have a shrouded actuator with the following characterization.

Table 30 Shrouded actuator characterisation

property	α	C_l	$D_t/2c$
Value	12°	$2\pi \sin\alpha$	1

With (213), $\hat{\xi}$ shows the following behaviour as a function of A_r.
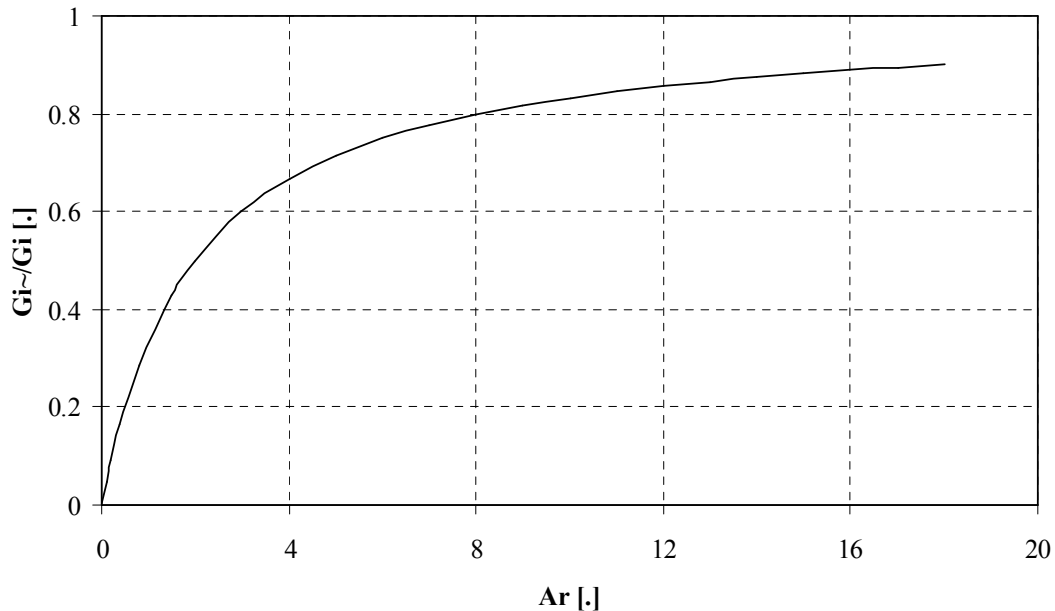
Figure 78 Example of $\hat{\xi}$ of a shrouded actuator as a function of A_r.

The decrease in $\hat{\xi}$ for buildings that normally (see Figure 65) have $A_r = 4 \sim 8$, is a considerable 20% ~ 35%. End plates on the airfoils can be used to reduce the effect of finite A_r and increase $\hat{\xi}$.

6.5 The ducted small wind turbine

A ducted small wind turbine is defined as a wind turbine that experiences the local velocity in the ducts as a free stream velocity. This section gives the derivation of the relative size the small wind turbine compared to the size of the duct. Furthermore, this section gives the derivation of the free stream velocity that is experienced by the ducted small wind turbine.

6.5.1 Allowed stream tube size

A wind turbine with diameter D_t has a stream tube with a length of approximately $6D_t$ (see section 2.2). If the velocity around that stream tube $u \approx$ constant , the power P of that wind turbine is found with (1) as $P = C_P \frac{1}{2}\rho\, u^3 A_t$. Let a wind turbine with diameter D_t and power P be sited at (a,b) between the airfoils. Assume that $u(x,y) = u(a,b)$ if $u(x,y) = u(a,b) \pm 0.05\, u(a,b)$. It then follows that

$$P = C_P \tfrac{1}{2}\rho\, u(a,b)^3 A_t \tag{214}$$

if

$$u(x,y) = u(a,b) \pm 0.05\, u(a,b)$$

with

$$a - 2.5D_t \le x \le a + 3.5D_t \text{ and } b - \tfrac{1}{2}D_t \le y \le b + \tfrac{1}{2}D_t$$

The wind turbine will then be called small compared to the airfoils. A CFD calculation of the contour lines $u(x,y)/u_0 =$ constant is shown in Figure 79.
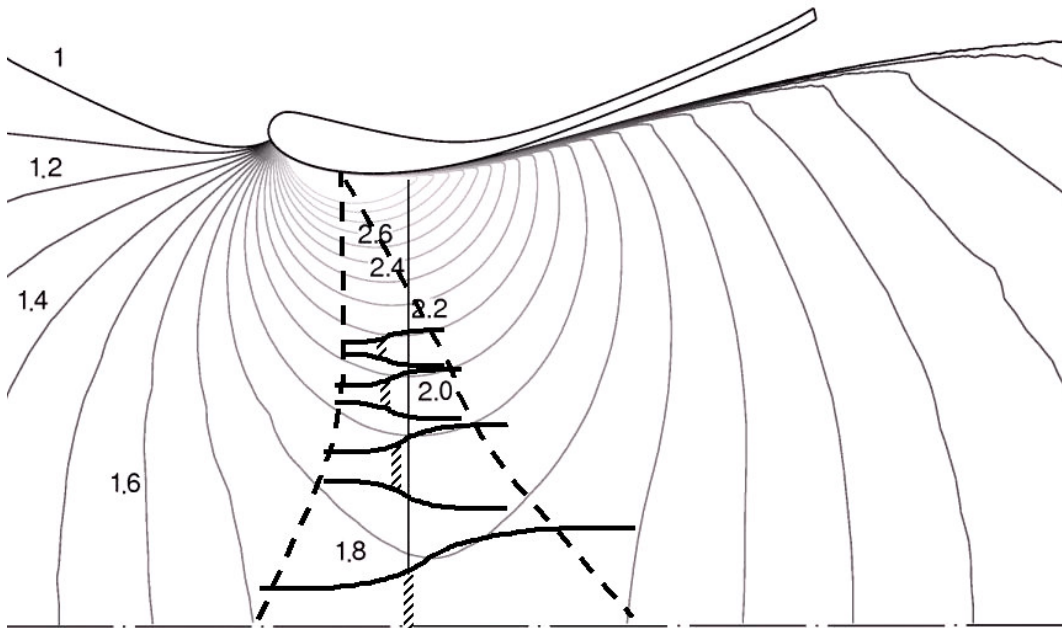
Figure 79 CFD calculation of $u(x,y)/u_0 =$ constant between cambered airfoils (configuration Table 25) and maximum stream tube sizes of small wind turbines.

According to Figure 79,
- the maximum length of the stream tube then varies from $6D_t \approx 0.7c \rightarrow D_t/c = 0.1$ at the axis to $D_t/c \ll 1$ close to the airfoils,
- the velocity close to the airfoils is highest.

The ratio D_t/c for which (214) applies varies with shrouded wind turbine configuration.

6.5.2 Velocity between the ¼-chord points

Suppose, such a small wind turbine is sited between the ¼-chord points: the location where the velocity is approximately the highest. Furthermore, assume flow parallel to the axis between the airfoils. Then, this small wind turbine experiences the velocity found with summation of the induced velocity of the airfoils ((266) in Appendix G) and the free stream velocity u_0 :

$$
\begin{aligned}
u(y) = u_0 + \frac{\Gamma}{4\pi c}&\left[3\arctan\left(\frac{3c}{4(R_t - y)} \right) + 3\arctan\left(\frac{c}{4(R_t - y)} \right) \right] \\
&+ \frac{\Gamma}{4\pi c}\frac{2(R_t - y)}{c}\ln\left(\frac{16(R_t - y)^2 + c^2}{16(R_t - y)^2 + 9c^2} \right) + \\
\frac{\Gamma}{4\pi c}&\left(3\arctan\left(\frac{3c}{4(R_t + y)} \right) + 3\arctan\left(\frac{c}{4(R_t + y)} \right) \right) \\
&+ \frac{\Gamma}{4\pi c}\frac{2(R_t + y)}{c}\ln\left(\frac{16(R_t + y)^2 + c^2}{16(R_t + y)^2 + 9c^2} \right)
\end{aligned}
\tag{215}
$$

In this equation c is the chord length of the airfoil, R_t is half the distance between the ¼-chord point on the airfoils ($R_t = \frac{1}{2}D_t$), y is the distance to the symmetry axis between the airfoils and Γ is found with (187):

$$
\Gamma = \tfrac{1}{2}C_l u_w c
$$

The velocity u_w in (187) can be found with an analogue derivation that leads to (194) with absence of the induced velocity from the wake of the rotor (185) as the wake of the small wind turbine does not induce a velocity on the airfoil. u_w is then found as

$$
u_w = u_0 + \chi_s \frac{\frac{1}{2}C_l u_w c}{2\pi D_t\left(1 + \left(\frac{c}{2D_t} \right)^2 \right)}
\tag{216}
$$

After grouping u_w this results in

$$
u_w = \frac{u_0}{1 - \dfrac{\chi_s C_l c}{4\pi D_t\left(1 + \left(\dfrac{c}{2D_t} \right)^2 \right)}}
\tag{217}
$$

$u(y)$ can now be calculated and compared to a CFD calculation. The result is shown in Figure 80.
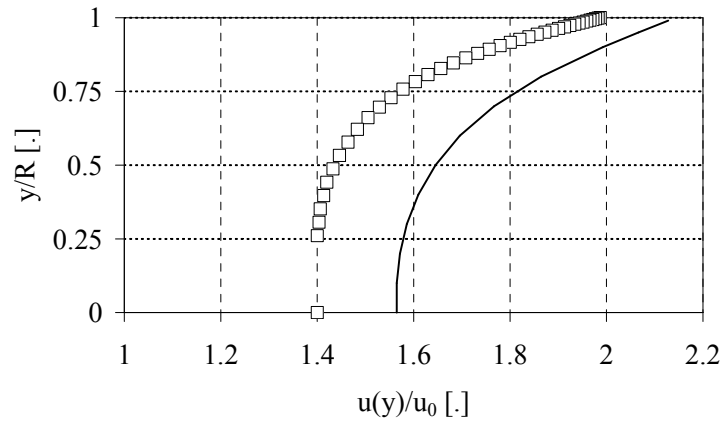
Figure 80 Velocity $u(y)$ **for a small shrouded wind turbine (configuration Table 25).**
The markers show the CFD results while the solid line shows the result of (215).

Figure 80 shows a maximum of 14 % difference between the CFD results and $u(y)$ from (215).

6.6 The shrouded H-Darrieus

The configuration of the shrouded H-Darrieus is shown in Figure 81 (H-Darrieus sketched as a tube).
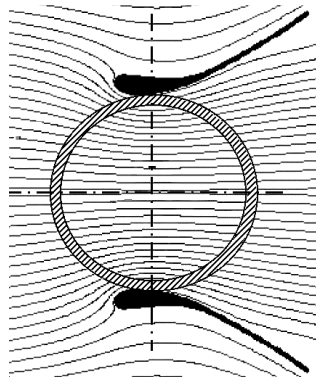
Figure 81 Configuration of the shrouded H-Darrieus.

Wilson & Lissaman [84] give a simple model for an H-Darrieus. The model shows that the H-Darrieus extracts the energy where the blades move crosswind and cannot extract energy where the blades move along-wind. Hence, the energy extracting part of the H-Darrieus lies in the location with the lowest velocity around the symmetry axis between the airfoils (section 6.5). This results in a smaller power augmentation compared to a shrouded HAWT. The shrouded H-Darrieus is therefore not studied.

6.7 Yawed and opposite flow

Within the context of the thesis, buildings form the concentrator of the wind turbine. The concentrator is consequently too heavy to yaw into the direction of the wind. Operation of the shrouded wind turbine at various yaw angles is inevitable. It is therefore interesting to study the behaviour of the shrouded wind turbine in yawed flow. Such is done in 6.7.1. One of yawed flow conditions is flow from the back of the shrouded wind turbine or opposite flow. The behaviour in opposite flow is treated in 6.7.2.

6.7.1 Yawed flow

The configuration of a shrouded rotor in yawed flow is shown in Figure 82. As a result of the yawed flow, the angle of attack of the downwind airfoil decreases $\alpha \rightarrow \alpha_-$ and the angle of attack of the upwind airfoil increases $\alpha \rightarrow \alpha_+$.
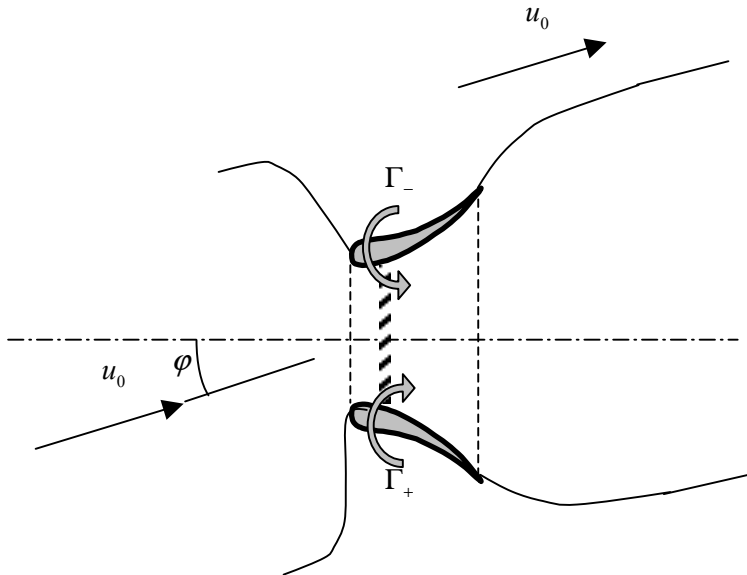
Figure 82 Shrouded rotor in yawed flow.

If the airfoils are operated well below stall, $\alpha \rightarrow \alpha_-$ will lead to $C_l(\alpha_-) < C_l(\alpha)$ while $\alpha \rightarrow \alpha_+$ leads to $C_l(\alpha_+) > C_l(\alpha)$. As ξ of the shrouded rotor in yawed flow consists of a contribution from both airfoils, the overall effect of these changes on C_P will be small. If the airfoils are operated just below stall, $\alpha \rightarrow \alpha_-$ will lead to $C_l(\alpha_-) < C_l(\alpha)$ but $\alpha \rightarrow \alpha_+$ leads to $C_l(\alpha_+) \approx C_l(\alpha)$. This shows that the relative change in C_P of a shrouded rotor in yaw is higher if the airfoils have $\alpha = \alpha_{stall}$ compared to a configuration with $\alpha \ll \alpha_{stall}$.

Measurements of $C_{P,\max}$ of a shrouded rotor in yaw, with cambered airfoils at $\alpha = 15^\circ \approx \alpha_{stall}$, are found in Phillips et al. [6]. Their measurements show the following decrease of $C_{P,\max}$ as a function of the yaw angle.

Figure 83 Decrease of $C_{P,\max}$ of a shrouded rotor in yaw with $\alpha = 15^\circ \approx \alpha_{stall}$.

This shows a slightly lower $C_{P,\max}$ in yawed flow than $C_{P,\max}$ of a HAWT in yawed flow derived by Glauert momentum theory (Figure 49).

6.7.2 Opposite flow

There is a widespread misunderstanding of the operation of a shrouded rotor in opposite flow ($\varphi = 180^{\circ}$, see Figure 82 for the definition of φ) where the large area of the shrouded rotor is directed upwind. Many non-aerodynamicists expect a large concentrator effect and the configuration is thought to be an "air catcher". This paragraph sheds some light on the performance of the shrouded rotor in opposite flow. The configuration is shown in Figure 84.
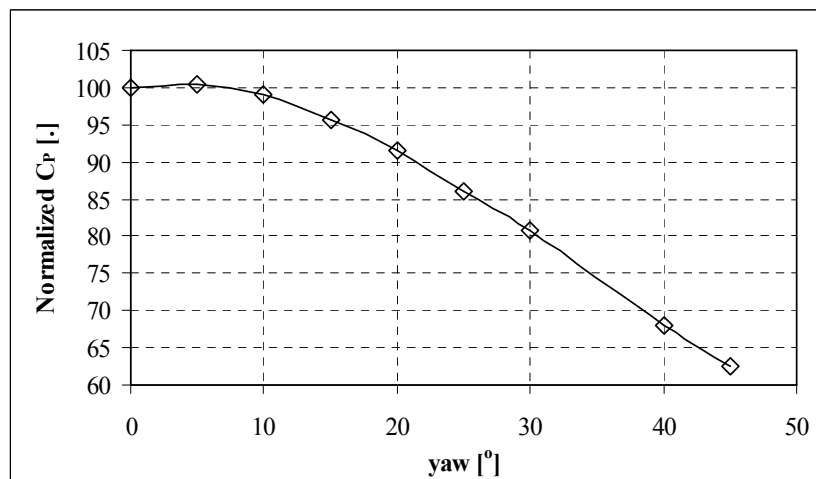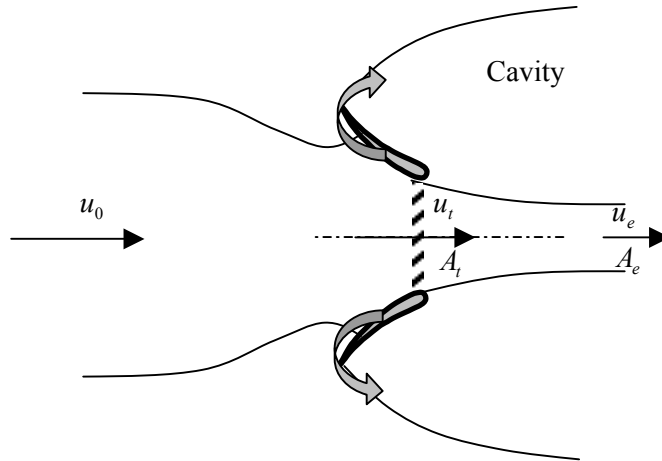

Figure 84 Shrouded rotor in opposite flow, with lift of the airfoils modelled by bound vortices shown as circular arrows.

In contrast to the acceleration of the flow caused by the bound vortices in normal flow, the bound vortices of the airfoils now induce a velocity that decelerates the flow through the entrance of the duct. The sharp leading edge of the airfoils causes separation and a cavity is formed downwind of the airfoils. Vortex sheets cannot model the cavity downwind of the airfoils. A derivation of a vortex model for the shrouded wind turbine in opposite flow is therefore not possible. It is convenient to look for other ways to model the shrouded rotor in opposite flow.

Because of the analogue flow conditions, a shrouded rotor in opposite flow, as shown in Figure 84, can be considered as a ducted rotor. A model for wind turbines in ducts through buildings is developed in chapter 7. In section 7.3, an approximated plate concentrator model is presented, valid for well-rounded duct inlets. According to this model, the performance of a concentrator in a configuration with a cavity yields

$$C_{P,\max} = \frac{2\beta}{3\sqrt{3}}\left(\frac{u_s}{u_o}\right)^3$$

where β is the area contraction behind the actuator and u_s is called the separation velocity, which is a measure for the velocity around the cavity. u_s is unknown but according to the similarity with the flow around the plate concentrator in section 7.3, u_s can be taken equal to u_s found for the plate concentrator. For symmetrical airfoils, the wake of the actuator will contract as a consequence of the duct shape (section 7.1.2). With cambered airfoils, the wake

will show approximately zero contraction, as the flow in the duct is parallel downwind of the actuator. It can therefore be assumed that $\beta = 1$ for cambered airfoils. From these considerations (235) leads to (236) and (237), which read

$$C_{P,\max} \approx 0.85 \approx \tfrac{16}{27} \times 1.43$$

for a 2D shrouded rotor with cambered airfoils in opposite flow and

$$C_{P,\max} \approx 0.67 \approx \tfrac{16}{27} \times 1.13$$

for a 3D shrouded rotor with cambered airfoils in opposite flow. Hence, the concentrator effect is small in 3D (13%) but considerable in 2D (43%).

At small variations around $\varphi = 180^\text{o}$ (see Figure 82 for the definition of φ), the decrease in $C_{P,\max}$ is small as u_s around the cavity does not change much (section 7.5).

6.7.3 Zero power output

There is a range of φ with $0^\text{o} < \varphi < 90^\text{o}$ that causes a cavity at the inlet and outlet of the shrouded rotor. At one particular $0^\text{o} < \varphi < 90^\text{o}$, the cavity pressures at "inlet" and "outlet" of the shrouded wind turbine are equal so that the power of the shrouded wind turbine is zero (Figure 85). It is likely that this particular φ is approximately perpendicular to the line that connects the leading and trailing edge of the airfoil because in that case the cavities at inlet and outlet approximately experience equal separation conditions. Hence, the power output of the shrouded wind turbine is likely to be approximately zero as $\varphi \approx 90^\text{o} - \alpha$.
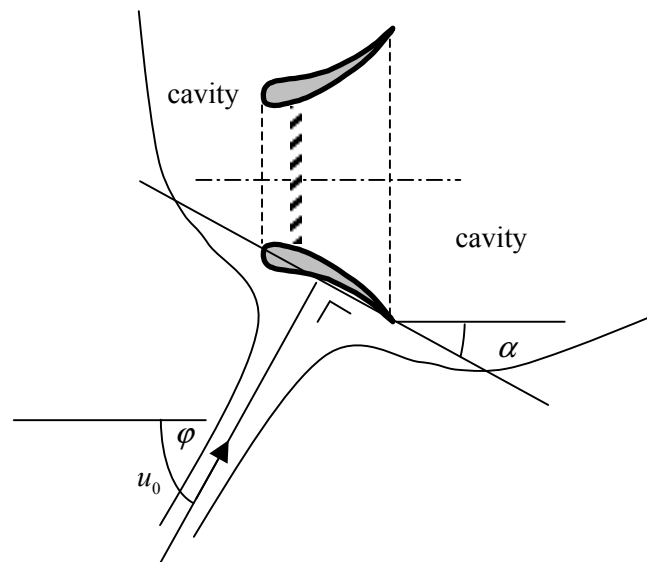
Figure 85 Flow condition at zero power output of the shrouded wind turbine.

6.8 The energy yield of the shrouded rotor

This section discusses the power output of a shrouded rotor in omnidirectional wind. Based on the knowledge shown in the previous sections, it is possible to give estimates of the power output at all flow angles. This allows a first order calculation of the energy yield of the shrouded rotor in omnidirectional wind.

The energy yield calculation will be based on the 2D configuration of the shrouded rotor with cambered airfoils as shown in Table 25, with $D_t/c = 1.1$. According to Table 26 and (202), the airfoils give a power augmentation of 1.76 at $\varphi = 0^o$ (see Figure 82 for the definition of φ). The discussion and measurement results in section 6.7 make clear that the power output slowly decreases with increasing yaw angle. The decrease in power with increasing yaw angle is approximated with the measurement results shown in Figure 83. Zero power output is expected at $\varphi \approx 90^o - \alpha = 78^o$. At $\varphi = 180^o$, the measurements and models in section 6.7 give a power augmentation of 1.43. This will slowly decrease with increasing variation from $\varphi = 180^o$. With the previous considerations, $C_{r,i}$ can be calculated by (62). A smooth curve through the $C_{r,i}$ data, gives $C_{r,i} \approx 0.3$ at $\varphi = 90^o$. The result is shown in Figure 86.
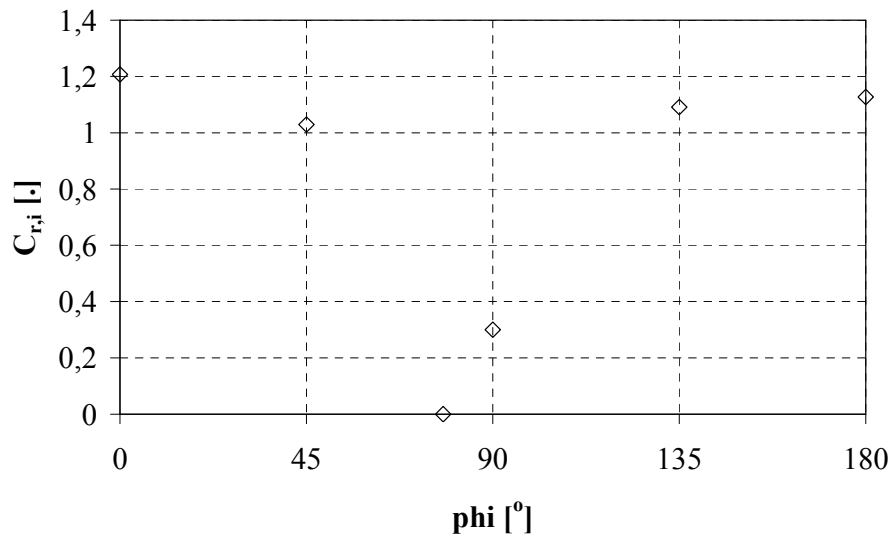
Figure 86 Assumed $C_{r,i}$ for a BAWT between 2D airfoils as a function of φ (phi).

In order to allow comparison of the energy yields of various BAWT's in section 8.2.2, the starting point for all BAWT's is equal, i.e. it is assumed that $u_0 = 5.0$ m/s at $z_0 = 0.03$ and $u_0 = 3.3$ m/s at $z_0 = 1$ (section 3.1.1). With (60) and Figure 86, this gives the following energy yields.

Table 31 Energy yield of a ducted 2.5 kW BAWT.

site	Energy yield $kWh/(m^2 year)$
$u_0 = 5.0$ m/s at $z_0 = 0.03$ m	360
$u_0 = 3.3$ m/s at $z_0 = 1$ m	95

7 Wind turbines in ducts through buildings

The blockage of the building causes low velocities at the upwind façade of the building and high velocities at the sides of the building. This results in a high pressure at the upwind façade and a low pressure at the sides and downwind façade of the building (Bernoulli's theorem). These pressure differences induce a flow in a connection between high- and low pressure. In everyday life, this induced airflow is known as draught when one opens a window on a windy day. A wind turbine can perhaps operate in this draught. In this chapter, such a concept is studied in its basic configuration: a wind turbine in a duct through a disk or plate, which will be called "the plate concentrator".

7.1 The plate concentrator model

The model for the performance of the wind turbine in the plate concentrator, with area A_p (duct area included), is based on the following assumptions:

1. the flow around the plate concentrator is characterized by $Re \gg 1$ and can thus be approximated with potential flow (see section 3.2.1),
2. the wake of the plate concentrator can be approximated by a cavity i.e. the velocities in the wake are assumed to be zero,
3. the duct area $A_t \ll A_p$ so that the influence of the mass flow through the duct on the mass flow around the plate and wake can be neglected,
4. the wind turbine in the plate concentrator can be modelled by an actuator.

The flow around the axi-symmetric plate concentrator (2D or 3D) is shown in Figure 87 and is characterized as follows. At the upwind edge of the plate, the boundary layer separates (iii) and a cavity downwind of the plate is formed (iv). A jet (v) that originates from the pressure difference between the upwind and downwind side of the plate vents into the cavity (iv).
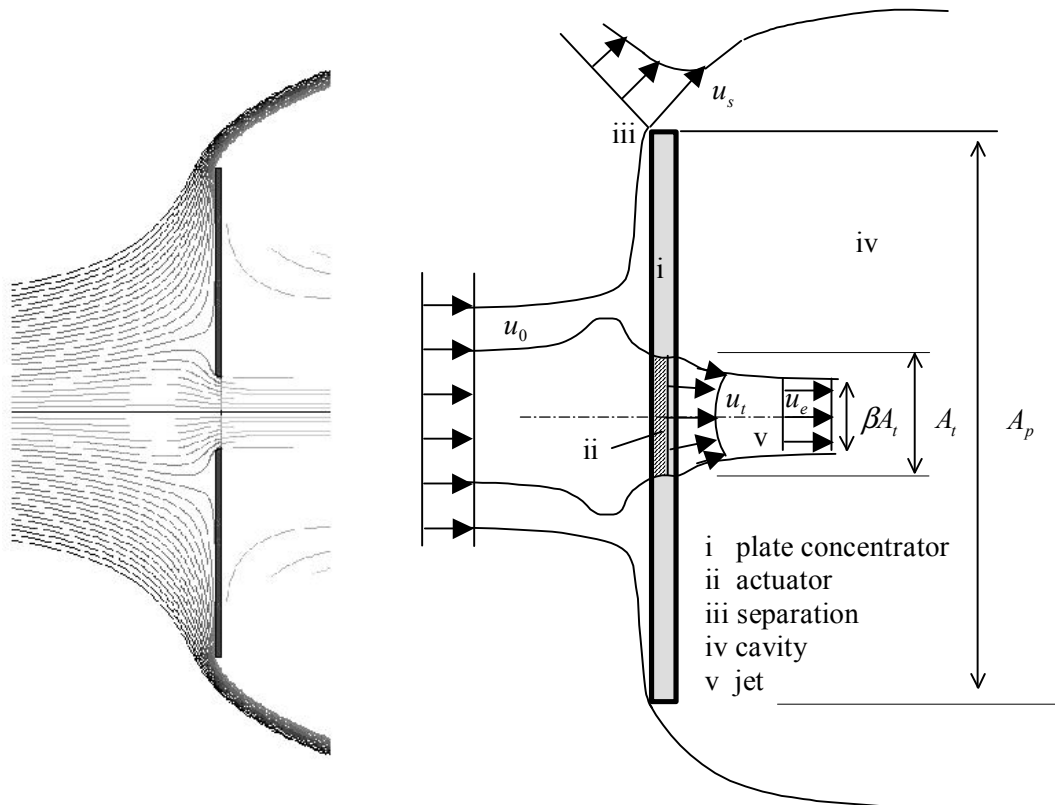
Figure 87 Flow around the plate concentrator in parallel flow perpendicular to the plate. Left: CFD calculation of the streamlines, right: flow characterization.

In section 7.1.2, it is shown that the jet contraction depends on the inlet rounding of the actuator.

7.1.1   Power coefficient

According to Bernoulli's theorem, the local static pressure at the upwind side of the actuator p_+ reads

$$p_+ = p_0 + \tfrac{1}{2}\rho\left(u_0^2 - u_t^2\right) \tag{218}$$

where u_t is the local velocity at the actuator.

With Bernoulli's theorem and the cavity model (section 3.3.5), the uniform pressure in the cavity p_c is found as

$$p_c = p_0 + \tfrac{1}{2}\rho\left(u_0^2 - u_s^2\right) \tag{219}$$

where u_s is the so called separation velocity that reproduces the measured p_c by substitution in (219).

The actuator in the plate concentrator absorbs maximum power if all air through the actuator is decelerated with the same optimal amount. At maximum power output we thus have a uniform velocity u_e at jet area βA_t with parallel streamlines (see Figure 87). In order to find the maximum power absorbed by the actuator, it is thus assumed that u_e is uniform. Mass conservation in the jet downwind of the actuator then gives

$$u_e \beta A_t = \int_0^{A_t} u_{t,x} dA \rightarrow u_e = \frac{\overline{u_{t,x}}}{\beta} \tag{220}$$

where the bar above $u_{t,x}$ denotes averaging over the actuator area A_t.

At jet area βA_t, the streamlines are parallel and the pressure in the jet is equal to the cavity pressure p_c. Hence, Bernoulli's theorem on a streamline in the jet downwind of the actuator gives the downwind pressure on the actuator p_- as

$$p_- = p_c + \tfrac{1}{2}\rho\left(u_e^2 - u_t^2\right) \tag{221}$$

This gives a pressure drop across the actuator Δp of

$$\Delta p = p_+ - p_- = \tfrac{1}{2}\rho\left(u_s^2 - u_e^2\right) \tag{222}$$

Note that Δp in (222) does not depend on u_t and that a uniform u_e results in a uniform Δp across the actuator. At $\Delta p = 0$, (222) shows that $u_s = u_e$. CFD calculations in Bottema [22] support the result of (222) that $u_s = u_e$ at $\Delta p = 0$ for building shapes similar to the plate concentrator and for a cross-shaped building arrangement with the duct at the centre of the cross[25].

Substitution of (220) in (222) gives

$$\Delta p = \tfrac{1}{2} \rho \left(u_s^2 - \frac{\left(\overline{u_{t,x}}\right)^2}{\beta^2} \right) \tag{223}$$

For uniform u_e and according to (222) consequently uniform Δp, the power absorbed by the actuator P can be found from

$$P = \int_0^{A_t} \Delta p \ u_{t,x} \ dA = \Delta p \int_0^{A_t} u_{t,x} \ dA = \Delta p A_t \overline{u_{t,x}} \tag{224}$$

with (1) and (223) this gives C_P of the actuator as

$$C_P = \left(\left(\frac{u_s}{u_0} \right)^2 - \left(\frac{\overline{u_{t,x}}}{\beta u_0} \right)^2 \right) \frac{\overline{u_{t,x}}}{u_0} \tag{225}$$

According to (225) the highest C_P is achieved with β as large as possible. At this moment, $C_{P,\max}$ cannot be found by differentiation of C_P in (225) with respect to $\overline{u_{t,x}}$ as β is unknown and possibly a function of $\overline{u_{t,x}}$. The nature of β is therefore analysed in the next section.

7.1.2   Jet contraction

Momentum conservation considerations in the area behind the actuator give the necessary background for β. The control volume is taken as shown in Figure 88.

---
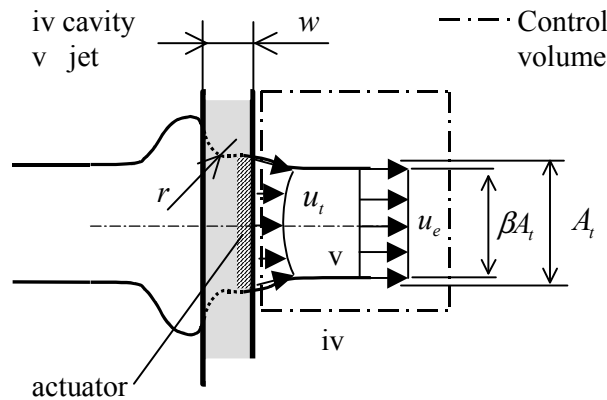
25 In section 7.7, this building arrangement is shown and called "the combined plate concentrator".

Figure 88 Control volume for momentum conservation in the jet.

Conservation of axial momentum in a control volume reads (section 4.1.3)

$$\sum_i F_{i,ax} = I_{i,out,ax} - I_{i,in,ax} \tag{226}$$

With the pressures and velocities in the control volume, (226) reads

$$-p_c A_t + \int_0^{A_t} p_- \, dA = \rho A_e u_e^2 - \rho \int_0^{A_t} u_{t,x}^2 \, dA \tag{227}$$

Substitution of (219), (220) and (221) in (227) gives a quadratic equation in β, which provides

$$\beta = \gamma \left[1 \pm \sqrt{1 - \frac{1}{\gamma}} \right] \tag{228}$$

with $\gamma = \left(\overline{u_{t,x}} \right)^2 \Big/ \left(\overline{u_{t,x}^2} - \overline{u_{t,r}^2} \right)$ and $\overline{u_t^2} = \overline{u_{t,x}^2} + \overline{u_{t,r}^2}$ where $u_{t,r}$ denotes the local radial velocity. Equation (228) directly reveals that β is no function of A_t i.e. β is equal for a 2D and 3D jet.

When using the minus sign in (228) and putting $\overline{u_{t,x}^2} \downarrow \overline{u_{t,r}^2}$ i.e. $\gamma \to \infty$, the jet contraction reads

$$\beta_{\gamma \to \infty} = \tfrac{1}{2} \tag{229}$$

which is the well known result for "Borda's mouthpiece" (see for instance Batchelor [2]).
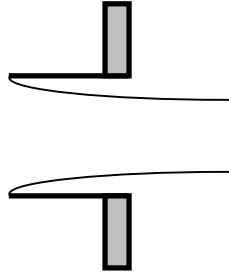
Figure 89 Borda's mouthpiece

The plus sign in (228) gives $\beta_{\gamma \to \infty} = \infty$, which does not suite the assumed flow pattern. Hence, only the minus sign in (228) gives meaningful results for ducted plates.

For $\left(\overline{u_{t,x}} \right)^2 = \overline{u_{t,x}^2}$ and $\overline{u_{t,r}^2} = 0$, $\gamma = 1$ so that (228) gives

$$\beta_{\gamma \to 1} = 1 \tag{230}$$

which is the well known result for a "slowly converging mouthpiece" (see for instance Batchelor [2]).
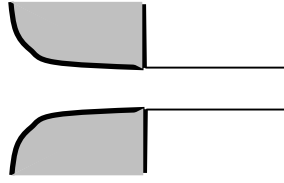
Figure 90 Slowly converging mouthpiece

We thus know that $\frac{1}{2} \leq \beta \leq 1$ with the accompanying duct shape and velocity distribution that lead to this result. By other means, it can be shown that the ducted plate shows $\beta = 0.6$ (see for instance Batchelor [2]).

The equations (225) and (228) allows one to calculate C_P of the plate concentrator from the velocity distribution at the actuator. They will be referred to as the "plate concentrator model". $C_{P,\max}$ cannot directly be calculated with the plate concentrator model but should be estimated from interpolation between the C_P values at different loads of the actuator.

7.2 Verification of the plate concentrator model

The verification of the plate concentrator model is based on measurements and CFD calculations at a plate concentrator with the following configuration details.

Table 32 Configuration details verified plate concentrator.

	3D plate concentrator	2D plate concentrator
A_t/A_p	3.24%	18.5%
r/w	0.75	0.75

The CFD calculations are first compared with measurements in order to verify the CFD calculations. Secondly, the detailed output of the CFD calculations, that could not be obtained with measurements, is used to verify the plate concentrator model.

The measurements are described in Ytsma [91]. A set of screens with various porosity simulated the actuator at various loads. For all screens, the local pressure drop across the screen together with the local total velocity just downwind of the screen were measured. The pressure drop was measured with an array of static pitot tubes, while the local total velocity was measured with a hotwire.

Details of the CFD calculation are given in Appendix C. It was shown in section 4.3.1 that the $\kappa - \varepsilon$ models give a spuriously large generation of turbulent kinetic energy around the stagnation point. This turbulent kinetic energy is transported downwind, where it influences u_s by intense turbulent mixing of the low velocity in the wake with the high velocity just outside the wake. As the flow shows a stagnation condition upwind of the plate concentrator, the $\kappa - \varepsilon$ models give an inaccurate simulation of the actual flow. The RSM does have this problem. It is therefore used to simulate the flow around the plate concentrator.

7.2.1   Verification of the jet velocity

Figure 91 shows the measured and simulated velocity profiles at a distance $0.2 R_{duct}$ downwind of the actuator with zero pressure drop across the actuator.
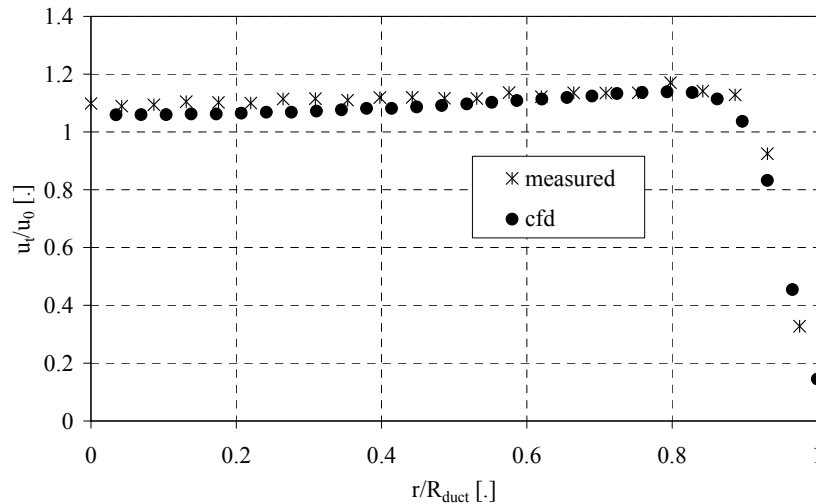
Figure 91 Measured and CFD (turbulence model see Appendix C) results of the velocity profiles at an axial distance $0.2R_{duct}$ downwind of the actuator at zero pressure drop across the actuator for a disk plate concentrator.

The simulated total velocity shows a discrepancy of less than 10% compared to the measured velocity. The errors in the measurement (see section 4.2.2) make it not worthwhile to try to get a better agreement by using the various options in the RS model.

7.2.2 Verification of the jet contraction

The jet contraction β at different loads of the actuator is calculated by (228) from the simulation of a 2D and 3D (disk) plate concentrator. Furthermore, β was calculated from the ratio of the jet diameter at the actuator and the jet diameter at the plane with parallel streamlines. An example of the simulated streamline contraction is shown in Figure 92. The jet contraction for the 2D plate concentrator could not be taken from the streamline contraction because the 2D jet was not stationary and moreover not symmetrical (Figure 92).
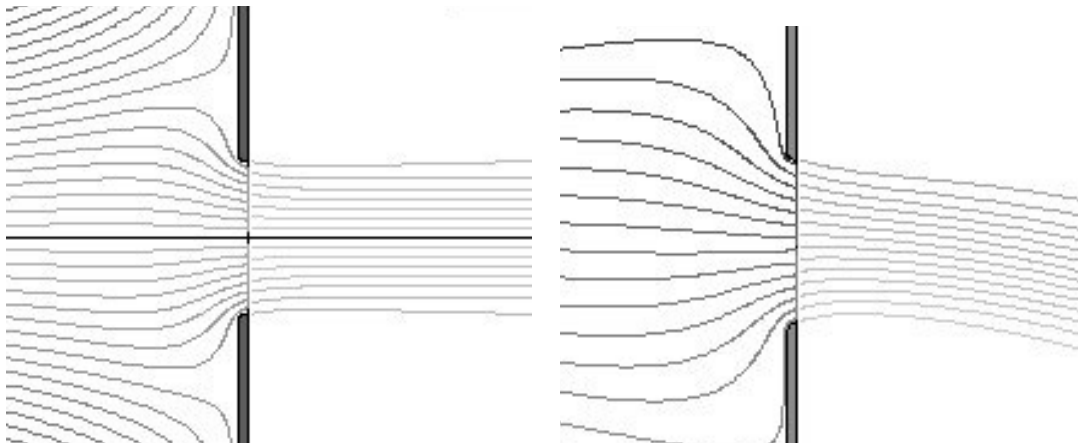
Figure 92 CFD results of the jet contraction for the 3D (left) and 2D (right) plate concentrator with zero actuator load.

The results of β calculated by (228) and β taken from the streamline contraction are shown in Figure 93. The induction factor a at the x-axis is calculated from $\overline{u_{t,x}} = (1-a)u_0$.
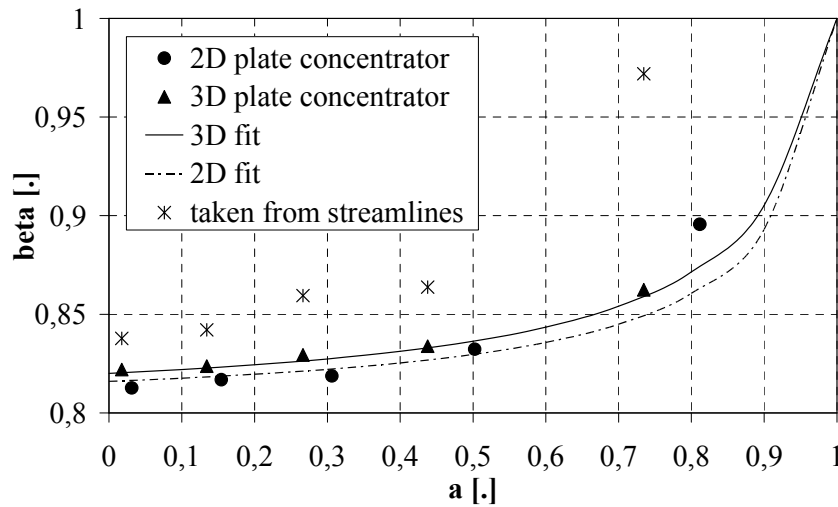
Figure 93 CFD results of the jet contraction versus induction factor calculated with (228) and jet contraction taken from the streamline contraction in the CFD results for a 3D plate concentrator.

The jet contraction taken from the streamline contraction shows a discrepancy of 4% for $a \le 0.5$. The discrepancy increases with increasing a. This is mainly caused by the fact that the jet vanishes at high a as the duct is blocked at high a.

In section 7.1.2, it was shown that β does not depend on the flow dimension (2D or 3D). This is confirmed by the small difference of only 0.6% between the 2D and 3D values for β found by (228) and shown in Figure 93. A good fit through those β values is achieved with

$$\beta = 0.8 + \frac{0.2}{8\dfrac{\overline{u_{t,x}}}{u_0} + 1} \tag{231}$$

with $\overline{u_{t,x}} = (1-a)u_0$. This fit is used for further verification of the plate concentrator model. For $a < 0.8$, the discrepancy between fit and $\beta = 0.82$ is less than 2%. Hence, $\beta = 0.82 = \text{constant}$ is a good approximation for $a < 0.8$.

7.2.3   Verification of the pressure drop across the actuator

Δp across the actuator as a function of the velocity at the axis downwind of the screen can be accurately measured at a 3D plate concentrator and compared with a CFD calculation. The same measurement at a 2D plate concentrator is less reliable as it is difficult to establish a 2D flow in the circular open jet wind tunnel used for the measurements. The results are shown in Figure 94. The measurements are fit with (223) and (231), which gives u_s.
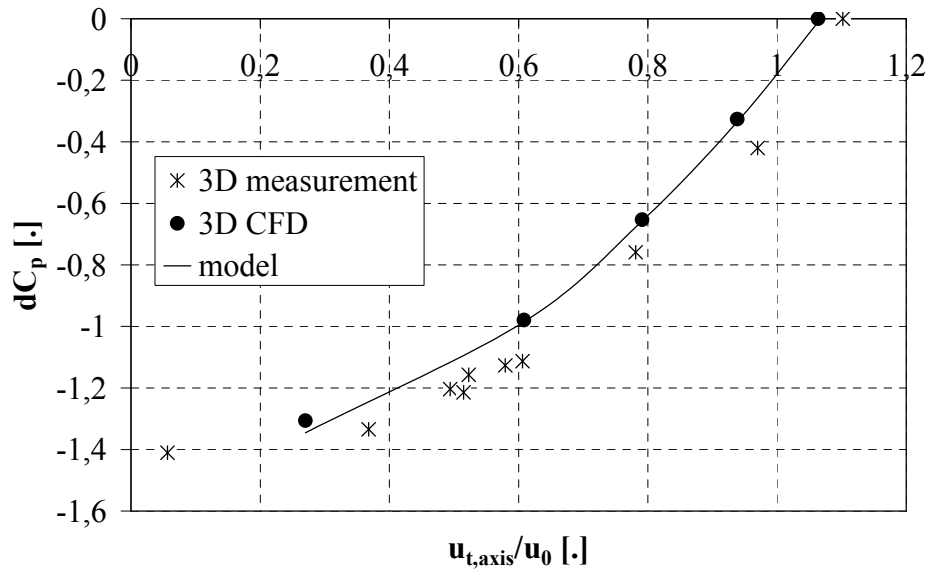
Figure 94 ΔC_p **across the actuator of a 3D plate concentrator as a function of** $u_{t,axis}/u_0$ **.**

The results show that the CFD calculation gives a too small pressure drop across the actuator. This is in agreement with the result plotted in Figure 91 where the calculated velocity profile around the axis of the actuator is slightly lower than the measured velocity. Fitting of ΔC_p from the CFD calculation with (223) and (231) gives

$$\frac{u_s}{u_0} = 1.2 \tag{232}$$

for a 3D plate concentrator. This is in agreement with the result in section 3.3.5, Table 8. Calculations of the flow velocity around a sharp edge in potential flow give an infinite high flow velocity at the edge. The finite u_s found in (232) is a result of viscous effects. In other words, the origin of u_s is the same for all sharp-edged bodies and consequently u_s should be roughly equal for all sharp-edged bodies.

The 2D configuration of the plate concentrator shows the following agreement between measurements and CFD calculation.
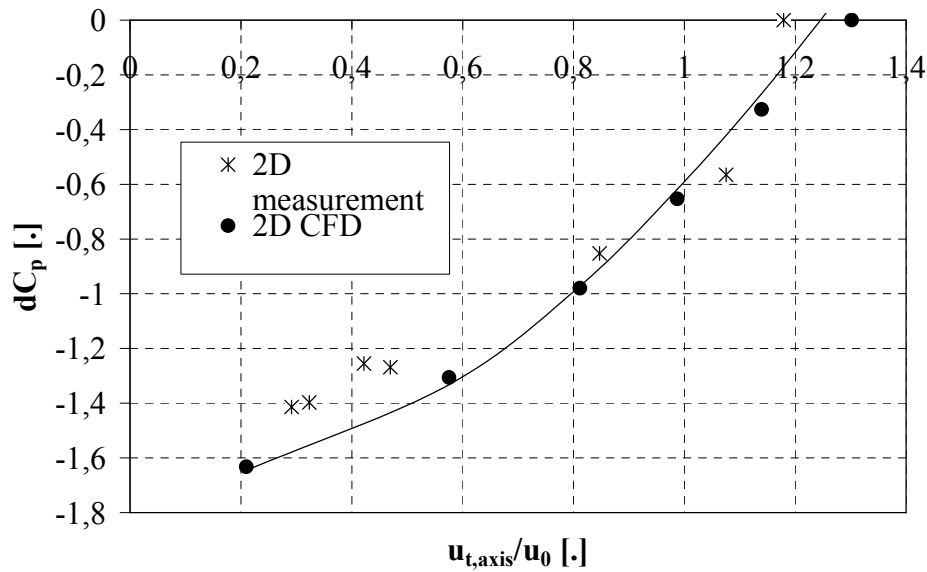
Figure 95 ΔC_p **across the actuator of a 2D plate concentrator as a function of** $u_{t,axis}/u_0$ **.**

Fitting of ΔC_p from the CFD calculation with (223) and (231) gives

$$\frac{u_s}{u_0} = 1.3 \tag{233}$$

for a 2D plate concentrator.

Figure 95 shows that the spreading in the measured ΔC_p at the 2D plate concentrator is higher than the spreading in the measured ΔC_p at the 3D plate concentrator shown in Figure 94. Furthermore, the CFD calculation gives a generally higher ΔC_p compared with the measurements. No conclusions are drawn from these observations as a real 2D flow is difficultly achieved in a circular open jet wind tunnel .

7.2.4   Verification of the power coefficient

The last verification concerns C_P as a function of a calculated from the measurements and CFD calculation. With u_s from (232) and (233), β from (231) and C_P from (225), the following results are calculated from the CFD calculations.
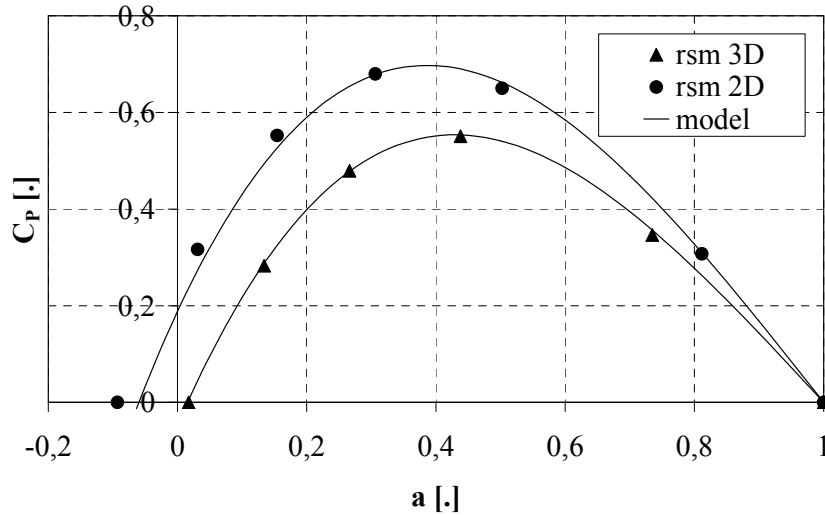
Figure 96 C_P **of the actuator in the plate concentrator calculated from CFD calculations and plate concentrator model with** $\overline{u_{t,x}} = (1-a)u_0$.

Figure 96 shows that C_P is accurately predicted by the plate concentrator model.

7.3 Approximated plate concentrator model

The verification of the jet contraction model in section 7.2.2 makes clear that $\beta \approx 0.8 = \text{constant}$ for $a < 0.8$. Furthermore, the accuracy of the plate concentrator model confirms that one may put $u_s = \text{constant}$. If $\beta \approx \text{constant}$ and $u_s = \text{constant}$, differentiation of C_P given by (225) with respect to $\overline{u_{t,x}}$ gives

$$\overline{u}_{t,x,opt} = \frac{\beta}{\sqrt{3}}u_s \tag{234}$$

Substitution of this in (225) gives

$$C_{P,\max} = \frac{2\beta}{3\sqrt{3}}\left(\frac{u_s}{u_o}\right)^3 \tag{235}$$

where u_s can be found with (232) or (233). As $C_{P,\max}$ is proportional to the third power of u_s, a change in u_s (see section 3.2.2, 3.3.5 and 3.3.6 for background on u_s) results in a large increase of $C_{P,\max}$. The set of equations (234), (235) and (232) or (233) will be referred to by "the approximated plate concentrator model".

According to the approximated plate concentrator model, a well-rounded duct inlet ($\beta = 1$) gives

$$C_{P,\max} \approx 0.85 \tag{236}$$

for a 2D plate concentrator and

$$C_{P,\max} \approx 0.67 \tag{237}$$

for a 3D plate concentrator.

It is interesting to compare the thrust force of a solid plate $F_{T,plate}$ with the sum of the thrust force of the ducted plate and actuator $F_{T,plate\ conc}$ at $C_{P,\max}$ of the actuator. Assume stagnation pressure at the total upwind area of the solid plate and the ducted plate. With (223) and (234) it then follows that

$$\frac{F_{T,plate\ conc}}{F_{T,plate}} = 1 - \frac{1}{3}\frac{A_t}{A_p} \tag{238}$$

where A_p denotes the projected area of the solid plate and A_t denotes the duct area. This shows that $F_{T,plate\ conc}$ at $C_{P,\max}$ is smaller than $F_{T,plate}$ of a solid plate, independent of β or u_s.

7.4 Discussion on the validity of the model

The results in section 7.2, justify the conclusion that the performance of the verified plate concentrator configuration is accurately modelled by the plate concentrator model.

With $\beta = 0.8$, the approximated plate concentrator model gives

Table 33 $\overline{u}_{t,x,opt}$ **and** $C_{P,\max}$ **according to the approximated plate concentrator model.**

Dimension	$\overline{u}_{t,x,opt}$	$C_{P,\max}$
2D	0.55	0.53
3D	0.60	0.68

Comparison with Figure 96 shows that the approximated plate concentrator model gives a good approximation for $\overline{u}_{t,x,opt}$ and $C_{P,\max}$ if $\beta = 0.8$.

Wieselsberger et al. [85] found by measurements that C_d of a ducted disk changes less than 9% if $A_t/A_p \leq 25\%$. The cavity model (81), used for the derivation of the plate concentrator model, shows that $u_s \propto \sqrt{C_d}$. We thus find less than 3% change in u_s for $A_t/A_p \leq 25\%$. With (232), the final conclusion reads that $u_s = 1.2 = \text{constant}$ is a good approximation if $A_t/A_p \leq 25\%$.

According to Hoerner [26], a plate has a Strouhal number of $S = 0.13$. With (43), the shedding frequency of the vortices at one side of a plate f reads $f = \dfrac{Su_0}{D} = 0.13\dfrac{u_0}{D}$. For normal building sizes D and moderate wind velocities u_0, it follows that $f < 1$. Hence, the static performance calculation of a wind turbine in a plate concentrator as shown in this chapter is normally allowed.

7.5 Yawed flow

Measurements of the thrust coefficient $C_{t,p}$ of a plate and disk in yawed flow with yaw angle φ show that $C_{t,p} \approx \text{constant}$ if $\varphi \leq \phi_{crit}$. In section 5.3.2, it is shown that $\varphi_{crit} = 35^{\circ}$ for a 3D

plate concentrator and $\varphi_{crit} = 50^{\circ}$ for a 2D plate concentrator with $A_r = 5$. Hence, Δp across a plate or disk in yaw is expected to be roughly constant for $-\varphi_{crit} \leq \varphi \leq \varphi_{crit}$. For φ well above φ_{crit}, $C_{t,p}$ and accordingly Δp decrease with increasing φ (see section 5.3.2).

Yaw also changes the flow phenomena at the inlet of the duct. As φ increases, the local crosswind velocities at the upwind side of the plate concentrator will increase too. This leads to local separation at the duct inlet and a decrease in β with increasing φ (Figure 97).
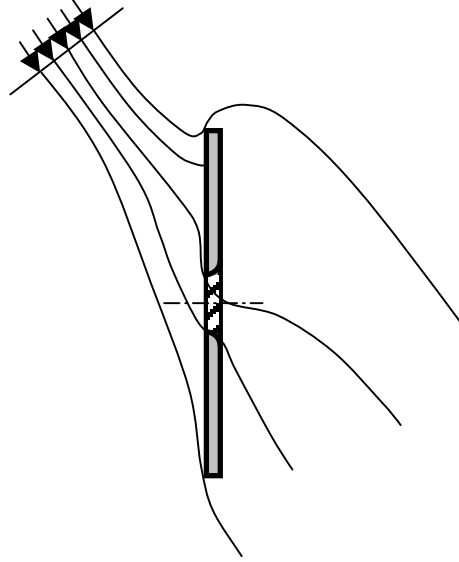
Figure 97 Plate concentrator in yawed flow with separation at the duct inlet.

The roughly constant Δp for $-\varphi_{crit} \leq \varphi \leq \varphi_{crit}$ in combination with a decreasing β at increasing φ result in a decrease in $C_{P,\max}$ at increasing φ. For φ well above φ_{crit}, where Δp as well as β decrease with increasing φ, the decrease of $C_{P,\max}$ with increasing φ will be higher. The power output at $\varphi = 90^{\circ}$ is zero as the pressure difference across the plate concentrator is zero at $\varphi = 90^{\circ}$.

7.6 *The energy yield of a plate concentrator*

This section discusses the power output of a wind turbine in a plate concentrator with well-rounded duct entrance in omnidirectional wind. Based on the knowledge shown in the previous sections, it is possible to give estimates of the power output at all flow angles. This allows a first order calculation of the energy yield of a wind turbine in a plate concentrator in omnidirectional wind.

$C_{P,\max}$ of a plate concentrator is highest for wind perpendicular to the plate surface and decreases with increasing yaw angle to the axis normal to the plate surface (section 7.5). There is no pressure difference across the duct for wind perpendicular to the duct axis. Hence, $C_{P,\max}$ at wind perpendicular to the duct axis is zero. $C_{P,\max}$ for a well-rounded duct entrance and wind perpendicular to the plate surface is found by (236) and (237). At $\varphi = 45^{\circ}$, it is assumed that the jet contraction $\beta \approx 0.7$, while Δp across the plate is equal to Δp at flow perpendicular to the plate surface. Hence, $C_{P,\max}$ at $\varphi = 45^{\circ}$ is 70% of $C_{P,\max}$ calculated by

(236) and (237). With the previous considerations, $C_{r,i}$ can be calculated by (62). The result is shown in Figure 98.
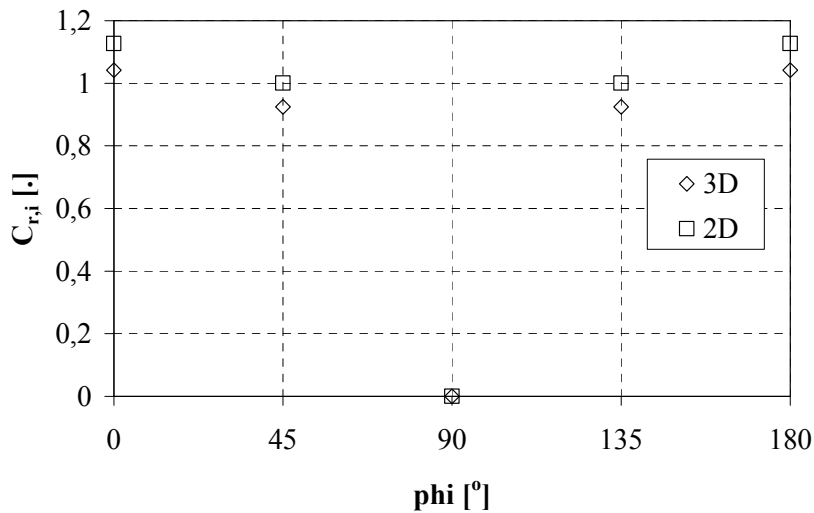
Figure 98 Assumed $C_{r,i}$ for a BAWT in a plate concentrator as a function of φ (phi).

In order to allow comparison of the energy yields of various BAWT's in section 8.2.2, it is assumed that $u_0 = 5.0$ m/s at $z_0 = 0.03$ and $u_0 = 3.3$ m/s at $z_0 = 1$ (section 3.1.1). With (60) and Figure 98, this gives the following energy yields.

Table 34 Energy yield of a 2.5 kW BAWT in a plate concentrator.

site	Energy yield $kWh/(m^2 year)$ 2D plate concentrator	Energy yield $kWh/(m^2 year)$ 3D plate concentrator
$u_0 = 5.0$ m/s at $z_0 = 0.03$ m	312	247
$u_0 = 3.3$ m/s at $z_0 = 1$ m	79	59

7.7 Energy yield of a combined plate concentrator

In the previous section it is shown that the concentrator effect of the plate concentrator is highest at flow parallel to the normal vector on the largest building façade ($\varphi = 0^o$, $\varphi = 180^o$). A flow direction parallel to the largest façade of the building reduces the power output of the actuator to zero ($\varphi = 90^o$, $\varphi = 270^o$). For omnidirectional wind, this significantly reduces the concentrator effect of the plate concentrator averaged over all φ. Two plate concentrators in a cross-configuration cause an additional concentrator effect at $\varphi = 90^o$ and $\varphi = 270^o$, which increases the concentrator effect averaged over all φ. The cross-configuration is shown at the left of Figure 99. The actuator in such configuration suffers from the wake of the plates at $\varphi = 0, 90^o, 180^o, 270^o$. An aerodynamic shape of the plates helps to prevent this[26]. Such

---

[26] The strong adverse pressure gradient towards the combined plate concentrator makes it difficult to completely prevent separation.

configuration is shown at the right of Figure 99. It will be referred to as the "combined plate
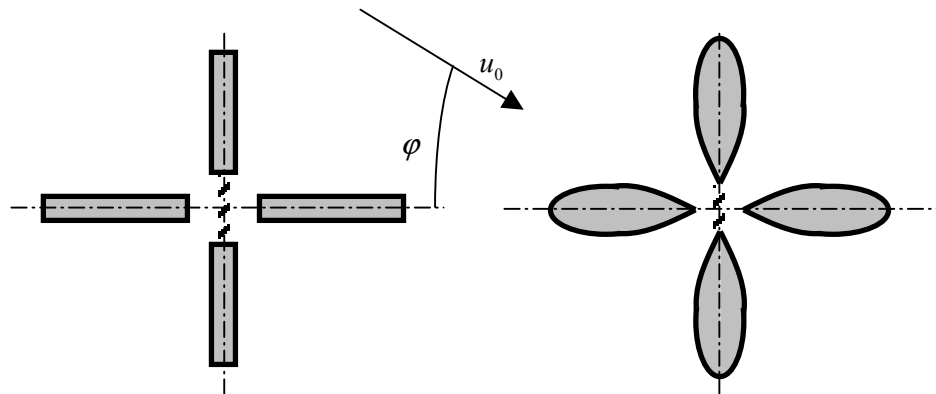
concentrator".

Figure 99 Top view of a combined plate concentrator.

For $\varphi = 0, 90^\circ, 180^\circ, 270^\circ$, the duct entrance has sharp edges so that the jet contraction β is equal to $\beta = 0.6$ of a ducted plate (section 7.1.2). For $\varphi = 45^\circ, 135^\circ, 225^\circ, 315^\circ$, the duct entrance can be characterized as well-rounded while the duct downwind of the actuator acts as a diffuser (see Figure 100).
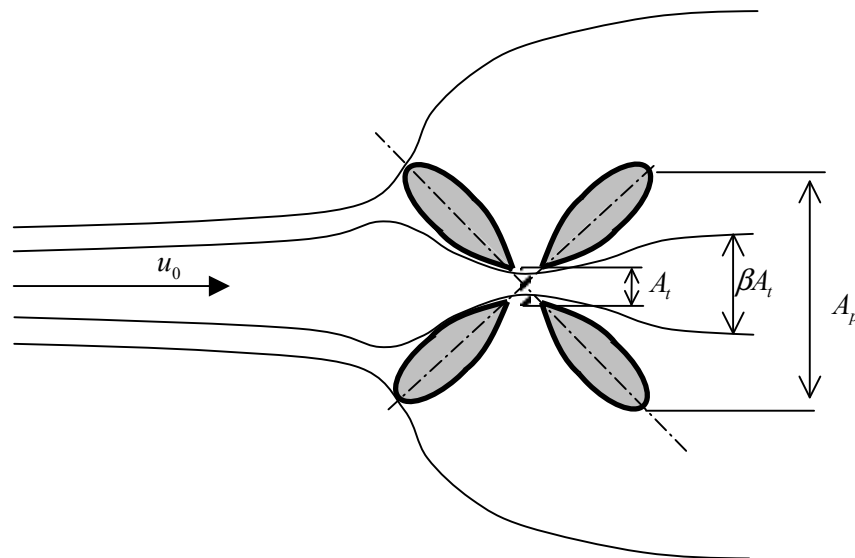
Figure 100 Top view of a combined plate concentrator in diffuser operation.

According to section 7.1.2, it is thus expected that $\beta > 1$ at $\varphi = 45^\circ, 135^\circ, 225^\circ, 315^\circ$. Diffusers have attached flow for diffuser cone angles up to approximately 20° (see Patterson et al. [24]). The geometry of the diffuser with boundary condition of separation at cone angle 20° leads to β. For this example calculation it will be assumed that $\beta = 1.2$ at $\varphi = 45^\circ, 135^\circ, 225^\circ, 315^\circ$. The flow conditions close to the separation points are similar to the conditions at the plate concentrator and it is assumed that $A_t / A_p \leq 25\%$ so that the flow through the duct does not influence the separation velocity u_s. Under such conditions, one may use the results obtained for the plate concentrator. u_s can be approximated by (232) and (233) and $C_{P,\max}$ is found by (235). Analogue to the plate concentrator, the difference in concentrator effect at small yaw angles to $\varphi = 0, 90^\circ, 180^\circ, 270^\circ$ and $\varphi = 45^\circ, 135^\circ, 225^\circ, 315^\circ$

is expected to increase with increasing yaw angle. With the previous considerations, $C_{r,i}$ can be calculated by (62). The result is shown in Figure 101.
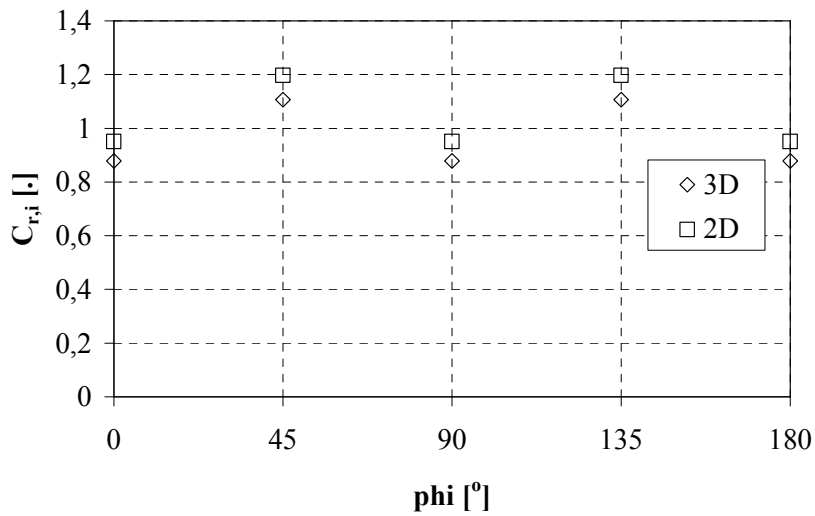
Figure 101 Assumed $C_{r,i}$ for a BAWT in a combined plate concentrator as a function of φ (phi).

With the same wind conditions as used for Table 34, (60) and Figure 101, give the following energy yields.

Table 35 Energy yield of a 2.5 kW BAWT in a combined plate concentrator.

site	Energy yield $kWh/\left(m^2 year\right)$ 2D plate concentrator	Energy yield $kWh/\left(m^2 year\right)$ 3D plate concentrator
$u_0 = 5.0$ m/s at $z_0 = 0.03$ m	461	369
$u_0 = 3.3$ m/s at $z_0 = 1$ m	122	92

8 Results and conclusions

The thesis is focussed on the aerodynamics of wind turbines close to buildings. Within that focus, the aerodynamics of the flow around buildings and the aerodynamics of the interaction of that flow with the wind turbine are analysed. The thesis makes clear that the performance of a Building-Augmented Wind Turbine (BAWT) at a particular location depends on many issues. Models that allow calculation of detailed information on these issues are presented in this thesis. But the results are also helpful in (research) areas other than wind energy in the built environment.

In the first section of this chapter, the applicability of the results in (research) areas other than wind energy in the built environment is discussed. The second section discusses the achievements of the thesis for wind energy in the built environment. Based on these achievements, the last section of this chapter discusses the future of wind energy in the built environment and research on the aerodynamics of wind energy in the built environment.

8.1 Summary of results for general use

Apart from the indispensable information on the analysis tools (chapter 4), the most useful information for this thesis is found in sources concerning:
- wind energy,
- wind engineering,
- meteorology,
- wind driven ventilation,
- aerospace engineering,
- exhaust stack design.

The overlap between these areas and the topic of the thesis is apparently appreciable. Hence, these areas are most likely to benefit from the achievements of the thesis. They therefore form the headings of the following paragraphs if there are possible benefits to mention.

Wind Energy
Sites of low roughness are preferred for wind turbines because of their high wind speeds and low turbulence level compared to sites with a high roughness. Most wind turbines are therefore found at sites with a low roughness. But the number of onshore low roughness sites for wind energy decreases because wind turbines already occupy an appreciable number of sites and because the population increases. For onshore siting in the future, it is consequently unavoidable to look for sites with a higher roughness. Examples of such sites are:
- industrial areas,
- sites close to works of infrastructure (bridges, dikes. etc),
- sites at sharp mountains or cliffs,
- sites in woods.

The considerations and models for high roughness sites in this thesis are mostly directly applicable to these sites.

Concerning fundamental research on wind energy, this thesis shows the value of using various modeling tools. Some results that are obtained with momentum theory could never be obtained with (simplified) vortex theory and visa versa. A dedicated use of the tools is necessary.

The following models on the aerodynamics of wind energy in the built environment are first[27] introduced in this thesis:

---

[27] Although sometimes partly based on existing models.

- the performance of a wind turbine in partly accelerated flow,
- the performance of an H-Darrieus in skewed flow,
- the vortex model for the performance of a shrouded wind turbine,
- the performance of a wind turbine in a plate concentrator.

Wind engineering/ Wind hindrance
A lot of the research in wind engineering or in the wind hindrance area deals with measurements or simulations of wind pressures around buildings. Such approach generates information on particular situations but it fails to explain the physics. It seems profitable to direct more effort on models to describe the physics of certain phenomena.

The focus of the thesis is directed on wind energy in the built environment but there are some models that may be interesting for wind engineering or wind hindrance colleagues. These models are:
- the vortex model for the shrouded wind turbine,
- the plate concentrator model,
- the probability distribution of the wind speed close to bodies,
- the height of the recirculation region on the flat roof of sharp-edged isolated buildings,

This thesis contains several models on the acceleration of the free stream wind speed by a building. This acceleration is coupled with the wind load of a building and the wind hindrance for pedestrians around the building. The models on the physics of the acceleration by buildings are therefore useful to avoid wind hindrance and predict the wind loads of a building. Moreover they allow calculation of the wind loads and wind hindrance during the design of the building. Such practice avoids the problems related to dealing with wind loads and wind hindrance in a later stage.

Meteorology
The roughness length of a particular site is mostly estimated by comparing a small number of reference pictures of sites with a known roughness with the site of interest. For the built environment, such reference pictures do not exist. Calculations of the roughness length from measurements of the velocity as a function of the height above cities show large -not yet understood- variations in the roughness length. It seems profitable to develop a model for the roughness length. This thesis introduces the standard deviation in the height of the buildings as a model parameter for the roughness length of cities. Future research is necessary for a verification of this idea.

Exhaust stack design/ Wind driven ventilation
The upwind edge or leading edge of a sharp-edged flat roof causes separation of the boundary layer. This causes a recirculation region at the roof that is enclosed by the separation trajectory. An exhaust below the separation trajectory causes the hazardous exhaust gases to be distributed to all building facades downwind of the leading edges. The exhaust gases are then sucked into the building by the ventilation intakes and cause a serious health hazard. The height of the separation trajectory above the roof thus fixes the minimum height of an exhaust stack at the roof.

This thesis discusses existing models and derives complementary models to calculate the height of the separation trajectory at the sides or roofs of sharp-edged 2D or 3D[28] buildings. It shows that the separation trajectory at the 2D buildings has a higher distance to the building so that the exhaust stacks at the roofs of 2D buildings need to be higher than at 3D buildings.

---

[28] The 3D model is not developed in this thesis but found in literature.

Wind driven ventilation uses the local pressure differences around a building to ventilate the building. It needs an outlet of the ventilation channel in a region with low pressures or high velocities, but the exhausted air should not be taken in again. Similar to the exhaust stack, the outlet of the ventilation channel should be located outside the recirculation region. The air intake should be located in a region with a high local pressure, at the stagnation point if possible. This thesis does also present information on the location of the stagnation point.

8.2 Summary of results for wind energy in the built environment

This section summarizes the achievements of the thesis concerning wind energy in the built environment. The achievements are also compared in this section and finally this section gives the conclusions that are drawn from this comparison.

8.2.1 Integration of wind turbine and building

The average wind speed in the built environment is low but on certain locations in the built environment close to buildings the wind speed can be appreciable. A wind turbine at such location profits from the acceleration of the free stream wind speed by the building. Such a wind turbine is called a Building-Augmented Wind Turbine (BAWT).

Aerodynamical integration
A BAWT experiences the acceleration of the free stream wind speed by the building and is therefore aerodynamically integrated with the building. The area around a building with an appreciable acceleration of the free stream wind speed is a fraction of the building area that causes the acceleration. Hence, the rotor area of the BAWT should be small compared to that area in order to profit from the acceleration.

Comparison of the acceleration factors at the along-wind-side of a cylinder, a 2D plate, a sphere and a disk shows that blunt 2D bodies cause the highest acceleration of the free stream wind speed. Hence, blunt 2D buildings are most promising for BAWT's.

Mechanical integration
The mechanical integration of wind turbine and building seems a logical consequence of the aerodynamical integration. Yet, it deserves much attention as it can lead to vibrations in the building. A wind turbine is a rotating device. Apart from the occurrence of aerodynamic vibrations that result from the interaction of the rotor blades with the wind, mechanical vibrations coupled with the unavoidable mass unbalance of the rotor will show up. Vibrations of the wind turbine can cause vibrations in the building if the wind turbine is mechanically coupled with the building. The vibrations of the wind turbine can hit the eigenfrequency of a building or part of a building. In that case, the connections of the wind turbine with the building should be damped. It seems wise to avoid mechanical coupling of wind turbine and building if possible. This is possible for the shrouded wind turbine and the wind turbine in the (combined) plate concentrator. Both configurations can exploit a wind turbine with a mast founded at the earth's surface.

8.2.2 Energy yield examples of Building-Augmented Wind Turbines

This section summarizes the starting points and energy yields of example BAWT's given at the end of the chapters 5, 6 and 7. The summary then allows an easy comparing all example BAWT's on the energy yields.

Reference data and starting point
All energy yield calculations in this section are found with a reference wind turbine with the following qualities.

Table 36 Data of the reference wind turbine.

$P_r =$	2.5 kW
$u_{ci} =$	4 m/s
$u_r =$	13 m/s
$u_{co} =$	20 m/s
$A_t =$	6 m^2
$\lambda =$	Variable
$C_P =$	0.3

The example energy yield calculations furthermore use the following starting point for the surrounding area of the BAWT's.

Table 37 Starting point example calculations.

$\rho =$	1.22 kg/m^3	
$u_p =$	4.5 m/s	
u_0 is omnidirectional and taken at	20 m	
z_0 of a city	$z_0 = 1$ m $\rightarrow$	$u_0 = 3.3$ m/s
z_0 of grassland	$z_0 = 0.03$ m $\rightarrow$	$u_0 = 5$ m/s

Energy yield bare wind turbine
The energy yield of the reference Wind Turbine (WT) in the free stream wind speed can then be found from the probability distribution (section 3.2.3) with $C_{r,i} = 1 \forall i$.

Table 38 Energy yield of a 2.5 kW bare WT.

site	Energy yield $kWh/(m^2 year)$
$z_0 = 0.03$ m	364
$z_0 = 1$ m	89

Comparison of the energy yields of the example BAWT's with the bare WT
The energy yields of the BAWT's, calculated in the chapters 5, 6 and 7 are summarized in Table 39. The table does also provide the Concentrator Ratio (CR), which is defined as the ratio of the energy yield of the BAWT divided by the energy yield of the bare wind turbine.

Table 39 Energy yields and Concentrator Ratios (CR's) of example BAWT's in omnidirectional wind at 20 m height with potential velocity $u_p = 4.5$ m/s.

z_0		Bare WT	Close to a building			Shrouded	Plate conc.	Comb. plate conc.
			Sharp-edged, roof centre	On top of a sphere	Beside a cylinder	2D	3D (2D)	3D (2D)
0.03 m	$\dfrac{kWh}{m^2 year}$	364	620	1032	617	360	247 (312)	369 (461)
	CR	1	1.7	2.8	1.7	1.0	0.7 (0.9)	1.0 (1.3)
1 m	$\dfrac{kWh}{m^2 year}$	89	174	353	268	95	59 (79)	92 (122)
	CR	1	2.0	4.0	3.0	1.1	0.7 (0.9)	1.0 (1.4)

Table 39 shows that the
- close-to-a-building configuration and the
- 2D combined plate concentrator configuration

have CR>1 while the
- shrouded and
- plate concentrator configuration

approximately have $CR \le 1$. CR is a result of two properties of the concentrators: the acceleration of the free stream wind speed and the direction sensitivity. At omnidirectional wind, it is the concentrator effect averaged over all flow angles that should be large to achieve a high energy yield. Apparently, the configurations with $CR \le 1$ are no net concentrators in omnidirectional wind!

According to Table 39, a bare WT in a rural area ($z_0 = 0.03$ m) has an energy yield of 364 $kWh/(m^2 year)$. This energy yield is mostly delivered to the grid. In contrast, a BAWT delivers its energy to the local grid in the building i.e. it delivers the energy behind the metre. The energy yield of the BAWT is thus felt as an energy saving of the building and accordingly reflected in energy savings on the customer's bill from the utility company. This is an approximately three times higher reimbursement compared to wind turbines in rural areas that deliver their energy to the grid. In order to have comparable or better economic prospects, the BAWT's thus need to generate more than $364/3 \approx 121 \, kWh/(m^2 year)$. According to Table 39, the BAWT's in the close-to-a-building configuration and the 2D combined plate concentrator have such energy yields. Hence, their economic prospects can be comparable with wind turbines in rural areas if their costs are comparable. This seems the case for the close-to-a-building BAWT where no extra effort has to be made for the siting of the wind turbine.

The close-to-a-building configuration shows the highest CR's. It is moreover the option that can be realized fast and is cheap, as the buildings exist. This configuration is therefore very attractive. Configurations with a high acceleration for few wind directions, like for instance with the cylinder configuration, are less attractive. Such configurations cause a low operational time of the BAWT.

8.2.3 Wind Turbines for the built environment

This section summarizes the qualities of a wind turbine needed to fit the built environment.

General

Compared to the lift-driven wind turbine, the drag-driven wind turbine has a high material usage in combination with low conversion efficiency of wind energy into mechanical power. This makes the drag-driven wind turbine too expensive for the generation of electricity.

Wind turbines for the built environment should be relative small in order to harvest the wind energy from frequently changing wind directions and profit from the small region near buildings where the wind speed is accelerated by the building. A Darrieus is preferable for such frequently changing wind directions, as it does not need a yaw mechanism.

A tip speed ratio $\lambda \approx 3$ seems to be a good guideline. A lower λ results in a rotor with high material usage and low energy yield. A higher λ results in an increased noise emission. As the noise emission is proportional to λ^5, the noise emission quickly increases with λ to unacceptable levels.

Close to a building

The flow on the roof of sharp-edged buildings is characterized by early separation on the upwind roof edge and accordingly skewed flow for the wind turbine above the roof. The H-Darrieus with low λ shows an increased power output in such skewed flow while the lift-driven HAWT has a decreased power output in skewed flow. Consequently, the H-Darrieus is not only favourable in the built environment in general but especially in the skewed flow above the roofs of sharp-edged buildings.

Wind turbines close to buildings are limited in size to approximately $10 \cdots 20\%$ of the characteristic building size. Such a wind turbine can optimally profit from the small region with concentrated wind energy around a building. Higher wind turbines use this concentrated wind energy less efficiently. For large wind turbines, only a fraction of the stream tube is within the accelerated wind speed. A wind turbine with only the wake in 1.2 times accelerated free stream wind speed produces approximately 90% of the power of a wind turbine with the whole stream tube within 1.2 times accelerated free stream wind speed.

Plate concentrator

This concentrator operates in two opposite wind directions. There are two possible rotors that can cope with this:
- a Darrieus rotor and
- a lift-driven HAWT
    - with variable pitch of the rotor blades of 180 degrees and a generator that is able to operate in opposite directions or
    - with a yaw mechanism of the rotor.

Except for the pitch mechanism, the HAWT is equal to the common wind turbine in rural areas. No large design changes are needed. Furthermore, the Darrieus has a slightly lower power coefficient than the lift-driven HAWT. The lift-driven HAWT is consequently favorable for use in the plate concentrator.

Combined plate concentrator

This concentrator operates in all wind directions. The possible rotors for this configuration are:
- the Darrieus or
- the lift-driven HAWT with yaw mechanism.

The contour of the H-Darrieus seems most favourable because it fits well in the duct of the combined plate concentrator. Yet, the plate concentrator can be designed with footbridges that

provide the right contour for a HAWT. The lift-driven HAWT has a slightly higher power coefficient than the H-Darrieus. The lift-driven HAWT rotor is therefore preferred for the combined plate concentrator.

The shrouded wind turbine
This concentrator operates in two opposite wind directions. There are two possible rotors for this BAWT:
- a Darrieus rotor and
- a lift-driven HAWT with variable pitch of the rotor blades of 180 degrees with a generator that is able to operate in opposite directions.

The airfoils around the rotor cause the highest velocities in their proximity. Unfortunately, the Darrieus is not able to harvest the energy in the area with the high wind speeds close to the airfoils as the Darrieus blades move parallel to the wind at that location. Consequently, the lift-driven HAWT is favourable for the shrouded wind turbine configuration.

8.3 Expectations

This section sketches the expectations for wind energy in the built environment and research on wind energy conversion in the built environment.

8.3.1 Expectations for wind energy in the built environment

BAWT's are located at sites where the decision to influence the landscape is already taken. In contrast to wind turbines in rural areas, the BAWT's cause consequently no extra impairment of the landscape. Care should be taken to avoid the possible hindrance of BAWT's (noise emission, induced vibrations, shadow flickering, etc.). These technical problems seem technical solvable. Overall, there seem to be enough forces in favour of the BAWT to ensure that they become one of the serious local renewable energy sources in the built environment.

The BAWT in the close-to-a-building configuration is the first BAWT that is utilized as the buildings exist and only the BAWT's need to be developed. The relative simple configuration and efficient use of the acceleration by the building gives rise to the expectation that this BAWT will be one of the most widespread.

The choice of a concentrator configuration for a BAWT depends on the direction probability of the wind speed. A BAWT in unidirectional wind (trade winds around the equator) is best suited by a unidirectional concentrator. In that case, all the material of the concentrator is used to concentrate the wind energy for a single wind direction. This is not possible with an omnidirectional concentrator in unidirectional wind.

A BAWT in omnidirectional wind requires an omnidirectional concentrator. This ensures an appreciable concentrator effect averaged over all wind directions with a small variation as a function of the wind direction, which enables the use of a relative small generator.

8.3.2 Research on aerodynamics of Building-Augmented Wind Turbines

This thesis gives the main issues and first order guidelines for wind energy conversion in the built environment. In other words, additional research is welcome on most topics. Some of the research topics fulfill a key role in many other issues and research topics. Those topics are summarized hereafter.

Behavior of an H-Darrieus in skewed flow
Verification of the model for the H-Darrieus in skewed flow with measurements is very complicated. This is partly caused by the fact that the model needs input from measurements that is likely to be inaccurate. Such input is for instance the C_d and C_l of the Darrieus blades

at low Re. The complication with measurements can be avoided by simulating the H-Darrieus with known C_d and C_l values that are also used as input in the model. This seems to be a first valuable research effort.

Accurately modeling of the behavior of an H-Darrieus in skewed flow is also very complicated. This is caused by the many complex phenomena that are responsible for the behavior of the H-Darrieus in skewed flow. A better understanding of these phenomena requires additional research on:
- C_T of an actuator at high a, large γ and small λ,
- measurements or simulations of H-Darrieus with various geometries,
- the interaction of the flows through the single- and double-rotor part of the H-Darrieus.

This is a tremendous research effort.

Roughness length

An accurate prediction of the wind speed is essential for the prediction of the energy yield of a wind turbine. But the wind speed is a function of z_0, which is not often accurately known. Without measurements of the velocity profile above an area, the estimation of z_0 is mostly done with reference pictures. Such an approach is sensitive for interpretation. There is even less known concerning z_0 for cities. The models for z_0 based on area occupation by roughness obstacles seem too simple to be able to model the many quantities that lead to z_0. Systematic measurements combined with a good description of the observed city roughness are necessary. With such measurements it is perhaps possible to verify some first order models for z_0.

Acceleration around buildings

In order to be able to calculate the energy yield of a wind turbine close to a building, it is necessary to know the acceleration of the free stream wind speed by the building for various buildings, z_0 and angles of the wind to the building. It is laborious to generate such information but important for accurate predictions of the energy yields of BAWT's.

9 References

[1]   Abbott, I.H., Von Doenhoff, A.E. Theory of wind sections, Dover Publications Inc., New York, 1959

[2]   Batchelor, G.K., An Introduction to Fluid Dynamics, Cambridge University Press, 1988

[3]   Baines, W.D., Effects of velocity distribution on wind loads and flow patterns on buildings, Procedures of Symposium No 16 on "Wind Effects on Buildings and Structures", held at the National Physical Laboratory, Teddington England, 1965, pp 198-225

[4]   Betz, A., Das Maximum der theoretisch möglichen ausnützung des Windes durch Windmotoren, Zeitschrift für das gesamte Turbinenwesen, Volume 26, 1920, p. 307.

[5]   Blackwell, B.F., Sheldahl, R.E., Feltz, L.V., Wind Tunnel Performance Data for Two-and Three-Bucket Savonius Rotors, Sandia report 76-0131, July 1977

[6]   Bottema, M., Wind Climate and Urban Geometry, Thesis, Eindhoven University of Technology, ISBN 90-386-0132-8, 1993

[7]   Buildings Energy Databook, www.btscoredatabook.net, November 2003

[8]   Burton, T., Sharpe, S., Jenkins, N., Bossanyi, E., Wind Energy Handbook, John Wiley & Sons Ltd, Chichester, 2001

[9]   Bussel, G.J.W., An Assessment of the performance of diffuser-augmented wind turbines, proceedings of the 3rd ASME/JSME Joint Fluids Engineering Conference, San Francisco, California, July 18-23, 1999

[10]   Campbell, N.S., Stankovic, S., Wind energy for the built environment, project web, In the framework of the Non-nuclear energy programme Joulle III, Contract JOR3-CT98-0270, September 2001

[11]   Chandler, H., (Editor), Wind Energy the Facts, an analysis of wind energy in the EU-25, EWEA, 2004

[12]   Ellis, B.R., CUR rapport, Dynamisch gedrag van hoge gebouwen, rapport 97-5, Oktober 1997

[13]   Energy Information Administration Office of Integrated Analysis and Forecasting, U.S. Department of Energy, report #DOE/EIA-0484(2003), www.eia.doe.gov/oiaf/ieo/download.html, November 2003, Washington, DC 20585, May 2003

[14]   ESDU, Strong winds in the atmospheric boundary layer, ESDU 82026, part 1: mean-hourly wind speeds, September 1982

[15]   Ewald, B.F.R., Wind Tunnel Wall Corrections, AGARDograph 336, RTO/ NATO, ISBN 92-836-1076-8, 1998

[16]   Fluent Inc., Fluent 5 users guide, manual July 26, 1998

[17]   Fokkema, E., Metingen aan een model gebouw in een grenslaag in de open straal blaaspijp, Stageverslag, 2002.

[18]   Fokkema, E., Vergelijk van tunnelmetingen aan een vlakke plaat concentrator, Afstudeerverslag, december 2002

[19]   Foreman, K.M., Gibert, B., Oman, R.A., Diffuser augmentation of wind turbines, Journal of Solar Energy, Vol. 20, 1978, pp 305-311.

[20]   Froude, R.E., On the part played in propulsion by differences of fluid pressure, Transactions of the Institute of Naval Architects, Volume 30, 1889, p 390

[21]   Garratt, J.R., The internal boundary layer, a review, Boundary layer Meteorology, 50, 1990, pp 171-203

[22]   Glauert, K.H., The Lancester-Betz limit, Journal of Energy, Volume 3, No 6, 1935

[23]   Hansen, M.O., Effect of placing a diffuser around a wind turbine, Journal of Wind Energy, 3, DOI: 10.1002/we.37, 2000, pp 207-213

[24]   Hau, E., et al., The next generation of large wind turbines, summary of the final report, Munich, ETAPlan, May 1991

[25]   Holten, van Th., Performance analysis of a windmill with increased power output because of tip vane induced diffusion of the air stream, Memorandum M-224, Delft University of technology, November 1974

[26]   Hoerner, S.F., Fluid dynamic drag, L.A. Hoerner, 1985 Hoerner

[27]   Hoerner, S.F., Fluid dynamic lift, L.A. Hoerner, 1975

[28]   Hussain, M., A study of the wind forces on low rise buildings and their application to natural ventilation methods, PhD Thesis, Dept. of Build. Sc. Univ. of Sheffield, 1978

[29]   Igra, O., Shrouds for aerogenerator, 14th AIAA aerospace sciences meeting, AIAA paper no. 76-181. January 26-28, 1976

[30]   Jacobs, E.N., Sherman, A., Airfoil section characteristics as affected by variations of the Re number, NACA report No. 586, 1937

[31]   Jacobs, E.N., Airfoils with $A_r = 6$ in NACA variable density tunnel, 78 related test sections, technical report 460, 1933

[32]   Jensen, M., The model law for phenomena in natural wind, Ingenioeren 2, 1958

[33]   Katz J., Plotkin, A., Low-speed aerodynamics, from wind theory to panel methods, McGraw-Hill, Inc, International edition, 1991

[34]   Kelvin, L., Mathematical and Physicl Papers 4, Transcriptions of the Royal Society of Edinburgh, No. 25, 1869

[35]   Kim, S.E., Boysan, F., Application of CFD to environmental flows, Journal of Wind Engineering and Industrial Aerodynamics, No. 81, 1999, pp 145-158

[36]   Küchemann, D., Weber, J., Aerodynamics of propulsion, McGraw-Hill book company, 1953

[37]   Lancester, F.W., A contribution to the theory of propulsion and the screw propeller, Transactions of the Institution of Naval Architects, Volume 145, 1915, p. 287

[38]   Leishman, J.G., Principles of Helicopter Aerodynamics, Cambridge University Press, 2000

[39]   Madsen, H.A., Sorensen, N.N., Schreck, S., Yaw aerodynamics analysed with three codes in comparison with experiment, ASME Wind Energy Symposium, contribution nr. AIAA-2003-0519, 2003.

[40]   Melet, E., Duurzame Architectuur, streven naar een contrastrijke omgeving, NAi Uitgevers, Rotterdam, 1999

[41]   Milne-Thomson, L.M., Theoretical aerodynamics, Dover publications, Inc., New York, 1958

[42]   Mertens, S., Wind energy in urban areas, concentrator effects for wind turbines close to buildings, Refocus, March/ April 2002

[43]   Mertens, S., Power coefficient prediction of a wind turbine integrated in a building, The world wind energy conference and exhibition, Berlin, July 2002

[44]   Mertens, S., Turby, University of Technology Delft, DUWIND report 009, 2002

[45]   Mertens, S., Wind description for roof location of wind turbines, Global Conference and exhibition on Wind Energy, Paris, 2002

[46]   Mertens, S., Haal windenergie uit je gebouw, Gezond Bouwen en Wonen, Nr. 3, November 2003

[47]   Mertens, S., Kuik, G. van, Bussel, G. van, Performance of an H-Darrieus in skewed flow on a roof, special Wind Energy issue of the Journal of Solar Energy and Engineering, DOI 10.1115/1.1629309, November 2003

[48]   Mertens, S., Kuik, G. van, Bussel, G. van, Performance of a High Tip Speed Ratio H-Darrieus in the skewed flow on a roof, ASME Wind Energy Symposium Proceedings at the 41st AIAA Aerospace Sciences Meeting and Exhibit, Reno, NV, 6-9 January 2003

[49]   Mertens, S., The energy yield of roof mounted wind turbines, Journal of Wind Engineering, volume 27, No. 6, 2003, pp 507-517

[50]   Murakami, S., Current status and future trends in computational wind engineering, Journal of Wind Engineering and Industrial Aerodynamics, 67 & 68, 1997, pp 3-34

[51]   Nieuwstadt, F.T.M., Turbulentie, Epsilon uitgaven, Utrecht, 1992

[52]   Panofsky, H.A., Dutton, J.A., Atmospheric turbulence, John Wiley & Sons, Ltd, New York, 1984

[53]   Paraschivoiu, I., Wind Turbine Design, With Emphasis on Darrieus Concept, Ecole Polytechnique de Montreal, 2002

[54]   Patterson, G.N., Gibson, A.H., Diffuser behaviour, a review of past experimental work, relevant today, Journal of Aircraft Engineering, April 1974

[55]   Peterka, J.A., Cermak, J.E., Wind Engineering study of one Williams center, Tulsa. Technical report CER72-75 J AP-JEC25, Fluid Dynamics Diffusion laboratory, Collorado State University, Fort Collins, pp 188, 1974

[56]   Phillips, D.G., Flay, R.G.J., Nash, T.A., Aerodynamic analysis and monitoring of the Vortec 7 diffuser-augmented wind turbine, IPENZ Transactions, Vol. 26, No. 1, 1999

[57]   Phillips, D.G., Nash T.A., Oakey A., Flay R.G.J., Richards P.J., Computational Fluid Dynamic and Wind Tunnel Modelling of a Diffuser-augmented Wind Turbine, Journal of Wind Engineering, Volume 23, No. 1, 1999

[58]   Plomp, H., Video of a wind tunnel study concerning the behavior of a model wind turbine in the built environment, 2006

[59]   Prandtl, L., Tietjens, O.G. Applied Hydro- & Aeromechanics, Dover Publications Inc., New York, 1935

[60]   Prandtl, L., Tietjens, O.G. Fundamentals of Hydro- & Aeromechanics, Dover Publications Inc., New York, 1934

[61]   Saffman, P.G., Vortex dynamics, Cambridge Monographs on Mechanics and Applied Mathematics, Cambridge University Press, 1992

[62]   Sardo, J.A., Theory and measurements on H-Darrieus turbines in skewed flow, Master project at the Delft University of technology, report WE-03193, Delft, The Netherlands, August 2003

[63]   Schlichting, H., Boundary layer theory, Mc Graw-Hill, New York and London, Seventh edition, 1979, pp 817

[64]   Seto, L.Y., Galbraith, R.A., The effect of pitch rate on the dynamic stall of a NACA 23012 aerofoil, Eleventh European Rotorcraft Forum, paper no. 34, 1985

[65]   Sharan, V.K., On the characteristics of flow around building model with view to simulating the minimum fraction of the natural boundary layer, International journal of mechanical sciences, 17, issue 9, September 1975, pp 557-563

[66]   Sheldahl, R.E., Klimas, P.C., Aerodynamic Characteristics of Seven Symmetrical Airfoil Sections through 180-Degree Angle of Attack for Use in Aerodynamic Analysis of Vertical Axis Wind Turbines, Sandia National Laboratories Technical Report, SAND80-2114, March 1981.

[67]   Simiu, S., Scanlan, R.H., Wind effects on structures, John Wiley & Sons, New York, 1996

[68]   Taylor, J.R., An Introduction to Error Analyses, University Science Thesis, Mill Valley, 1982

[69]   Tennekes, H., Lumley, J.L., A first course in turbulence, MIT Press, 1972

[70]   Thoma, D., Grundsätsliches zur einfachen Strahltheorie der Schraube, Zeitschrift für Flugtechniek und Motorluftschiffahrt, 1925

[71]   Throen I., Petersen, E.L., European Wind Atlas, RISO National Laboratory, ISBN 87-550-1482-8, 1989

[72]   Toet, S., Vermeer, N., Modificaties blaaspijp Instituut voor Windenergie en beschrijving huidige situatie, report IW-91049M, September 1991

[73]   Verkerk, G., et al., Binas informatie boek, Wolters Noordhoff Groningen, derde druk, 1992

[74]   Vermeer, N.J., Wind tunnel experiments on a rotor model in yaw, Proceedings of the 12th symposium on the aerodynamics of wind turbines in Lyngby Denmark on December 3-4 1998, Technical University of Denmark ISSN 0590-8809, 1998, pp. 11-20.

[75]   Vries, E. Conversation with Eize de Vries and visit to a small wind turbine on the roof of a mid-rise building that suffers from frequent yawing, April 2006

[76]   Vries, O., Fluid Dynamic aspects of Wind Energy Conversion, Agard-AG-243, 1979

[77]   VROM, ministry of, Research of the European Union, www.vrom.nl/international/, www.vrom.nl/milieuhandboek, November 2003

[78]   Ward-Smith, A.J., Internal Fluid Flow, The fluid dynamics of flow in pipes and ducts, Clarendon press, Oxford, 1980

[79]   Wieringa J. & Rijkoort, P.J., Windklimaat van Nederland, Staatsuitgeverij 's-Gravenhage, 1983

[80]   Wieringa, J., Estimation of meso-scale and local-scale roughness for atmospheric transport modelling, Proceedings NATO/ CCMS conference Amsterdam 1980, 1981

[81]   Wieselsberger, C., Betz, A., Prantl, L., Ergebnisse der Aerodynamischen Versuchsanstalt zu Göttingen, II Lieferung, druck und verlag von R. Oldenburg, München und Berlin, 1923.

[82]   Wilcox, D.C., Turbulence modelling for CFD, DCW Industries, 1993

[83]   Wilson, D.J., Flow patterns over flat-roofed buildings and application to exhaust stack design, ASHRAE Transactions, vol. 28, nr2., 1979, pp 284-294

[84]   Wilson, R.E., Lissaman, P.B.S., Applied aerodynamics of wind power machines, Oregon State University, May 1974

[85]   Wit, de, M.H., Wind in de gebouwde omgeving, Technische Universiteit Eindhoven, Faculteit Bouwkunde, Capaciteitsgroep FAGO, Najaar 2001.

[86]   Wood, D.H., Internal boundary layer growth following a step change in surface roughness, Boundary-Layer Meteorology, No. 22, 1982, pp 241-244

[87]   www.envirotruth.org/myth8a.cfm, November 2003

[88]   www.peakoil.org, November 2003

[89]   Turby, www.turby.nl, November 2003

[90]   Windwall, www.windwall.nl, November 2003

[91]   Ytsma, S., Comparison of the predictions from two theoretical models with wind tunnel measurements on a flat plate concentrator, internship report Delft University of Technology WE-0319, July/ August 2003

Additional information on the photos

Figure 1   AES wind turbine, www.aes-energie.de, November 2004. This photo shows the AES near the A5 close to Apeldoorn, The Netherlands
Figure 2   Tulipo, www.tulipower.nl, November 2003
Figure 3   Windside, www.northwest.com, November 2003
Figure 4   AES and Turby (www.turby.nl), November 2003
Figure 7   VAWT of utility ENECO called Globuan

Appendices

Appendix A Stream tube length in viscous flow

The performance of a wind turbine is simulated in a CFD calculation by a fan with a pressure drop across its area. The fan models an actuator. The pressure drop at maximum energy extraction by an actuator is calculated from the Lancester-Betz limit in section 2.1. This pressure drop is used to simulate the optimal performance of the modelled wind turbine.

The areas of the stream tube A_f (the dotted area with diameter D_t) at a distance to the fan l_f are found from the CFD results. These areas are calculated at the downwind and upwind side of the fan. It is assumed that the energy extraction takes place between the areas A_0 and A_e where the streamlines at the boundary of the simulated flow through the actuator disk are parallel.
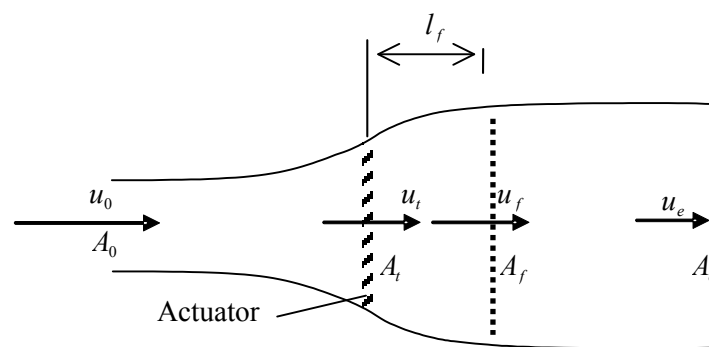
Figure 102 Actuator in parallel flow.

The CFD calculation gives the values of A_f/A_0 and A_f/A_e as a function of $\left|l_f\right|/D_t$ that are shown in Figure 103.

Figure 103 Areas A_f/A_0 and A_f/A_e as a function of l_f/D_t calculated with CFD.

From the figure, it can be deduced that in viscous flow, the energy is extracted in a stream tube with length $l_f \approx (2.5 + 3.5)D_t = 6D_t$: a finite length. While in inviscid flow, the stream tube length goes to infinity (same figure).

Appendix B Measurements plate concentrator

The measurements on the plate concentrator are described in Ytsma [91]. For convenience, the measured configurations are summarized here.

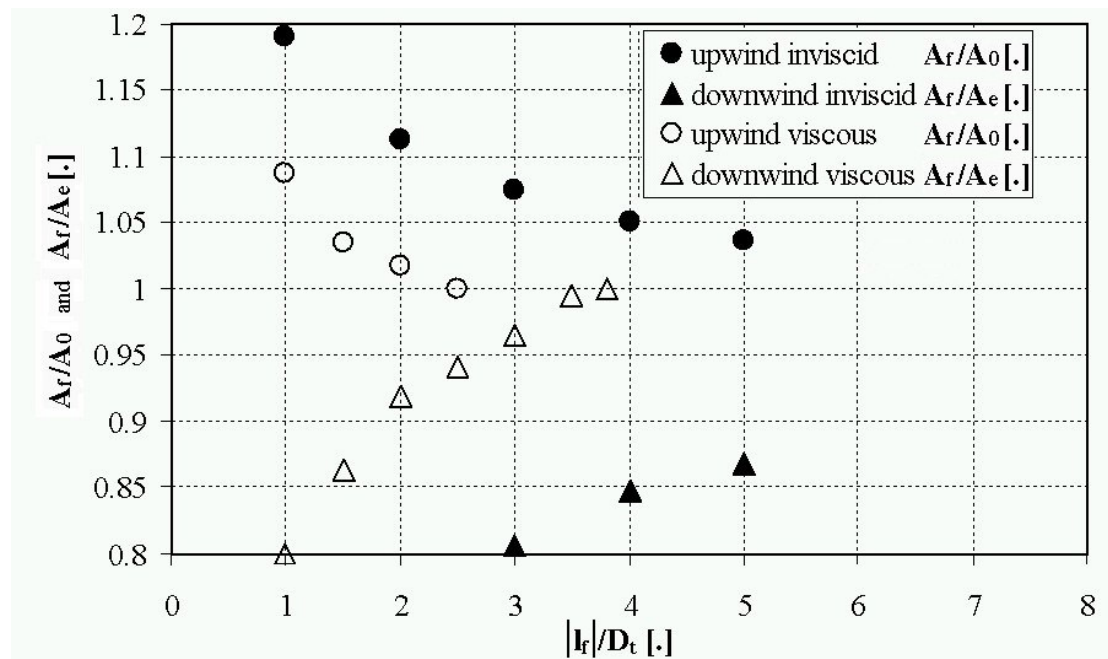A 2D and 3D configuration of the plate concentrator is tested in the open jet wind tunnel of Delft University of Technology (section 4.2.1). In order to minimize the error in the measurements (section 4.2.3), the tests were carried out at the highest possible wind speed of the tunnel: 14 m/s. The sizes of the plate concentrators are summarized in the table below.

	Diameter plate/ width plate[m]	Diameter duct/ width slot [m]	Rounding radius duct/ slot [m]
2D plate	0.2	0.037	0.02
3D plate	0.5	0.09	0.02

Sizes and tunnel velocity ensured a Re number well above the values where the drag coefficient of plates changes because of changes of the vortex pattern in the wake ($Re \approx 2000$, see Hoerner [26]).

During the measurements, the width of the 2D plate concentrator was decreased in order to avoid 3D effects and tunnel blockage. It was observed that the 2D plate splits the open jet into two jets for the higher size (width 0.5 m). The decrease in width of the 2D plate resulted in a higher relative rounding radius for the 2D plate ($0.02/0.037 \approx 0.54$) compared to the 3D plate ($0.02/0.09 \approx 0.22$).

The 2D flow was provided by two large end plates at the outer region of the jet of the tunnel.

The measurement of the pressure drop across the screens was carried out with a total pressure rake connected to a HyScan2000 unit. Each tube of the rake was connected to two pressure sensors in order tom minimize the measurement error. The rake that existed of 13 tubes with 0.01 m separation between them measured the static pressure 0.005 m downwind the screen. Different screens in the slot or duct were used to simulate the different operating states of the wind turbine.

The velocities through the screens were measured with a traverse with a hotwire approximately 0.02 m downwind of the screens. The resolution of the steps of the traverse was 0.002 m.

Appendix C Used turbulence models CFD calculations

All calculations are carried out in the steady state with a first order upwind scheme except if stated otherwise.

Topic	Non uniform Grid	Turbulence Model	Wall function	Domain (x,y,z) or (x,r) in terms of the characteristic size	Performed as
Actuator of Appendix A	Str. Quadral.	k-e realizable	Stand. wall funct.	(-40~80,0~40, /)	Axi-symm.
Plate concentrator in chapter 7	Str. Quadral.	RSM, Wall bound. Cond. from k equation, wall refl. effects	Stand. wall funct.	(-20~20,0~30, /) and (-20~20,-30~30, /)	Axi-symm. and 2D conf.
Separation in section 3.3.2	Unstr. Tetrah.	RSM, Wall bound. Cond. from k equation	Non-equil. wall funct.	(-10~10,0~30, /) and (-7~20,0~10,-10~10)	2D and 3D conf.
Flat plate in section 4.3.5	Str. Quadral.	k-e realizable and RSM, Wall bound. Cond. from k equation and quadratic press. Coupl.	Stand. wall funct.	(-40~40,0~40, /) and (-40~40,-40~40, /)	Axi-symm. (steady) and 2D (unsteady) conf.
Boundary layer in section 4.3.5	Str. Quadral.	k-e realizable and RSM, Wall bound. Cond. from k equation and quadratic press. Coupl., wall reflection effects	Stand. wall funct.	(0~8,0~1, /)	2D
NACA 0018 in section 4.3.5	Str. Quadral.	k-e realizable	Stand. wall funct.	(-16~16,0~25, /)	2D

Appendix D Data high-lift cambered airfoil Da2-1999

A high-lift airfoil for special purposes designed at Delft University, section wind energy is given below. The contour of the airfoil is depicted in Figure 104.
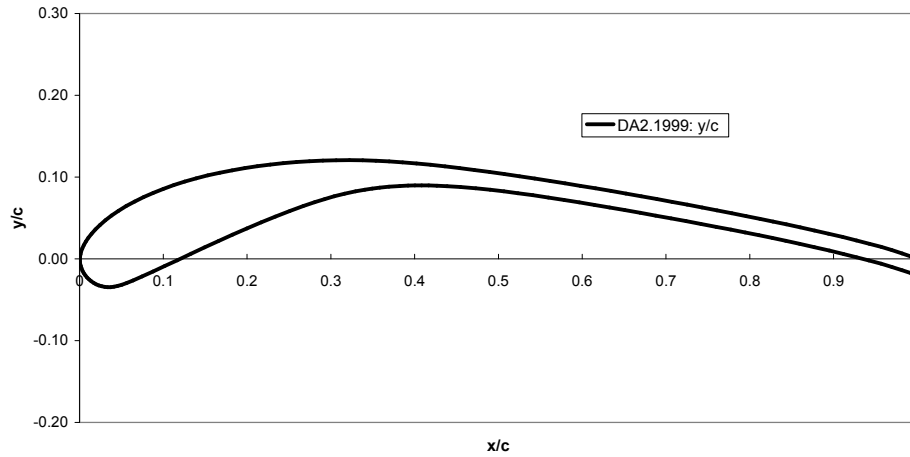

Figure 104 Da2-1999 high-lift cambered airfoil.

The lift curve of this airfoil is calculated with r-foil. The results are given in Figure 105.
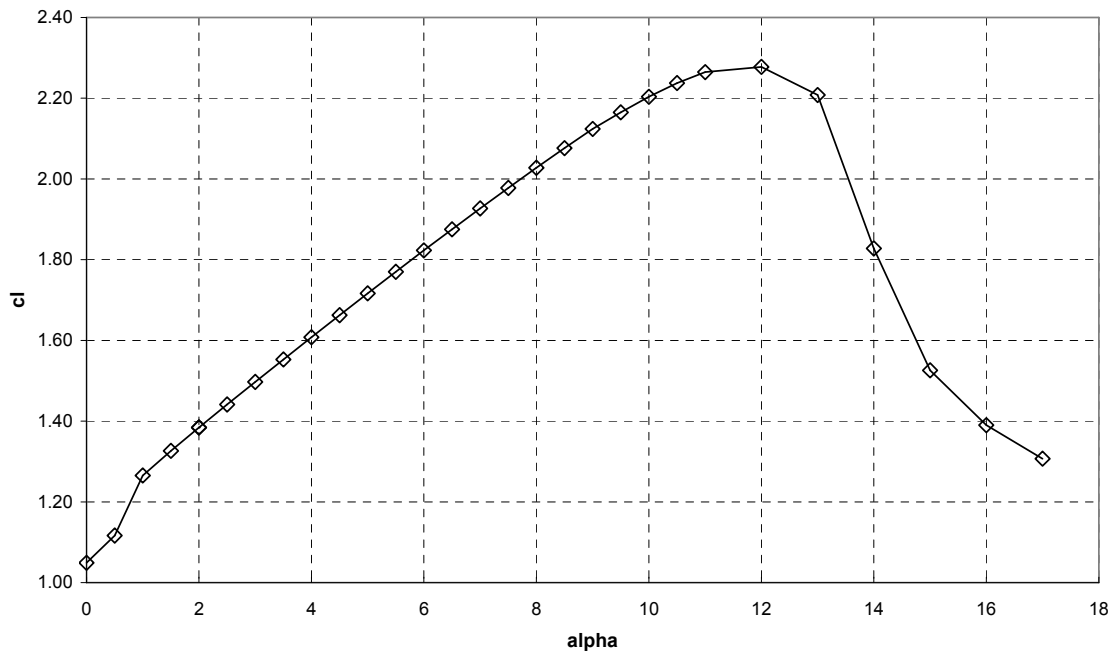

Figure 105 Lift curve of the Da2-1999 high-lift cambered airfoil.

According to Katz & Plotkin [33] the lift coefficient of a thin cambered airfoil in potential flow can be found with

$$C_l = 2\pi \frac{\sin(\alpha + \beta)}{\cos \beta} \tag{239}$$

Equating this lift coefficient with the r-foil data at $\alpha = 10^o$ gives the camber angle as $\beta \approx 11^o$.

Appendix E Induced velocities by a wake

With Biot-Savart, it can be shown that an infinite long straight vortex sheet induces a uniform velocity with opposite sign on both sides of a vortex sheet (see for instance Milne-Thomson [41]). Suppose we have the following 2D configuration.
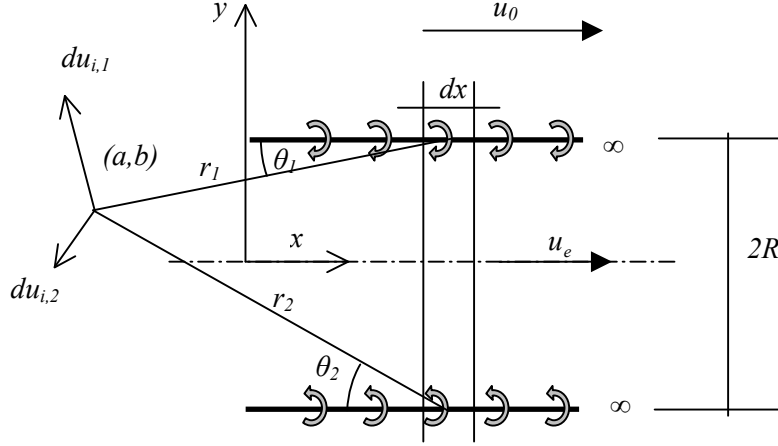

Figure 106 Configuration of induced velocities by a wake

The velocity u_e at $x \rightarrow \infty$ can thus be considered as uniform. The vortex strength per metre vortex sheet is denoted by γ. The induced velocities at coordinate (a,b) can be found with Biot-Savart (see for instance Batchelor [2])

$$du_{i,1} = \frac{\gamma dx}{2\pi r_1}$$

$$du_{i,2} = \frac{\gamma dx}{2\pi r_2}$$

(240)

This results in the following induced velocities in x- and y-direction at (a,b)

$$du_{i,x} = \frac{\gamma dx}{2\pi r_1} \sin\theta_1 + \frac{\gamma dx}{2\pi r_2} \sin\theta_2$$

(241)

and

$$du_{i,y} = \frac{\gamma dx}{2\pi r_1} \cos\theta_1 - \frac{\gamma dx}{2\pi r_2} \cos\theta_2$$

(242)

Integration across the total length of the vortex sheets gives the total induced velocity at coordinate (a,b) as

$$u_{i,x} = \frac{\gamma}{2\pi} \lim_{l \rightarrow \infty} \int_0^l \frac{R-b}{(x-a)^2 + (R-b)^2} + \frac{R+b}{(x-a)^2 + (R+b)^2} \, dx$$

(243)

and

$$u_{i,y} = \frac{\gamma}{2\pi} \lim_{l \to \infty} \int_0^l \frac{x-a}{(x-a)^2 + (R-b)^2} - \frac{x-a}{(x-a)^2 + (R+b)^2} \, dx \tag{244}$$

Solving the integral gives

$$u_{i,x} = \frac{\gamma}{2\pi} \lim_{l \to \infty} \left[\arctan\left(\frac{x-a}{R-b}\right) + \arctan\left(\frac{x-a}{R+b}\right) \right]_{x=0}^{x=l}$$

$$= \frac{\gamma}{2\pi} \lim_{l \to \infty} \left[\arctan\left(\frac{l-a}{R-b}\right) + \arctan\left(\frac{l-a}{R+b}\right) - \arctan\left(\frac{-a}{R-b}\right) - \arctan\left(\frac{-a}{R+b}\right) \right] \tag{245}$$

and

$$u_{i,y} = \frac{\gamma}{4\pi} \lim_{l \to \infty} \left[-\ln\left|(x-a)^2 + (R-b)^2\right| - \ln\left|(x-a)^2 + (R+b)^2\right| \right]_{x=0}^{x=l}$$

$$= \frac{\gamma}{4\pi} \lim_{l \to \infty} \left[\ln\left|\frac{(l-a)^2 + (R-b)^2}{(l-a)^2 + (R+b)^2}\right| - \ln\left|\frac{a^2 + (R-b)^2}{a^2 + (R+b)^2}\right| \right] \tag{246}$$

Evaluating the limit results in

$$u_{i,x} = \frac{\gamma}{2\pi} \left[\pi - \arctan\left(\frac{-a}{R-b}\right) - \arctan\left(\frac{-a}{R+b}\right) \right] \tag{247}$$

and

$$u_{i,y} = -\frac{\gamma}{4\pi} \ln\left|\frac{a^2 + (R+b)^2}{a^2 + (R-b)^2}\right| \tag{248}$$

Appendix F Prony brake
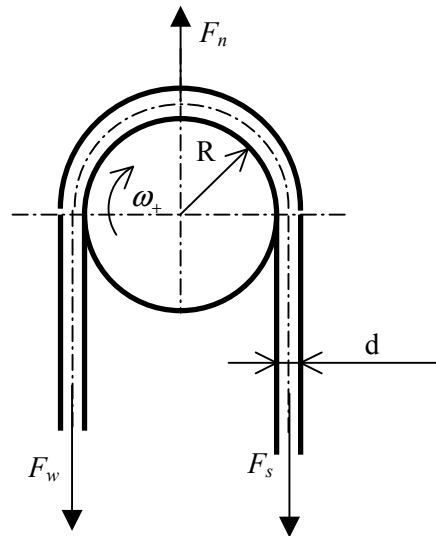
Figure 107 Prony brake.

The normal force F_n on the surface of the wheel is equal to the downward force of the pulley.

$$F_n = F_w + F_s \qquad (249)$$

The friction force of the pulley on the wheel is related with this normal force on the wheel as

$$F_f = \mu\, F_n \qquad (250)$$

where $\mu > 0$ is the friction coefficient of the pulley on the wheel. This friction coefficient depends on the material properties of the wheel and the pulley and the temperature of both.

The power absorbed $P(\omega_+)$ by the wheel can be found from

$$P = F_f R \omega_+ \qquad (251)$$

Substitution of (95) and (249)-(251) in the equation for the absorbed power results in

$$P(\omega_+) = \xi_+ F_w R \omega_+ \qquad (252)$$

with augmentation/ amplification factor ξ_+ given by

$$\xi_+ = \frac{2\mu}{1 + \dfrac{\mu R}{R + \frac{1}{2} d}} \qquad (253)$$

If the opposite rotational direction of the wheel ω_- is used we have

$$P(\omega_-) = \xi_- F_w R \omega_- \qquad (254)$$

with augmentation/ amplification factor ξ_- given by

$$\xi_- = \frac{2\mu}{1 - \dfrac{\mu R}{R + \frac{1}{2}d}} \qquad (255)$$

The augmentation factor for both configurations with opposite rotational direction is plotted in Figure 108 for $d \ll R$.
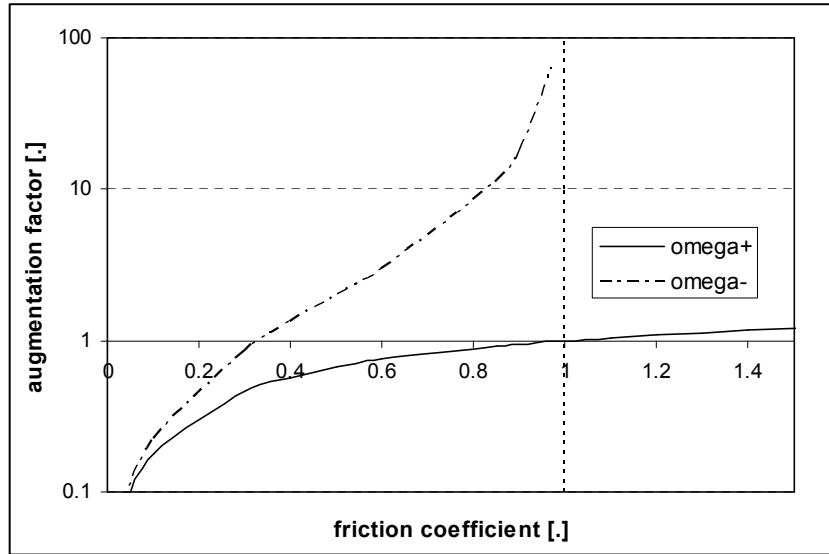
Figure 108 Augmentation factor of the Prony brake for opposite rotational directions.

According to Figure 108 there is a totally different behaviour of the power absorbed in both configurations for a small change in friction coefficient μ. For friction coefficients around 1, we find that $\xi_- \to \infty$ while $\xi_+ \to 1$ and accordingly a change in μ results in a much higher change in the power absorbed by the Prony brake for the ω_- rotational direction. Consequently, the ω_- rotational direction is not suitable for measurements and we can only use the ω_+ rotational direction as depicted in Figure 107.

Appendix G Triangular chord-wise vortex distribution

This appendix gives the derivations of some equations for the vortex model that are not directly important for understanding of the vortex model. Two approximations are used to avoid results that are too complex too use in the vortex model. It is assumed that:

- the airfoils have a triangular chord-wise vortex distribution and
- in calculations of the airfoil geometry, the angle of attack of the airfoils $\alpha \ll 1$.

A triangular chord-wise vortex distribution approximates the vortex distribution at an airfoil found with potential theory (see for instance Katz & Plotkin [33]). It avoids the singularity at the leading edge of the airfoil. The assumption $\alpha \ll 1$ avoids the lengthy equations that result by taking α into account.

Triangular chord-wise distribution

The triangular chord-wise vortex distribution $\gamma(x)$ reads

$$\gamma(x) = \frac{\Gamma_0}{c}\left(1 - \frac{x}{c}\right) \tag{256}$$

for $\{x \in \mathbb{R} \mid 0 \le x \le c\}$ where $\gamma(x = 0) = \Gamma_0 / c$ is the strength of the bound vortex at the leading edge of the airfoil with chord length c as depicted in Figure 109.
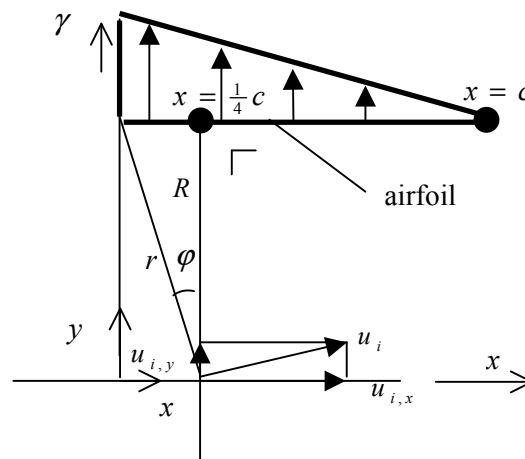
Figure 109 Triangular chord-wise vortex distribution on an airfoil with chord length c.

The bound vortex strength of an airfoil section with length dx is equal to $\gamma(x)dx$. With Biot-Savart, the induced velocity in x-direction $u_{i,x}$ at a distance r from the ¼-chord point reads (see for instance Batchelor [2])

$$du_{i,x} = \frac{\dfrac{\Gamma_0}{c}\left(1 - \dfrac{x}{c}\right)}{2\pi\, r}\cos\varphi\, dx \tag{257}$$

From Figure 109 it can be found that this results in

$$du_{i,x} = \frac{R \dfrac{\Gamma_0}{c}\left(1 - \dfrac{x}{c}\right)}{2\pi\left(R^2 + \left(\frac{1}{4}c - x\right)^2\right)} dx \tag{258}$$

The total induced velocity is found by

$$u_{i,x} = \int_0^c du_{i,x}\, dx \tag{259}$$

which gives with (258)

$$u_{i,x} = \frac{\Gamma_0}{8\pi c}\left[3\arctan\left(\frac{3c}{4R}\right) + 3\arctan\left(\frac{c}{4R}\right) + 2\frac{R}{c}\ln\left(\frac{16R^2 + c^2}{16R^2 + 9c^2}\right)\right] \tag{260}$$

At infinite distance from the airfoil, where $R \gg c$, $u_{i,x}$ has the following limit

$$u_{i,x} \overset{R \gg c}{=} \frac{\Gamma_0}{8\pi c}\left(3\left(\frac{3c}{4R} + \frac{c}{4R}\right) - 2\frac{R}{c}\left(\frac{8c^2}{16R^2 + 9c^2}\right)\right) \tag{261}$$

After some algebraic manipulation this reads

$$u_{i,x} \overset{R \gg c}{=} \frac{\Gamma_0}{4\pi\, R} \tag{262}$$

With Biot-Savart and a single-bound vortex on the airfoil with strength Γ, the induced velocity at large distances from the airfoil $R \gg c$ reads

$$u_{i,x} \overset{R \gg c}{=} \frac{\Gamma}{2\pi R} \tag{263}$$

We thus find that

$$\Gamma_0 \overset{R \gg c}{=} 2\Gamma \tag{264}$$

which gives

$$u_{i,x} = \frac{\Gamma}{4\pi c}\left[3\arctan\left(\frac{3c}{4R}\right) + 3\arctan\left(\frac{c}{4R}\right) + 2\frac{R}{c}\ln\left(\frac{16R^2 + c^2}{16R^2 + 9c^2}\right)\right] \tag{265}$$

where Γ denotes the vortex strength of a single-bound vortex at the airfoil.

The induced velocity at the shrouded actuator
Assume a distance $2R_t$ between the ¼-chord points on the airfoils. With (265), the velocity at a distance y from the symmetry axis reads

$$u_{i,x}(y) = \frac{\Gamma}{4\pi c}\left[3\arctan\left(\frac{3c}{4(R_t - y)}\right) + 3\arctan\left(\frac{c}{4(R_t - y)}\right)\right]$$

$$+ \frac{\Gamma}{4\pi c}\frac{2(R_t - y)}{c}\ln\left(\frac{16(R_t - y)^2 + c^2}{16(R_t - y)^2 + 9c^2}\right) +$$

$$\frac{\Gamma}{4\pi c}\left(3\arctan\left(\frac{3c}{4(R_t + y)}\right) + 3\arctan\left(\frac{c}{4(R_t + y)}\right)\right)$$

$$+ \frac{\Gamma}{4\pi c}\frac{2(R_t + y)}{c}\ln\left(\frac{16(R_t + y)^2 + c^2}{16(R_t + y)^2 + 9c^2}\right)$$

(266)

The average axial velocity between the airfoils is found from

$$\overline{u_{i,x}} = \frac{1}{R_t}\int_0^{R_t} u_{i,x}(y)dy$$

(267)

In order to avoid lengthy equations like (266), $\overline{u_{i,x}}$ in the vortex model is written as (190)

$$\overline{u_{i,t,shroud}} = 2\chi_a \frac{\Gamma}{2\pi\frac{1}{2}D_t}$$

That is as if two bound vortices at the ¼-chord points of the airfoils induce a velocity at the symmetry axis between the ¼-chord points. This should represent the triangular vortex distribution so that $\overline{u_{i,t,shroud}} = \overline{u_{i,x}}$. The correction factor χ_a can thus be found from

$$\chi_a = \frac{\overline{u_{i,x}}\pi D_t}{2\Gamma}$$

(268)

χ_a is calculated and plotted in Figure 110. A simple power function gives a good approximation of the lengthy equation for χ_a

$$\chi_a = 0.5051\ \ln\left(\frac{R_t}{c}\right) + 1.4447$$

(269)

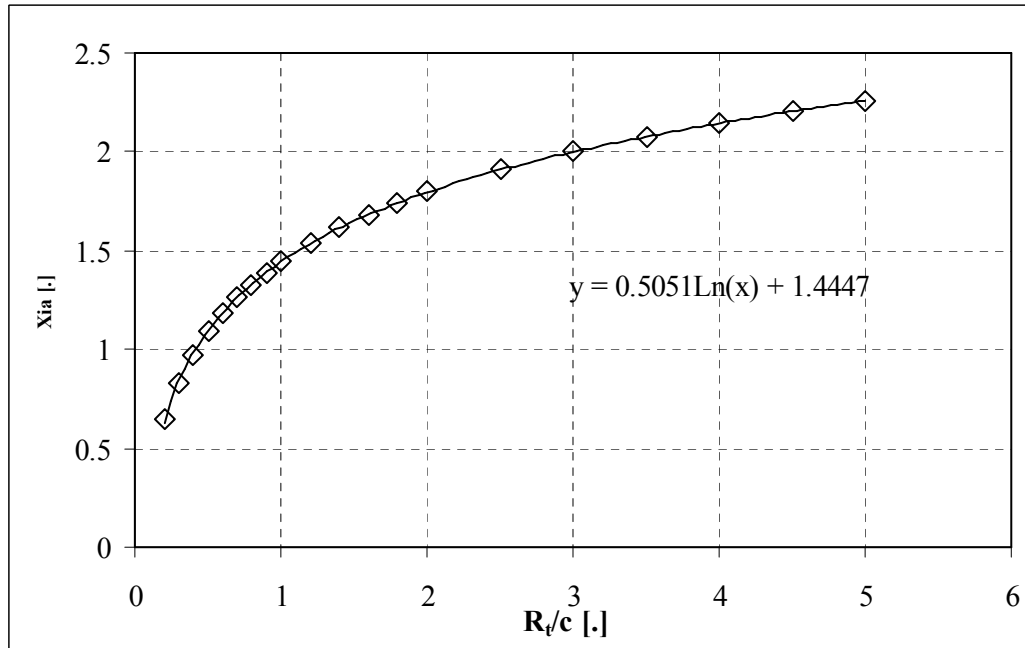for $\quad 0.2 \leq \dfrac{R_t}{c} \leq 5$.

Figure 110 χ_a **as a function of** R_t/c **for a triangular chord-wise vortex distribution on the airfoils of a 2D shrouded rotor.**

It should be kept in mind that the airfoil's orientation is assumed parallel to the flow ($\alpha \ll 1$). Fortunately, this restriction is not as severe as may be thought. The major source of $\overline{u_{i,x}}$ and $u_{i,x,axis}$ is located at the upwind side of the airfoils as that part of the airfoils has the largest bounded vortex strength. Hence, the major source of $\overline{u_{i,x}}$ and $u_{i,x,axis}$ is close to the ¼-chord point on the airfoils and introduction of α will have a small influence on $\overline{u_{i,x}}$ and $u_{i,x,axis}$.

The induced velocity of one airfoil on the ¾-chord point on the other airfoil
Assume a vortex strength $\gamma(x=0) = \Gamma_0/c$ at the leading edge of the airfoils and distance $D_t = 2R_t$ between the ¼-chord points on the airfoils. The induced velocity can be found with the same derivation that led to (265). Yet, the induced velocity at the ¾ chord point is wanted so that

$$du_{i,x} = \frac{D_t \dfrac{\Gamma_0}{c}\left(1 - \dfrac{x}{c}\right)}{2\pi\left(D_t^2 + \left(\tfrac{3}{4}c - x\right)^2\right)}dx \tag{270}$$

This gives

$$u_{i,x} = \frac{\Gamma}{4\pi c}\left[\arctan\left(\frac{3c}{4D_t}\right) + \arctan\left(\frac{c}{4D_t}\right) + 2\frac{D_t}{c}\ln\left(\frac{16D_t^2 + 9c^2}{16D_t^2 + c^2}\right)\right] \tag{271}$$

In (186), the velocity at the ¾ chord point is written as

$$u_{i,w,shroud} = \chi_s \frac{\Gamma}{2\pi D_t \left[1 + \left(\dfrac{c}{2D_t} \right)^2 \right]}$$

This should represent the triangular chord-wise vortex distribution so that χ_s is found with (271) as

$$\chi_s = \frac{D_t}{2c} \left[1 + \left(\frac{c}{2D_t} \right)^2 \right] \left[\arctan \left(\frac{3c}{4D_t} \right) + \arctan \left(\frac{c}{4D_t} \right) + 2 \frac{D_t}{c} \ln \left(\frac{16 D_t^2 + 9c^2}{16 D_t^2 + c^2} \right) \right] \qquad (272)$$
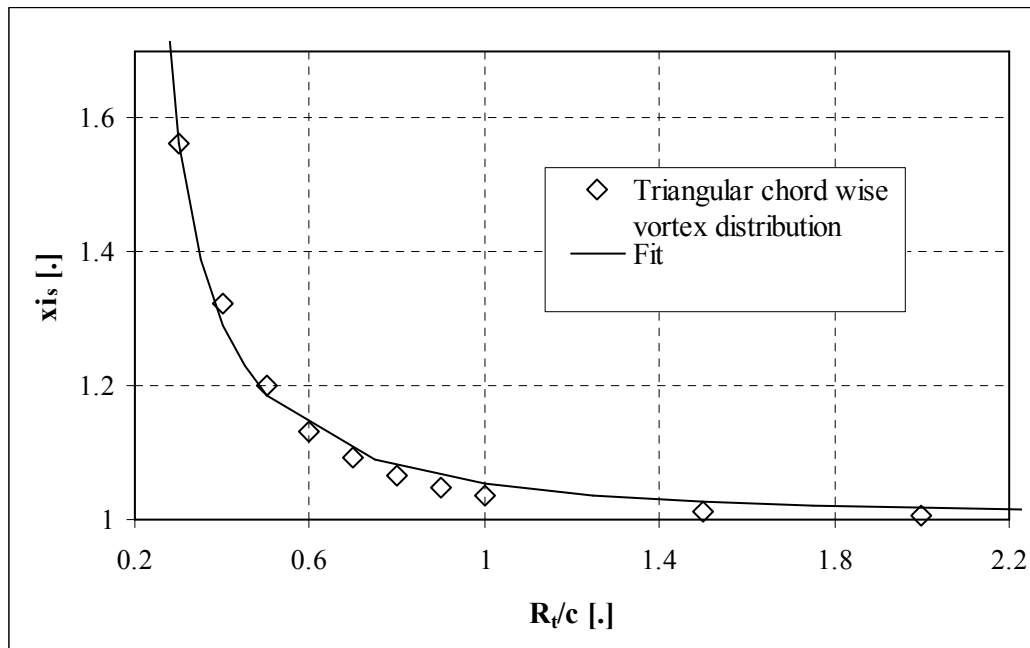
This relation is again plotted and fitted

Figure 111 χ_s as a function of R_t/c for triangular chord-wise vortex distribution of a 2D shrouded rotor.

The fit is achieved with

$$\chi_s = \frac{1}{1 + m \left(\dfrac{D_t}{2c} \right)^n} \qquad (273)$$

with $m = -0.051123$, $n = -1.621119$ for $\dfrac{D_t}{2c} \geq 0.3$.

Appendix H Suitable turbulence model for calculation of flow around airfoil

The lift of the airfoils found with CFD is compared with measurements. The CFD calculations are carried out on a C-H-grid with quadrilateral cells. The y+ value varies around the chord of the airfoil but stays below 3 so that the flow properties are calculated all the way down to the viscous sub layer. This calculation set-up should provide us with the best results, especially for the drag coefficient. The calculation conditions are mentioned in Table 40.

Table 40 calculation conditions

NACA 0018	
Chord length	1m
angle of attack	8º
Re	2.10^6
Ti	0.1%
Turbulent length scale	1
y+	<5

Several turbulence models are compared with the results in Paraschivoiu [53] at this angle of attack. The results are mentioned in Table 41.

Table 41 Comparison of CFD calculations of the lift coefficient

source	C_l	C_d
Paraschivoiu [53]	0.8439	0.0111
Ke standard	0.6533	0.0928
Ke-rng	0.7398	0.0503
Ke-real	0.7605	0.0356
Ke-real 2nd order upwind	0.785	0.0228
RSM, default options	Diverging starts at the boundaries because of grid stretching	/

Appendix I Calculated lift- and drag coefficient data for a NACA 0018 airfoil

The airfoil was tripped at 20% and the calculation was carried out with the panel code RFOIL. Beyond 2D stall, the data are synthesized from data in Paraschivoiu [53] and Jacobs [30].

Table 42 With RFOIL calculated lift coefficient of a NACA 0018 airfoil tripped at 20% at different Re numbers and angles of attack (Aoa).

Aoa	Re number					
[^{o}]	30×10^3	60×10^3	80×10^3	150×10^3	350×10^3	700×10^3
0	0	0	0	0	0	0
1	0.08226	0.08811	0.09099	0.09432	0.09765	0.10017
2	0.1638	0.17568	0.18162	0.18828	0.19503	0.20016
3	0.24381	0.26244	0.27153	0.28143	0.29178	0.29961
4	0.32121	0.34776	0.35946	0.37332	0.38745	0.39825
5	0.39429	0.43101	0.44496	0.46332	0.48159	0.49581
6	0.46089	0.51093	0.52749	0.55053	0.5733	0.59157
7	0.51804	0.58626	0.60579	0.63351	0.66114	0.68184
8	0.55836	0.65538	0.6786	0.71001	0.7389	0.7641
9	0.58878	0.71928	0.74646	0.77949	0.806	0.83682
10	0.344	0.775	0.79	0.82611	0.864	0.89937
11	0.32	0.631	0.689	0.802	0.875	0.95886
12	0.342	0.554	0.595	0.715	0.837	0.984
13	0.36	0.512	0.552	0.657	0.769	0.895
14	0.378	0.493	0.535	0.622	0.709	0.835
15	0.397	0.485	0.52	0.603	0.688	0.792
16	0.418	0.487	0.519	0.607	0.698	0.785
17	0.44	0.49	0.519	0.634	0.707	0.8
18	0.455	0.496	0.52	0.653	0.709	0.827
19	0.471	0.498	0.524	0.667	0.71	0.837
20	0.488	0.511	0.53	0.682	0.727	0.845
21	0.499	0.52	0.54	0.688	0.741	0.845
22	0.512	0.532	0.546	0.695	0.749	0.829
23	0.528	0.548	0.556	0.714	0.766	0.774
24	0.544	0.57	0.57	0.727	0.771	0.793
25	0.56	0.59	0.59	0.763	0.8	0.832

Table 43 With RFOIL calculated drag coefficient of a NACA 0018 airfoil at different Re numbers and angles of attack (aoa).

Aoa	Re number					
[^{o}]	30×10^3	60×10^3	80×10^3	150×10^3	350×10^3	700×10^3
0	0.02772	0.022491	0.020748	0.017504	0.01428	0.012212
1	0.027857	0.022596	0.020822	0.017556	0.014312	0.012243
2	0.028308	0.02289	0.021063	0.017735	0.014427	0.012317
3	0.029096	0.023384	0.021473	0.018018	0.014616	0.0131
4	0.030272	0.024108	0.022082	0.018449	0.014889	0.0136
5	0.031962	0.025106	0.022911	0.019026	0.0164	0.0142
6	0.0343	0.026429	0.024014	0.019803	0.0169	0.0149
7	0.03923	0.02921	0.025463	0.020843	0.0178	0.016
8	0.0428	0.035	0.027416	0.02297	0.02	0.0173
9	0.0486	0.0415	0.030114	0.02616	0.0235	0.0195
10	0.06	0.0531	0.045	0.03215	0.0275	0.0235
11	0.09	0.0792	0.07	0.049	0.0419	0.0359
12	0.1137	0.1062	0.099	0.078	0.0646	0.0564
13	0.135	0.1302	0.123	0.102	0.0872	0.0763
14	0.155	0.1507	0.1435	0.1225	0.1046	0.093
15	0.1753	0.1725	0.1648	0.1438	0.1269	0.11
16	0.195	0.1934	0.1861	0.1651	0.1479	0.13
17	0.215	0.215	0.2066	0.1856	0.1703	0.1539
18	0.235	0.235	0.2288	0.2078	0.1904	0.1749
19	0.2579	0.2579	0.25	0.229	0.2137	0.1982
20	0.28	0.28	0.275	0.254	0.2388	0.2224
21	0.305	0.305	0.3	0.2836	0.272	0.258
22	0.3279	0.3279	0.3245	0.3128	0.3	0.2904
23	0.354	0.354	0.35	0.3416	0.3329	0.3256
24	0.3746	0.374	0.3783	0.3717	0.3662	0.3594
25	0.4	0.4	0.4	0.4018	0.4009	0.4018

Appendix J Quick siting guideline

First, a good site for a small wind turbine is characterized by a high average wind speed. In the built environment, such sites are found above the average height of the buildings. We are therefore looking for the higher buildings to site our wind turbine (section 2.2). Moreover, a wind turbine sited between buildings suffers from turbulence and the resulting frequent changes in wind direction and high fatigue load. Such high fatigue load is off course coupled with the probability of damaging the wind turbine and the risks for trespassers that could be hit by (part of) a fractured blade (section 2.2). Furthermore, the frequent changes in wind direction cause frequent yawing of a HAWT so that the HAWT is hardly aligned with the flow. Such average misalignment causes a drop in energy yield (section 5.2). A VAWT is better suitable to perform in such turbulent environment, as yawing is not required for a VAWT. But the rotor size of the VAWT should be small in order to avoid the unsteady effects coupled with frequent changes in wind direction and in order to profit from the local speed up close to buildings (section 2.2).

Secondly, the concentrator effect of the building in combination with the wind rose should be considered. The concentrator effect of the building should fit the wind rose. Acceleration of the undisturbed wind speed by the building for only one wind direction and deceleration for all other wind directions in an omni-directional wind climate is not very profitable for the energy yield. Table 39 in section 8.2.2 gives a quick start for the choice of the concentrator effect in combination with the wind rose.

Thirdly, the most suitable wind turbine for the site should be chosen. Compared to drag driven wind turbines, lift driven wind turbines have better prospects to become economic (section 2.1.4). The choice between a VAWT and a HAWT depends nevertheless on several additional issues. The frequent wind direction changes in the built environment are already mentioned. On roofs of sharp edged buildings the flow angle should also be considered. The flow direction close to the edges of a sharp edged building is not parallel to the roof and as a consequence, a HAWT in that flow from below shows a power drop compared to a HAWT in horizontal flow. The power output of a small H-Darrieus or lift driven VAWT increases in flow from below. The H-Darrieus is therefore preferred for that flow. For concentrator buildings such as the plate concentrator and the shrouded configuration, the HAWT is preferred because the rotor of an H-Darrieus is not able to extract power from the total rotor surface.

Last but not least, there are numerous non-aerodynamical issues that should be tackled for a successful siting of a small wind turbine close to a building. Some important issues are: safety risks, noise emission, introduction of vibrations into the building and shadow flicker by the rotor blades (section 2.2). Most of these issues can be technically solved. Yet, they need a careful study as they can prevent successful siting.

Appendix K Curriculum vitae author

Sander Mertens is geboren op 21 Mei 1968 in Haarlem. Hij studeerde van 1987 tot 1991 Werktuigbouw aan de Hogeschool Haarlem. Na het behalen van zijn diploma Werktuigbouw studeerde hij van 1991 tot 1996 Technische Natuurkunde aan de TU Delft. Als breed opgeleid natuurkundig en werktuigkundig ingenieur heeft hij toen een tweetal jaren bij Syntens als consultant gewerkt op het gebied van innovaties voor het midden en klein bedrijf. Hierna maakte hij de overstap naar Stork Product Engineering als onderzoeker supersone aardgas droging. Toen ook de geldstroom voor dit onderzoek opdroogde werkte hij van 1999 tot 2005 als Toegevoegd Onderzoeker bij de sectie Windenergie van de Technische Universiteit Delft. Vanuit deze functie kon hij aan een promotie schrijven over kleine wind turbines nabij gebouwen. Na het beëindigen van zijn onderzoek ging hij naar DHV waar hij werkt als senior consultant en trekker van de Wind groep. Zijn groep Sustainable Wind realiseert in de diverse projecten de ombuiging van windhinder naar wind benutten door het ontwerpen met wind bij opdrachtgevers te introduceren.